

Heart optogenetics

for *in vivo* intrinsic and extrinsic cardiac applications in mice

von Pauline, Marie, Cécile Frech

Inaugural-Dissertation zur Erlangung der Doktorwürde
der Tierärztlichen Fakultät der Ludwig-Maximilians-Universität
München

Heart optogenetics
for *in vivo* intrinsic and extrinsic cardiac applications in mice

von Pauline, Marie, Cécile Frech
aus Colmar (Frankreich)

München 2022

Aus dem Veterinärwissenschaftlichen Department der Tierärztlichen Fakultät der
Ludwig-Maximilians-Universität München

Lehrstuhl für Tierphysiologie

Arbeit angefertigt unter der Leitung von: Univ.-Prof. Dr. Thomas W. Göbel

Angefertigt am Deutschen Zentrum für Herzinsuffizienz des Universitätsklinikums
Würzburg

Mentorin: PD Dr. med. Anna Frey

Gedruckt mit Genehmigung der Tierärztlichen Fakultät
der Ludwig-Maximilians-Universität München

Dekan: Univ.-Prof. Dr. Reinhard K. Straubinger, Ph.D.

Berichterstatter: Univ.-Prof. Dr. Thomas W. Göbel

Korreferenten: Univ.-Prof. Dr. Heidrun Potschka
Prof. Dr. Gerhard Wess
Univ.-Prof. Dr. Bernhard Aigner
Univ.-Prof. Dr. Nikolai Klymiuk

Tag der Promotion: 30. Juli 2022

TABLE OF CONTENTS

I.	INTRODUCTION	1
II.	LITERATURE REVIEW	3
1.	Optogenetics	3
1.1.	Origins, mechanisms and expression of opsins in optogenetics	3
1.1.1.	Origins of opsins and their applications	3
1.1.2.	Mechanism of channelrhodopsin activation	4
1.1.3.	Opsin adaptation to experimental purposes	5
1.1.4.	Opsin expression in specific cell types	6
1.2.	Development of optogenetics	7
1.2.1.	Optogenetics in the central nervous system	7
1.2.2.	Optogenetics in the peripheral nervous system	7
1.2.3.	Cardiac optogenetics	8
2.	Electrical conduction system of the heart	9
2.1.	Structural organization of the heart	9
2.2.	Action potential in cardiomyocytes and pacemaker cells	10
2.3.	Tuning of pacemaker activity	11
2.3.1.	Specific channels for funny currents in pacemaker cells	11
2.3.2.	Interactions of pacemaker cells with the autonomous nervous system	12
3.	CD4⁺ lymphocytes	13
3.1.	Development and function of T cells	13
3.2.	The role of T cells in the infarcted heart	14
3.2.1.	T cell mobilization in the context of myocardial injury	14
3.2.2.	Myocardial repair and scar formation	16
3.3.	Activation and polarization of T cells	16
3.3.1.	Cytokines and their receptors	16
3.3.2.	T cell chemotaxis	16
III.	MATERIALS AND METHODS	19
1.	Mice and animal welfare	19
1.1.	Source, housing and transport	19
1.1.1.	Mice source	19
1.1.2.	Mice housing	19
1.1.3.	Mice transport	20
1.2.	Mouse strains	21
1.3.	Animal welfare during experiments	21
1.3.1.	Severity classification of the procedures	21
1.3.2.	Scoring protocol	22
1.4.	Ethical aspects	24
2.	Technical aspects of optical stimulation at heart level	24
2.1.	Selecting the appropriate wavelength	24
2.2.	Optogenetics system	26
3.	Mice preparation prior to device implantation	27
3.1.	Drugs and pain management	27
3.1.1.	Perioperative analgesia	27
3.1.2.	Intraoperative anesthesia	28
3.2.	Preparations and anesthesia procedure	29
3.2.1.	Surgical instruments	29
3.2.2.	Anesthesia procedure	29

Table of contents

3.3.	Preparation of the surgical field	30
4.	Monitoring the effect of the device implantation on the myocardium	31
4.1.	Weight development	31
4.2.	Histological assessment of heart damage	31
4.2.1.	Principle of histology and Masson's trichrome staining	31
4.2.2.	Organ removal and processing	32
4.3.	Echocardiography	33
4.3.1.	Principle of echocardiography	33
4.3.2.	Echocardiographic measurements to assess heart function	33
4.3.3.	Performing echocardiography in anesthetized mice	36
4.4.	Computed tomography scan for <i>in situ</i> representation of the device implantation	36
4.4.1.	Principle of single-photon emission computed tomography	36
4.4.2.	Mouse preparation and imaging	37
5.	Opsin expression in intrinsic cardiac cells of interest via a viral vector	38
5.1.	Strategy for specific spatial opsin expression	38
5.1.1.	AAV as viral vector	38
5.1.2.	Cre-dependent recombination of the floxed expression cassette	39
5.1.3.	Combination of viral vector and Cre-mice for specific spatial expression of the opsin	39
5.2.	Selecting the appropriate AAV vector and the expression cassette	40
5.2.1.	Selection of the promoter driving the construct expression	40
5.2.2.	Selection of the capsid to transduce the cells of interest	40
5.2.3.	Selection of the appropriate expression cassette	41
5.2.3.1.	Selection of the opsin	41
5.2.3.2.	Additional construct elements	41
5.3.	Production of AAV vectors	43
5.4.	Systemic AAV injection	43
6.	Monitoring heart rate <i>in vivo</i> and viral transduction of intrinsic cardiac cells	44
6.1.	Electrocardiography to record heart rate modulation	44
6.1.1.	Principle of electrocardiography	44
6.1.2.	Electrode assembly and implantation in mice	45
6.1.3.	Electrocardiography recording and heart rate calculation	47
6.1.4.	Optogenetic stimulation protocol for heart rate modulation	48
6.2.	Quantitative polymerase chain reaction to assess opsin expression	49
6.2.1.	Principle of SYBR Green qPCR	49
6.2.2.	Primer design for qPCR	50
6.2.3.	Organ removal and tissue preparation for qPCR	51
7.	Engineering photoactivable CD4⁺ lymphocytes	53
7.1.	Development of photoactivable lymphocytes	53
7.1.1.	Origin of the photoactivable chemokine receptor	54
7.1.2.	Adaptation of the photoactivable chemokine receptor	54
7.2.	Production of photoactivable lymphocytes	55
7.2.1.	Spleen collection from a donor mouse on day 0	55
7.2.2.	CD4 ⁺ lymphocyte isolation on day 0	56
7.2.3.	Transduction of isolated murine CD4 ⁺ lymphocytes on day 1	57
7.2.4.	Proliferation of transduced CD4 ⁺ lymphocytes from day 2 to day 4	58
7.2.5.	Assessment of the viral transduction rate on day 4	60
7.3.	Adoptive PA-CXCR4 cell transfer	60
7.3.1.	Finalization of the cell preparation prior transfer on day 5	60
7.3.2.	Injection of photoactivable CD4 ⁺ lymphocytes	60
7.4.	<i>In vitro</i> assessment of PA-CXCR4-lymphocyte photoactivation	61
7.4.1.	<i>In vitro</i> readout for lymphocyte activation	61

Table of contents

7.4.2.	<i>In vitro</i> validation of photoactivation of the engineered cells	61
8.	Monitoring light-induced T cell migration	62
8.1.	Whole-body clearing for visualization of intrathoracic illumination	62
8.1.1.	Principle of whole-body clearing	62
8.1.2.	Whole-body clearing protocol to visualize intrathoracic light scattering	63
8.2.	Organ collection after <i>in vivo</i> illumination	64
8.3.	Flow cytometry analysis for the detection of PA-CXCR4 cells	64
8.3.1.	Principle of fluorescence and immunostaining	64
8.3.2.	Principle of multicolor flow cytometry analysis	65
8.3.3.	Flow cytometry-based discrimination of transferred PA-CXCR4 lymphocytes	65
8.4.	Light sheet microscopy for the detection of PA-CXCR4 cells	69
8.4.1.	Immunofluorescence	69
8.4.2.	Principle of Light Sheet Fluorescence Microscopy	70
8.4.3.	LSFM staining and clearing protocol for detection of PA-CXCR4 lymphocytes in the thymus	70
8.4.4.	LSFM image acquisition and processing for detection of PA-CXCR4 lymphocytes	71
9.	Statistics and figures	73
IV.	RESULTS	75
1.	Development of a surgical procedure for device implantation on the beating heart	75
1.1.	Device preparation and mouse positioning for the implantation	75
1.2.	Intrathoracic device implantation	76
1.3.	Surgery related effects	79
1.3.1.	Weight evolution	79
1.3.2.	Histological assessment of myocardial damage	80
1.3.3.	Echocardiographic assessment of left and right ventricular function	82
2.	Light-induced manipulation of the electrical conduction system of the heart and intrinsic cholinergic cardiac ganglia	84
2.1.	Experimental design to modulate the heart rate	84
2.2.	Heart rate modulation under optogenetic stimulation	84
2.2.1.	Optogenetic stimulation of cardiac pacemaker cells	85
2.2.2.	Optogenetic stimulation of cardiac cholinergic cells	87
2.3.	Verification of opsin expression in intrinsic cardiac cells of interest with qPCR	91
2.3.1.	Verification of primer specificity	91
2.3.2.	Opsin and RFP expression in the target cells	92
3.	Light-induced PA-CXCR4 lymphocyte migration	94
3.1.	Experimental design to attract PA-CXCR4 lymphocytes into the myocardium	94
3.2.	<i>In vitro</i> photoactivation of PA-CXCR4 lymphocytes	95
3.3.	Visualization of intrathoracic light scattering	96
3.4.	<i>In vivo</i> migration of PA-CXCR4 lymphocytes	97
3.4.1.	Flow cytometry-based detection of PA-CXCR4	97
3.4.2.	Spatial distribution of PA-CXCR4 in the illuminated thymus	100
V.	DISCUSSION	103
1.	Adaptation of wavelength and device to the purpose	103
1.1.	Choice of the wavelength	103
1.2.	Choice of the device and adaptation for intrathoracic implantation	104
2.	Surgery	105
2.1.	Development of a novel surgical technique to illuminate the heart in freely moving mice	105

Table of contents

2.2.	Surgery effects on general condition, heart structure and heart function _____	106
3.	Optical heart rate modulation via intrinsic heart cells _____	107
3.1.	Rationale and experimental design for heart rate modulation _____	108
3.2.	Focused illumination of the region of interest in freely moving mice _____	109
3.2.1.	Modulation of the pacemaker activity of intrinsic cardiac HCN4 cells _____	109
3.2.2.	Modulation of intrinsic cardiac cholinergic cells _____	110
3.3.	Verification of opsin expression in the target cells after systemic delivery _____	111
3.4.	Conclusion: <i>in vivo</i> model for heart rate modulation _____	112
4.	Optical T cell migration _____	112
4.1.	Rationale and experimental design for the migration of photoactivable lymphocytes_	113
4.2.	Properties of <i>in vitro</i> photoactivation and intrathoracic illumination pattern _____	113
4.3.	<i>In vivo</i> migration of extrinsic photoactivable lymphocytes _____	114
4.4.	Conclusion: <i>in vivo</i> model for optical control of lymphocyte migration _____	115
5.	Translational outlooks and limitations of cardiac optogenetics _____	116
VI.	SUMMARY	119
VII.	ZUSAMMENFASSUNG	121
VIII.	ABBREVIATIONS	123
IX.	REFERENCES	127
X.	APPENDIX	147
1.	Individual heart rate modulation in HCN4-Cre mice _____	147
2.	Digital appendix _____	147
XI.	INDEX OF TABLES	149
XII.	INDEX OF FIGURES	151
XIII.	ACKNOWLEDGMENT	153

I. INTRODUCTION

Proper organism function relies on finely balanced communication between different organs. The cardiovascular system represents a closed system providing the whole body with blood and has a vital role in homeostasis. Heart failure is the result of structural changes leading to an impairment of the heart function. In 2021, prevalence of heart failures was estimated around 1 to 2% in adults and increases with age to reach values around 10% in people aged over 70, thus represents a leading cause of hospitalization and death worldwide [1]. The aetiology of heart failure varies and this pathologic condition often shows comorbidities such as diabetes, arrhythmia, hypertension and neuropsychiatric disorders. Indeed, 51% of patients with coronary heart diseases suffer from depression (reviewed in [1, 2]); moreover, the severity of both conditions, heart failure and depression, positively correlates [3]. Remodeling processes influence the grade of heart failure and are characterized by the mobilization of different immune cell populations to specific time points in order to coordinate scar formation in the injured tissue (reviewed in [4]). The cellular interactions at heart and organism level play a major role in the development of heart diseases, but the networks ensuring homeostasis as well as underlying pathomechanisms remain poorly understood.

Optogenetics is a new technology discovered in the early 2000s combining optics and genetics ([5] and reviewed in [6]). This method provides high spatiotemporal accuracy through activation or inhibition of specific cell populations at millisecond-scale with light [7]. Optogenetics was first established for application in the central nervous system (CNS) but is increasingly gaining ground to study peripheral circuits within and between organs (reviewed in [8]).

To date, no model for cardiac optogenetics has been established in freely moving animals. In order to understand causal relationships between the heart function and its connections within the organism on a larger scale, modulating approaches are required. Cardiac optogenetics represents a new way to control cellular activity with high spatiotemporal precision and can help to gain insight, on the one hand, into underlying mechanisms of heart-brain interactions, and on the other hand, into myocardial healing mechanisms.

With the present work, we sought to achieve fundamental and preliminary milestones to highlight the heart function at the core of complex mechanisms by establishing the first *in vivo* models for cardiac optogenetics. An intrinsic as well as an extrinsic approach were developed in order to meet the purposes of two overarching goals. Our first aim was the optogenetic manipulation of heart rate (HR) via intrinsic control of either pacemaker or cholinergic cardiac cells (figure 1, B) in order to dissect the circuitry linking the heart to other organs - such as the brain- with the ultimate goal to better understand relations between heart dysfunction and anxiety disorders. Second, we aimed at controlling the trafficking of extrinsic cells within the heart (figure 1, C) as a powerful tool to improve the outcome after myocardial infarction (MI), which secondarily leads to heart failure. In particular, mobilization of CD4⁺ lymphocytes subsets can exert a cardioprotective effect in healing processes [9, 10]. Both aspects, intrinsic HR modulation and extrinsic cell-trafficking control, share a common technical bottleneck: bringing light to the heart (figure 1, A).

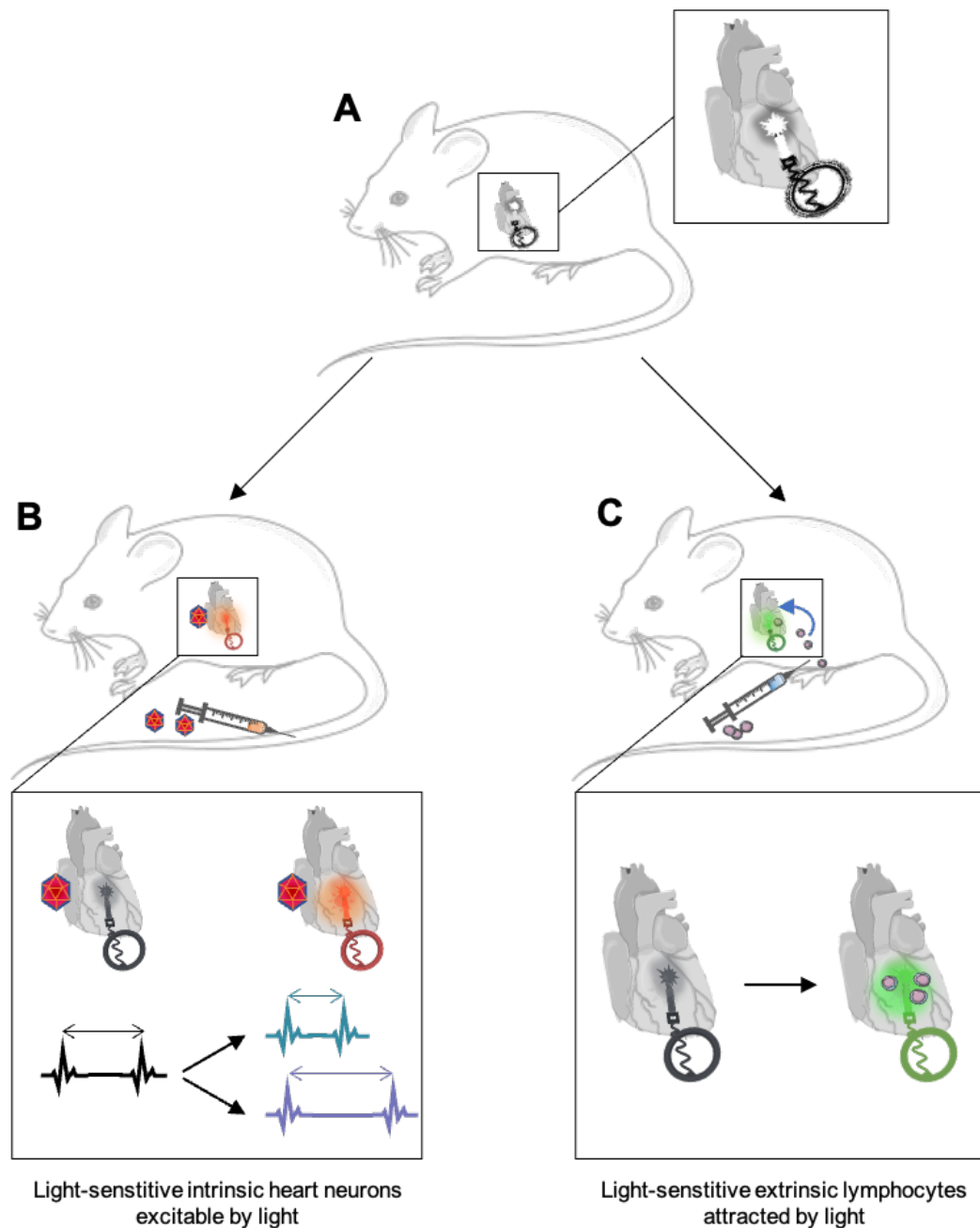


Figure 1| Milestones of the establishment of *in vivo* cardiac optogenetics based on two approaches with a common bottleneck

(A) Technique development to illuminate the heart (bottleneck): implantation of a light emitting device on the beating heart. (B) Systemic administration of a viral vector to deliver the light-sensitive protein in intrinsic cardiac cells. Subsequent actuation of the cells of interest with light to achieve HR modulation and induce either HR increase or decrease. (C) Intraperitoneal injection of engineered photoactivable cells to be resorbed and reach the circulation. Light-induced attraction of photoactivable cells into the heart to study their effect on the tissue.

II. LITERATURE REVIEW

1. Optogenetics

Optogenetics represents a novel technology in constant development since the early 2000s. In 2005 Deisseroth et al. introduced in vivo optogenetics in mice as a method resulting from the advancement of different techniques including optical (fluorescence microendoscopy, imaging dynamics at cellular level) and genetical methods (transgenic mouse strains) in order to control neuronal activity at millisecond-scale (reviewed in [5, 11]). Optogenetics relies on the expression of light-sensitive proteins, called opsins, in the cells of interest and adapted optical stimulation. Photosensitive proteins were known to regulate transmembrane ion flow in microorganisms [12], but only in 2003 a study revealed the feasibility to express microbial opsins in mammalian cells inducing depolarization by illumination [13]. Since then, optogenetics has led to groundbreaking insight into the brain function and has widened our knowledge in the field of physiology, pathology, cognition and behavior by manipulating cellular activity in intact tissues (reviewed in [8]).

1.1. Origins, mechanisms and expression of opsins in optogenetics

1.1.1. Origins of opsins and their applications

Opsins are divided in bacterial and animal opsins also known as type-I, respectively type-II rhodopsins (reviewed in [14]). Microbial rhodopsins can be pumps, channels and light-sensors (see section II.1.1.2. figure 2, A). Channelrhodopsin 1 and 2 (ChR1, ChR2) were discovered in green algae (*Chlamydomonas*) where they generate photocurrents as depolarizing light-gated cation channels to induce oriented swimming towards light [15]. The discovery of ChR2 is at the origin of optogenetics and is the most used opsin in the field (reviewed in [8]). ChR2 absorbs maximally at 460 nm and functions itself as non-specific cation channel. Exposure to this wavelength induces a conformational change of the channel allowing cations (hydrogen, sodium, potassium and calcium ions) to diffuse passively down their concentration gradients, leading to depolarization of the plasma membrane, therefore triggers action potentials. Indeed, after its expression in *Xenopus* oocytes, HEK 293 (Human embryonic kidney cells) and BHK (baby hamster kidney cells) cells, photostimulation led to depolarization. Besides fast activation, ChR2 closes rapidly and is able to respond to light pulses from 1 - 40 Hz [16], thus providing a new tool to control activity of mammalian cells with high temporal accuracy [13].

Besides depolarization, hyperpolarization can be induced by bacteriorhodopsin and halorhodopsin expressed in *Archea* (*Halobacterium salinarum*). Indeed, in halorhodopsin, the first discovered opsin [12], light induces chloride inflow into the cell, while bacteriorhodopsin is a light-driven outward proton pump (see section II.1.1.2. figure 2, A; reviewed in [14]). Those opsins are used for inhibitory purposes to silence neural activity for instance (reviewed in [8]).

Sensory rhodopsins belong to the microbial opsin group but function as phototactic or photophobic receptors to induce movement of bacteria (*Halobacterium salinarum*, *Salinibacter*) towards or, respectively, away from the light source [17].

In contrast to microbial opsins, animal opsins are specialized G-protein coupled receptors (GPCR) playing a role as photoreceptors in vertebrate and invertebrate eyes. For example, the rhodopsin found in rod and cones in vertebrate activates cyclic guanosine monophosphate (cGMP) phosphodiesterase which in turn activates secondary reaction cascade and ultimately leads to cellular response [18]. Animal rhodopsins are highly sensitive and capable of converting a single photon into physical stimulus. Among animal opsins, bovine visual rhodopsin is a model for the study of GPCRs (reviewed in [14]).

1.1.2. Mechanism of channelrhodopsin activation

Rhodopsins are photoreceptors able to sense and respond to light. Microbial and animal rhodopsins are composed of a chromophore, retinal, covalently bound to the opsin, a protein composed of seven transmembrane alpha-helices (figure 2, B and C). Retinal derives from β -carotene and undergoes photoisomerization on a femtosecond timescale from all-*trans* to 13-*cis* in microbial rhodopsins or 11-*cis* to all-*trans* configuration in animal rhodopsins [19]. Under illumination, retinal is able to perform photoconversion thus absorbs photon and converts it into an electrical current. By appropriate illumination (wavelength, intensity), the change of retinal conformation opens the transmembrane protein to which it is bound, enabling the ions to flow through. Intracellular charge shifts occur and, in turn, initiate cascades of secondary reactions (reviewed in [14, 18]). Most rhodopsins respond to light between 400 and 700 nm [14]. Color tuning of the opsin is determined by the efficiency of photon absorption, which is influenced by interactions of the chromophore with surrounding proteins. The protonation state of the chromophore is crucial too. Both, chromophore-protein interactions and protonation state, determine the energy gap between ground and excited state of the retinal upon exposition to photons (figure 2, C). The larger the gap between the ground and excited state, the lower the wavelength of electronic excitation (blue-shifted opsins); in opposite, a small energy gap leads to a red-shift of the absorption [14]. When light stimulation stops, the channel closes, ion permeation is interrupted, thereby restoring the resting membrane potential of the cells.

In optogenetics, the stimulation of the opsins is mostly achieved with light-emitting diodes (LED), or lasers coupled to an optical fiber adapted in size and shape for implantation in laboratory animals. The use of an external implant for light excitation is often bound to an invasive implantation procedure leaving the animal with physical tethers, which in turn may influence the behavior and negatively impact experiment reproducibility. Implantations of miniaturized wireless devices therefore represent promising alternatives for consistent performance of experiments with devices delivering the necessary light output for tissue penetration and opsin activation (reviewed in [20]).

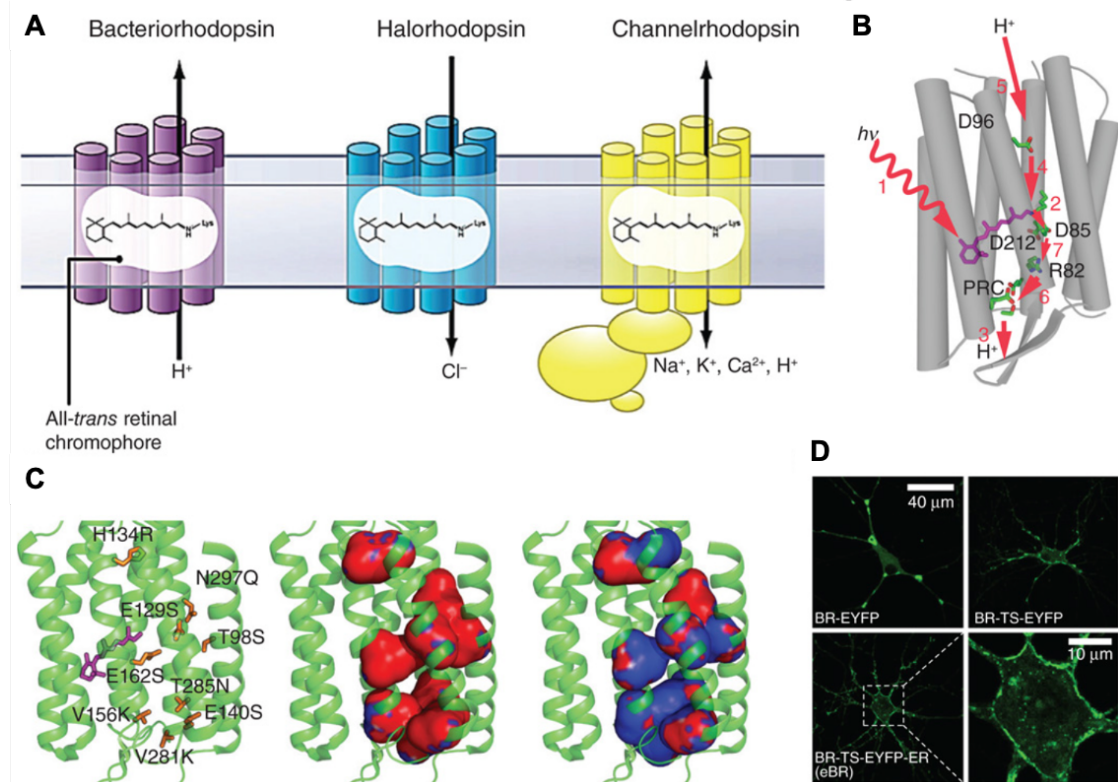


Figure 2| Structure and activation mechanism of microbial opsins

The biochemical foundations of the study of microbial light-activated proteins. **(A)** The three major classes of microbial proteins used for single-component optogenetics (adapted from ref. 5, Elsevier). **(B)** Light-activated transmembrane current mechanism of the proton pump bacteriorhodopsin (BR)⁵. Photon ($h\nu$) absorption initiates a conformational switch, leading to discontinuous proton transfers involving Asp85, Asp96, Asp212, Arg82 and the proton release complex (PRC), and net charge movement across the membrane. The core concept of single-component light-activated transmembrane ion conductance had become textbook material by the 1980s⁸ (reproduced from ref. 5, Elsevier). **(C)** Elucidation of channel-type conductance. The channelrhodopsin crystal structure⁹ revealed positioning of transmembrane helices (green), the binding pocket of *all-trans* retina (purple), and angstrom-scale positioning of residues lining the pore (left). In the course of testing the pore model, structure-guided mutagenesis¹⁰ of the residues in orange (left) shifted expected pore electrostatics from largely negative (red, center) to largely positive (blue, right) and switched ion selectivity from cation to anion (chloride) conductance¹³. **(D)** All three classes of microbial opsin-derived proteins suffer to some degree from formation of aggregations within metazoan host cells^{18,50,51}, but in all cases this can be addressed with membrane trafficking motifs borrowed from mammalian channels^{18,50,51,90}. Shown: original BR fused to enhanced yellow fluorescent protein (EYFP); upper left depicts accumulations seen with wild-type BR expression in mammalian neurons, upper right shows the effect on surface membrane expression of adding a neurite targeting motif (TS), and the lower row shows the effect of combined TS and ER (endoplasmic reticulum export) motif provision (reproduced from ref. 18, Elsevier). Adapted from Deisseroth et al. [6]

1.1.3. Opsin adaptation to experimental purposes

Opsins occur naturally in algae, fungi, prokaryotes and eukaryotes but were also adapted for experimental purposes to enable bidirectional control of cell lines by either inhibiting or activating them (reviewed in [21, 22]). As mentioned in section 1.1.1., microbial opsins can induce depolarization (channelrhodopsins) or hyperpolarization (bacteriorhodopsins and halorhodopsins). Through engineered modifications, the responsiveness of the opsins could be adapted to different activation wavelengths, pulse frequencies and light intensities (reviewed in [8, 16]). Step-function opsins represent an

alternative to classical opsins to circumvent damages caused by high light intensities and are able to maintain cell activation over several minutes without light [23], at the cost of precise temporal control by the experimenter. The limited penetration depth of blue light could be circumvented by shifting the responsiveness towards red light (reviewed in [24]). Longer wavelengths penetrate deeper into tissue as they are less absorbed, reflected, and scattered than shorter wavelengths (see section III.2.1.).

In a nutshell, the diversity of opsins makes their deployment in a broad range of application possible. Moreover, the kinetics of opsins provide high spatial and temporal resolution with photoactivation within a millisecond (reviewed in [24, 25]).

1.1.4. Opsin expression in specific cell types

Depending on the tissue, transduction can be achieved by electroporation, viral transduction and transgenesis [26].

Electroporation uses electric pulses to permeate membranes and enable subsequent influx of DNA. This technique is rather used for selective transduction in a particular developmental stage in embryonic or perinatal rodents [27].

The use of transgenic animals expressing the opsin linked to a specific promoter represents a safe and consistent way to have the light-sensitive protein in the cells of interest. Furthermore, limitations due to the use of viral vectors, including hurdles from the production to the injection, can be overcome (reviewed in [28]). However, the Cre/*lox*-system, which combines the injection of floxed viral vectors and transgenic Cre-driver transgenic mouse strains, enlarges the field of possibilities through the numerous ways to associate opsins and mouse strains [29].

The Cre/*lox*-system offers the possibility to achieve opsin expression restricted to a specific cell type [30]. Such spatial specificity is crucial to understand the function of defined cell populations and required to dissect the effects related to their stimulation (see section II.1.2.1.). The use of lentiviral or adeno-associated viral vectors (AAV) to deliver recombinase-dependent opsins *in vivo* (Cre/*lox* models) is widely employed and represents a strategy commonly adopted to achieve the expression of light-sensitive proteins in mice. The viral vector containing the opsin can either be associated to a transgenic animal line expressing the Cre recombinase in the target cells [30], or can be used in a Cre recombinase-based two-virus strategy by combining it with a second viral vector expressing the Cre recombinase [31]. Opsin expression can be improved by local vector delivery in the anatomical region of interest [24]. Lentiviral vectors have a large packaging size (10 kbp) compared to AAV (4.7 kbp) enabling the delivery of longer gene sequences. However, lentiviruses are larger in size (100 nm) than AAV (20 nm), what could restrict their diffusion into the tissue [32]. Another major difference between lentiviruses and AAV is that the former integrate into the host genome, while the latter remain episomal. Thus, the use of AAV represents a safer method, providing a translational potential as a tool for *in vivo* gene therapy [33]. Indeed, viral transduction represents a promising approach with translational potential for clinical

applications [26]. In addition to localized Cre-expression in transgenic mouse strains, the use of a cell specific promoter can further increase the specificity of opsin expression in the cells of interest [34]. Nonetheless, limitations to the use of viral vectors are reported such as the variability in vector genome production, the lack of understanding the mechanisms of vector uptake and intracellular trafficking, and immunogenic properties (reviewed in [35]).

1.2. Development of optogenetics

1.2.1. Optogenetics in the central nervous system

Optogenetics is a revolutionary tool in neurosciences and is used to selectively inhibit or activate cell populations of interest with different functions. It already enabled to better understand neuronal circuits and the role of brain in general states as well as in pathological conditions. For instance, anatomical and physiological pathways for normal sensory, motor and cognitive functions were mapped to better understand neuropsychiatric diseases such as epilepsy and alcohol addiction (reviewed in [36] and [37]). Neural circuits linking homeostatic needs such as sleeping and eating were also investigated by the means of optogenetics [38]. Furthermore, selective optical activation or inhibition of glutamatergic fibers linking the basolateral *Amygdala* to the *Nucleus accumbens*, demonstrated the role of this neuronal circuit in reward-related behavioral responses [39]. Pathways underlying anxiety and fear were dissected highlighting the function of the medial prefrontal cortex and the basomedial *Amygdala* and showed that activation of the latter reduced fear-related behavior [40]. Neuronal circuits involving the central nucleus of the *Amygdala* and the periaqueductal grey in defensive behavior such as freezing and flight were elucidated too [41]. Optogenetics also enabled to gain insight into pain mechanisms, where the role of spinal microglia was demonstrated in nociception and generation of chronic pain [42]. Moreover, optogenetic stimulation was able to promote nerve regeneration through triggering the secretion of various factors upon light exposure as well as promote neuroplastic effect in the brain [43]. Further, myelin repair in neurons of the neocortex expressing ChR2 in a model of multiple sclerosis was achieved under repeated photostimulation [44]. Those various examples illustrate the use of optogenetics in understanding both, physiological as well pathological mechanisms, and reflect its translational potential to provide new therapeutics. Many studies were conducted in the CNS, but more recently, optogenetic tools started to be used in the PNS [8].

1.2.2. Optogenetics in the peripheral nervous system

Application of optogenetics in the periphery has started in the second decade of this century. As in the CNS, the use of optogenetics in the periphery is a groundbreaking tool and, compared to traditional stimulation methods, such as electrical, magnetic and pharmacological stimulation, provides high spatial and temporal precision (reviewed in [8]). First, the ability to control peripheral nerves was demonstrated in motor neurons by measuring muscle activity under optical stimulation [45]. Then, neuronal

regeneration was promoted by optogenetic calcium release [46]. Moreover, light-induced release of neurotrophic factors also supported neurite outgrowth and axonal regeneration *in vitro* [47]. In culture, the optical control of differentiation of pluripotent stem cell-derived neurons as well as optical induction of Schwann cell proliferation was reported; thus, optogenetics could be a powerful tool to support peripheral nerve regeneration and myelination after injury, and to implement treatments for neurodegenerative pathologies [48, 49].

1.2.3. Cardiac optogenetics

The development of cardiac optogenetics started almost ten years ago. In 2010, optical pacing of developing zebrafish hearts was performed; halorhodopsin or ChR2 were expressed in pacemaker cells to achieve both, activation and inhibition. The maturation of the electrical conduction system (ECS) and its localization during embryonic development were followed by illuminating different cell patches. Heart pacing and arrest were achieved, and the stimulation of only a few pacemaker cells initiated heartbeats in zebrafishes [50]. Since non-mammalian and mammalian ECS present similar features and developmental stages, those results encouraged the establishment of cardiac optogenetics in mammals [51].

Optical control of murine hearts *in vitro* and *in vivo* was described in 2010 too, using ChR2 constitutively expressed in the myocardium [52]. After successful optogenetic stimulation of single cardiomyocytes *in vitro*, the method was applied to a syncytium of heart cells to initiate beats propagating through a two-dimensional cell layer of connected cardiomyocytes. In the next step, optical stimulation was performed in adult hearts, and depolarization of cardiomyocytes could be achieved with millisecond light pulses. Atrial and ventricular pacing were successfully performed leading to longer atrial depolarization and ectopic heart beats, respectively. Noteworthy, depolarization of atrial cells required higher light intensities than the ventricular myocytes. Moreover, the study demonstrated that only 0.05 mm², an area that spans a few cells, needed to be illuminated to initiate pacing. These major findings were performed in anesthetized mice with open chest. Initiation of local pacing with light was further demonstrated in isolated perfused rat hearts [53]. Intramyocardial vector delivery was performed to express ChR2 in cardiomyocytes and heart beats were induced by illumination of several regions of the apex and ventricles. Optical mapping with a voltage sensitive dye confirmed that the pacemaker activity originated from the illuminated cells and demonstrated that the stimulus spread from the illumination sites throughout the myocardium to evoke a heartbeat. Hence, the induction of heart contraction could be achieved from different sites and carries potential for cardiac pacing and arrhythmia therapies.

Manipulation auf parasympathetic and sympathetic circuits regulating the HR was described in mice expressing ChR2 in the cells of interest [54]. Anatomical and functional connections between intrinsic cardiac cholinergic and noradrenergic neurons with the ECS were highlighted. The neuron projections from the sympathetic stellate ganglion to the heart were labeled and mostly found craniomedially on the heart. Open-chest studies enabled to stimulate the right stellate ganglion, what led to tachycardic response. Moreover, the study confirmed that most of the neurons in the

heart are cholinergic, interact with the ECS and innervate both, atria and ventricles. Further, *ex vivo* stimulation of those neurons led to HR decrease which was dependent on light power, pulse frequency and duration.

In summary, cardiac optogenetics represents an emerging field which can be approached from different perspectives. Initiation of ectopic heart beats originating in cardiomyocytes relies on the functional syncytium formed by the cardiomyocytes, while stimulation of cardiac neurons leads to indirect manipulation of the ECS. So far, cardiac optogenetics techniques have not been implemented *in vivo* in freely moving animals. To investigate the function of the heart within the organism by reproducing physiological conditions as closely as possible, represents a crucial step in the establishment of cardiac optogenetics. In a similar way to the works achieved in the CNS, developing cardiac optogenetics in freely moving animals is essential to understand fine circuitry linking the heart to other organ systems.

2. Electrical conduction system of the heart

2.1. Structural organization of the heart

Unlike other organs, structural organization and function of the mammalian heart was well conserved during evolution (reviewed in [55]) thus enables the transfer of knowledge from one species to another.

The heart is located in the middle mediastinum enveloped in the pericardium. Epicardium and endocardium cover the heart muscle, myocardium, from outside, respectively inside. Heart contraction propagates from the atria to the apex to evoke the contraction of the ventricles and pump blood into the circulation. The direction of the blood flow is ensured by the septum between left and right heart and also by the atrioventricular and semilunar valves, located at the atrioventricular junctions and between the ventricle and their great vessels, respectively. The mitral valve separates the left atrium (LA) from the left ventricle (LV) and closes during heart contraction (systole) while the aortic valve separates the LV from the aorta and closes during heart relaxation (diastole). The right heart is composed of right atrium (RA) and right ventricle (RV). In the right heart, the tricuspid valve and the pulmonic valves are the respective equivalents to the mitral and the aortic valves present in the left heart. The latter supplies the systemic circulation while the right heart pumps blood into the pulmonary circulation for blood oxygenation. The four cardiac valves are in a plane forming the “skeleton” of the heart and are surrounded by fibrotic tissue (*Anulus fibrosus*) playing a role as insulator during electrical propagation of the depolarization wave leading to a heartbeat [56, 57].

The pumping function of the heart relies on proper contraction for blood ejection and total relaxation for ventricle filling. A cardiac cycle comprises systole and subsequent diastole. HR is set by the electrical conduction system of the heart (ECS) which is in close interaction with the autonomous nervous system (ANS) to adapt heart function to

the needs of the organism. Proper heart contraction relies on the directional depolarization of the myocardium (see section II.2.2.).

Cardiomyocytes make up the largest volume of the myocardium, are striated but involuntary [58]. Besides muscle cells, connective tissue plays a role in the cohesion of the myocardium. The heart does not form an anatomical but a functional syncytium. Indeed, cardiomyocytes are interconnected with gap junctions and connexins (connexin 40, 43 and 45) enabling the electrical current flow to spread throughout the heart. Those connections are located at the intercalated disks (*Disci intercalares*), which also provide an anchor to the myofilaments. Depolarization of the sarcolemma leads to opening of voltage-dependent calcium (Ca^{2+}) channels, which in turn support the opening of calcium-activated channels, thus the intracellular calcium concentration necessary for the contraction of myofilaments within the cells further increases [59]. Both, the coupling of heart cells and the fibrous insulation, shape the way of the anisotropic electrical propagation initiating a heartbeat, which is crucial for myocardial contraction in unison (reviewed in [60]).

2.2. Action potential in cardiomyocytes and pacemaker cells

Cardiomyocyte depolarization is divided in four phases. In phase 4, the cell is at rest and its membrane potential is by -90 mV. Phase 0 corresponds to the depolarization and is mostly influenced by a fast and passive sodium (Na^+) inflow. Subsequently, the threshold potential of -70 mV is reached leading to further opening of Na^+ channels and L-type calcium channels (with long-lasting activation), thereby resulting in a voltage increase ($+50$ mV). In phase 1, the Na^+ channels close, potassium (K^+) channels open briefly enabling the outflow of positively charged ions, and therefore evoke a slight decrease of the action potential. Phase 2, also called plateau phase, is typical for cardiomyocytes and protects from irregular heartbeats. This phase is characterized by a membrane potential remaining constant through an equilibrium between potassium outflow, calcium and chloride inflow. At the end of the plateau phase lasting $200 - 400$ ms, the Ca^{2+} channels close while the K^+ outflow continues, thus introduce the repolarization. During phase 3, the Ca^{2+} channels stay closed and the K^+ channels remain open, thereby resulting in a negative change in the membrane potential and causing cell repolarization.

Cardiomyocytes have two refractory periods: a relative refractory period immediately following phase 3, and an absolute refractory period corresponding to the plateau phase between de- and repolarization, therefore preventing irregular heartbeats and tetanic contraction. Unlike other myocytes, the action potential does not only depolarize one cell, but travels through the entire myocardium to initiate a contraction. The functional syncytium built by the cardiomyocytes responds to the “all-or-none law” [61].

Physiologically, synchronized contraction depends on a hierarchy within the ECS components. The electrical pulse arises in the sinoatrial node (SAN, *Nodus sinuatrialis*) located in the RA. This stimulus is led through the myocardium to the atrioventricular node (AVN, *Nodus atrioventricularis*). From there, it travels to the His bundle (*Fasciculus atrioventricularis*) and is then transmitted to the ventricular branches (*Crus sinistrum* and *Crus dextrum*) before finally reaching the highly ramified Purkinje fibers

(figure 3, A; [58]). Cells of the electrical conduction system are specialized myocardial cells; they contain more glycogen and their resting potential is around -60 mV, thus less negative than in cardiomyocytes. Pacemaker cells depolarize cyclically and their action potential is less steep than in cardiomyocytes. After repolarization, the membrane potential is unstable, reaches quickly its threshold potential and depolarizes again. Due to so-called “funny currents” (I_f), pacemaker cells depolarize and repolarize spontaneously and are never at rest (figure 3, B). During phase 4 of the action potential, the membrane potential increases slowly through Na^+ inflow until the threshold value of -40 mV is reached. Phase 0 is defined by the opening of L-type calcium channels which activate slowly. Phase 1 and 2 are missing in pacemaker cells. Finally, during phase 3, K^+ channels open, leading to outward directed hyperpolarizing K^+ currents as well as inactivation of L-type Ca^{2+} channels; hence the cell repolarizes. Although the SAN initiates the heartbeat, the AVN is able to fire electrical signals with a lower frequency. In pacemaker cells, the plateau phase during depolarization is missing, therefore the action potential is shorter than in cardiomyocytes [61].

The ECS works independently but stays in close interaction with the ANS to regulate the HR and adapt its function to the needs of the organism [61].

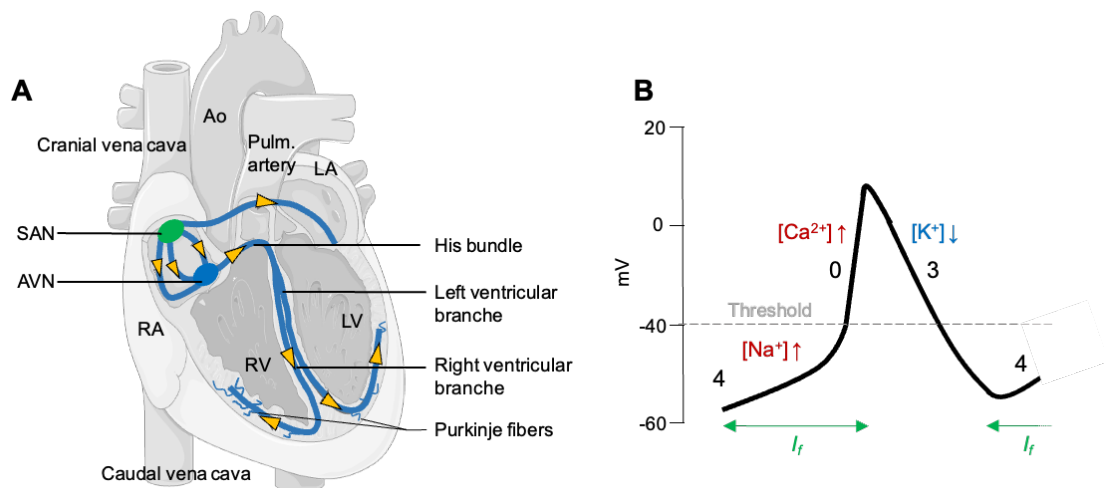


Figure 3| Electrical conduction system of the heart and action potential in the sinoatrial node

(A) Directional propagation of the depolarization wave throughout the different components of the ECS. (B) Action potential in the pacemaker cells (SAN).

Ao.: Aorta; Pulm. artery: pulmonary artery; LA, RA: left, right atrium; LV, RV: left, right ventricle; I_f : funny currents; red: depolarization currents; blue: hyperpolarizing current; arrows: evolution of ion concentration in the cells.

2.3. Tuning of pacemaker activity

2.3.1. Specific channels for funny currents in pacemaker cells

Funny currents (I_f) describe spontaneous inward currents in pacemaker cells and are essential for autonomous activity and HR control. The depolarization of the pacemaker cells in the SAN (phase 4) occurs during diastole. This diastolic depolarization is evoked by I_f during heart relaxation which determines the steepness of phase 4 of the action potential, therefore the frequency of depolarization. Indeed, the steeper the phase 4, the faster the depolarization and the shorter the interval between two action potentials

(reviewed in [62]). However, I_f are only arising during phase 4 and do not change the threshold voltage or the action potential properties during phase 3; they only occur when the cell is in an hyperpolarized state. The activation range of I_f (-40 to -15 mV) overlaps the membrane voltage during depolarization and is the result of change in K^+ and Na^+ permeability during the diastolic depolarization [62]. Hyperpolarization-activated cyclic nucleotide-gated channels (HCN) represents the molecular correlate of the I_f . Those channels are represented by four subtypes but only three of them are in the heart (HCN1, HCN2 and HCN4) with distinct regional expressions. HCN4 is present in pacemaker cells throughout development and in adulthood [63]. HCN4 is the predominant isoform in the SAN and marks the whole ECS. AVN expresses both, HCN1 and HCN4 while the atrioventricular bundle shows exclusive expression of HCN4 and the bundle branches express the three isoforms present in the heart (reviewed in [64]). These voltage-gated channels are activated by hyperpolarization (-50 mV threshold) as well as cyclic adenosine monophosphate (cAMP), which enhances the activation kinetic and voltage dependence of the channels. Indeed, by increased cAMP concentrations HCN channels are opening faster and more complete, leading to an acceleration of the action potential kinetics. The reverse effect is observed by decreased cAMP concentration. Thus, HCN channels are activated by both, electrical inputs (membrane potential) and chemical signals (neurotransmitter inducing the cAMP cascade). I_f can be activated or inhibited by β -adrenergic and muscarinic M2 receptors, respectively; hence depolarization of pacemaker cells is influenced by sympathetic and parasympathetic tones ([65] and reviewed in [66]).

2.3.2. Interactions of pacemaker cells with the autonomous nervous system

Sympathetic innervation of the heart comes from the caudal cervical and cranial thoracic segments of the spinal cord. Pre- to post-ganglionic sympathetic signal transfer occurs in the stellate ganglion (or cervicothoracic ganglion, *Ganglion cervicothoracicum*) corresponding to the fusion of the caudal cervical ganglion and the cranial thoracic ganglion. Sympathetic influence is transmitted by acetylcholine in synapses between pre- and postganglionic neuron and by noradrenaline to α - and β -receptors in the heart [67, 68]. Noradrenaline is the neurotransmitter at the synapse between postganglionic neuron and heart [61]. Noradrenaline stimulates both receptors but the β -adrenergic effect, on β_1 - and β_2 -receptors, predominates on the heart and increases contractility as well as beating frequency, while α_1 -adrenergic receptors increase the tone of arterioles [69]. Thus, sympathetic efferent to the heart, *Nervi cardiaci*, are positively chronotropic, dromotropic, bathmotropic and inotropic while the parasympathetic influence has respectively antagonistic effects. Sympathetic and parasympathetic fibers compose the cardiac plexus close to the heart and relay information from the ANS.

Parasympathetic innervation of the heart comes from the *Medulla oblongata* in the brainstem; the vagus nerve passes through the carotid sheath and travels in caudal direction. The cervical and thoracic parts of the vagus nerve send efferent fibers for heart innervation (*Nervus depressor* and *Rami cardiaci*) [67] which transmit signals to postganglionic neurons close to the effector organ [68]. Atria and ventricles receive parasympathetic innervation. The right vagus nerve preferentially innervates the RA and

the SAN, whereas the left one rather innervates the LA and the AVN. More precisely the parasympathetic fibers reach the heart caudally at the base of the heart between the confluence of the great veins (*Venae cavae*) into the RA and the pulmonary veins [70] where they shape interconnected intrinsic cardiac plexuses. There are three to eight ganglia forming three plexus respectively in proximity of the SAN, the AVN and the pulmonary veins which are 0.001 - 1.5 mm² in size [71]. Pre- and postganglionic parasympathetic neurons use acetylcholine as transmitter. Postganglionic neurons activate muscarinic M2 receptors and are inhibited by atropine.

Acetylcholine is synthesized by the enzyme choline acetyltransferase involving the compounds choline and acetyl coenzyme A present in both, preganglionic sympathetic and parasympathetic neurons, as well as in parasympathetic postganglionic neurons [72]. Adrenergic and muscarinic receptors transmitting the sympathetic respectively the parasympathetic tone to the heart, are GPCRs. Activation of β -adrenergic receptors with noradrenaline leads to activation of the second messenger cAMP which in turn promotes the calcium entry into the cells, thus depolarizing them. In opposite, occupation of the muscarinic receptor by acetylcholine inhibits the production of cAMP and the resulting secondary reactions, therefore reduces contractility and HR [61].

The heart is able to work as an autonomous system but remains responsive to external factors to adapt its function to the environment and needs of the organism. This enhances the existence of a collaborative network between heart and other organ systems to maintain homeostasis. Optical actuation of cells involved in pacemaker activity, phenylethanolamine-N-methyl Pmnt⁺ cardiomyocytes, has been performed on sinoatrial preparations [73]. Moreover, stimulation of cardiomyocytes or cholinergic cells has been described on whole heart preparations ([52, 54]; see section II.1.2.3). Taken together these findings encourage the development of cardiac optogenetics for HR modulation either through direct manipulation of pacemaker cells, or through indirect control of the heart activity via optical influence on the ANS.

3. CD4⁺ lymphocytes

3.1. Development and function of T cells

T lymphocytes are leucocytes belonging to the adaptative arm of the immune system. Unlike all the other hematopoietic cells, T cells do not complete their development in the bone marrow but derive from hematopoietic cells which migrate throughout life into the thymus. Lymphopoiesis is composed of multiple developmental steps, which determine the fate of the lymphocytes and commits them to a cell lineage [74]. T lymphocytes are characterized by their T cell receptors (TCR) present on their surface which recognize antigens presented on major histocompatibility complex (MHC) molecules. Through genetic recombination, a wide antigen receptor repertoire is available, providing a multitude of TCR with unique features; thus, enabling the

recognition of a considerable number of different antigens. In the thymus, the T cells are subjected to TCR gene rearrangement, proliferation and selection (reviewed in [74, 75]). Moreover, a major verification of self-tolerance, which tests TCR autoreactivity, takes place in the thymus. First, positive selection probes the ability to recognize endogenous MHC molecules, which present the antigens in the course of immune reactions. Second, the negative selection checks the absence of self-reactivity against autoantigens. Positive selection is regulated by cortical thymic epithelial cells, while negative selection is mediated by medullary thymic epithelial cells and thymic dendritic cells [76, 77]. The majority (95%) of the cells do not fulfil the criteria and undergo apoptosis. After passing those selections, TCR differentiate either to CD4⁺ helper or CD8⁺ cytotoxic T cells. CD4⁺ cells orchestrate the activation and differentiation of further immune cells such as B lymphocytes, macrophages and cytotoxic T cells. The latter are able to “kill” infected cells and use cytokines to recruit other cell types to enhance the immune response. CD4⁺ T cells expressing the transcription factor Foxp3, which is necessary for their development and function, exhibit a regulatory phenotype and act as mediators of tolerance against self-antigens in peripheral tissues. After an infection, some T cells become memory cells and are able to recognize quickly the encountered antigen in future infections and elicit a secondary immune response [74].

3.2. The role of T cells in the infarcted heart

Heart failure is defined as “a complex clinical syndrome resulting from structural or functional impairment of ventricular filling or ejection of blood” (definition from the American College of Cardiology) and represents a major cause of mortality in the world. MI leads to myocardial cell death triggered by prolonged ischemia during vessel occlusion (reviewed in [4]) and can lead to heart failure. Infectious myocarditis can also be a substrate for heart failure. Due to the limited ability of cardiomyocytes to divide in the adult heart, damaged myocardial tissue is repaired, thus leaving a scar at the injury site (reviewed in [4, 78]).

3.2.1. T cell mobilization in the context of myocardial injury

In a homeostatic context, the heart is protected from T cell recruitment; however, when cardiac cells are infected, an immune response is built up against the pathogen to eliminate it. Occlusion of vessels leads to ischemic injury and induces myocardial inflammation. Inflammatory reactions lead to damaging effects on the surrounding tissue and to the release of cardiac antigens. The latter activate an immune response against endogenous heart structures and the recruitment of different T cells to the heart (figure 4). Indeed, antibodies against cardiomyocytes were reported in heart failure patients (reviewed in [79]). Especially, the release of α -myosin heavy chain (MYHCA) causes autoreactivity; since this endogenous peptide is not encountered by the T cells during negative selection in the thymus, no tolerance is acquired by the effector cells [10, 80]. Both, sterile (MI) and infectious inflammation of the myocardium can be precursors of acute or chronic heart failure.

T cells mediate remodeling and influence the function of the heart (reviewed in [4, 81]). When myocardial inflammation occurs, endothelial cells upregulate the expression of

adhesion molecules (selectin, integrin) facilitating the extravasation and the transendothelial migration of circulating leucocytes towards the damaged tissue (reviewed in [82]). Cardiac repair after permanent occlusion (MI) is determined by different phases during which different cell subsets play a role. The proinflammatory phase is characterized by sterile inflammation and leucocyte infiltration. Dying neutrophils are cleared by macrophages which support the infiltration of CD4⁺ cells [83]. The following reparative phase promotes wound healing with fibrosis to replace the loss of cardiomyocytes, which, if badly orchestrated, can lead to heart failure and arrhythmia (reviewed in [3, 4]). CD4⁺ and CD8⁺ lymphocytes are gradually infiltrating the tissue with a peak observed seven days following MI [4]. The necessity of CD4⁺ to promote wound healing and modulate tissue repair has been demonstrated; indeed, their depletion in mice models worsens the outcome after MI [9]. Moreover, a reduced proportion of regulatory T cells (Treg) as well as a reduction of their suppressive activity was reported in heart failure patients [84, 85]. Additionally, the cardioprotective effect of Tregs has been demonstrated [10, 83]. Those results support the key role played by CD4⁺ cells and Tregs in the mediation of healing mechanisms after cardiac injury.

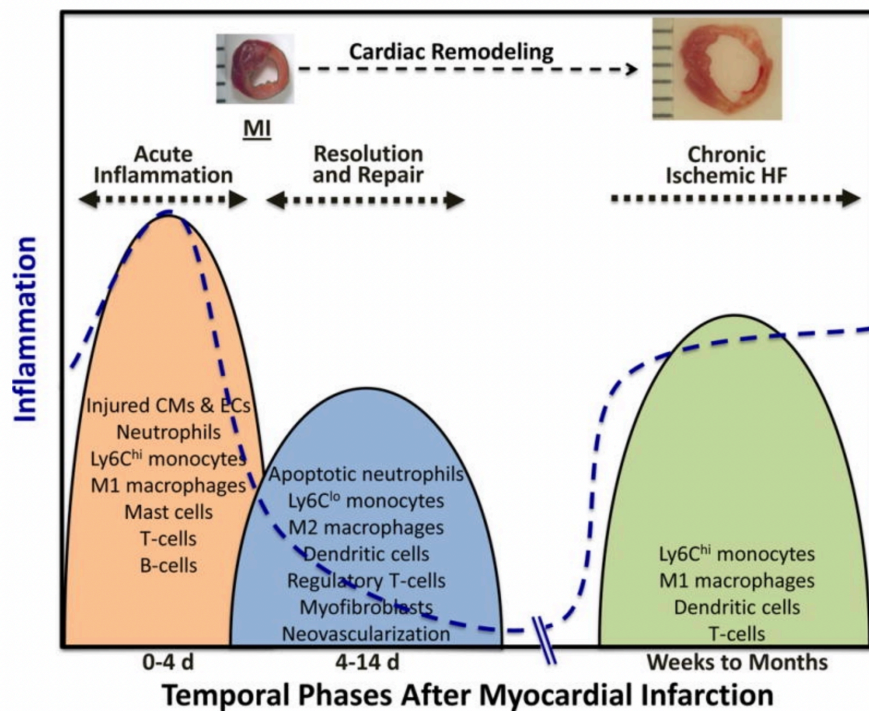


Figure 4| Myocardial healing phases after ischemic damage

Early and late inflammation after myocardial infarction (MI). The early inflammatory phase after MI (~4 d in mice) is characterized by robust innate and adaptive immune cell infiltration and tissue digestion. This is subsequently followed a phase of resolution, myofibroblast proliferation, and wound repair (lasting ~10–14 d in mice), during which immune cells are polarized toward an anti-inflammatory state. However, larger infarcts with more pronounced inflammatory activation exhibit progressive ventricular dilatation and heart failure over the long-term, together with persistent inflammation and tissue immune cell infiltration. Chronic inflammation may represent incomplete inflammation resolution during the reparative phase and subsequent amplification with time, or a second wave of resurgent immune activation in response to poorly defined factors.

Adapted from Prabhu et al. [86]

3.2.2. Myocardial repair and scar formation

An important heterogeneity and plasticity of cells is involved in myocardial inflammation and repair (figure 4; reviewed in [4, 82]). Cardiac remodeling is marked by a fibrotic scar replacing the cardiomyocyte lost because of ischemia or infection. Myofibroblasts shape a collagen scaffold in the damaged area, thus govern architectural scar formation (reviewed in [87]). While T cell infiltration promotes fibrosis, Tregs foster scar maturation of the infarct zone and improve survival after infarction [88]. According to the stage and the nature of ischemic injury (transient or permanent), CD4⁺ T cells appear to have either adverse or beneficial effect. Indeed, in the context of transient ischemia, CD4⁺ lymphocytes exacerbate the inflammation, hence trigger additional tissue damage. In contrast, in the context of permanent ischemia, those cells encourage myocardial healing and improve the outcome after MI [9, 10, 89].

3.3. Activation and polarization of T cells

3.3.1. Cytokines and their receptors

Cytokines are proteins secreted by immune cells and modulate cellular recruitment, growth, polarization, differentiation and activity of additional cells [74]. Interleukin, tumor necrosis factors, interferons, chemokines and colony-stimulating factors are cytokines. Chemokines are small proteins ranging from 8 – 10 kDa and influence migration and activation of immune cells by binding a chemokine receptor. More than 40 chemokines are regrouped in four families. Chemokine with the CXCL motive mainly influence neutrophils and T cells, while the CCL family mostly modulates monocytes and macrophages; XCL as well as XC chemokines interact with lymphocytes. The CX₃CL group is only composed of one chemokine attracting T cells and monocytes [90].

Chemokine receptors display 18 receptor types, which are classified in four groups; CXCR, CCR, XCR, CX₃CR, respectively binding to their ligand CXCL, CCRL, XCL, CX₃CL. Those receptors are present at the cell surface and are GPCRs.

The interactions between chemokines and their receptors play a role in development, homeostasis and reactivity of the immune system. The expression pattern of inflammatory cytokines depends on pro-inflammatory stimuli and orchestrates the recruitment of cells to sustain the immunological response and healing mechanisms [74].

3.3.2. T cell chemotaxis

Activation of the CXCR4 receptor drives proliferation and migration of cells, thereby chemokines secreted by cells at the site of inflammation regulate lymphocyte trafficking (reviewed in [91]). CXCL12, also called stromal cell-derived factor 1 (SDF-1), is predominantly produced in the bone marrow and involved in the recruitment of immune cells. Upon binding on its receptor CXCR4, the ligand CXCL12 activates the α - and $\beta\gamma$ -subunits of the G protein, which in turn activates protein kinases, respectively phospholipase C (figure 5). As a consequence, expression of integrin on the cell surface

is up-regulated enabling rolling and adhesion of the cells to enter the inflamed zone. CXCL12-binding also leads to β -arrestin activation which also promotes cell migration [92]. After activation and phosphorylation, the CXCR4 receptor is internalized and can be recycled or degraded (reviewed in [93]). In addition to the G-protein signaling cascade, chemokine binding to their cognate receptor on the T cell surface, induces the reorganization of the cytoskeleton and polarization of the lymphocyte. Protrusions such as lamellipodia and filopodia at the leading edge and uropod at the trailing edge of the cell, enable directional movement and are regulated by Rho GTPases which orchestrate actin polymerization (reviewed in [94], [95]). Polarization is the result of an exposure to chemokines and also enables the trafficking along a chemokine gradient [96]. Among those chemokine/receptor associations, the CXCL12/CXCR4 couple plays a crucial role in T lymphocyte migration. Moreover, binding of the CXCR4 leads to activation of phospholipase C- β in T cells and results in intracellular calcium mobilization which is crucial for chemotaxis [97].

Several cytokine patterns are secreted by different CD4⁺ cells to induce different types of immune responses such as pro- or non-inflammatory immunity and autoimmunity. The links between them and their cooperation to initiate an immune response is not completely elucidated yet [74].

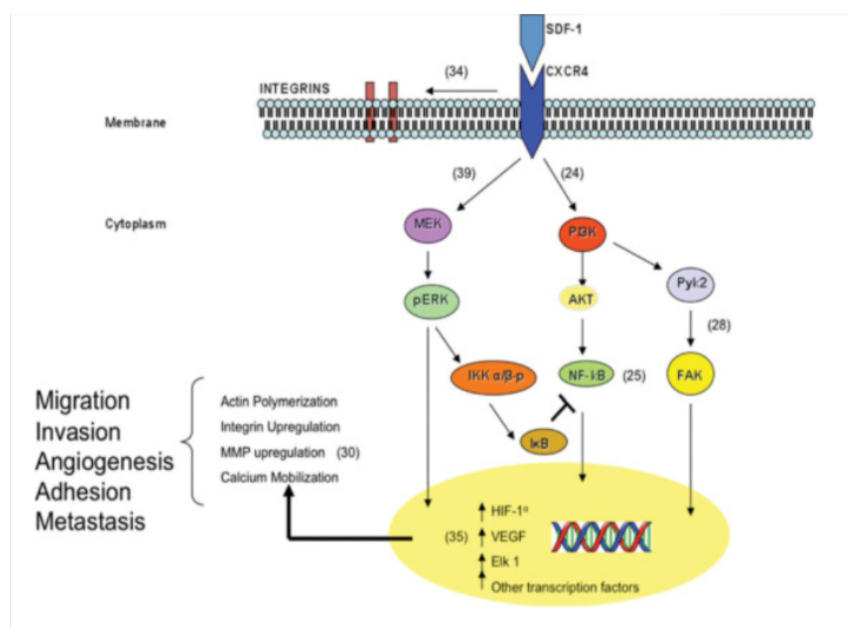


Figure 5| Signaling pathway induced by CXCR4 activation

Schematic illustrating molecular pathways by which CXCR4 acts. Stromal cell derived factor (SDF-1) bound-CXCR4, possibly after incorporation into lipid rafts, acts via G α_i , to activate the phosphoinositol-3-kinase (PI3K) and mitogen activated protein kinase (MAPK) signaling pathways. Activated CXCR4 increases intracellular calcium mobilization and induces phosphorylation of focal adhesion components such as focal adhesion kinase (FAK) and Pyk2. The activated signal transduction pathways contribute to chemotaxis, cell migration, and secretion of various matrix metalloproteinases (MMP's) including MMP-2 and MMP-9. Supporting references in brackets.

Adapted from Otsuka et al. [98]

In summary, scar formation after myocardial injury relies on a finely orchestrated recruitment of different leucocytes to different time points to first clear and then replace the damaged tissue. The cellular communication and activation of specific cell subsets is ensured by chemokines/receptor interactions. CD4⁺ lymphocytes play a role in wound healing and scar formation but their balanced and chronologic recruitment is necessary to promote proper healing to avoid exacerbated immune reaction. So far, optogenetics has not been used to investigate the trafficking of cells in the heart. A study initiating light-induced migration of T lymphocytes into melanoma in a mouse ear has been conducted and proved the feasibility to control leucocyte trafficking [99]. To shift the responsiveness of CD4⁺ lymphocytes towards light instead of chemokine, would provide a tool to investigate the nuanced role and the dynamics of different cell subsets in different heart failure stages. A better understanding of the fine-tuned recruitment of cells leading to myocardial repair would help to develop immunomodulatory therapies to improve the outcome after myocardial damage.

III. MATERIALS AND METHODS

1. Mice and animal welfare

Mice (*Mus musculus*) are mammals commonly used in laboratory research and numerous transgenic mouse strains are commercially available to respond to the purpose of diverse studies. Due to their small size, housing and breeding mice require little space, which simplifies their handling and offers economic advantages. Gestation lasts 19 – 21 days and a breeding cycle occurs within seven weeks, thus goes along with a short generation time [100]. Since mice present anatomical, physiological and genetic similarities to humans (99%), they are preferably used as experimental animals in numerous disease models [101]. In addition, inbreeding transgenic strains prevents genetic variability and ensures standardized conditions, repeatability and reproducibility of experiments [102]. Altogether, those arguments spoke in favor of a model for cardiac optogenetics established in mice.

The animal experiments were performed in accordance with §8 of the German Animal Welfare Act (Tierschutzgesetz from 18.05.2006, last amended by Article 280 on 19.06.2020) and under the terms of the animal experiment applications approved by the government of Lower Franconia (application numbers: 55.2.2-2532-2-941 and 55.2-2532-2-1016).

1.1. Source, housing and transport

1.1.1. Mice source

Animals for all experiments were either bred on site in the Centre for Experimental Molecular Medicine (ZEMM) or commercially purchased from The Jackson Laboratory and from Charles River Laboratories (Sulzfeld, Germany).

1.1.2. Mice housing

Health status of the imported and housed mice

After their transport, the mice were housed in the animal facility of the Comprehensive Heart Failure Center (CHFC), or in the Institute of Clinical Neurobiology (ICN). Only animals with complete health certificates were imported into the facilities. Upon delivery and before involving the animals in trials, they were thoroughly examined; thus, only healthy animals were used for experiments. In order to give the animals time to adapt to their new environment, they spent at least one week in the facility before undergoing any experimental procedure. There, the animal health monitoring was performed according to the current recommendations of the Federation of European Laboratory Animal Science Association (FELASA) from 2014. Examinations to detect the presence of pathogens took place quarterly. For this purpose, samples were taken directly from selected animals as well as from used cage materials, surfaces (swab preparations) and exhaust air filters (sedimentation in agarose plates). Pathogens were detected directly by PCR in specialized institutions (Harlan Laboratories). The animal facilities and connected rooms were accessed in full protective gear via a hygiene sluice.

Housing conditions

Housing conditions in both, the CHFC and ICN, were similar. An automated light program (160-180 lux) split the day into two twelve-hours phases, corresponding to light and dark cycles respectively. Humidity was kept between $55 \pm 15\%$ and the temperature was 22 ± 2 °C. In the CHFC up to five mice from the same sex were housed in Makrolon type II L cages with grid and hood (ZOONLAB GmbH, Castrop-Rauxel, Germany), whereas in the ICN maximum two mice were in Makrolon type II (Tecniplast). In both facilities, dust-extracted wood shavings or shred for rodent was used as bedding material (Lignocel BK 8 – 15, in the CHFC and Lignocel BK 3 – 4S in the ICN, both from J. Rettenmaier & Söhne GmbH, Rosenberg, Germany). Nesting and shelter material such as egg carton and cellulose (6-piece egg carton, Schmutte, Damme, Germany; unbleached cellulose) were always available in the cage. The mice had *ad libitum* access to water in drinking bottles and special food for rodents (Ratte/Maus Haltung Standard, pellet 10 mm autoclavable, ssniff Spezialdiäten GmbH, Soest, Germany in the CHFC and 1324 – 1 mm pellet, Altromin Spezialdiäten, Lage, Germany in the ICN). Once a week, the animals were moved into cleaned cages. All materials, including feed and water, were autoclaved before entering the area. Animals under experiment were kept in separate experimental rooms within the facility. Both facilities, in the CHFC and ICN, could only be entered by staff members.

The transport of the mice within a department was performed using dedicated routes in opaque transport cages and within few minutes. Procedures took place in rooms associated to the animal facility and with the same hygiene level.

Up to 48 hours after surgery, the mice could be housed in a separate ScanTainer (ScanTainer Classic, Scanbur A/S, Denmark). The animals could then recover nearby the experimental room, hence facilitating close monitoring after the procedure.

Single housing after ECG electrode implantation

For electrocardiographic recording of the HR, electrocardiogram (ECG) electrodes were implanted subcutaneously. Only a small part of the electrode (connector, 3 mm high, see section III.6.1.2. figure 10, C) protruded above the skin surface dorsally on the head. The mice implanted with ECG electrodes could not reach the connector themselves; however, when kept together, mice could gnaw the connector fixed on the skull of cage mates, making it unusable for recordings. Housing the mice individually was the only alternative to prevent such damages. According to the government approval, these mice were single-housed after surgical implantation of ECG electrodes until the end of the experiment (experimental application number 55.2.2-2532-2-941).

1.1.3. Mice transport

After echocardiographic examination and surgical intervention, some of the animals were transported from the animal facility of the CHFC to the ICN in order to perform ECG measurements. The animals were transported in adequate transport boxes containing sufficient amount of food. The transfer lasted a few minutes and was in accordance with the Animal Transport Regulation (Tierschutztransportverordnung).

1.2. Mouse strains

To establish cardiac optogenetics in the mouse model, several mouse strains were used and are described in greater detail below. For the sake of animal welfare and to reduce the number of animals bred, mice of both sexes (except Balb/c), aged from eight to twelve weeks, underwent experiments. None of the used strains shows genotype-related burden.

C57BL/6J

C57BL/6J, “Black 6” (or B6, B6J, B6/J), is the most commonly used inbred strain in numerous research areas, including cardiovascular research. C57BL/6J are also taken as background strain to generate transgenic mouse strains. Animals of this genotype were either taken from the breeding-surplus of the ZEMM or purchased from Jackson (strain #000664).

BALB/c

Balb/c mice (BALB/cAnNCrl) are used in numerous research fields, including cardiovascular and immunological research. These animals were purchased from Charles River (strain #028). As required by the experimental application, only males of this mouse line were used.

ChAT-Cre

In this mouse strain, expression of the enzyme Cre recombinase is linked to the choline acetyltransferase (ChAT) promoter without affecting the endogenous ChAT expression. The use of this mouse line allows targeted expression of the opsin in cholinergic neurons. This mouse line was initially purchased from The Jackson Laboratory (strain #006410) and further bred in our husbandry. Homozygous transgenic animals, which are viable and fertile and do not present burden [103], were used in the experiments.

HCN4-Cre

The isoform 4 of HCN channels is expressed in the first heart field of differentiating myocytes in the developing cardiac crescent and preferentially found in cells of the SAN and AVN in the heart and in cortical, as well as subcortical, brain areas [104]. The ionic current through HCN4 channels controls the rhythmic muscular activity of the heart by depolarizing the cells of the conduction system (see section II.2.3.1. and [105]) The expression of Cre recombinase is under the control of the HCN4 promoter and thus allows the targeted expression of the opsin in cells of the ECS of the heart. Breeding pairs were kindly provided by Prof. Ludwig from the Institute for Experimental and Clinical Pharmacology and Toxicology in Erlangen, Germany. Heterozygous mice, which are viable and fertile, were used in the experiments; the homozygous genotype is lethal during embryonic stages.

1.3. Animal welfare during experiments

1.3.1. Severity classification of the procedures

The thoracotomy necessary for the implantation of the light source was defined as major burden. Pain monitoring and therapy as well as precisely chosen humane endpoints reduced the stress intensity and duration (see section III.1.3.2.).

According to the directive 2010/63/EU, Annex VIII, of the European Parliament and of the Council, echocardiographic examinations, subcutaneous ECG electrode implantation and recordings, as well as subcutaneous, intraperitoneal and intravenous administration of substances are classified as procedures of mild severity. Thoracotomy accompanied by an appropriate pain management is assigned to the category of moderate severity.

Based on the directive 2010/63/EU, Annex VIII, of the European Parliament and of the Council, the severity of those cumulative procedures was classified, in total, as moderate.

1.3.2. Scoring protocol

Since the transthoracic device implantation has not been described previously, no specific distress assessment for this type of procedure has been reported so far. A scoring protocol, similar to the one used for distress assessment after MI in the CHFC, was used for welfare monitoring in mice after device implantation. Indeed during both procedures, LED implantation and MI induction, thoracotomy and manipulations at the heart are performed [106] and are likely associated with comparable pain. In addition to the general condition and regular weighing of the animals, the Mouse Grimace Scale (MGS scale) was determined, which is suitable for the assessment of visceral pain. Indeed, the changes in facial expressions in mice subjected to pain correlates with the severity of the burden [107, 108]. To assess the severity grade, accurate observation of orbital tightening, nose and cheek bulge, ear position and whisker change were performed [109].

The scoring of the mice was based on a point system (see tables 1, 2 and 3). If the total score of 20 points was reached, the mouse was immediately euthanized. Other endpoint criteria as wound healing disturbance, 20% bodyweight reduction post-surgery, immobility and self-induced trauma, were determined. The evaluation criteria differed slightly depending on whether the animals were examined within three days (d0 to d3) after surgery or from the fourth day after the procedure onward.

During the whole experimental period, the mice were examined at least once a day. In addition, the first three days following intrathoracic device implantation or subcutaneous electrode implantation for the recording of ECG, animals were examined and treated with buprenorphine twice a day (see section III.3.1.1.).

Table 1| Scoring protocol from d0 to d3 post-surgery

Observation	Score
<u>Bodyweight</u>	
Spine and pelvis not visible	0
Spine visible or weight loss < 5%	5
Spine and pelvic bones can be easily identified by palpation or weight loss < 10%	10
Spine and pelvic bones easily visible or weight loss 10 to 20%	15
Single vertebrae visible or weight loss > 20%	20
<u>Physical appearance</u>	
Hair coat and eyes normal	0
Minor changes in hair coat	5
Lack of grooming	10
Rough hair coat, nasal and/or ocular discharge	20
<u>Behavior</u>	
Normal (responsive by handling, active, normal breathing, normal posture)	0
Slight changes in behavior (activity, posture)	1
Unusual behavior, posture or movements (hyperkinesia or hypokinesia)	5
Lethargy, isolation or hyperkinesia, hypokinesia, ataxia	10
Self-mutilation	20
<u>MGS Score</u>	
No pain manifestation according to MGS	0
Mild or moderate pain manifestation according to MGS	5
Severe pain manifestation according to MGS	15
<u>Wound healing</u>	
Skin normal, proper healing	0
Reddened or weeping wound	5
Gaping wound	10

Table 2| Scoring protocol from d4 post-surgery onwards

Observation	Score
<u>Bodyweight</u> (weight at least once a week)	
Spine and pelvis not visible	0
Spine visible or weight loss < 5%*	5
Spine and pelvic bones can be easily identified by palpation or weight loss < 10%*	10
Spine and pelvic bones easily visible or weight loss 10 to 20%*	15
Single vertebrae visible or weight loss > 20%*	20
<u>Physical appearance</u>	
Hair coat and eyes normal	0
Minor changes in hair coat	5
Lack of grooming	10
Rough hair coat, nasal and/or ocular discharge, hypothermia, tremor	20
<u>Behavior:</u>	
Same as from d0 to d3	
<u>MGS Score</u>	
Same as from d0 to d3	
<u>Wound healing</u>	
Same as from d0 to d3 until complete healing	

Table 3| Taken measures according to the scoring result

Total score (Σ Score)	Evaluation	Measure
0	No burden = burden level 0	Scoring repeated within twelve hours
1 – 9	Mild burden = burden level 1	
10 – 19	Moderate burden = burden level 2	Involve a veterinarian, consider additional analgesia Scoring repeated and treatment within three hours as long as stress level 2 persists Euthanasia level if stress persists for more than 72 hours
≥ 20	Severe burden = burden level 3	Immediate euthanasia

1.4. Ethical aspects

The described experiments are moderately biocentric and pathocentric. The animals were subjected to burden which may contribute to a substantial gain of knowledge and help to develop therapeutic approaches for heart failure and anxiety disorders in both, humans and animals. So far, clinically applied therapies for heart failure or anxiety disorders have been primarily developed in small animal models [101]; hence we chose the mouse as species to establish the first *in vivo* model for cardiac optogenetics in freely moving animals.

The experimental procedures were designed to minimize burden for the experimental animals. Standard housing conditions, appropriate pain management and close-meshed examinations were ensured. The selected mouse strains did not carry any burden and the use of both sexes led to a reduction of the breeding surplus. Reliance on the 3Rs principle (Replacement, Reduction, Refinement) was constantly ensured too.

2. Technical aspects of optical stimulation at heart level

2.1. Selecting the appropriate wavelength

The excitability of opsins is wavelength specific (see section II.1.1.2.). Numerous structures containing endogenous chromophores (hemoglobin, flavin, melanin) absorb light and prevent its penetration deep into the tissue [110]. Due to its electromagnetic properties, long-wave light, in the (far-)red or near the infrared part of the spectrum, penetrates deeper into the tissue than shortwave light in the blue or near the ultraviolet spectrum. Light absorption and scattering decrease with increasing wavelength [111], but the energy decreases with increasing wavelength too [112]. Weighing the pros and the cons to choose an appropriate wavelength for optical stimulation was crucial and required to make a compromise in either penetration depth or photon energy. Besides the wavelength, the size of the light source, its distance to the region of interest and its power also influence the photon density at the illumination site [113, 114]. The latter decreases with increasing tissue thickness (figure 6, A; [115]).

The manufacturer of the chosen optogenetics system, NeuroLux (Northfield, USA), provides LEDs (Light-Emitting Diode) with four different wavelengths in the visible spectrum: blue: 470 nm, green: 530 nm, orange: 590 nm and red: 630 nm. The implantable device (unilateral device for brain, probe 4 or 6 mm, NeuroLux) has a diameter of 9.8 mm, is 1.3 mm thick and weighs approximately 30 mg. The actual light source (μ LED, micro light-emitting diode) is located at the end of the lancet-shaped part – the so-called “probe” - and is 220 x 270 x 50 μ m in size (figure 6, Band C). The entire surface of the device is covered by a protective layer composed of parylene and polydimethylsiloxane (PDMS) [116].

The choice of the device wavelength was adapted depending on the purpose.

On the one hand, we intended to modulate HR via optical stimulation of intrinsic cardiac neurons or part of the cardiac electrical conduction system. Those structures are more abundantly located in the RA, near the *Sinus venosus* and embedded in the *Septum* (see section II.2.2.). The deep location of these target cells combined with the light scattering caused by the myocardium and blood, led to the choice of a “red-shifted” opsin, ChRmine (see section III.5.2.3.1.; [117]). The orange and red LEDs were used for stimulation after ChRmine expression (figure 6, C).

On the other hand, we sought to induce the migration of modified cells into the heart with light. Before carrying out *in vivo* trials, *in vitro* experiments to test the photoactivability of phototactic lymphocytes provided evidences that the modified cells were best activated by green light (see section IV.3.2.). Thus, the experiments for the induction of lymphocyte migration were performed with green LEDs (figure 6, C).

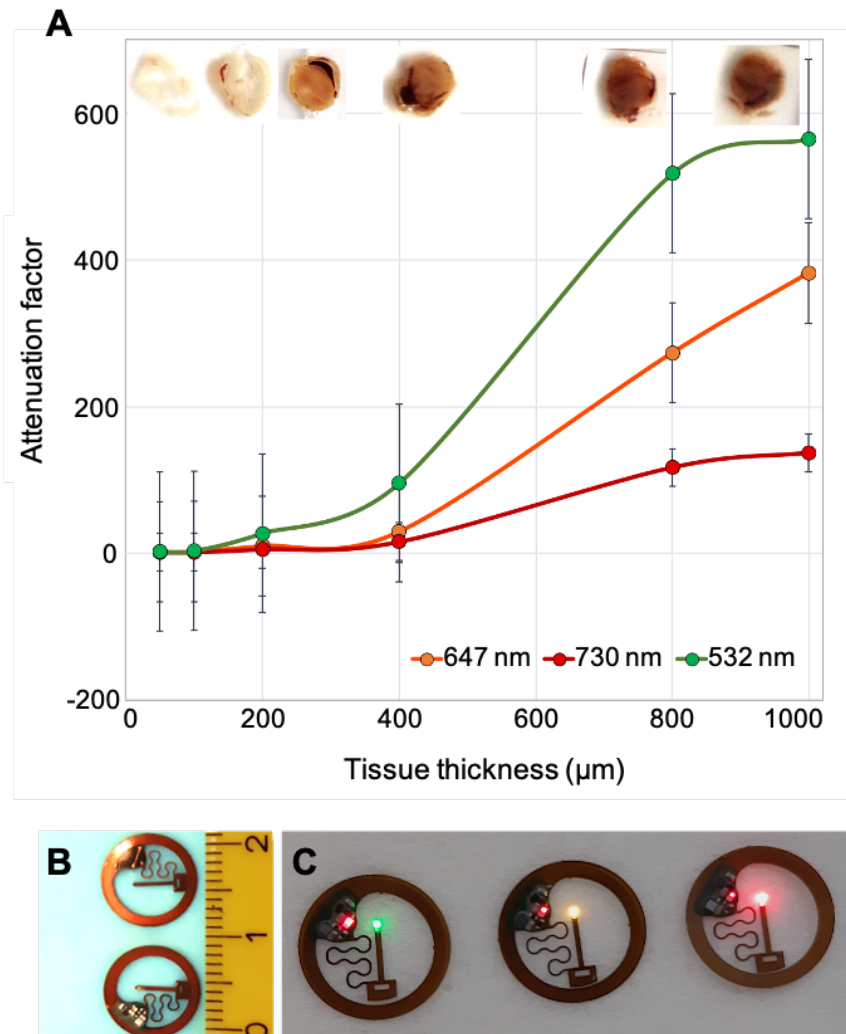


Figure 6| Thickness- and wavelength-dependent light absorption in the myocardium

(A) Attenuation factor of heart tissue depending on the wavelength. The longer the wavelength, the deeper the penetration into the tissue. (B) Back (on the top) and front (on the bottom) of the device. (C) Selected μ LED for lymphocyte migration (green) and HR modulation (orange and red).

Graph (A) provided by courtesy of the Laboratory of Prof. Katrin Heinze (Rudolf Virchow Center for Integrative and Translational Bioimaging in Würzburg, Germany).

2.2. Optogenetics system

By establishing a model for cardiac optogenetics *in vivo*, we required to find a system that would minimally restrict the mice behavior in order to avoid an influence of external factors on the studied parameters. The selected optogenetics system (figure 7; [116]) allowed wireless activation of the implanted device, thus enabled to conduct measurements without interfering with the mouse, which could freely move and behave during illumination. The light intensity and stimulation frequency were set via the NeuroLux software. The chosen μ LED were able to generate high light powers, up to 200 mW/mm^2 , which correspond to values previously published in optogenetic experiments ([11, 118, 119] and reviewed in [7]).

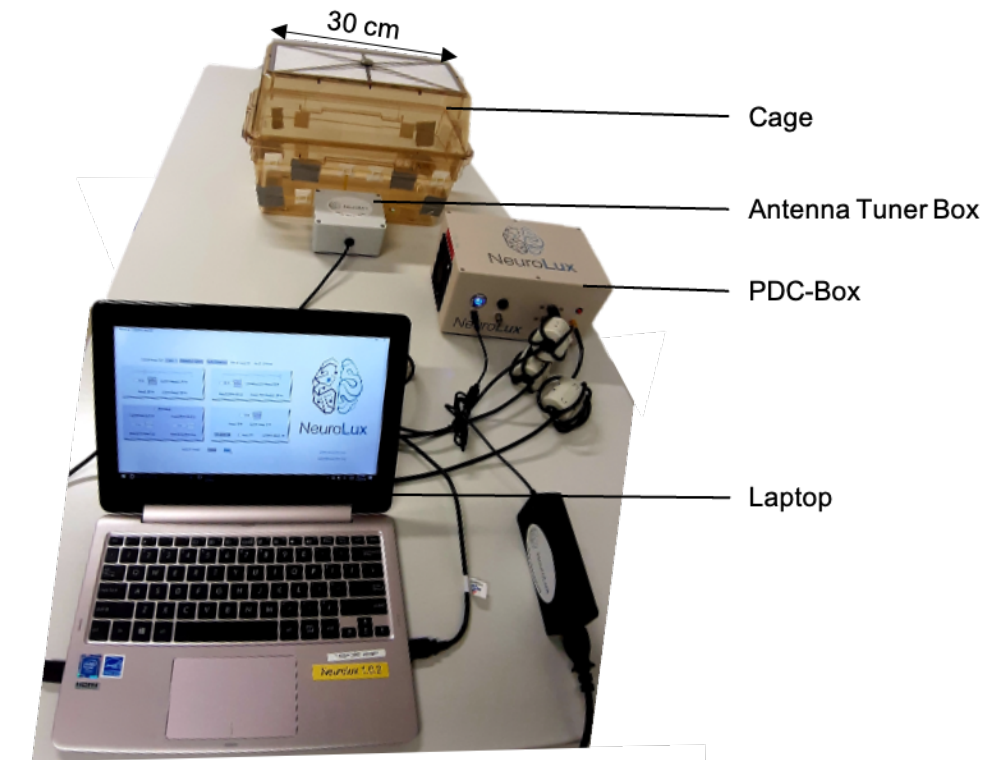


Figure 7| NeuroLux Optogenetics System for wireless optical stimulation of implanted devices

Stimulation parameters set with the laptop and sent to the PDC-Box for pulse production were transmitted to the radiofrequency-controlled antenna surrounding the cage. The power transfer from the double-transmission loop antenna to the device placed within this area induced voltage in the device coil leading to μ LED activation according to the settings.

3. Mice preparation prior to device implantation

3.1. Drugs and pain management

Procedures in the thoracic region are classified as moderate distress according to the directive 2010/63/EU, Annex VIII, of the European Parliament, and require both, intraoperative and perioperative analgesic treatment. Echocardiographic examination under anesthesia, subcutaneous, intraperitoneal or intravenous substance applications as well as subcutaneous electrode implantation represent low levels of distress and do not require additional analgesia.

3.1.1. Perioperative analgesia

Buprenorphine acts on the spinal as well as supraspinal level as a partial agonist on μ -receptors and thus ensures central analgesia. In addition to μ -receptors, buprenorphine also binds to ORL1 (opioid receptor like-1 receptor) receptors, moderately to κ - and slightly to δ -receptors. Due to its high affinity, buprenorphine is able to displace other μ -agonists from the receptor. Buprenorphine binds its receptor longer than morphine, leading to a longer duration of action [120]. Buprenorphine is classified as a long-acting opioid with an effect lasting eight to ten hours and is 30 times more potent than

morphine [121]. This drug may also be associated with less withdrawal syndrome than by the use of other opioids. It is metabolized to norbuprenorphine in the liver and excreted in urine and faeces (reviewed in [120]).

The maximal potential of action of buprenorphine is reached around 30 minutes following administration; thus, when used for intraoperative analgesia, the delayed onset of action should be compensated by injection prior to surgical procedure [121]. By using this drug, the “ceiling effect” has also to be kept in mind, which occurs after the maximum effect was reached and leads to a decrease of the analgesic effect when the dose is further increased [121]. Buprenorphine hardly affects the cardiovascular system, but has a respiratory depressant effect when combined with other anesthetics. Other side effects are hyperalgesia, constipation, nausea and allotriophagia (reviewed in [122]). The opioid receptor antagonist naloxone can reverse the effect of buprenorphine [121].

Buprenorphine administration

The delayed onset of action was compensated by preemptive administration 30 minutes before surgery, to ensure effective intraoperative analgesia during the procedure. Postoperatively, the buprenorphine was re-dosed six hours after surgery and administered twice daily for two more days. Analgetic treatment after LED or ECG implantation lasted therefore three days in total. Buprenorphine (Buprenovet sine 0.3 mg/ml, 6 x 2 ml, Bayer Vital, Leverkusen, Germany; diluted 1:25 in sterile NaCl 0.9%, Fresenius Kabi Deutschland GmbH, Homburg, Germany) was injected subcutaneously (s.c.) for analgesic treatment.

The mice were manually restrained for repeated s.c. injections. After placing the animal on the cage lid and holding it by the tail with the preferred hand, it was quickly and firmly picked up behind the ears forming a skin fold between thumb and index finger of the other hand. The tail was then fixed between palm and little finger and restrained while injecting the substance into the nuchal skin fold with a 25G cannula (BD Eclipse Needle, 25G x 5/8 (0.5 x 16 mm), #305760BD GmbH, Heidelberg, Germany) creating a s.c. depot for slow infusion of the substance. According to the recommendations of the GV-SOLAS Committee for Anesthesia (Pain management for laboratory animals, July 2020) the buprenorphine posology was 0.1 mg/kg and the injected volume was maximum 10 ml/kg bodyweight.

3.1.2. Intraoperative anesthesia

Isoflurane has a sedative, hypnotic and muscle relaxant effect, but no or barely any analgesic effect. The analgesic component of anesthesia was ensured by the preemptive administration of buprenorphine (see section III.3.1.1.). Due to its low first-pass effect and its low minimum alveolar concentration value (MAC, 1.3%), isoflurane anesthesia is easy to control, thus enables rapid adjustment of the depth of anesthesia and a rapid postoperative recovery phase. Isoflurane is only metabolized to 0.2%, and is neither hepatotoxic nor nephrotoxic, but causes vasodilation, hypotension and malignant hyperthermia (more often in pigs and sheep). In the MAC range, isoflurane does not affect electrical conduction in the myocardium and does not cause a decrease of the myocardial oxygen consumption, but induces myocardial depression above a MAC of 2.0%. Its respiratory depressant effect is dose-dependent [121, 123].

Intraoperative hypnosis, relaxation and analgesia were ensured by the combination of isoflurane and buprenorphine. Such balanced anesthesia presents the advantage that smaller amounts of drugs are used and adverse effects are reduced [124].

Anesthetic management is described under III.3.2.2.

3.2. Preparations and anesthesia procedure

3.2.1. Surgical instruments

The surgical procedure was performed using autoclaved instruments. A set of surgical tools was composed of two angled forceps (Graefe Forceps, #22049-10, Fine Science Tools GmbH, Heidelberg, Germany), a pair of scissors (Fine Scissors – Sharp, #14060-09, Fine Science Tools GmbH), a cutting needle holder (Micro Needle Holder with Suture Cutter, #12075-14, Fine Science Tools GmbH), a classic needle holder (Castroviejo Micro Needle Holders, #12060-02, Fine Science Tools GmbH) and four wound retractors (Lone Star Elastic Stays, 5 mm blunt hook, CooperSurgical Inc., Trumbull, USA). An electrocautery kit (Small Vessel Cauterizer Kit, #18000-00, Fine Science Tools, GmbH) was used to pass through the intercostal muscles by preventing bleeding. Swabs were kept ready to absorb any fluids.

The entire procedure was performed with the help of an operating microscope (OPMI pico, Carl Zeiss Meditec AG, Oberkochen, Germany) on a heat pad (HK 25 heat pad, Beurer GmbH, Ulm, Germany). The video of the surgery (see digital appendix, video 1) was recorded with a camera (Canon DS126201) fixed on the microscope.

3.2.2. Anesthesia procedure

After preemptive analgesia was ensured, the mouse was put in balanced general anesthesia. Isoflurane (Isofluran CP 1 ml/ml, 250 ml, CP-Pharma, Burgdorf, Germany) was mixed with 100% oxygen (1.0 l/min) in the vaporizer (Appolo TEC3 Vaporiser, NORTHERN VAPORISERS LTD, Skipton, UK) before being inhaled by the animal. An aspiration system ensured absorption of the exhaled gas (Fluovac System with Fluosorber Activated Charcoal Filter Canister, Harvard Apparatus, Holliston, USA). After anesthesia induction, intubation was necessary for proper ventilation. Indeed, when opening the chest, the iatrogenic pneumothorax leads to normalization of the transpulmonary pressure and pulmonary collapse, hence the lung is no longer able to follow respiratory movements. The loss of function of the lung must be compensated by mechanical ventilation and atelectasis formation is prevented by setting a positive end-expiratory pressure (PEEP) [125].

Anesthesia induction and intubation

The induction phase was performed in a closed induction chamber using isoflurane inhalation at 3.0 – 5.0 volume% until position reflexes vanished and the paw pinch reflex did not lead to limb withdrawal. Subsequently, the mouse was intubated endotracheally using a peripheral intravenous catheter capillary without needle (Vasofix Safety 0.90 x 25 mm 22G blue PUR, B. Braun, Melsungen, Germany) and maintained under anesthesia using isoflurane (1.0 – 2.5 volume%). For the intubation, the mouse was fixed in supine position, head towards the surgeon, by passing an elastic band

lingually to the maxillary incisors and stretching the mouse by fixing it with tape (3M Durapore Surgical Tape, Neuss, Germany) to the surgical table. The tongue was gently pulled and its base lifted using an angled forceps. The intravenous catheter capillary was introduced into the trachea with the needle. After intubation the needle was withdrawn and the infusion port was connected to the tubing system linked to the ventilator. Proper endotracheal intubation was assessed by the pressure value (12.0 - 18.0 mmHg) and respiratory movements synchronized with the ventilator. Afterwards, the mouse was fixed in half-supine position to perform the surgery described under IV.1.2.

Anesthesia maintenance

Open-chest surgeries require ventilation and were performed using a ventilator for small rodents (VentElite Small Animal Ventilator, #55-7040, Harvard Apparatus, Holliston, USA; settings: Tidal volume = 500-600 μ l, PEEP = 2.0 cmH₂O, ventilation rate = 150 breaths/minute, pressure = 12,0 – 18,0 cmH₂O).

Under anesthesia, eyelids of the mice remain open. Therefore, to prevent the cornea to dry out, the eyes were covered with an eye ointment (eye and nose ointment with 5% dexpanthenol, Bepanthen, Bayer AG, Leverkusen, Germany). As control for anesthesia depth, the absence of paw pinch reflex was regularly checked during the course of the surgical procedure.

After surgical procedure and disinfection of the skin suture, the isoflurane supply was interrupted. Once the mouse showed proper answer to reflex testing, it was extubated.

Anesthesia recovery

To recover, the mouse was put in a clean cage with fresh materials and placed under a heating lamp during the anesthetic recovery phase. Indeed, due to their low body mass, mice are particularly susceptible to perioperative hypothermia. Hypothermia has an arrhythmogenic effect, increases the risk of infection and impairs postoperative recovery [124]. Therefore, mice were kept on a heated metal plate intraoperatively and under an infrared lamp postoperatively.

The recovery of normal breathing was monitored. After the procedure, the mice had *ad libitum* access to food and water and were intensively observed during the first postoperative hours.

3.3. Preparation of the surgical field

Mouse positioning

After proper intubation, the mouse was carefully positioned in half supine position (see section IV.1.1.; figure 16, D and E). For device implantation on the right ventricle, the left forelimb was stretched at a 90° angle and the right forelimb at a 50° angle from the rostral median and fixed to the operating table using adhesive tape with its head on the left hand side of the surgeon. The hindlimbs were fixed in a left lateral position. When the surgery was performed on the LV, the mouse was fixed the other way around.

Asepsitization of the surgical field

In order to create aseptic working conditions, the animals were first clipped (Isis cordless clippers, Aesculap AG, Tuttlingen, Germany) and the remaining fur was

removed using depilatory cream (Pilca Hair Removal Cream). The surgical field was then disinfected three times (octeniderm, Schülke & Mayr GmbH, Norderstedt, Germany) with enough time between each disinfection step to allow the solution to dry out and therefore ensuring effective disinfection. To improve hygiene conditions, a surgical drape (Mölnlycke BARRIER surgical drape 45 x 75 cm, 2-ply., #800430, Malmö, Sweden) was tailored to cover the mouse during the thoracotomy and fixed to the surgical table with tape. Before starting the operation, it was verified that the state of surgical tolerance was reached (anesthesia stage III2 according to Guedel's classification; [121]). After checking the absence of paw pinch reflex, skin incision was performed and the surgery continued. During the whole procedure, the surgery table was kept warm by a heat pad.

The implantation of the device on the RV is described in section IV.1.2.. The attachment of the device to the LV was performed according to the same principle in a reversed mirror manner.

4. Monitoring the effect of the device implantation on the myocardium

4.1. Weight development

Weighing animals represents an objective way to assess normal food intake, which decreases under distress situation [126]. According to the approved scoring system, the mice had to be weighted at least once a week. In order to record more accurately the weight evolution of the animals in the acute phase following the procedure, we weighted them every day during the first week following the intervention. After bodyweight recovery was confirmed, the mice were weighted once a week until the end of the experiment.

4.2. Histological assessment of heart damage

4.2.1. Principle of histology and Masson's trichrome staining

Histology

Histology enables the visualization of the microscopic anatomy and structure in thin slices. After collection, tissue pieces are fixed or frozen, next the samples are cut in the desired orientation and thickness using a microtome and affixed on microscope slides. The thinner the slices, the better the detail visualization. Through staining, diverse structures and cell types can be colored, thus enabling the examination of tissue composition and organization. For interpretation, knowledge about anatomy and the physiological tissue organization are required [127].

Masson's trichrome staining

Masson's trichrome staining is used for visualization of connective tissue in histological sections, including collagenous scar tissue produced by fibroblasts and inflammatory cells after myocardial damage. Repairing fibrosis is characterized by type I and II

collagen deposition [128]. The Weigert's iron hematoxylin solution stains cell nuclei black, while Biebrich Scarlet-acid fuchsin labels cytoplasm, muscle and erythrocytes red. In contrast, the staining step with aniline blue makes to collagen fibers appear blue. This method was chosen to histologically understand the extent of tissue damage caused by the surgery.

4.2.2. Organ removal and processing

First, the blood was removed from the circulation through transcatheter perfusion, second the organs were collected, third embedded and finally frozen. Later, the samples were cut and stained.

Transcatheter perfusion

The mouse was anesthetized deeply with isoflurane in the closed induction chamber and euthanized with cervical dislocation. The mouse was fixed in supine position with surgical tape. Using forceps, the abdominal wall was lifted and opened with scissors. The diaphragm was cut to reach the heart and transcatheter perfusion was performed with heparin (heparin sodium 25,000 IU, Ratiopharm, Ulm, Germany) diluted 1:100 in phosphate-buffered saline (PBS) solution. Within 5 minutes, 5 ml of the ice-cold solution were gently and continuously flushed into the LV using a 27G cannula (Sterican, B. Braun, Melsungen, Germany). The solution went through the body circulation before flowing out of the animal through an opening previously made in the right ventricle. Proper perfusion was assessed by the fading of the liver while the perfusion progressed.

Organ collection and embedding

After transcatheter perfusion, the blood vessels supplying the atria were cut and the heart was extracted from the thorax. Pericardial adipose tissue and adjacent organs were carefully removed and the heart was generously embedded in Tissue-Tek (Tissue Tek O.C.T. Compound, A. Hartenstein GmbH, Würzburg, Germany) in a small dish, *Facies atrialis* down. The sample was immediately stored on dry ice and ice-cold 2-methylbutane (2-methylbutane, isopentane, #78784, Sigma-Aldrich, Merck KGaA, Darmstadt, Germany) was poured on the embedded heart to fasten the freezing and removed once the embedding medium hardened. Embedding provides tissue support during sectioning. The organ was then stored at -80°C until cutting.

Sample sectioning

To generate overview images, 15 μm sagittal sections were cut using a microtome (Rotating cryostat mikrotom CM3050 S, Leica Biosystems Nussloch GmbH, Germany) and applied to adhesion slides (SuperFrost ULTRA plus slide, #03-0061, R. Langenbrinck GmbH Labor- und Medizintechnik, Emmendingen, Germany). After drying for two hours at room temperature, the sections were stored overnight at -20°C .

Staining procedure

Prior to staining, the frozen sections were thawed at room temperature for two hours.

Masson's trichrome staining was performed using a staining kit (Masson's Trichrome Staining Kit, #25088-1, Polysciences Europe GmbH, Hirschberg an der Bergstraße, Germany) and stained using the protocol for cryosections provided by the manufacturer.

Pictures were taken with a camera (Canon DS126201) fixed on a microscope (Axioskop 2 plus, Zeiss, Carl Zeiss Vision GmbH, Aalen, Germany) and imaged with transmitted light. Acquisition was performed using 1.25x and 10x objectives (Plan-NEOFLUAR 1.25x/0.035 and A-Plan 10x/0.25, Zeiss).

4.3. Echocardiography

4.3.1. Principle of echocardiography

Ultrasound are waves propagating in longitudinal motion through matter. Depending on the tissue density, they spread at different speeds. The transducer sends ultrasound pulses, and also records their reflection which arise on surfaces – so-called piezoelectric effect. Those reflections generate an electrical signal used to produce the typical sonographic images. The differences in the acoustic impedances of juxtaposed media characterize the reflection of the sound wave. The higher the density of the tissue and the larger the impedance differences between two tissues, the stronger the reflection [129, 130]. Ultrasound waves are attenuated with increasing penetration depth. The higher the transmission frequency, the lower the depth of penetration into the tissue but the better the resolution [131]. Due to their small body size and high HR, mice are examined with high frequencies, above 10 Hz and up to 70 Hz [132-134].

In this work, brightness mode (B-mode) and motion mode (M-mode) imaging were performed. Pulsed-wave (PW) Doppler sonography was used to measure the blood flow velocity through the mitral and pulmonary valves [134]. The B-mode displays two-dimensional pictures. The short axis is perpendicular to the long one. With the M-mode, information along a single axis is imaged, and a one-dimensional analysis with high spatial and temporal resolution of the heart motion is performed. The Doppler method is based on the reflection of ultrasound waves on particles moving parallel to the direction of sound – in our case blood cells. This movement is color-coded: red for movements towards the transducer, blue for movements away from the transducer; the faster the movement, the brighter the color [133].

Echocardiography is a non-invasive examination method that can be used to determine systolic and diastolic heart function as well as the extent of remodeling of the heart (infarction, dilated cardiomyopathy). Anatomy as well as functional state of the organ can be evaluated [132, 133, 135].

4.3.2. Echocardiographic measurements to assess heart function

Systolic heart function was assessed by recording ejection fraction and fractional shortening, whereas diastolic heart function was measured with the mitral valve flow. Tricuspid annular plane systolic excursion and pulmonary artery flow were used to evaluate right heart function (figure 8).

Ejection fraction

Ejection fraction (EF) is an indicator for left ventricular function and describes the percentage of blood pumped out of the left ventricle with each contraction. The EF is therefore dependent on the left ventricular end-diastolic (LVEDV) as well as the

end-systolic (LVESV) volumes [133, 134]. In order to measure the ventricular volume accurately, EF was calculated according to the Simpson method [134]. This required B-mode imaging during systole and diastole of the longitudinal axis (parasternal long axis, PLAX) to measure the ventricle length, as well as cross-section in short axis (parasternal short axis, PSAX) at the level of the heart base, papillary muscles and apex to measure the ventricle area (figure 8, C and D).

$$EF (\%) = \frac{LVEDV - LVESV}{LVEDV} \times 100$$

Fractional shortening

Fractional Shortening (FS) is an indicator of systolic heart function and describes the size reduction of the heart during systole and therefore myocardial contractility. Cross-sectional images were recorded in M-mode to calculate the left ventricular end-diastolic (LVIDd) and end-systolic (LVIDs) inner diameters [133, 134] on the heart base, papillary muscle and apex level (figure 8, E).

$$FS (\%) = \frac{LVIDd - LVIDs}{LVIDd} \times 100$$

Tricuspid annular plane systolic excursion

Tricuspid annular plane systolic excursion (TAPSE) refers to the displacement (in millimeters) of the *Anulus fibrosus cordis* surrounding the tricuspid valve. It describes the heart shortening along its longitudinal axis and is an indicator for right heart function [134, 136]. TAPSE is measured using the M-mode in the apical four-chamber view (figure 8, F).

Pulmonary artery flow

The velocity peak in pulmonary artery flow (PA flow) was measured in PSAX at the heart base as an additional parameter for right ventricular heart function. Its value (in mm/s) changes by remodeling processes in the right heart or pulmonary hypertension [136, 137] (figure 8, G).

Mitral valve flow

Doppler sonography of the mitral valve flow is used to assess the diastolic heart function. The biphasic filling phase of the LV during diastole is described by the E (early) and A (atrial filling) waves. The E wave occurs after the opening of the atrioventricular valves and represents the passive blood inflow from the LA into the LV, while the A wave is due to active atrial contraction. The E/A ratio changes by altered ventricular relaxation or altered atrial contraction [133, 134]. The velocities (mm/s) were acquired in the apical four-chamber view (figure 8, H).

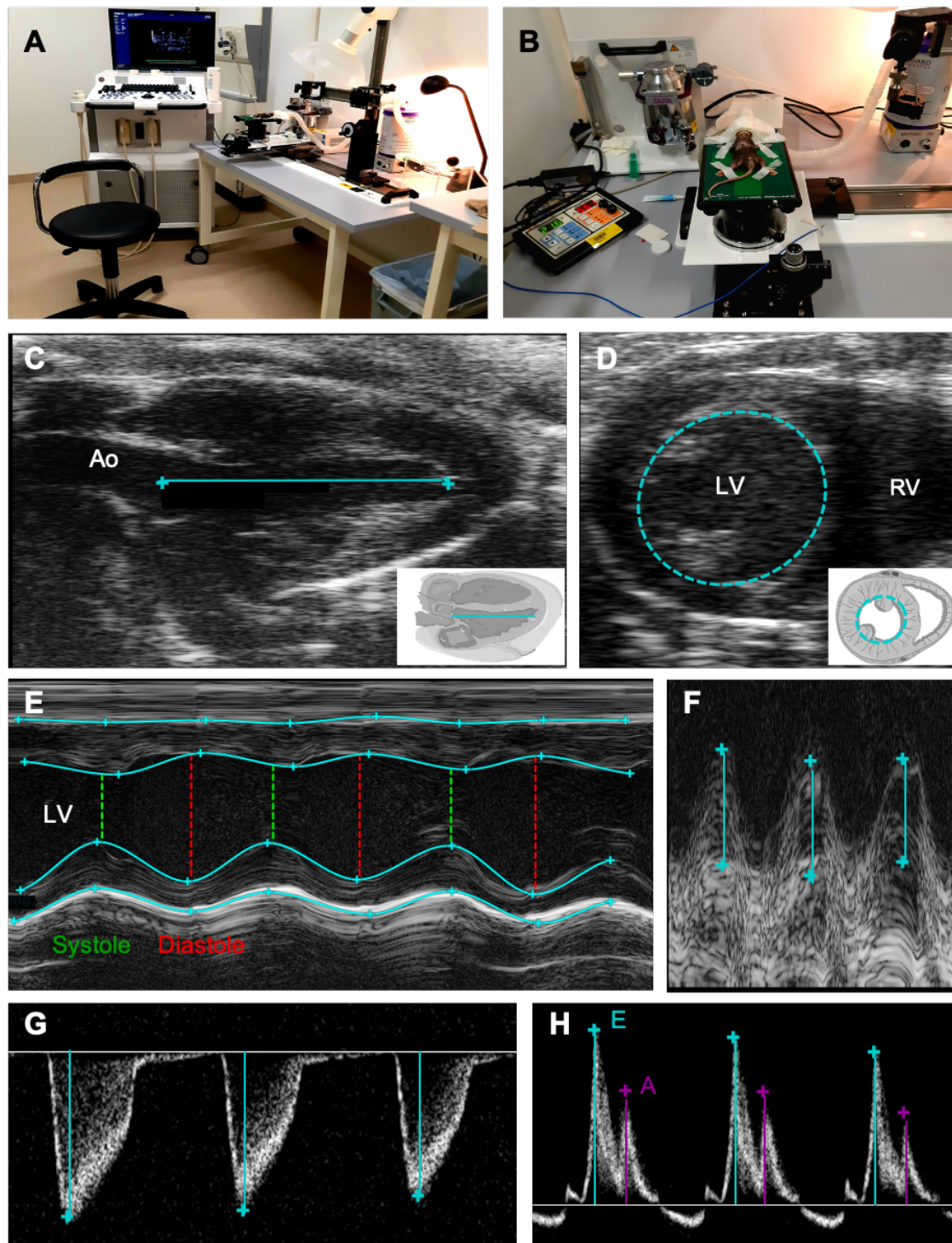


Figure 8| Representative examples of transthoracic echocardiography in anesthetized mice

(A) Recording station with ultrasound machine. (B) Anesthetized mouse fixed in supine position on examination table. (C) Measurement of the left ventricle length in PLAX view, B-Mode, for calculation of EF. (D) Measurement of left ventricle inner area in PSAX view, B-Mode, for calculation of EF. (E) Measurement of left ventricle motion in PSAX view, M-Mode, for calculation of FS; green: systole; red: diastole. (F) Measurement of the heart contractility by TAPSE, M-Mode. (G) Measurement of the pulmonary artery flow, pw-Doppler. (H) Measurement of the mitral valve flow, pw-Doppler for calculation of the E/A-ratio. Ao: Aorta, LV: left ventricle, RV: right ventricle.

4.3.3. Performing echocardiography in anesthetized mice

The echocardiographic measurements were performed in accordance to the approved applications for animal experiments and the experimental designs.

Anesthesia during echocardiography

Non-invasive transthoracic echocardiography was performed within 35 – 45 minutes in anaesthetized mice without any premedication. Anesthesia was induced as described under III.3.2.2., with the only difference that they were maintained under anesthesia (0.5 – 1.5 volume% isoflurane) by means of a mask instead of being intubated. Protection of the cornea and hair removal were performed as described under III.3.2.2. and III.3.3.

Mouse monitoring during data acquisition

In parallel to the examination, ECG was recorded to assess the HR and detect possible arrhythmias. The paws were fixed to the electrodes of a heated examination table (Mouse Handling Table II, 50249, FUJIFILM VisualSonics Inc., Canada) using surgical tape. The coupling to the electrodes was done using electrode gel (electrode gel Ratiomed, # MEG 152.0250, megro GmbH & Co. KG, Wesel, Germany), whereas the coupling between mouse chest and transducer was ensured by ultrasound gel (CAELO ultrasound contact gel, #7873, Caesar & Loretz GmbH, Hilden, Germany). To obtain comparable measurements, body temperature ($37^{\circ}\text{C} \pm 0.5^{\circ}\text{C}$) and HR were monitored in each animal and kept in the same reproducible range (450 ± 50 beats per minute (bpm)).

Ultrasound equipment

The measurements were carried out with a high-frequency (32 – 56 MHz) linear probe that transmits parallel waves and produces a rectangular image. Its features are particularly suitable for imaging superficial structures, and therefore appropriate for the small thorax depth of the mice. The transducer was connected to an ultrasound machine designed for cardiovascular research (Vevo 1100 Imaging System, 50797, transducer MS550D, FUJIFILM VisualSonics Inc., Canada). Image analysis was performed using Vevo LAB 3.2.6 software (FUJIFILM VisualSonics Inc., Canada). The measurements were always performed in three successive cardiac cycles (each including a diastole and subsequent systole) from which the mean value was calculated.

4.4. Computed tomography scan for *in situ* representation of the device implantation

4.4.1. Principle of single-photon emission computed tomography

Computed tomography (CT) is a medical imaging tool used in radiology to visualize specific cross-sectional layers of the body. Through mathematical reconstruction, image projections are sent to a computer and processed to build up two- or three-dimensional pictures. Using a large number of those projections, areas or whole bodies can be reconstructed and provide fine information about internal structure and anatomical organization. First, the data are acquired, then the images reconstructed and eventually displayed [138, 139]. For data acquisition, the patient is slowly moved through a rotating

X-ray tube. This spiral/helical path enables volume scanning of tissue. The X-ray sent through the object are attenuated differently by the tissues. The attenuated signal is detected and converted into an electronic signal which in turn is converted into digital images using reconstruction algorithms; the resulting images are displayed and digitally processed. Thereby, acquired transverse axial images can be reformatted to other sectional views for diagnostic purposes such as sagittal, coronal and paraxial views. Moreover, color can be adjusted and the images processed to three-dimensional pictures [138].

Single-photon emission computed tomography (SPECT) enables the detection of gamma rays emitted by a tracer injected into the patient; its distribution can then be recorded. The use of SPECT for myocardial perfusion imaging has a high value for the prognostic of coronary artery disease [140] and the diagnostic of vascular stenosis. The systemic administration of contrast media leads to opacification of the lumen of the vessels, increases the vascular attenuation and therefore enhances the contrast between blood and surrounding tissue [141].

4.4.2. Mouse preparation and imaging

CT was used to visualize the position of the device after implantation.

Device implantation was performed on the right ventricle as described under IV.1.2. Subsequently, the mouse was sacrificed with cervical dislocation under deep anesthesia with isoflurane. In order to provide more stability and rigidity to the neck during the procedure, the animal was fixed with tape to the surgery table and intubated as described in section III.3.2.2.

Perfusion with contrast agent

A longitudinal skin incision (1 cm) was performed on the ventral cervical region. Blood and blood clots formed following cervical dislocation, were removed with saline solution (NaCl 0.9%, Fresenius Kabi Deutschland GmbH, Homburg, Germany) and swabs. Parotid glands and cervical muscles were pulled laterally with retractors in order to get access to the right carotid artery. The latter was carefully separated from the vagus nerve, afterwards three suture threads (Silk, 6/0, 2 x DR-10, 45 cm Vömel, Kronberg, Germany) were placed from cranial to caudal beneath the visible portion of the carotid artery and secured with loose simple interrupted sutures. The cranial thread was tightened and fixed to the table, while the suture in the middle remained loose and was only used to stabilize the artery. The caudal suture thread was gently pulled just to maintain it in the desired position and make the artery accessible without applying too much pressure onto the vessel. Two to three drops of physiological saline were poured on the artery to keep it moisturized and ensure good elasticity of the vessel wall while a tiny incision between the cranial and caudal thread was made, using a microincision scissors (sharp/sharp tip Vannas Micro Scissor, 85 mm, #OC498R, B. Braun, Meslungen, Germany). The tip of fine forceps (Micro Forceps, Jeweler Patterns, 110 mm Braun Aesculap BD329R, B. Braun) was introduced in the incision made in the artery and used to guide a polyethylene catheter (800/100/100, 0.28 mm internal diameter, 0.61 mm external diameter, Portex, fine bore tubing, Hartenstein GmbH, Würzburg, Germany) filled with heparin (5000 I.E./0,2 ml, Ratiopharm, Ulm,

Germany) into the vessel. Then the catheter was carefully pushed forward until the LV was reached. Proper catheter position was assessed through perception of a resistance when entering the LV, as well as the length of the inserted tube (≈ 2 cm). Next, the caudal suture thread previously placed around the artery was tightened to fix the catheter within the vessel. About 0.1 ml of heparin solution was injected via the catheter and a cardiac massage was performed to distribute the solution in the circulation. Then the visible end of the catheter was connected to a syringe containing 1 ml Imeron 350 (Iomeprol, 350 mg Iod/ml, Bracco IMAGING Deutschland GmbH, Konstanz, Germany). The contrast agent was injected slowly and again, cardiac massage was performed to distribute the medium through the body circulation. The carotid artery and sutures were wet with saline solution and the caudal suture thread around the carotid artery was opened to release the catheter which was gently pulled out and removed. Finally, the caudal suture was tightened to ligate the carotid artery and avoid leakage of the contrast agent.

Computed tomography imaging

The mouse was placed in an imaging bed and scanned with SPECT (VECTOR 5 SPECT/CT, MILabs, Houten, Netherlands). Imaging was performed with 55 kV, 0.33 mA, 1 x 1 binning, step angle of 0.5° with one projection per step and 40 ms exposure time. Images were reconstructed with $90 \mu\text{m}$ isotropic voxels and three-dimensional images were generated in AMIDE [142].

Imaging was performed in the CHFC in collaboration with Prof. Higuchi and Lars Mayer from the Nuclear Cardiology Department.

5. Opsin expression in intrinsic cardiac cells of interest via a viral vector

5.1. Strategy for specific spatial opsin expression

Optogenetic manipulation of cells relies on opsin expression in the cells of interest. Cre-conditional was used to achieve accurate opsin expression in the target cells through combination of a viral vector containing an expression cassette with Cre-conditional, and specific mouse strains.

5.1.1. AAV as viral vector

Recombinant adeno-associated viruses (rAAV) are widely used for *in vivo* gene transfer and have a high security level (“biologische Sicherheitsstufe 1” according to the local regulation Gentechnikgesetz and Gentechnik-Sicherheitsverordnung). AAV are non-pathogenic for mammals and belong to the *Parvoviridae* family, the subfamily *Parvovirinae* especially infects vertebrates (reviewed in [143]). Adeno-associated viruses (AAV) are non-enveloped viruses with an icosahedral capsid ranging from 18 to 26 nm and containing a single-stranded linear DNA. Their packaging capacity is around 4,7 kbp and the genome is located between two inverted terminal repeats (ITRs), which play an important role in DNA rescue, replication, integration in the host and

encapsidation. Three open reading frames (ORFs) *rep*, *cap* and *aap* encode proteins for viral replication, structure and assembly, respectively [143, 144]. After reaching the nucleus via the endosomal pathway, the virus uncoats, its DNA is released and, in the presence of helper viruses, transcribed and expressed. Without the presence of helper viruses, AAV can remain episomal or integrate into chromosomes at very low level (reviewed in [143, 145]). AAV show expression over years in dividing as well as in non-dividing cells such as neurons or cardiomyocytes. Immunogenicity of AAV is controversial [35], but they seem to have a low immunogenic potential [146] and do not influence cardiac function [147].

In the present work, AAV vectors were used to deliver the expression cassette encoding the opsin.

5.1.2. Cre-dependent recombination of the floxed expression cassette

Cre recombinase acts like topoisomerase to achieve site specific recombination between recognition sites (*lox* sites). The enzyme is a tyrosine recombinase, belongs to the integrase family and derives from the P1 bacteriophage (reviewed in [148]). Cre recombinase is extensively used in molecular biology and provides a tool for conditional transgenesis. The enzyme recognizes *lox* sites flanking a DNA sequence (floxed sequence) and their orientation [149]. The latter determines the way the Cre recombinase processes the floxed sequence. If the orientation is the same, excision occurs; when they are in reciprocal position, the sequence is inverted and last but not least, if the *lox* sites are in different DNA molecules, the enzyme catalyzes translocation [148, 149]. Thus, a floxed sequence is only expressed after recombination, which can exclusively occur in the presence of Cre recombinase.

5.1.3. Combination of viral vector and Cre-mice for specific spatial expression of the opsin

Tissue-specific expression of genes of interest was achieved with a Cre/*lox*-system described above. An AAV vector was used for the systemic delivery of a floxed sequence, coding for the opsin, into mice expressing Cre recombinase in cells of the electrical conduction system and intrinsic cardiac neurons. In the chosen AAV containing the expression cassette, two pairs of *lox* sites flanked the sequence coding for the opsin and the red fluorescent protein (RFP). Thus, Cre recombinase first inverted the sequence (*loxP* in reciprocal orientation), then excised it from the plasmid sequence (*lox2272* in same orientation) enabling its subsequent transcription into a functional protein (see section III.5.2.3.2., figure 9). The floxed construct encoding the opsin was linked to a ubiquitous promoter (see section III.5.2.1.), but the Cre recombinase expression was driven by a specific promoter present in the cells of interest, therefore ensured that the recombination remained restricted to the target cells. This strategy for conditional transgenesis provided spatial specificity [148].

In order to modulate the HR, two mouse lines were selected, each to serve a different approach: to transduce the electrical conduction system of the heart, HCN4-Cre mice were used, whereas ChAT-Cre mice were chosen for opsin expression in intrinsic cardiac cholinergic neurons (see section III.1.2.).

5.2. Selecting the appropriate AAV vector and the expression cassette

5.2.1. Selection of the promoter driving the construct expression

Promoters are DNA regions bound by RNA polymerase to initiate gene transcription. Thus, they are crucial for the transcription of genes into their corresponding mRNA which is in turn translated into the functional protein. In differentiated tissues, gene expression is initiated by cell-type specific promoters [148]. Therefore, in addition to the AAV serotype, a localized expression of the genes of interest can be linked to a promoter expressed specifically in the target cells [148]. The frequency of recombination correlates with the promoter activity [151]. Since in this work, tissue-specific expression was given by the presence of Cre recombinase exclusively in the cells of interest, the ubiquitous promoter from the human elongation factor 1 alpha (EF-1 α) was used in both vectors, AAV9 as well as AAV-PHP.S (see section III.5.2.2.). EF-1 α is a mammalian promoter with strong and constitutive expression and is broadly employed in research for expression regardless of the cell type [150].

5.2.2. Selection of the capsid to transduce the cells of interest

Tissue tropism of AAV vectors is assimilated to their capsid. Natural and engineered capsids have been described, involving a variety of receptors implicated in their tissue affinity [143, 147]. Thus, by using different viral capsids, distinct cells can be preferentially infected (reviewed in [152]).

In this work, the targeted cells belonged to the electrical conduction system of the heart or intrinsic cholinergic ganglia; both are largely located in the heart base in proximity of the *Sinus venosus* but are different cell type.

Transduction of the electrical conduction system of the heart

Physiologically, heart beats are initiated in the SAN located in the RA. Cells of the SAN predominantly express the HCN4 channel [153], but these are also detectable throughout the whole conduction system [154]. In order to specifically transduce these cells, Cre-conditional was bound to cells expressing this channel (HCN4-Cre mouse strain). AAV9 outperforms other serotypes in the transduction of cardiomyocytes *in vivo* [147, 155, 156] by binding the laminin receptor (LamR) and the terminal galactose on the cell surface [156]. Cells of the ECS are modified cardiomyocytes [153, 154]. Taken together we chose an AAV serotype 9 (AAV9) to transduce the ECS.

Transduction of intrinsic cholinergic cardiac neurons

Cells of the conduction system are in close interaction with sympathetic and parasympathetic cells within the heart. The majority (83%) of intrinsic cardiac neurons express ChAT and are under efferent vagal influence [70, 157]. To specifically transduce these cells, Cre-conditional was linked to cells expressing ChAT (ChAT-Cre mouse strain). ChAT-expressing cells carry the properties of neurons and are part of the parasympathetic nervous system. We chose to use a new capsid variant with tropism for the peripheral nervous system, AAV-PHP.S, to transduce them in the heart [54, 158].

5.2.3. Selection of the appropriate expression cassette

5.2.3.1. Selection of the opsin

On the one hand, features of the myocardium must be considered, as its density and dark color represent an obstacle to light penetration. On the other hand, light properties have a major influence on its penetration into the tissue. Indeed, longwave light is lower in energy, but penetrates deeper into the tissue (see section III.2.1.), thus could better reach the target cells within the myocardium. The choice of an opsin responding to long wavelengths was made to circumvent the high tissue absorbance of the dark myocardium. The red-shifted opsin “ChRmine” was isolated from a marine microorganism, *Tiarina fusus*, its sequence then modified to optimize its expression in mammals. ChRmine responds within milliseconds to photostimuli at both 585 nm and 630 nm, and recovers quickly after activation [117]. Its structure forms a trimer with seven transmembrane proteins and is similar to ion-pumping opsins, yet ChRmine functions as a cation channel [159]. Recently, it has also been shown that, after systemic administration, a transcranial excitation of the opsin with red light (635 nm, initial irradiance 400 mW/mm²) is possible up to 7 mm depth in the brain [160]. Hence, the chosen red-shifted excitatory opsin ChRmine offered a promising tool to manage optogenetic manipulation of cells in the myocardium.

5.2.3.2. Additional construct elements

Apart from the opsin, the delivered construct contained a fluorescent protein as tag and a sequence to support gene expression.

Red fluorescent protein

Genetically encoded fluorescent proteins (FP) were first isolated from living organisms (bacteria and *Cnidaria*, corals [161]) and genetically modified to be adapted for the use in mammalian systems and generate variously colored mutants [162]. FP are proteins containing a chromophore (fluorescent molecule) which after light absorption, spontaneously emits light (described in section III.8.3.1.). Their physical properties and spectral range are constantly improved, which widens the field of applications [163]. Red fluorescent proteins (RFP) are suitable as reporters in deep tissues, for their emission is in the infrared part of the spectrum (> 600 nm) [164]. Most RFP were isolated from corals and anemones [162] but the RFP mScarlet used here was synthetic. mScarlet shows both, high brightness and increased fluorescence lifetime compared to other RFP. Its excitation and emission spectra peak at 569 nm and 594 nm, respectively [165]. Here, mScarlet was integrated into the expression cassette and used as reporter for proper viral transduction in quantitative polymerase chain reaction (qPCR) (see section III.6.2.2.).

Post-transcriptional regulatory element

The woodchuck hepatitis virus post-transcriptional regulatory element (WPRE), known to improve gene expression *in vivo* [166], was included into the construct.

In summary, to modulate the HR, two mouse lines were selected, each one meant for a different approach: HCN4-Cre mice were used for transduction of the ECS, whereas ChAT-Cre mice were chosen for opsin expression in intrinsic cardiac cholinergic

neurons. The use of the *Cre/lox*-system combining Cre-mouse strains with a floxed AAV, ensured spatial control of opsin expression restricted to the cells of interest (figure 9). To deliver the genetic information encoding the opsin, Cre-dependent AAV with tropism for the cells of interest were chosen according to their capsid. The ubiquitous promoter EF-1 α drove the expression of ChRmine under Cre-conditionality in the cells of interest. Taken together, those elements guaranteed the expression of the opsin and the RFP spatially restricted to two cell populations of interest (HCN4 and ChAT) with different functions within the heart.

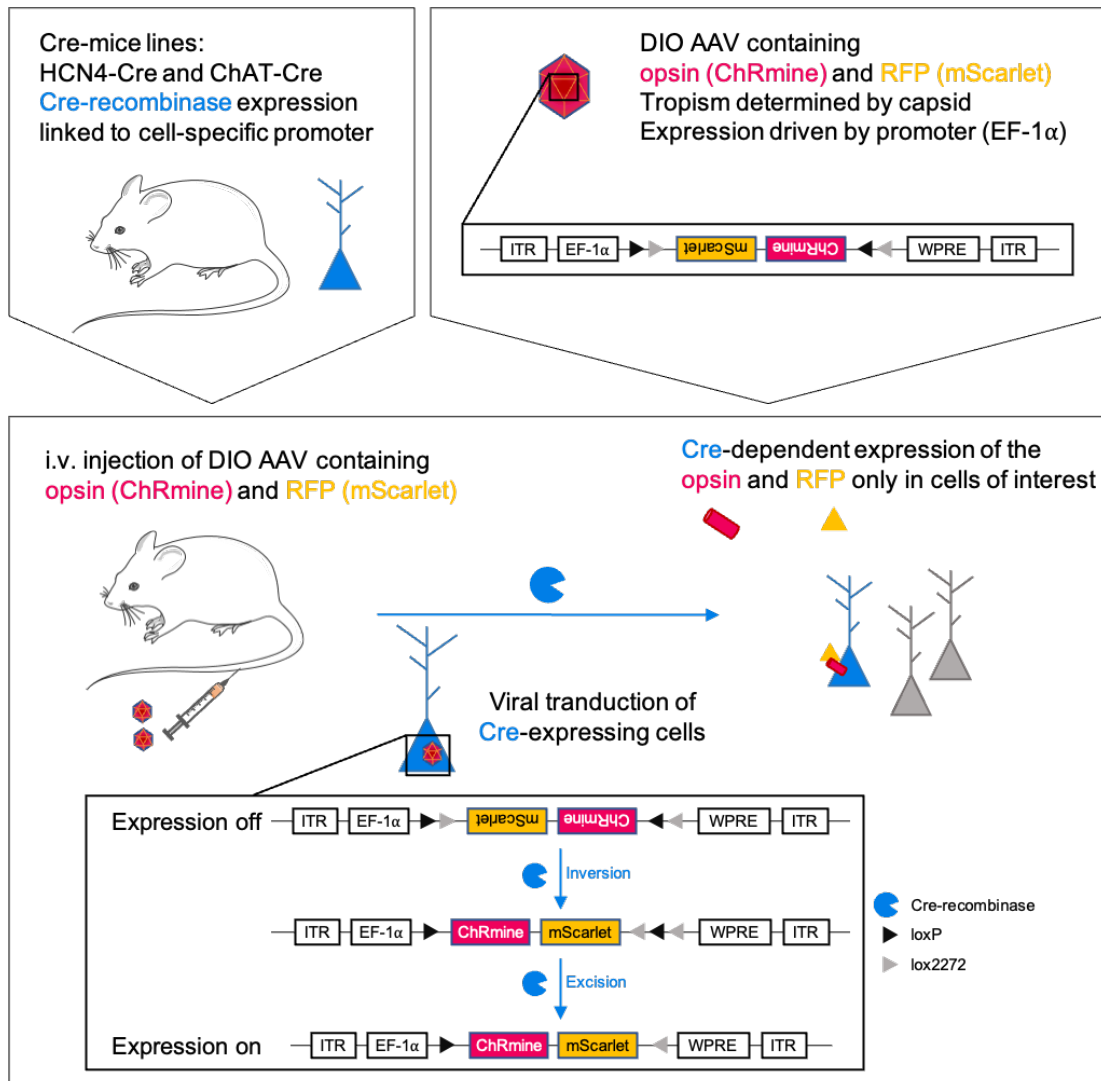


Figure 9| Cre-mediated opsin expression in cells of interest for spatial control of opsin expression

Cre recombinase is only expressed in target cells of the transgenic mouse line. AAV vector contains the expression cassette and transduces the target cells. Inversion of the sequence flanked by *loxP* and subsequent excision of the sequence flanked by *lox2272*, turns gene expression on. Inversely, *lox2272* can serve for inversion and *loxP* for excision (not illustrated here) leading to the same result. Both reactions are Cre-dependent and therefore only occur in the Cre-expressing cells, thus the cells of interest. DIO: double-floxed inverse open reading frame; ITR: inverted terminal repeat; WPRE: woodchuck hepatitis virus post-transcriptional regulatory element.

5.3. Production of AAV vectors

Tailored AAV particles were produced in the Defense Circuits Lab (ICN) by combining the selected capsids with the expression cassette of choice.

Plasmid selection

The plasmids required for the production of AAV particles were all purchased by Addgene (Waterton, USA). The floxed expression cassette (pAAV-Ef1a-DIO-ChRmine-mScarlet-WPRE Addgene plasmid #130998, gift from Karl Deisseroth to Addgene, [117]) contained the opsin (ChRmine) and the RFP (mScarlet) and, depending on the purpose, was integrated into the AAV9 capsid (pAAV2/9n, Addgene plasmid #112865, gift from James M. Wilson to Addgene) for injection in HCN4-Cre mice, or into AAV-PHP.S capsid (pUCmini-iCAP-PHP.S, Addgene plasmid #103006, gift from Viviana Gradinaru to Addgene, [167]) for injection in ChAT-Cre mice.

AAV production

First the plasmids encoding the capsid and the construct were grown. Second, both vectors, AAV9 and AAV-PHP.S, were produced according to the protocol established by Rosemary C. Challis for systemic delivery in rodents [158]. To produce AAV, three plasmids were needed: the plasmid containing the construct, the one encoding the *rep/cap* as well as the helper plasmid. Briefly, bacterial stocks containing the different plasmids were retransformed in *Escherichia coli* overnight, afterwards the produced plasmid DNA were harvested, then isolated and their integrity verified by restriction digestion. HEK293 cells contain the adenovirus early region 1 gene (E1) necessary for the production of viral particles and were transduced with the three plasmids. Five days after transfection start, the AAV particles were harvested and subsequently purified for *in vivo* injections. Virus titration was performed by qPCR using a primer to detect the WPRE sequence. Per batch, around 100 μ l with 10^{13} to 10^{14} vg/ml were yield, providing enough viral particles for systemic injections of several mice.

The vector production was not part of this thesis work.

5.4. Systemic AAV injection

For homogenous circulation and distribution, the viral vector was injected intravenously (i.v.). Moreover, systemic injection in the lateral tail vein is less invasive than direct injection locally into the beating heart. Concentrations in a range of 10^9 to 10^{13} viral genom particles (vg) per mouse are described for i.v. delivery [155]. Regardless from the serotype, 10^{11} vg/mouse appeared to provide consistent transduction of tissue after systemic injection [147, 158, 168]. The virus solution was diluted in sterile PBS (DPBS, no calcium, no magnesium, Gibco, #14190144, ThermoFischer Scientific, Darmstadt, Germany) to reach a concentration of 10^{11} vg/mouse in the final volume. According to the Recommendation for administration of substances to laboratory animals from the Committee for Animal Welfare Officers (GV-SOLAS, March 2017), a volume of 5 ml/kg of the diluted virus solution was administrated. The solution containing the viral particles was drawn up into a syringe with integrated needle to minimize dead volume (Omnican-F, 0,30 x 12 mm / G 30 x 1/2", 1 ml, #9161502S, B. Braun, Meslungen, Germany) and injected as bolus. Prior to injection, bubbles were withdrawn to avoid air

embolism.

Vector administration

In order to evoke vasodilatation and facilitate the vein puncture, the cage containing the animal was put under a heating lamp for about 15 minutes. Alternatively, once fixed, the tail could also be warmed up for 30 seconds with an exam glove filled with warm water. After picking up the mouse by its tail, it was fixed in a restrainer. The tail was held by the non-dominant hand during the whole procedure. The tail base was gently squeezed between index and middle finger to occlude the vein and make it more visible, while the tail end was fixed between thumb and ring finger in order to keep the tail under soft tension. With the preferred hand, the injection site was disinfected and the needle inserted in the middle third of the vessel. The needle was slid around 2 mm under the skin in a 25° angle in cranial direction, following the course of the vein with the bevel facing up. By successful insertion, the needle slid easily into the vein. Subsequently, the occlusion at the tail base was released and the solution injected over around 3 seconds to avoid hemodilution. During proper administration, no resistance should be felt and the vein should become clear as the blood is briefly replaced by the solution in the vessel. Blanching of the vein or swelling indicated subcutaneous injection. If the injection failed, a new attempt was performed a few millimeters cranial from the first injection site or in the contralateral tail vein. After successful injection, the needle was left in the vein for 2 seconds to enable the solution to be flushed into the circulation without any loss by return flow. Directly after needle removal, hemostasis was performed with a dry cotton gauze until bleeding stopped. Afterwards, the mouse was released from the restrainer, put back into its home-cage and observed at least during 15 minutes for any complications.

6. Monitoring heart rate *in vivo* and viral transduction of intrinsic cardiac cells

6.1. Electrocardiography to record heart rate modulation

6.1.1. Principle of electrocardiography

Electrocardiography is based on the measurement of the cardiac action potential over time. Its representation as a curve in the ECG shows the transmission of the electrical impulses through the electrical conduction system of the heart inducing rhythmic depolarization and repolarization of the myocardium. During a cardiac cycle, corresponding to one diastole and the following systole, electrical charge shifts occur that can be recorded at the body surface [169]. The sum of these voltage differences defines the integral vector. The electrical cardiac axis corresponds to the average direction of the integral vector during depolarization of the ventricles. Thus, its direction depends on the orientation of the cardiac muscle fibers and is the largest between the base and the apex. Usually, the heart is located to a greater extent in left thorax side, which, in addition to the high left ventricular mass, leads to a general orientation of the electrical cardiac axis in the mouse to the left, as in most mammals [170]. The electrical

signal originates in the SAN and the depolarization wave propagates through the myocardium. The integral vector draws three ellipsoidal loops during a cardiac cycle, which describe the spatial as well as temporal propagation of excitation in the heart. ECG traces result from its two-dimensional projection onto a plane. The atrial loop arises first, corresponds to atrial depolarization and is represented as “P wave” on the ECG trace. The ventricular loop describes the ventricular depolarization and appears as “QRS complex” on the curve; the “R wave” corresponds to the moment of greatest expansion of the integral vector. Finally, the repolarization loop is detected and recorded as “T wave” in the ECG. Repolarization occurs in reverse order, i.e. the first depolarized cell repolarizes last, therefore the T wave is usually positive [170].

The ECG curve describes the propagation of the signal in the heart and enables to assess myocardial work. The “PQ interval” describes the conduction time between the atria and the ventricles. The resulting delay is due to filtering properties of the AVN. Cells of the AVN are heterogeneous, can act as pacemakers and, due to high parasympathetic influence, the propagation of the excitation within the node is slow [171]. The distance between two successive R waves corresponds to the duration of a cardiac cycle. In mice, the “ST segment” and the T wave are not clearly separable from the QRS complex; repolarization of the ventricles occurs very early in the mouse and corresponds to a “J wave” that directly follows the QRS complex [172].

6.1.2. Electrode assembly and implantation in mice

ECG signals were recorded via custom made electrodes implanted subcutaneously.

Electrode assembly

The electrodes were used to derive the electrical activity of the heart at the body surface. In order to perform experiments in freely moving mice, they were implanted subcutaneously and remained permanently in the mouse. Three electrodes consisting of a thin Teflon-coated wire (diameter = 140 μm , #7SS-1T, Science Products GmbH, Hofheim am Taunus, Germany) were conductively welded to a connector (6 Position Male Nano-Circular Miniature Circular Connector, #NCP-06-DD, Omnetics Connector Corporation, Minneapolis, USA; figure 10, A). This connector was fixed on the skull of the mouse and, by plugging it in with its corresponding socket (6 Position Female Nano-Miniature Circular Connector, #NCS 06-DD, Omnetics Connector Corporation, Minneapolis, USA), enabled the derivation of the potential difference between the electrodes (figure 10, C and D). During surgical implantation, the ends of the wires were shortened and stripped to ensure better coupling. One wire was placed on the skull as grounding and the other two wires were fixed subcutaneously on the chest on the left and right side respectively (figure 10, B).

Subcutaneous electrode implantation

For electrode implantation, the animals were first prepared as described in section III.3.2.2., anaesthetized and maintained under anesthesia with a mask.

Starting in prone position, the skull was scalped longitudinally on about 4 mm between the ears with a fine pair of scissors (Fine Scissors – Sharp, #14060-09, Fine Science Tools GmbH, Heidelberg, Germany). The mouse was then fixed in supine position and

two small skin incisions were made on the thorax. These sites were chosen far enough from the device to avoid contact with the subcutaneous coil and therefore possible interferences. The left skin incision was on the ventral thorax at the level of the elbow joint while the right incision was more cranial, ventral at the level of the shoulder joint (figure 10, B). Hence, the electrodes were located on an imaginary diagonal line running through the heart. Starting from those skin incisions, the subcutaneous tunnelling for the passage of the electrode wires was carried out with the help of a button cannula (Luer Olive button, #21.072, unimed, Wadern, Germany). The tunnel for the left electrode ran caudodorsally of the elbow towards the scalped skull, while the one on the right side ran cranioventrally of the shoulder joint. One side at a time, the electrode wires were threaded through the button cannula from the skull in direction of the thorax, and pushed until they became visible on the other side at the level of the skin incision. The button cannula was then withdrawn, leaving the wire subcutaneously in the preformed tunnel. The wire was shortened, leaving about 7 mm overhang to allow the wire to slide subcutaneously and avoid tension during movements of the mouse. Approximately 5 mm of the visible wire end was stripped using fine surgical forceps (Fine Forceps – Mirror Finish, #11-41211, Fine Science Tools GmbH, Heidelberg, Germany). A small ball of cyanoacrylate (Ultra Gel Matic, Pattex, Düsseldorf, Germany) was formed at the end of the stripped wire in order to prevent the wire from slipping through after it was attached to the subcutis with a simple interrupted suture (Polypropylene 5/0, HR-16, monofil, 75 cm, Vömel, Kronberg, Germany). The skin incision was closed with two simple interrupted sutures and the same procedure was repeated with the second wire. Afterwards, the mouse was rotated back in prone position in order to secure the connector on the skull, by forming a cyanoacrylate cap. The grounding of the electrode was first shortened to about 3 mm, then stripped and fixed subcutaneously, oriented rostrally on the top of the skull. Thereafter, the skull was swabbed and its surface roughened with a scalpel (Cutfix, #8508216, B. Braun, Meslungen, Germany) the connector was attached to the parietal and frontal bones using cyanoacrylate. To accelerate the hardening of the cyanoacrylate, one to two drops of Paladur liquid (Paladur, Kulzer GmbH, Hanau, Germany) were applied to the cyanoacrylate. The plug was gradually embedded in adhesive and finally, for aesthetic reasons, the last layer of the cap was formed with black cyanoacrylate (#WK 2400, Weckem GmbH, Bergkamen, Germany). Care was taken to ensure that the plug of the connector was not embedded in adhesive (figure 10, C) to be able to connect it (figure 10, D). The isoflurane supply was terminated, the surgical sites were disinfected with the skin antiseptic and the mouse allowed to recover as described under III.3.2.2.

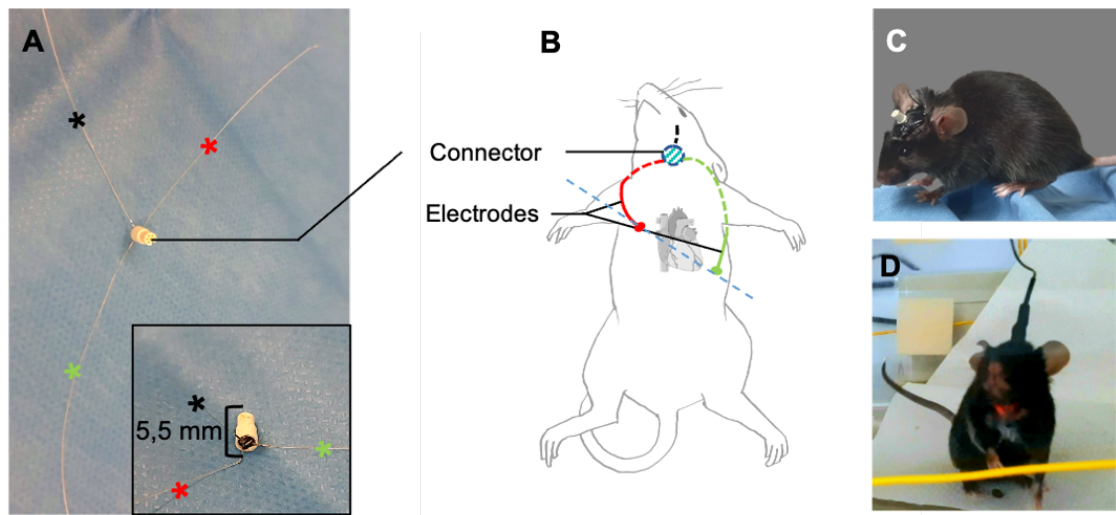


Figure 10| Structure and implantation of the ECG electrodes

(A) Soldered electrode ready for implantation; view from above. Zoom in: soldering points connecting the wires to the connector; view from below. (B) Illustration of electrodes and connector positioning after implantation. Dorsal elements appear as dashed lines, ventral elements as filled lines. (C) Mouse after ECG implantation. Only the cap with the connector is visible. (D) Mouse during ECG recording after connection of the plug to the socket.

Black: grounding; green: left electrode; red: right electrode.

6.1.3. Electrocardiography recording and heart rate calculation

HR was determined by extraction of the R waves recorded in the ECG signal.

ECG recording

An OmniPlex biopotential recording system (Neural Recording Data Acquisition System, Plexon, Dallas, USA) was used to record and subsequently digitize analogue as well as digital signals. Stimulation protocols were written with the Radiant software. The PlexBright system (Optogenetic Stimulation System, Plexon, Dallas, USA with analogue and digital outputs) enabled external control of the coupled NeuroLux optogenetics system and coordinated the stimulation with the ECG recording. The ECG connector implanted in the mouse was plugged into its complementary socket and the ECG signal was recorded at 5 kHz via an amplifier (DPA-2FX, NPI Electronic GmbH, Tamm, Germany) which in turn was connected to the OmniPlex system. Depending on the signal quality, the ECG was derived either as a potential difference between the electrodes or directly from one electrode.

ECG extraction and heart rate evaluation

Monitoring of the HR was performed during optical stimulation. For this purpose, the R waves in the ECG were detected and their frequency determined using a MATLAB custom code (MATLAB 2019b, The MathWorks, Natick, USA) written by Dr. J r my Signoret-Genest (Defense Circuits Lab, ICN). The external trigger launching the stimulations led to noises and artefacts, which appeared synchronously to the stimulation and needed to be filtered. First, the exact time of the onset as well as the offset of a stimulation had to be known. Thereafter, a corresponding artefact model was calculated using a second MATLAB custom code in order to fit each stimulation artefact to a model. Next, the created model was subtracted from the actual signal. Once free

from artefacts, the signal was further denoised with a band-pass filter. The ECG trace was then magnified to better represent the spacing between the R peaks and smoothed with a Gaussian filter. A threshold was set to extract heartbeats. Based on HR values and similitudes with the beat template (average of the beats within a defined amplitude percentiles range), an algorithm was used to remove aberrant peaks in order to generate a trace from the extracted putative heartbeats. The resulting signal was then manually checked again for deviations, which were deleted if necessary.

The frequency of the R peaks was used as the actual HR and processed using a sliding window of 0.6 seconds ending at each peak, and resampled to a fixed sampling rate.

6.1.4. Optogenetic stimulation protocol for heart rate modulation

Stimulation strategies to optically modulate the heart rate

At least one day elapsed between two sessions of ECG recordings during optogenetic stimulation. A session consisted of three sequences, each with different stimulation types. Within a sequence, the same stimulation type, defined by frequency and pulse width, was repeated three times in a row (table 4 and figure 11). The stimulation lasted 30 seconds and was performed at maximum power of the optogenetic system (10 W). Before and between each stimulation, a 60-seconds break (“baseline”) was taken to allow the stimulated cells to recover and to assess the reproducibility of the stimulation effects. HR (in bpm) was recorded continuously throughout the sequence.

To evaluate changes in cardiac activity, the mean HR during the “baseline” and the mean HR during stimulation, both lasting 30 seconds, were calculated and compared.

Table 4| Selected stimulation parameters for optogenetic stimulation of the ECS and cholinergic cardiac cells

PlexBright settings (frequency, pulse width)	μLED status during stimulation (30 s)		
	Cycle duration (ms)	On (ms)	Off (ms)
10 Hz, 10 ms (ChAT-Cre)	100	10	90
15 Hz, 15 ms (HCN4-Cre)	67	15	52
15 Hz, 30 ms (HCN4-Cre)	67	30	37
50 Hz, 15 ms (ChAT-Cre)	20	15	5
Constant	-	Continuously	-

Strategy to evaluate the effect of stimulation order and stimulation time point

The stimulation settings remained the same in all sessions, but the order of the sequences was changed between sessions (figure 11). This enabled to observe a possible effect of a stimulation type on the following one, as well as a possible effect of absolute time on the stimulation outcome. Thus, not only the effect of the type of stimulation was analyzed, but also whether its characteristics may have influenced the next one.

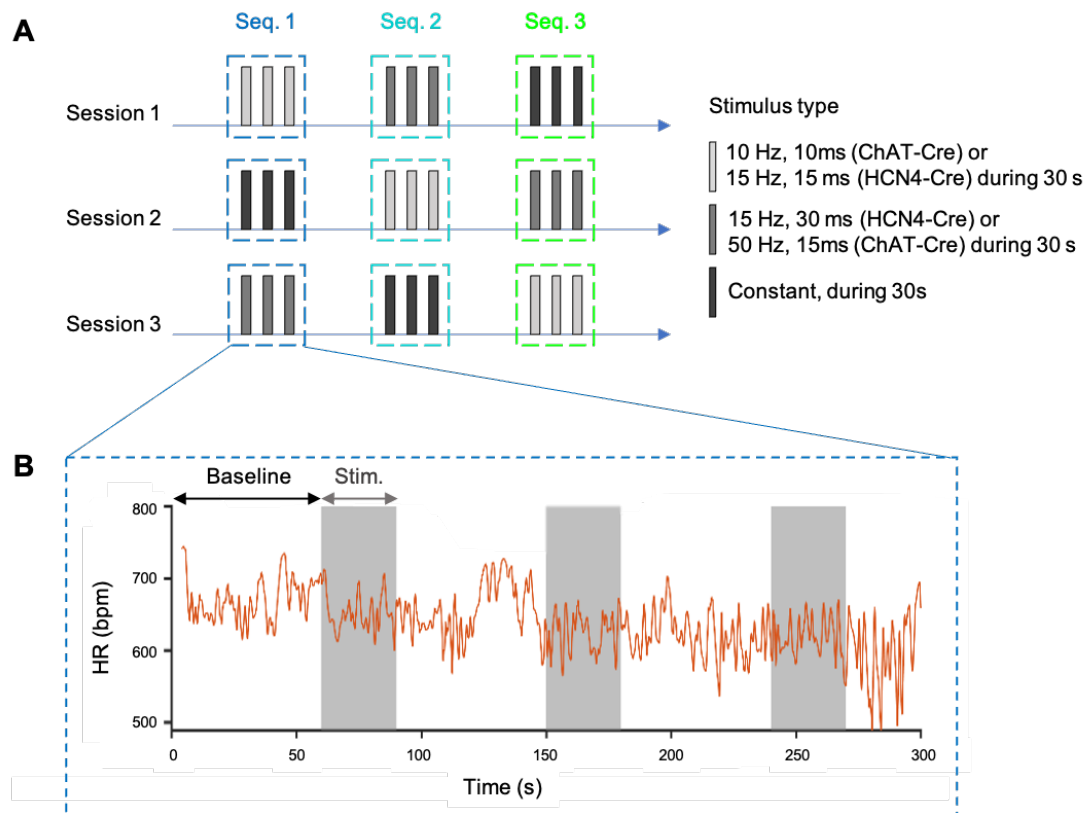


Figure 11| Stimulation protocol for heart rate modulation

(A) Each session was performed on a different day. On those days, the stimulation types were repeated three times in a row within a sequence (Seq.). The order of the stimulus type changed in each session. (B) Representative denoised HR trace showing the evolution of the frequency (bpm) over time. HR recorded during a sequence and three stimulations (Stim.) in a row with the same settings. 60 seconds “baseline” without stimulation separated stimulations from each other.

6.2. Quantitative polymerase chain reaction to assess opsin expression

To assess viral transduction of the cardiac tissue, a two-step quantitative polymerase chain reaction (qPCR) was carried out.

6.2.1. Principle of SYBR Green qPCR

In the first qPCR step, the mRNA contained in the sample is transcribed into complementary DNA (cDNA). During the second step, the amount of cDNA, which is proportional to the initial mRNA, is quantified [173]. During the qPCR cycle, cDNA is denatured, allowing the primers to hybridize specifically with the sequence of the gene of interest, which in turn enables the DNA polymerase to bind and synthesize the complementary strand during the so-called elongation. In the course of elongation, besides nucleic acids, a fluorescent dye (SYBR Green) is integrated into the synthesized DNA complementary strand. Its intercalation into the small groove of the left-handed DNA double helix results in increased fluorescence [174]. Each of these reactions occurs with a specific temperature optimum. The cycles repeat successively and the fluorescence increases proportionally to the number of synthesized amplicons. The quantification of the signal is recorded in real time. The Ct value (cycle threshold value) defines the cycle in which the measured fluorescence has crossed a certain fluorescence threshold. If the target gene is present in large quantities, a high number of fluorescent

amplicons is produced in the early cycles, hence the threshold is crossed rapidly and results in a low Ct value [174].

qPCR is a sensitive method for quantifying nucleic acids, even if they are only present in small quantities. However, its significance depends on various parameters [173]. Indeed, the quality of the mRNA as well as the specificity of the primers for the gene of interest are crucial [173]. The SYBR Green-qPCR detects all double-stranded DNA, and therefore also self-complementarity or dimer formed by primers. To check the specificity of the reaction, a melt curve analysis is performed [175]. The melt curve is obtained after the last qPCR cycle by measuring the fluorescence under slow and constant temperature increase. The gradual increase in temperature causes denaturation of double strands, which dissociate into two single strands, leading to the separation of the fluorescent dye from the DNA, thus resulting in a fluorescence decrease. The melting temperature (T_m) depends on the base composition and the length of the DNA-fragments. Mathematical derivation of the melt curve can be used to make statements about the quality of the PCR products [174]. As a matter of fact, primer dimers have a lower melting point than double-stranded amplicons and different PCR products have different melt curve peaks [175]. Similarly, if a primer binds to several DNA-sequences, the resulting qPCR products will have different lengths and therefore display several melt peaks.

6.2.2. Primer design for qPCR

Specific primers for both ChRmine (opsin) and mScarlet (RFP) contained in the expression cassette were not commercially available, therefore the sequences of the respective primer pairs were self-designed.

A primer pair consists of a forward and a reverse primer. Since each newly synthesized amplicon serves as a template for the DNA polymerase during the next cycle, only the sequence between the two primers is gradually amplified in the course of the qPCR, producing the so-called amplicon.

Primer properties

The amplicon should range from 90 to 150 base pairs (bp) while the primers themselves should count 18 to 25 nucleotides, have no self-complementarity and have a Guanine/Cytosine content of around 50%. The T_m of the primers should remain in the range of $60 \pm 5^\circ\text{C}$ and T_m of both primers, forming a pair, should not be more than 2°C difference [173, 176].

Primer design

First, the elements constituting the AAV were labelled in the vector map (link in supplementary materials of the original publication [117]) using ApE (A plasmid Editor by M. Wayne Davis) and the sequences of interest identified. Second, primer pairs were respectively chosen within the sequences of ChRmine and mScarlet (table 5) using the Primer3Plus website [177]. Third, care was taken that the primer did not show complementarity to the host genome to avoid cross-reactions. Indeed, the specificity of the primers for the genes of interest was a prerequisite for the accurate detection of the opsin. Using BLAT, a BLAST-like alignment tool [178], the primer sequences were compared with the mouse genome and it was ensured that no matches exist. The

designed primer pairs were produced by Metabion GmbH (Planegg, Germany).

Table 5| Properties of the primers used for qPCR

Primer		Primer-Sequence (5'→3')	Primer length (bp)	GC content (%)	T _m (°C)	Amplicon length (bp)
ChRmine	Forward	GTAACAGGACTTGGCCACGA	20	55	60	140
	Reverse	TCGCCGTGTTTACCTTCTCC	20	55	60	
mScarlet	Forward	AACTTGCGGTCCACGTTGTA	20	50	60.2	122
	Reverse	GGCGACATTAAGATGGCCCT	20	55	60.2	
GAPDH	Forward	ACCACAGTCCATGCCATCAC	20	55	70.3	
	Reverse	TCCACCACCCTGTTGCTGTA	20	55	70.3	

A: Adenin; C: Cytosin; G: Guanin; T: Thymin.

ChRmine and mScarlet: self-designed primers; GAPDH (Glyceraldehyde 3-phosphate dehydrogenase) taken as housekeeping gene (see below).

Quantification of the gene expression

For relative quantification of gene expression, the Ct values were normalized to the expression of the housekeeping gene GAPDH (Glyceraldehyde 3-phosphate dehydrogenase). Primers for GAPDH were commercially available (Eurofins Genomics, Ebersberg, Germany). Relative gene expression for each sample was given by $2^{-\Delta Ct}$, where $\Delta Ct = Ct_{(sample)} - Ct_{(GAPDH)}$ [174]. Gene expression was compared to negative controls corresponding to naïve animals which did not receive virus.

6.2.3. Organ removal and tissue preparation for qPCR

Organ collection for qPCR

RNases are ubiquitous and degrade RNA, including the mRNA, to be isolated for detection of opsin and RFP expression. To protect the samples, the field where organ removal was performed was thoroughly sprayed with RNase decontamination solution (RNase away, #83931, Sigma-Aldrich, Merck KGaA, Darmstadt, Germany). The samples were stored in sterile tubes free of RNase, pyrogen, RNase, DNase, DNA, ATP and PCR inhibitors (Safe-Lock Tubes 2.0 ml, Eppendorf BIOPUR, #0030 121.597, Eppendorf AG, Hamburg, Germany) until RNA isolation and manipulated only with instruments which were regularly decontaminated with RNase away during the procedure.

The mouse was sacrificed by cervical dislocation under anesthesia with isoflurane and transcardial perfusion was performed as described under III.4.2.2. Then “clean” instruments, previously sprayed with RNase away were used to cut the heart into three pieces. In order to be able to note possible differences in gene expression between the heart regions, the dorsal half of the heart up to approximately 1 mm below the base was divided into RA, LA and ventricle base (V). Each sample (three per heart) weighed approximately 30 mg. Afterwards, the samples were each stored in 1.0 ml RNAlater solution (RNAlater Stabilization Solution, #AM7021, ThermoFisher Scientific, Darmstadt, Germany) overnight at 4°C to protect the RNA in the intact tissue and, the

next morning, the samples were frozen in empty sterile tubes at -80°C .

gDNA elimination, mRNA isolation and determination of its concentration

Elimination of the gDNA (genomic DNA) and mRNA isolation were performed according to the protocol enclosed to the used kit (RNeasy Plus Mini Kit, #74134, Qiagen, Hilden, Germany).

To determine the RNA concentration and its purity the absorption spectrum of the sample was assessed. The greater the absorbance (A), the higher the RNA content in the solution [179] and therefore the concentration. To evaluate the purity, absorbance of the sample was measured at 260 (corresponding to the absorption maximum of nucleic acids) and 280 nm. If the A260/A280 ratio is approximately 1.8 to 2.0, the sample is considered as protein-free [180]. The ratio decreases by proteins and phenol contamination, which can happen during mRNA isolation. The ratio increases when the solution is basic. Furthermore, the A260/A230 ratio serves as an indicator for the purity of the sample and should be 1.8 to 2.2. Its value decreases in acidic environments or when contaminated with phenols and carbohydrates [181].

The purity as well as the concentration of the isolated RNA was immediately determined using a spectrophotometer (Thermo Scientific NanoDrop 2000c, ThermoFisher Scientific, Darmstadt, Germany). The spectrophotometer was first calibrated with RNase free water, then 1 μl of each sample was used for the measurement. Between each measurement, the spectrometer was gently wiped.

Each sample was diluted with RNase-free water to achieve a final concentration of 500 ng RNA in 15 μl .

Transcription of the mRNA into cDNA

The isolated mRNA was transcribed into cDNA by reverse transcription according to the protocol attached to the kit (iScript cDNA synthesis Kit, #1708891, Bio-Rad Laboratories GmbH, Feldkirchen, Germany). Afterwards, reverse transcription was performed in a thermal cycler (C2000 Touch Thermal Cycler, #1851148, Bio-Rad Laboratories GmbH, Feldkirchen, Germany) according to the settings specified in the protocol. Subsequently, each cDNA sample was diluted 1:10 using RNase-free water before being processed for qPCR. If the qPCR could not be performed right away, the samples were frozen at -20°C .

Running the qPCR

If previously stored at -20°C , the samples were first thawed slowly on ice.

Gene expression was verified in the samples by means of specific primers: ChRmine, mScarlet, and GAPDH as the housekeeping gene. A master mix consisting of a primer pair (forward and reverse), SYBR Green fluorescent dye (Fast SYBR Green Master Mix, #4385610, ThermoFisher Scientific, Darmstadt, Germany) and RNase free water was prepared for each primer pair individually. Primer stock solutions (100 μM) were diluted 1:10 with RNase-free water. qPCR was run in individual plates for each primer pair.

Table 6| qPCR-mastermix composition

Reagent		Volume in mastermix (μ l)*
Primer	Forward	$0.75 \times n + 10\%$
	Reverse	$0.75 \times n + 10\%$
Fast SYBR Green Master Mix		$7.5 \times n + 10\%$
RNase-free water		$6.0 \times n + 10\%$

*3 samples per heart (LA, RA, V). Triplicates were prepared for each sample:
 n (number of wells) = number of hearts \times 3 (number of samples) \times 3 (triplicates) + 3 (blank)
 To compensate pipetting errors, 10% of each reagent was prepared in excess.

Per well, 15 μ l of the prepared master mix was pipetted into the plate corresponding to the primer (Multiplate PCR Plates, 96-well, white, #MLL9651, Bio-Rad Laboratories GmbH, Feldkirchen, Germany). 5 μ l cDNA solution were added, resulting in a final volume per well of 20 μ l. To recognize any pipetting errors, triplicates were pipetted for each sample into the qPCR reaction plate, including the blank (Mastermix with RNase free water instead of sample). Next, the plate was sealed with a foil (Microseal 'B' PCR Plate Sealing Film, adhesive, optical, #MSB1001, Bio-Rad Laboratories GmbH, Feldkirchen, Germany) to avoid evaporation of the samples during the measurement and centrifuged for 1 minute and 400 g (Centrifuge 5810R, #581112073 Eppendorf AG, Hamburg). Subsequently, qPCR was performed in the thermal cycler (C2000 Touch Thermal Cycler, #1851148, Bio-Rad Laboratories GmbH, Feldkirchen, Germany) and the results were visualized using the Bio-Rad CFX Manager 3.1 software. The three plates (ChRmine, mScarlet, GAPDH) were analyzed one after another and stored protected from light at 4°C until measurement.

Table 7| Thermal profile of the qPCR protocol set in the thermal cycle

Test	Step	Temperature (°C)	Duration (s)
qPCR	Polymerase activation	95	20
	Denaturation	95	3
	Annealing and polymerization	60	30
		65	31
Melt curve	Temperature ramp	From 65 to 95 in 0.5°C steps	5
		72	120
	End	4	Forever

} 40 repetitions

7. Engineering photoactivable CD4⁺ lymphocytes

7.1. Development of photoactivable lymphocytes

Responsiveness to light was a prerequisite for light-induced cell migration and was achieved by the use of a photoactivable chemokine receptor. Since we sought to study the effect of T cells on the myocardium, we turned the chemotaxis induced by activation of the CXCR4 receptor into phototaxis.

7.1.1. Origin of the photoactivable chemokine receptor

The photoactivatable chemokine receptor 4 (PA-CXCR4, Photoactivatable-chemokine C-X-C motif receptor 4) was first engineered by Xu et al. [99]. The bovine rhodopsin was used as a light sensitive component and combined with the transmembrane chemokine receptor 4 (CXCR4). More precisely, the cytoplasmic domain of bovine rhodopsin was coupled with the human CXCR4 and mCherry (RFP) to form a DNA chimera (figure 12). Consequently, lymphocyte polarization was not induced through binding of the natural chemokine CXCL12, but by light. In their work, Xu et al., demonstrated so-called positive phototaxis of the developed PA-CXCR4 receptor by assessing the migration of the modified cells towards a light source (505 nm) *in vitro* and *in vivo*.

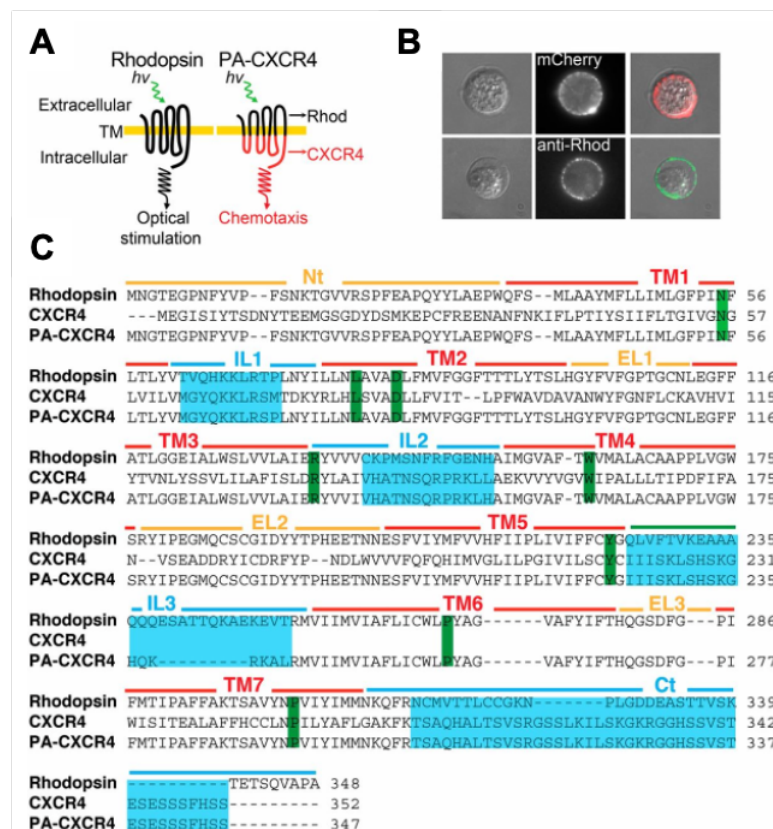


Figure 12| Engineering of photoactivatable CXCR4 (PA-CXCR4)

(A) PA-CXCR4 design. Rhod, rhodopsin. (B) Expression of PA-CXCR4-mCherry in human primary T cells. (C) Primary structure alignment of WT rhodopsin, WT CXCR4, and PA-CXCR4. Green, highly conserved residues; cyan, swapped intracellular domains (Nt, N terminus; TM, transmembrane domain; IL, intracellular loop; EL, extracellular loop; Ct, C terminus).

Adapted from Xu et al. [99].

7.1.2. Adaptation of the photoactivable chemokine receptor

The construct developed by Xu et al. was further adapted in the CHFC. The modifications were carried out by Dr. Murilo Delgobo (Immuno Cardiology Lab, CHFC) and were not part of this thesis. First, a retroviral vector containing the photoactivatable construct was produced in order to transduce isolated murine CD4⁺ cells. Retroviruses show rapid as well as efficient and long-lasting transduction of dividing cells [182]. Murine Stem Cell Virus (MSCV) was chosen to modify isolated

CD4⁺ cells *in vitro* (see section III.7.2.3.). The PA-CXCR4 motif was customized too. Indeed, to adapt the plasmid to our experimental purposes, the fluorescent protein mCherry was replaced by the green fluorescent protein (GFP). GFP was the first discovered FP, originates from the jellyfish species *Aequorea victoria* and is used in numerous applications [161]. After excitation at 488 nm, it emits a wavelength of 507 nm [183]. Due to its fluorescent properties, GFP is easily detectable in flow cytometry (FC) analysis, and was used as a readout to assess successful transduction of the cells as well as their migration into the tissue. To promote the separate translation of the PA-CXCR4 construct from GFP, an internal ribosome entry site (IRES) element was inserted between them (reviewed in [184]). The appropriate construct was designed and produced by VectorBuilder (VectorBuilder GmbH, Neu-Isenburg, Germany). The coding DNA plasmid was then replicated in our laboratory in Platinum Retroviral Packaging Cell Lines (Plat-E cells) which express the packaging proteins for the MSCV [185]. The cells and the protocol for the production of the retroviral vector were provided from Dr. Martin V  th (Institute for Systems Immunology, University of W  rzburg, Germany; and detailed in [186]). The production had a yield of 1.05 – 1.12x10⁹ viral particles/ml. Similar to the cells engineered in the work of Xu et al., the modified cells should no longer respond to a chemokine gradient, but show light-induced migration.

7.2. Production of photoactivable lymphocytes

Photoactivable lymphocytes were produced by viral transduction of CD4⁺ cells with the support of Dr. Murilo Delgobo and Emil Weiss (Immuno Cardiology Lab, CHFC) and handed over for injection. The CD4⁺ lymphocytes were isolated from the spleen of a donor mouse and made photoactivable before being injected into the recipient animals. In general, the number of cells isolated from one donor spleen was sufficient to produce photoactivable lymphocytes for transfer into two recipient animals, receiving up to 5.0 x 10⁶ PA-CXCR4 cells each.

First the splenocytes were collected from the spleen of a donor mouse. Second, among those cells, CD4⁺ lymphocytes were isolated for primary cell culture. Third, the isolated cells were transduced with the retroviral vector containing the photoactivable construct and proliferated until being finally transferred into recipient mice. Prior transfer, the transduction efficiency was assessed. Apart from the spleen collection from the donor mouse, all steps were performed under sterile cell culture conditions.

7.2.1. Spleen collection from a donor mouse on day 0

The spleen was collected from a donor animal to isolate CD4⁺ cells from the splenocytes.

Plate preparation for primary culture

Prior to organ collection (day 0), a 6 well plate (CELLSTAR 6 Well Cell Culture Plate, sterile with lid, #657160, Greiner Bio-One International GmbH, Frickenhausen, Germany) was coated with antibody for CD4⁺ lymphocyte attachment. The antibody (Rabbit Anti-Hamster IgG fraction, MP Biomedicals) was diluted 1:40 in PBS (DPBS, no calcium, no magnesium, Gibco, #14190144, ThermoFischer Scientific, Darmstadt,

Germany) then, 1 ml was added per well and the plate was incubated for two hours at 37°C. The number of wells coated was equal to the number of recipient mice.

Spleen collection and splenocyte extraction

After cervical dislocation the spleen was removed carefully and immediately immersed in 1 ml ice-cold HBSS/BSA solution (Hanks' balanced saline solution (HBSS), Sigma-Aldrich, #9394-500ML, Merck KGaA, Darmstadt, Germany containing 0.5% Bovine serum albumin fraction V, NZ-Origin, 200 g, #8076.4, Carl Roth GmbH + Co. KG, Karlsruhe, Germany).

The organ was then immediately processed for cell extraction. The splenic capsule was opened by grinding thoroughly the organ using the flat side of a 2 ml syringe plunger (BD Discardit II – 2-part syringes, #300928, BD, Heidelberg, Germany) against a 30 µm cell strainer (MACS SmartStrainers 30 µm, #130-098-458, Miltenyi Biotec, Bergisch-Gladbach, Germany). The released cells were collected into a 15 ml tube (tube, 15 ml, pp, 17/120 mm, conical bottom, CELLSTAR, #188271, Greiner Bio-One International GmbH, Frickenhausen, Germany). During the process, the cell strainer was rinsed three times with 2 ml HBSS/BSA to achieve the highest possible yield. The tube was then centrifuged for 5 minutes at 4°C and 400 g (Centrifuge 5810R, #581112073 Eppendorf AG, Hamburg) and the accumulated supernatant was poured off. Cells were resuspended in 2 ml erythrolysis buffer (RBS Lysis Buffer (10X), #420301, BioLegend, San Diego, USA; diluted 1:10 in distilled water (aqua ad iniectabilia, B. Braun, Melsungen, Germany) and kept on ice. Erythrolysis was interrupted after 2 minutes by adding 8 ml HBSS/BSA solution. The tube was centrifuged again with the settings described above and the supernatant discarded. To prevent aggregate formation, the cells were thoroughly resuspended in 1 ml PBS. From this solution, 20 µl were diluted 1:100 in trypan blue (Trypan Blue, 0.4% Solution prepared in 0.85% NaCl, 17-942E, Lonza, Biozym Scientific GmbH, Oldendorf, Germany), and used to determine the cell number. The count was performed with a Neubauer cell counting chamber (depth 0.100 mm, 0.0025 mm², LO – Laboroptik Ltd, UK) under the microscope (EVOS XL Core Cell Imaging System with Mechanical Stage, AMEX1200, Thermo Fisher Scientific, Darmstadt, Germany). The cell suspension was again diluted in a total volume of 10 ml PBS and centrifuged with the same settings and the supernatant thoroughly poured off.

7.2.2. CD4⁺ lymphocyte isolation on day 0

CD4⁺ lymphocytes were selected by magnetic cell separation (MACS, Magnetic Activated Cells Sorting) using a dedicated kit (CD4⁺ T Cell Isolation Kit mouse, #130-104-454, Miltenyi Biotec, Bergisch-Gladbach, Germany). This method allows a harmless and sterile negative selection as well as concentration of CD4⁺ T cells only. Magnetically coupled antibodies against surface antigens of all other cell populations, except CD4⁺ lymphocytes, are binding the cells that are not of interest to a column placed in a magnetic field. CD4⁺ cells, that are not magnetically coupled, do not interact with the column, thus simply flow through.

The cell suspension obtained from the spleen was centrifuged for 5 minutes at 4°C and 400 g and the supernatant was poured off. For resuspension, the necessary volumes of MACS buffer (40 µl/10⁷ cells) and antibody mix (10 µl/10⁷ cells) contained in the kit

were calculated according to the cell number determined above (see section III.7.2.1.) and pipetted into the tube. The tube was then kept on ice for 15 minutes. MACS buffer (30 μ l/ 10^7 cells) was added again, together with the microbeads binding to the antibodies (20 μ l/ 10^7 cells), thereby cells that were not of interest were magnetically labelled. During the following 10 min incubation period on ice, the column (LS Columns, #130-042-401, Miltenyi Biotec, Bergisch- Gladbach, Germany – suitable for sorting up to 10^8 cells) was activated by clipping it in the magnetic field and applying 3 ml MACS buffer on the membrane. Next, taking care not to produce bubbles, the cell suspension was pipetted in the middle of the column; the flow-through was collected in a 15 ml tube. Once the column was empty, the LS column was rinsed with 3 ml MACS buffer. The cells that were bound to magnetic antibodies remained in the column, while the collected solution contained the negatively selected CD4⁺ lymphocytes. To determine the cell number, 20 μ l of the separated cell suspension were diluted 1:10 in trypan blue and counted with a Neubauer cell counting chamber as described above (see section III.7.2.1.). The CD4⁺ cell suspension was centrifuged using the settings previously mentioned and the supernatant discarded. The obtained cell pellet was resuspended in complete RPMI medium (RPMI Medium 1640 (1X), Gibco, ThermoFisher Scientific, Darmstadt, Germany) to achieve a concentration of 1.25×10^6 cells/ml. The complete RPMI refers to supplemented RPMI medium composed of: 10% (vol/vol) FBS (Fetal Bovine Serum, qualified, Brazil, #10270106, ThermoFisher Scientific) supplemented with the following components, 1% penicillin/streptomycin (Penicillin-Streptomycin (10,000 U/mL), #15140122, ThermoFisher Scientific), 1% non-essential amino acids (NEAA, #10370021, Gibco, ThermoFisher Scientific), 1% GlutaMAX (GlutaMAX supplement, #35050061, Gibco, ThermoFisher Scientific), 1% sodium pyruvate (Sodium Pyruvate (100 mM), #11360070, Gibco, ThermoFisher Scientific) and 0,05% 2-mercaptoethanol (2-mercaptoethanol (50 mM), #31350010, ThermoFisher Scientific. Per milliliter of cell suspension, 2 μ l of anti-CD3 (Purified Hamster Anti-Mouse CD3e, #553058, BD Biosciences, Heidelberg, Germany), 2 μ l anti-CD28 (Purified Hamster Anti-Mouse CD28, #557393, BD Biosciences) and 0.5 μ l of rhIL2 (IL-2, rec Human, #PPT200-02, PeproTech, Hamburg, Germany) were added to bind and stimulate the CD4⁺ cells [187]. After meticulous mixing, 2 ml of the cell suspension – containing 2.5×10^6 cells according to the counting and dilution – were added per well. The plate was incubated for 24 hours at 37°C.

7.2.3. Transduction of isolated murine CD4⁺ lymphocytes on day 1

Under physiological conditions, “blasting” is observed after contact of the T lymphocytes with antigen-presenting cells. The lymphocytes then stop migrating and remain in contact with the dendritic cells for about 24 hours. The lymphocytes grow, double their size, corresponding to around 20 – 30 μ m for murine T cells, double their protein content and increase up to 30-fold their RNA content (reviewed in [188, 189]). Thus, the cells adapt their metabolism in order to proliferate ([190] and reviewed in [191]).

Blasting of the lymphocytes was checked 24 hours after isolation of cells. The cells should be enlarged and adhere to the plate. If the blasting of the cells was not

satisfactory, up to 48 additional hours were given to the cells to expand before proceeding with the viral transduction.

Prior to transduction, the retroviral vector containing the photoactivable construct, was slowly thawed on ice and was mixed with complete RPMI (preparation see section III.7.2.2.) in a ratio of 1:4. Polybrene (Polybrene, 10000 µg/ml, Santa Cruz Biotechnology) was added to achieve a concentration of 10 µg/ml.

The plate containing the cells was slightly tilted, the medium was carefully removed by pipetting at the edge of the wells without touching the bottom of the plate where the cells adhered. The medium was then transferred into a 50 ml tube (tube, 50 ml, pp, 30/115 mm, conical bottom, CELLSTAR, #227261, Greiner Bio-One International GmbH) and kept at 4°C. One to 2 ml of the virus solution were added onto the cells in the plate. The plate was sealed tightly using Parafilm (PARAFILM M, Sigma-Aldrich, Merck KGaA, Darmstadt, Germany) and then centrifuged for 90 minutes at 32°C, 1328 g without braking, to foster the penetration of the virus particles into the cells. Directly after centrifugation, the plate was incubated for 2 hours at 37°C. Meanwhile, the stored medium was centrifuged and only the supernatant, free of cells, was warmed up to 37°C. The virus solution was removed and the warm medium added to the plate again.

7.2.4. Proliferation of transduced CD4⁺ lymphocytes from day 2 to day 4

The next day (d2), cell density and blasting were checked under the microscope. Free-floating cells indicated that they had proliferated and could be further processed. First, the cells were thoroughly mixed by careful resuspension in the plate and transferred to a 15 ml tube. 20 µl of the suspension were taken for counting and stained 1:10 with trypan blue to determine the cell number with a Neubauer counting chamber as described above (see section III.7.2.1.). The plate was then rinsed with fresh RPMI medium and the rinsing solution added to the 15 ml falcon. The tube was centrifuged for 5 minutes at room temperature, 400 g and the supernatant discarded. To achieve a concentration of 1.25×10^6 cells/ml, the obtained cell pellet was resuspended in fresh RPMI with IL2 (50U/ml, reference: see section III.7.2.2.), CD3 as well as CD28 antibody (0.5µg/ml each, reference: see section III.7.2.2.). Then, 2 ml of the suspension were pipetted per well into a new 6 well plate and incubated for 24 hours at 37°C.

One day later (d3), the cells were transferred to a new 6 well plate and the medium supplemented with IL7 to improve their survival. As described on d2, the cells were first resuspended in the plate by pipetting up and down, second the cells were collected, the plate was washed with RPMI and the cells were counted. Third, the collected cells underwent centrifugation with the settings mentioned above and the supernatant was discarded. In parallel, fresh complete RPMI was prepared and supplemented with 3.125 ng/ml IL-7 (50 µg/ml, Recombinant Murine IL-7, #PPT217-17, PeproTech, Hamburg, Germany) and used to resuspend the centrifuged cell pellet to reach a concentration of 1.25×10^6 cells/ml. Finally, 2 ml of the cell suspension were pipetted per well and the plate incubated again for 24 hours at 37°C.

Throughout the culture of the T cells, attention was paid to any color change in the medium. This was taken as an indicator for the consumption of the medium.

Consequently, the cells were resuspended in fresh medium.

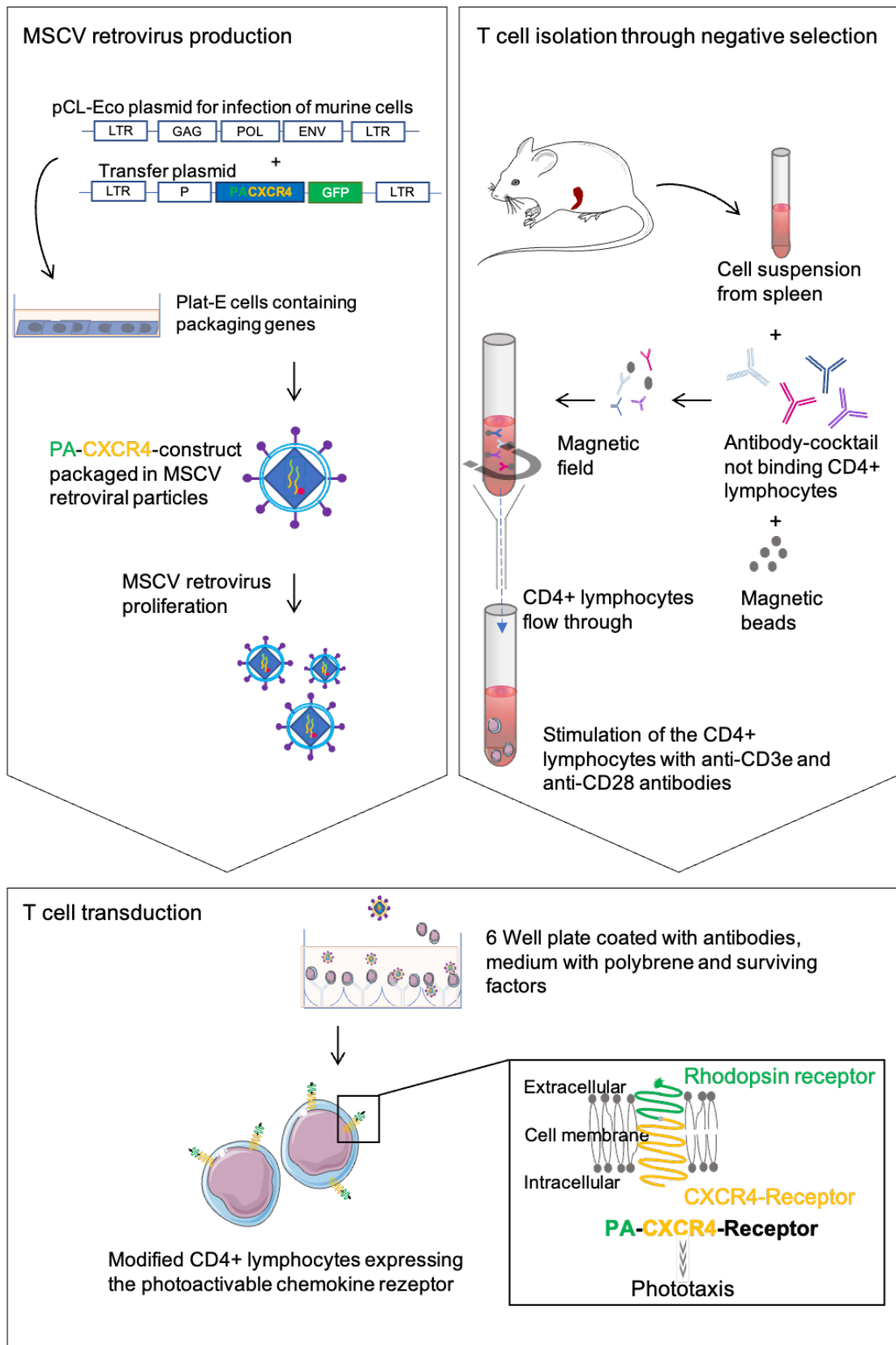


Figure 13| Summary of the steps to produce photoactivable CD4⁺ lymphocytes

First, the retroviral vector containing the photoactivable construct was produced. Second, murine CD4⁺ cells from a donor mouse were isolated. Third, the selected cells were transduced by the vector to finally express the PA-CXCR4 receptor and became photoactivable.

7.2.5. Assessment of the viral transduction rate on day 4

The cells were resuspended in the plate as described on d2 and d3, pipetted into a 15 ml tube and counted as previously mentioned (see section III.7.2.1.). To increase the yield, the RPMI used to wash out the plate was added to the tube containing the cells. Moreover, the complete collection of the cells was checked under the microscope and, if necessary, the plate was rinsed again with RPMI and the solution was added to the tube.

Successfully transduced cells were expressing the PA-CXCR4 construct coupled to the fluorescent marker GFP. This marker was used to determine the transduction rate by detection and quantification of the GFP with FC. For this purpose, 200 μ l of the cell suspension were analyzed. The gating strategy was the same as for tissue analysis (see section III.8.3.3.). Generally, the transduction rate was 55 to 70%.

Meanwhile, the cells were prepared for their transfer in recipient mice.

7.3. Adoptive PA-CXCR4 cell transfer

For administration, the modified cells were suspended in PBS and their number adjusted to $3.5 - 5.0 \times 10^6$ per recipient mouse.

7.3.1. Finalization of the cell preparation prior transfer on day 5

Preparation of the cells for transfer was performed in parallel to the FC analysis to assess the transduction rate. The cell suspension was centrifuged for 5 minutes at 4°C and 400 g, and the supernatant discarded. The cell pellet was resuspended with 1 ml PBS/ 10^7 cells. Transferred cells were labelled through addition of a cell tracer (CellTrace Violet Cell Proliferation Kit, for flow cytometry, #C34571, Thermo Fisher Scientific) in order to be distinguished from those of the recipient mice in later FC analysis. The dye was added to PBS at a ratio of 1:1000 and incubated for 20 minutes at 37°C. The reaction was interrupted by the addition of complete RPMI (ratio cell suspension: RPMI was 1:5) and the tube was incubated again for 5 minutes at 37°C. The tube was then centrifuged at 4°C and 400 g for 5 minutes and the supernatant discarded. The cell pellet was resuspended in 10 ml PBS and the cells counted one last time with a Neubauer counting chamber as described above. This final cell count in combination with the percentage of transduced cells assessed by FC analysis, was used to determine the absolute number of PACXCR4 cells expressing the construct.

Eventually, the cell suspension was centrifuged at 4°C and 400 g for 5 minutes, the supernatant discarded and the cells diluted in PBS based on the cell count to reach a concentration between $3.5-5.0 \times 10^6$ cells/200 μ l, depending on the yield.

7.3.2. Injection of photoactivable CD4⁺ lymphocytes

Two days after device implantation on the left ventricle, recipient mice received $3.5 - 5.0 \times 10^6$ PA-CXCR4 cells. The modified cells were diluted in PBS as described above (III.7.3.1.) to reach a final injection volume of 10 ml/kg bodyweight. The suspension containing the modified cells, was drawn up using a 1 ml syringe

(Omnifix-F, B. Braun, Meslungen, Germany) and injected intraperitoneally (i.p.) with a 25G cannula (BD Eclipse Needle, 25G x 5/8 (0.5 x 16 mm), #305760BD GmbH, Heidelberg, Germany). Volume and needle gauge corresponded to the recommendation for administration of substances to laboratory animals from the Committee for Animal Welfare Officers (GV-SOLAS, March 2017).

After placing the animal on the cage lid and holding it by the tail with the preferred hand, it was quickly and firmly picked up behind the ears with the other hand. The tail was then fixed between palm and little finger and restrained in a head-down position while injecting the substance, in order to shift the viscera cranially and avoid unintentional puncture of abdominal organs. To prevent accidental application into the caecum located in the left part of the abdomen, the needle was inserted paramedian at a 20 – 30° angle i.p. into the right lower quadrant abdomen avoiding genitals and nipples [192].

7.4. *In vitro* assessment of PA-CXCR4-lymphocyte photoactivation

7.4.1. *In vitro* readout for lymphocyte activation

Under physiological conditions, the intracellular calcium concentration $[Ca^{2+}]_i$ increases after activation of the CXCR4 receptor by its natural ligand CXCL12 (reviewed in [91]). Indeed, G protein-coupled signal transduction results in an increased $[Ca^{2+}]_i$ [97]. Similarly, to the work of Xu et al., the light-induced activation of the modified cells was demonstrated *in vitro* by measuring the shift of intracellular calcium concentration $[Ca^{2+}]_i$ after exposure to light [99]. When the PA-CXCR4 receptor was operational, light stimulus activated the photoactivable part of the modified receptor, which in turn activated the linked CXCR component. The activated PA-CXCR4 receptor triggered the intracellular G protein-coupled signaling cascade, leading to increased $[Ca^{2+}]_i$ required for chemotaxis and thus oriented cell migration. Hence, cell activation was not induced by chemokine but by light.

7.4.2. *In vitro* validation of photoactivation of the engineered cells

To carry out *in vitro* experiments to verify the responsiveness to light, the cells were first isolated and then transduced as described in section III.7.2. A green fluorescent calcium indicator, whose fluorescence increases by Ca^{2+} binding, was added directly to the cells. The detected fluorescence intensity is proportional to the measured calcium concentration, and was therefore taken as readout for the activation of the cells.

Determination of the best wavelength and power for photoactivation

Xu et al. published results for illumination by 505 nm [99]. A blue (470 nm) and a green (530 nm) device were available from NeuroLux. Once the best fitting wavelength was determined, we repeated the experiment using different powers (2.5, 5.0 and 10 W) to find out the best settings. Those experiments were carried out together with Dr. Murilo Delgobo (Immuno Cardiology Lab, CHFC) using the mouse thymoma cell line BW5147 which underwent the described transduction protocol. Afterwards, the protocol was performed the same way but with modified $CD4^+$ lymphocytes. Fluorescence was measured in the directly illuminated well and in the surrounding wells receiving

attenuated light. The latter represented the first and second neighbor wells in a plate row, which were at around 1, respectively 2 cm away from the light source.

Fluo-4 staining protocol to assess photoactivation *in vitro*

PA-CXCR4 cells were counted as described in section III.7.2.1. The fluorescent calcium indicator (Fluo-4, AM, cell permanent, #F14201, ThermoFisher Scientific, Darmstadt, Germany) was mixed with the cells in a concentration of $2 \mu\text{M}/10^6$ cells. Afterwards, two incubation steps were performed, both protected from light; the first lasted 30 minutes at 37°C , the second 10 minutes at room temperature. Next the cells were washed with HBSS buffer (Hanks' saline (HBSS) solution, Sigma-Aldrich, #9394-500ML, Merck KGaA, Darmstadt, Germany) containing 1% FBS (Fetal Bovine Serum, qualified, Brazil, #10270106, Thermo Fisher Scientific, Darmstadt, Germany) and centrifuged with the settings mentioned above. The washing and centrifugation were repeated one more time. Depending on the counted cell number, the volume for resuspension of the cell pellet with HBSS/1% FBS was adapted to reach a concentration of 5.0×10^5 cells/ml. Thereafter, 100 μl , thus containing 5.0×10^4 stained cells, were pipetted in three neighbor wells within a row in a transparent 96 well plate (Microplate, 96 well, ps, u-bottom, clear, #650101, Greiner Bio-One International GmbH, Frickenhausen, Germany). On the opposite side of the plate, the negative controls were pipetted the same way. Hence, negative control represents modified cells which were stained, but remained unexposed to the shining μLED . Subsequently, the well located at the end of one row was directly and constantly illuminated in the plate with the 530 nm-device at 10 W (optogenetics system settings) for 10 minutes. After illumination, fluorescence was measured by the Fluorescence Reader (Spark, Tecan Sales Switzerland AG, Männedorf, Switzerland) over 20 minutes in the directly illuminated well, its neighbor wells and in the negative controls. As positive control CXCL12, the natural ligand of the CXCR4 receptor was added to one separate well. After staining with the fluorescent dye, 100 nM CXCL12 (Recombinant Murine SDF-1 β (CXCL12), #250-20B, Peprotech, Hamburg, Germany), were added in the positive control-well containing 5.0×10^4 modified cells.

8. Monitoring light-induced T cell migration

8.1. Whole-body clearing for visualization of intrathoracic illumination

8.1.1. Principle of whole-body clearing

Whole-body and organ clearing was developed as a tool to identify and understand cellular mechanisms within the organism. Indeed, clearing protocols combined with fluorescent labelling and imaging with single-cell resolution enables to highlight cellular circuits (reviewed in [193]). Physical properties of tissues represent an obstacle for imaging. The goal of tissue clearing is to achieve imaging in deeper layers [194] by decreasing light scattering as well as light absorption, related to opacity and color of the tissue respectively, which prevent light penetration [193, 195]. Due to different optical densities, also called refractive indices, of tissue components (different organelles,

lipophilic membranes, hydrophilic proteins), penetrating light is scattered [196]. By passing through the different media, the angle and the speed of the incoming light is changed. Molecules that absorb the laser light emit waves in all directions, which in turn are absorbed and emitted by surrounding molecules in a different way. The summation of such interference amplifies light scattering [197]. Clearing protocols aim to dehydrate the tissue and dissolve the contained fatty acids; the sample turns transparent and the refractive index mismatch throughout the tissue components is significantly reduced, thus light scattering minimized [193, 196]. Pigments, in particular hemoglobin, absorb light, therefore need to be physically and chemically removed through organ perfusion and hydrogen peroxide for instance [110]. The increased transparency enables three-dimensional investigation of whole-mount samples in combination with immunofluorescence techniques [197] (see section III.8.3.).

8.1.2. Whole-body clearing protocol to visualize intrathoracic light scattering

Through transcatheter perfusion and whole-body immersion into hydrophilic CUBIC (Clear, Unobstructed Brain/Body Imaging Cocktails and Computational analysis) solution, delipidation and heme removal were achieved. Gradually, the animal became more transparent and the intrathoracic illumination pattern of the implanted μ LED was visualized, hence to figure out which organs were reached by the light *in vivo*.

This experiment was performed according to the protocol of Susaki et al. [198]. The ScaleCUBIC-1 solution was composed of 25 wt% urea, 25 wt% Quadrol (N,N,N',N'-tetrakis(2-hydroxypropyl)-ethylenediamine; EDTP) and 15 wt% Triton X-100 solution (all reagents purchased from Sigma-Aldrich, Merck KGaA, Darmstadt, Germany) diluted in distilled water.

Before starting the whole-body clearing, the device was implanted on the LV in order to reproduce the conditions after *in vivo* implantation.

Mouse preparation

After cervical dislocation, the mouse was perfused with 30 ml PBS supplemented with heparin (heparin sodium 25,000 IU, Ratiopharm, Ulm, Germany 1:100 in PBS) as described in section III.4.2.2. in order to remove the blood from the circulation. Subsequently, the device was implanted *post mortem* on the LV according to the procedure described under IV.1.2.

Mouse clearing

After device implantation, transcatheter perfusion was performed for tissue fixation with 150 ml 4% formaldehyde (Formaldehyde, 16%, methanol free, ultra pure, #18814-20, Polysciences Europe GmbH, Hirschberg an der Bergstrasse, Germany). A 10 ml formaldehyde vial was diluted in 30 ml buffer; the buffer consisted of 7.2 mg disodium hydrogen phosphite (#1065851000, Sigma-Aldrich, Merck KGaA, Darmstadt, Germany), dissolved in 900 ml distilled water. Next, the skin was removed from the body and the mouse perfused with 30 ml 1:2 ScaleCUBIC-1 solution (diluted 1:2 with distilled water). Eventually, the mouse was entirely immersed into ScaleCUBIC-1 solution and placed on an orbital shaker (Polymax 1040, 10° tilt angle, Heidolf Instruments GmbH & CO.KG, Kelheim, Germany), rotating continuously at 60 rounds per minute (rpm). During the first week, the solution was replaced daily; the

mouse could be stored longer by changing the solution twice a week.

8.2. Organ collection after *in vivo* illumination

Based on the observations made with the CUBIC protocol, different intrathoracic organs exposed to light were subjected to analysis, including, in addition to the heart, thymus and lungs. Following eight hours illumination *in vivo* by 10 W, organs were harvested and dissected in such a way to detect preferential migration into the illuminated tissue. After cervical dislocation, transcardial perfusion was quickly performed as described in section III.4.2.2., and the organ collection was done as fast as possible after illumination to avoid possible migration of the cells out of the tissue. In order to verify a light induced accumulation of the cells in the illuminated tissue, each organ was divided in a “light” and a “dark” side, respectively reported as “left” and “right”, which were analyzed separately and compared. The left illuminated side corresponded to the organ region close to the light source, whereas the right dark side described the contralateral part of the organ. Each piece was weighted in order to assess the number of modified cells per milligram tissue. The spleen was not reached by the light, but was collected for FC analysis and taken as baseline to assess the survival of the transferred cells in the recipient organism.

8.3. Flow cytometry analysis for the detection of PA-CXCR4 cells

8.3.1. Principle of fluorescence and immunostaining

Principle of fluorescence

Fluorescence is a two-step process defined as spontaneous emission of radiation from an excited molecule and is characterized by its spectrum, quantum yield and lifetime of the excited state [199]. Besides photon emission, the excitation energy undergoes internal conversion or/and intersystem crossing so that the emission spectrum is always red-shifted compared to the absorption spectrum [199]. Fluorescent molecules can be covalently bound to a species, e.g. an antibody, to fluorescently tag it. Such fluorescent label, also called fluorescent tags, are used as indicator, analytical or tracer tools in multiple immunoassays where the emitted fluorescence is detected and recorded [74].

Immunostaining

Immunostaining is a method for selective detection of antigens present in samples and is based on specific antibody-antigen affinity [74]. Fluorescent antibodies bind to their respective antigen present in the sample and, when excited with the appropriate wavelength, emit a fluorescent signal which is recorded. Antibodies can be polyclonal or monoclonal. Since polyclonal antibodies show reactivity against different epitopes of the antigen, they can more likely recognize different isoforms of the antigen, thus show broader reactivity. In contrast, monoclonal antibodies target a single epitope and are less prone to cross-reactivity [200]. Antibodies are covalently labelled with fluorophores (fluorescent chemical compound) thus mark the antigen of interest with fluorescence upon binding. Excitation and emission wavelength are fluorophore-specific. Thus, the use of multiple fluorophores to tag different antigens in the same experiment is possible to characterize colocalized structures [201].

8.3.2. Principle of multicolor flow cytometry analysis

Multicolor FC enables the detection of cells stained with fluorescent dyes. Thereby, with the help of fluorescence-labelled antibodies, cell populations and subpopulations can be distinguished from each other [74].

To perform FC analysis, cells are brought into suspension, then flow through a fine capillary individually and pass the beam of lasers with different excitation wavelengths. The scattered light is measured and defined by forward and sideward scatter (FSC respectively SSC). The denser and the more complex the cell, the larger the side scattering. FSC correlates positively with the size of the cell, while SSC describes the granularity (structure of the cell nucleus, contained vesicles) of the cell. Besides light scattering, the emitted fluorescence of the stained cells is recorded by optics at right angles to the excitation beam. The emitted photons are converted to an electrical signal which in turn is processed to a numerical signal. Quantity and intensity of the fluorescence are displayed [202].

Cells are defined by their antigen expression pattern. The emission spectrum of the chosen fluorescence-labelled antibodies against those cell-specific markers, allows to perform a so-called immunophenotyping of the cells, thus enables their identification. For example, the recognition of lymphatic cells and subsequently their fine differentiation between B or T lymphocytes is feasible [203]. Multiple antibodies can be applied in the same experiment. Overlaps (spillover) in the emission spectrum of the fluorochromes that may occur can be corrected to a certain extent (compensation) [204]. "Gates" are set on the displayed signal to surround cell populations sharing the same characteristics and select them for further analysis within the same experiment [205]. Hence, the gating strategy enables a step-by-step discrimination and the quantification of subpopulations of cells that exhibit the searched characteristics [206].

8.3.3. Flow cytometry-based discrimination of transferred PA-CXCR4 lymphocytes

To detect the phototactic cells transferred in the recipient mouse by flow cytometry, properties of the CD4⁺ cells as well as the fluorescence of GFP contained in the construct were used. First, the samples were processed to obtain a cell suspension, second, they were stained and finally analyzed in the FC machine.

Preparation of cell suspensions

Based on the observation made in the CUBIC-mouse, organs were harvested as described in section III.8.2. The left and right parts of the organs were weighed and put individually in tubes containing 1 ml HBSS/BSA solution and stored on ice during immediate processing. Non-lymphoid tissues were enzymatically digested before further processing in order to better release the cells. Each piece of heart and lung was incubated for 30 minutes at 37°C in 1 ml collagenase solution (Collagenase, Type 2, #LS004177, Worthington Biochemical Corporation, Lakewood, USA; dilution: 3.03 mg/ml PBS).

Each sample including buffer solution was placed individually into a cell strainer and grinded against the mesh using the flat side of a 2 ml syringe plunger as described for

splenocyte isolation (see section III.7.2.1.). The flow through, now free from tissue pieces or capsule, was collected in a 15 ml tube (tube, 15 ml, pp, 17/120 mm, conical bottom, CELLSTAR, #188271, Greiner Bio-One International GmbH, Frickenhausen, Germany). The cell strainer was additionally rinsed three times with 2 ml HBSS/BSA solution to maximize the yield. The final volume of cell suspension was around 7 ml. The tubes were then centrifuged for 5 minutes at 4°C and 400 g (Centrifuge 5810R, #581112073 Eppendorf AG, Hamburg) and the supernatant was poured off. Each centrifuged cell pellet was resuspended with the HBSS/BSA solution remaining in the tube before the samples were each pipetted into a well of a 96 well plate (Microplate, 96 well, ps, u-bottom, clear, #650101, Greiner Bio-One International GmbH, Frickenhausen, Germany). Due to the high cell density, the cell suspension obtained from the spleen was first resuspended in 2 ml PBS, and only 100 µl of it were pipetted into the plate. To set up the voltages in the FC machine left and right tissue from both, ventricles and lung were used.

FC staining

To achieve identification of the modified cells within tissues of the recipient mouse via flow cytometry, several antibodies against specific antigens (table 8) were combined. The specificity of the targeted antigen enabled to discriminate different cell populations.

Table 8| Antibodies and cell tracer for the detection of transferred PA-CXCR4-positive cells

Discrimination	Target antigen	Antibody / Tracer	Laser for excitation	Recorded emission (nm)	MMX composition and dilution Final volume per sample = 25 μ l*
Background reduction through blockade of the Fc receptors	CD16/CD32 (Fc-region of Ig γ)	Purified anti-mouse CD16/32 Antibody, #101302	-		5:1000 (0,125 μ l)
Live cells	Cell membrane integrity, non-permeant to viable cells	ZombieAqua Fixable viability Kit, #423102	Violet (405 nm)		1:100
Pan-leukocyte	CD45 (leukocyte common antigen) (Protein tyrosine phosphatase)	APC/Fire™ 750 anti-mouse CD45, #147714	Red (633 nm)	787	1:100 (0,25 μ l)
Myeloid lineage marker (for negative selection)**	CD11b (Integrin)	PerCP/Cyanine5.5 anti-mouse/human CD11b Antibody, #101227	Blue (488 nm)	690	1:100 (0,25 μ l)
T helper cells	CD4 (co-receptor for TCR during T cell activation by MHCII-binding)	PE anti-mouse CD4 Antibody, #100408	Yellow/Green (561 nm)	574	1:100 (0,25 μ l)
Pan T cells	CD3e (Ig, antigen recognition and T cell activation by binding MHC-complex)	PE/Cyanine7 anti-mouse CD3e Antibody, #100320	Yellow/Green (561 nm)	774	1:100 (0,25 μ l)
Transferred cells	Surface and intracellular staining	CellTrace Violet Cell Proliferation Kit, for flow cytometry, #C34571, Thermo Fisher Scientific	Violet (405 nm)		1:1000 (see section III.7.3.1.)
PA-CXCR4 cells	GFP	GFP fluorescence	Blue (488 nm)	510	- Contained in PA-CXCR4 cells

Except the cell tracer (see section III.7.3.1.), all antibodies as well as the dye for viability testing were purchased from Biolegend, San Diego, USA.

*Antibody dilution was done with FACS (fluorescence-activated cell sorting) buffer. For heart and lung samples, twice the amount was used (final volume = 50 μ l).

**T lymphocytes are CD11b negative.

The 96 well plate containing the cell suspensions of the collected organs was centrifuged at 4°C, 400 g for 3 minutes and the supernatant discarded with a sweeping motion. Each sample was washed with 200 µl PBS, centrifuged again with the same settings and the supernatant discarded. To distinguish living cells from dead ones, samples were resuspended with viability dye (ZombieAqua Fixable viability Kit, #423102, Biolegend, San Diego, USA, 1:100 in PBS to reach 100 µl). The dye penetrates damaged plasma membranes, and therefore stains dead cells. The plate was then incubated for 15 minutes at room temperature, protected from light. Subsequently, 100 µl FACS buffer (composed of: 1% BSA, 0.1% sodium azide, 1 mM EDTA, all purchased from Sigma-Aldrich, Merck KGaA, Darmstadt, Germany) were added to each sample, the plate centrifuged with the same settings and the supernatant discarded. The master mix of the selected antibodies (table 8) was prepared, each sample was resuspended with the antibody mix and incubated for 30 minutes at 4°C, protected from light. For heart and lung samples 50 µl master mix were used per sample, while for the remaining samples 25 µl were used. All antibodies were diluted 1:100 in FACS buffer. After the incubation period, 100 µl of FACS buffer were added into each well, the plate was centrifuged again with the same settings and the supernatant discarded. Prior to analysis, each sample was resuspended in 200 µl PBS. Then the plate was analyzed in the FC machine (Attune NxT, Invitrogen, Thermo Fisher Scientific, Darmstadt, Germany) according to the gating strategy described below.

Flow cytometry analysis

The staining strategy described above, labelled structures with fluorescent dye. The chosen gating strategy allowed a step-by-step identification of the transferred and photoactivable lymphocytes by selecting the GFP-expressing cells among CD4⁺ cells (figure 14). Comparative analysis of left and right organ parts allowed to assess preferential migration into tissue close to the light source. Data analysis was performed with the software FlowJo v10.

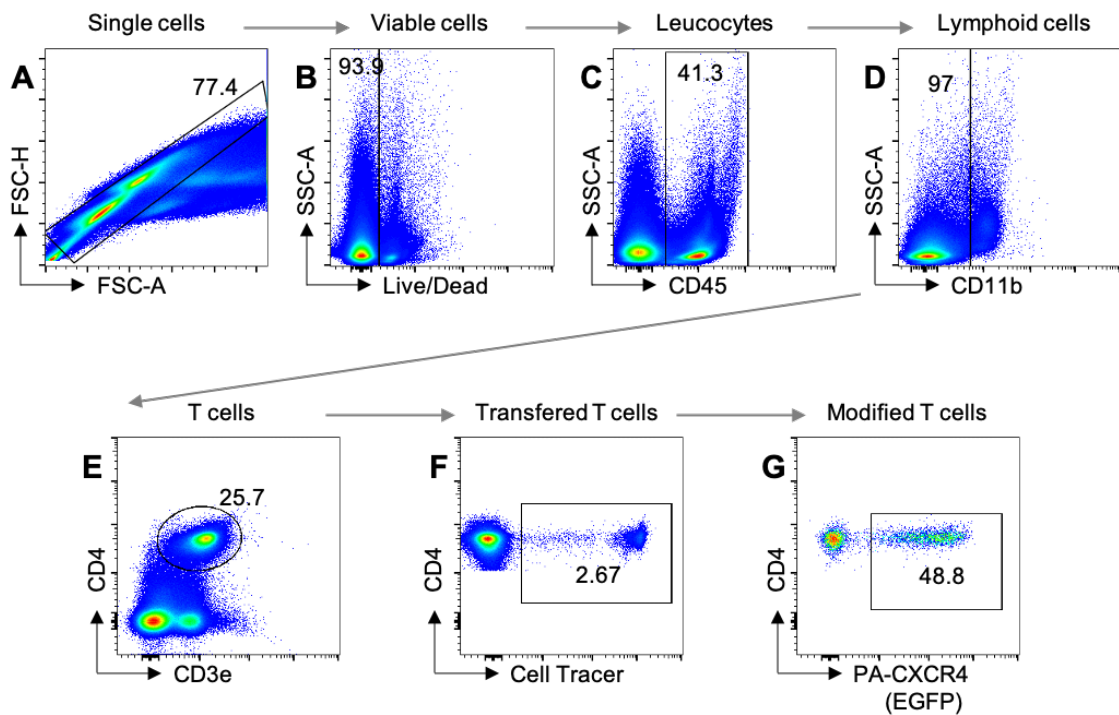


Figure 14| Gating strategy for PACXCR4 detection in different tissues by flow cytometry

(A) Morphological selection of single cells (singlets) using FSC-Height (H) FSC-Area (A). (B) Selection of living cells (the dye penetrates dead cells whose membrane is damaged). Living cells are negatively selected in this staining. (C) Selection of leukocytes (CD45 positive) among the living cells. (D) Negative selection of the lymphoid cells (CD11-negative) within the CD45-positive gate. (E) Selection of T helper lymphocytes (double positive for both CD4 and CD3e) among lymphocytes. (F) Selection of transferred T cells which contained the cell tracer. (G) Selection of PA-CXCR4-expressing cells among the transferred T lymphocytes.

Representative gating strategy performed on a spleen.

8.4. Light sheet microscopy for the detection of PA-CXCR4 cells

8.4.1. Immunofluorescence

Immunofluorescence marks target structures in tissues, with antibodies conjugated to a fluorophore. This staining procedure based on antigen recognition, assigns a fluorescent label to an antigen of interest, thus enabling its detection (see section III.8.3.1.). Immunolabelling of target antigens can be used as direct or indirect technique. Direct immunofluorescence is performed with fluorophores directly conjugated to the antibody recognizing the antigen in the sample. In contrast, indirect immunofluorescence employs two complementary antibodies: in the first step, the primary antibody binds to the specific antigen, next the secondary antibody binds to the primary antibody; only the secondary antibody carries the fluorescent label [207]. Direct labelling of the antibody with the fluorophore offers a shorter staining time and avoids cross-reactivity between secondary antibodies, however, the recorded fluorescence relies on the number of fluorophores bound to the antibody. Indirect labelling is more sensitive than direct labelling, as a primary antibody can be bound by several secondary antibodies, amplifying the fluorescent signal [208]. However, cross-reactivities between antibodies are possible when multilabel experiments are performed, thus indirect labelling is less specific.

8.4.2. Principle of Light Sheet Fluorescence Microscopy

Light sheet fluorescence microscopy (LSFM, also known as SPIM – Selective Plane Illumination Microscopy) enables three-dimensional imaging of larger pieces of tissue or whole organs (reviewed in [197]). Samples can be stained for whole-mount immunostainings with fluorescent labelled antibodies with distinct excitation and emission wavelengths and, similarly to whole-body clearing (see section III.8.1.1), the tissue is submitted to optical clearing. Fluorescence is recorded by optical sectioning of the whole sample [209] so that a three-dimensional image can finally be reconstructed. Unlike in a confocal microscope, the laser beam is not focused to a point, but only in one-dimension generating a “sheet of light”. This “light sheet” illuminates the sample and fluorescence can be selectively detected section by section when the sheet scans the sample. The fluorescence is spectrally filtered and passes the tube lens before being recorded with a camera. Image stacks are recorded in increments of few micrometers to allow full three-dimensional image reconstruction [210], revealing the respective tissue architecture. Optical clearing makes the tissue transparent by adjusting and homogenizing the refractive index of the specimen to minimize light scattering and eventually maximize transparency and thus contrast in the fluorescence. The most suitable clearing method needs to be carefully chosen to reduce negative effects such as tissue shrinkage or fluorescence quenching [211]. Here, a well-established protocol using a hydrophobic clearing solution composed of benzoic acid and benzyl benzoate (BABB) was used.

8.4.3. LSFM staining and clearing protocol for detection of PA-CXCR4 lymphocytes in the thymus

In order to assess the distribution of photoactivable cells in whole-mount organs, immunostaining against the transferred cells and tissue clearing were performed.

After illumination, organs were removed as described in section III.8.2., immediately fixed in methanol-free 4% formalin and stored for two hours, protected from light, at 4°C. Afterwards the organs were washed twice for 15 minutes in PBS on a rotary shaker (RS-60 Tube rotator, Bio San, Riga, Latvia) at 70 rpm. To avoid non-specific binding, a blocking solution composed of 2% FBS (Fetal Bovine Serum, qualified, Brazil, #10270106, ThermoFisher Scientific, Darmstadt, Germany) and 0.5% Triton X-100 solution (Sigma-Aldrich, Merck KGaA, Darmstadt, Germany), both diluted in PBS, was used. During the blocking step, the samples were swirled in the solution for two days on the rotatory shaker, protected from light, at 4°C. They were then washed with PBS for 15 minutes as described above. The intrinsic fluorescence of the GFP contained in the construct was reduced due to sample processing (BABB, dehydration) [197, 212, 213]. Therefore, GFP was labeled with a fluorescent antibody for better detection by light sheet microscopy and to better distinguish the cells from the background. To stain the photoactivable cells, an antibody against GFP, bound to the far-red fluorescent dye Alexa 647, was chosen (GFP Polyclonal Antibody, Alexa Fluor 647, #A-31852, ThermoFisher Scientific, Darmstadt, Germany). The anti-GFP antibody was diluted 1:100 in PBS and Triton X-100 was added to the solution to reach a concentration of 0.5%. The samples were continuously shaken in a tube

(Safe-Lock Tubes 2.0 ml, Eppendorf BIOPUR, #0030 121.597, Eppendorf AG, Hamburg, Germany) in 1.5 ml solution containing the antibody for seven days and protected from light, at 4°C.

Thereafter, the staining solution was discarded and the tissue washed twice overnight in PBS, protected from light, at 4°C. Then the samples were dehydrated in a graded ethanol series (30%, 50%, 70%, 80%, 90%, each for at least two hours at room temperature) and lastly immersed in 100% ethanol overnight. To further dehydrate the samples, they were immersed for 1.5 hours, protected from light, in 5.0 ml n-hexane (#104374, Sigma-Aldrich, Merck KgaA, Darmstadt, Germany). Clearing was performed with BABB (benzyl alcohol/benzyl benzoate mixture in a ratio of 1:2, both purchased from Sigma-Aldrich, Merck KgaA, Darmstadt, Germany). The n-hexane containing the samples was replaced by BABB solution in two steps, 2.5 ml each in an interval of 1.5 hours. Finally, the samples were stored in 5.0 ml fresh BABB solution, protected from light, until image acquisition.

8.4.4. LSFM image acquisition and processing for detection of PA-CXCR4 lymphocytes

In order to achieve optimal transparency, the samples remained immersed in BABB at least for 24 hours before image acquisition.

Imaging acquisition and visualization were performed using the LSFM-setup and software of the Laboratory of Prof. Katrin Heinze (Rudolf Virchow Center for Integrative and Translational Bioimaging, Würzburg).

Image acquisition with the light sheet microscope

The used LSFM setup (figure 15) was tailor-made for organ imaging and custom-built (not part of this work) previously in the Laboratory of Prof. Katrin Heinze. Major parts have been described elsewhere [214]. 488 and 640 nm excitation laser lines (Coherent OBIS) were used for image acquisition to record the emission of both, autofluorescence (laser power = 25%) and antibody-labeled GFP in the PA-CXCR4 construct (laser power = 3.2%), respectively. GFP was additionally counter-stained with anti-GFP-Alexa Fluor 647 (see section III.8.4.3.) to circumvent tissue autofluorescence in the GFP spectral range. The sample was mounted and immersed into the BABB-containing chamber previously filled with BABB (figure 15). To image whole organs, an alternating dual-side illumination was realized using a dual-axis galvanometer scanner (6210H; Cambridge Technologies, Bedford, MA, USA) and a theta lens (VISIR; Leica, Mannheim, Germany). A virtual light sheet image was then created and projected onto each side of the sample via a tube lens (Zeiss, Göttingen, Germany) and the illumination objective (EC Epiplan-Neofluar 2.5/0.06 M27; Zeiss). Fluorescence was collected perpendicularly to the light sheet by a 5x objective (HC PL Fluotar 5x/0.15; Leica, Mannheim, Germany) and an infinity-corrected tube lens (model Valentine RTC; Leica, Mannheim, Germany). Next, the image was projected onto a scientific complementary metal oxide semiconductor camera (sCMOS; Neo 5.5; Andor, Belfast, United Kingdom) with 2047 x 2047 pixels (6.5 µm) using 2 x 2 binning. For sequential imaging in the different color channels, exposure times for the autofluorescence and the stained cells were 1.0 and 0.2 second respectively. The

fluorescence was spectrally filtered by emission filters (BrightLine HC 525/50 for autofluorescence and HQ697/58 for Alexa Fluor 647; both from AHF Analysentechnik, Tübingen, Germany) representing the respective fluorophores and detection channels. Filters were automatically set by a motorized filter wheel placed in the collimated light path between detection objective and tube lens (HA110A Filter Wheel with ES10 controller; Prior Scientific GmbH, Germany). Image stacks were acquired in increments of 5 μm . The voxel dimension was 2.6 x 2.6 x 5 μm (x, y, z). The IQ 2.9 software (Andor, Belfast United Kingdom) controlled the hardware components for image acquisition (laser, camera, stage, filter wheel). Recorded images were saved as .tiff files and visualized as described below.

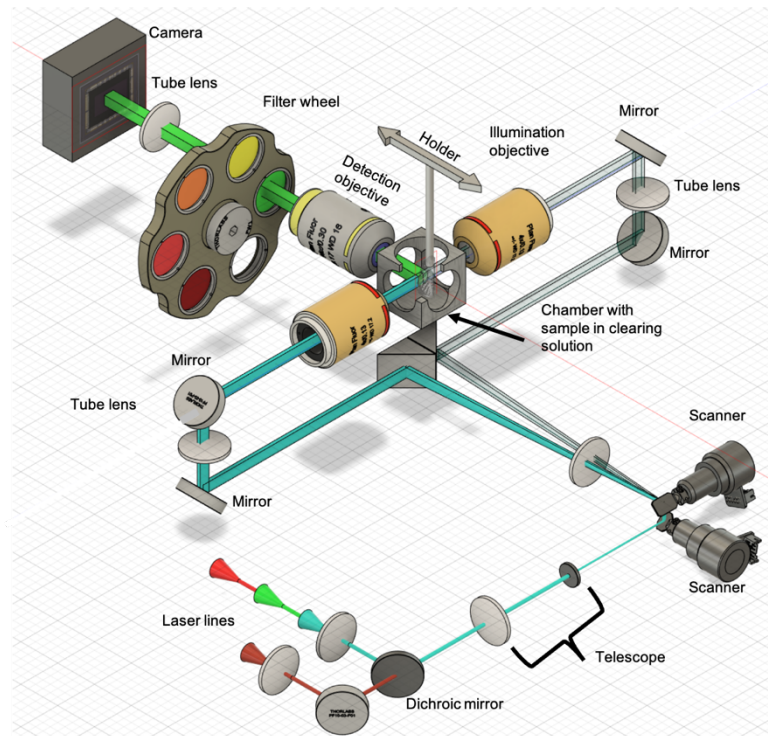


Figure 15| LSFM setup for whole organ imaging

A virtual light sheets of Laser lines (488 and 640 nm) combined by a dichroic mirror illuminate the sample via alternating double-sided illumination. Fluorescence from the sample is collected perpendicularly to the light sheet by an 5x objective, spectrally filtered, and then projected via the tube lens onto a scientific complementary metal oxide semiconductor (sCMOS) camera. The sample is mounted on a motorized sample holder and dipped into the chamber filled with clearing solution. The sample is scanned by moving the sample.

Figure provided by courtesy of the Laboratory of Prof. Katrin Heinze.

Image visualization

Results were converted into Imaris Classic format and visualized in Imaris (Imaris x64, version 9.8, Bitplane AG, Zurich, Switzerland). If needed, datasets were stitched to reconstruct a part of the organ using the XuV-tool [215]. The fluorescence intensity of the cells stained against GFP was used to localize PA-CXCR4 cells. The autofluorescence signal was used to provide orientation and depict organ morphology and show the distribution of PA-CXCR4 cells within the tissue. Videos available in the digital appendix (video 2 and 3), were generated using the Imaris recorder at 750 frames/s.

9. Statistics and figures

Graphs for the experiments to assess HR modulation under optical stimulation were plotted with MATLAB 2019b custom codes. Normality was checked using Lilliefors test for each set of data, and homoscedasticity was tested with Brown-Forsythe test. By comparing two data sets with normal distribution, Student's t test was used, and Wilcoxon signed-rank test was applied to non-parametric data. To compare baseline HR vs. stimulation HR, paired tests were used. By comparing more than two data sets, a one-way ANOVA test was used if the hypotheses of equal variance and normality were true for all, otherwise a Kruskal-Wallis test was performed, and in both cases followed by appropriate post-hoc test with Bonferroni correction.

Graphs and statistical analysis to assess weight loss and phototactic lymphocyte migration were performed with GraphPad Prism 9.

Weight loss was analyzed with one-way ANOVA for repeated measures to perform multiple comparison of the means; as post-hoc test, Tuckey's test was performed.

Analysis comparing two samples (spleen, lungs, thymus), was performed with unpaired two-tailed Student's t test. For the analysis of heart samples divided into LA, RA, LV, RV, one-way ANOVA was used.

In both cases, HR modulation and PA-CXCR4 migration, SEM (standard error of the mean) was indicated. Significance levels were marked with *; $P \leq 0.050$ displayed with *, $P \leq 0.01$ displayed with ** and $P \leq 0.001$ displayed with ***. If non-significant, P values were not mentioned.

Figures were designed with Microsoft PowerPoint Version 16.57. Organ illustrations were self-designed or downloaded from SMART (Servier Medical Art, smart.servier.com).

IV. RESULTS

1. Development of a surgical procedure for device implantation on the beating heart

1.1. Device preparation and mouse positioning for the implantation

The shape of the device developed for brain surgeries, did not make its implantation on the heart directly possible. Before starting the surgical procedure, the implantable device was adapted under aseptic conditions to enable its attachment to the beating heart.

The probe, which carries the light source (μ LED) at its tip, was pulled through a transparent plastic tube (800/100/200, 30 m, 0.58 mm internal diameter, 0.96 mm external diameter, Portex, fine bore tubing, Hartenstein GmbH, Würzburg, Germany). The tube was cut to the appropriate length, taking care to keep the μ LED uncovered by the tube to avoid light attenuation. The suture material (CV-8, 8K10A, GORE-TEX Suture), which was later used to stitch the device to the heart, was threaded into both ends of the plastic tube (suture 1 and 2, figure 16 A and B) and, in order to prevent the suture thread from slipping, fixed using a simple interrupted suture. The suture thread 1 was additionally threaded through the hole at the end of the probe and tied with a simple interrupted suture, thus ensuring that the plastic tube remained in place. The chosen suture material was developed especially for vascular surgery and offered great advantage since the needle diameter is hardly larger than the thread itself. As a result, the damage caused when stitching the device to the myocardium remained smaller compared to the use of a classic 8–0 monofilament polypropylene suture thread. Intraoperatively, major differences in favor of this suture material could be observed: less bleeding at the suture site, easy to knot, less cutting properties.

Preparation of the surgical field and positioning (figure 16 C, D and E) of the mouse in half-supine position are described in details in section III.3.3., but briefly depicted here in order to provide a better orientation in the next section explaining the surgical device implantation on the beating heart.

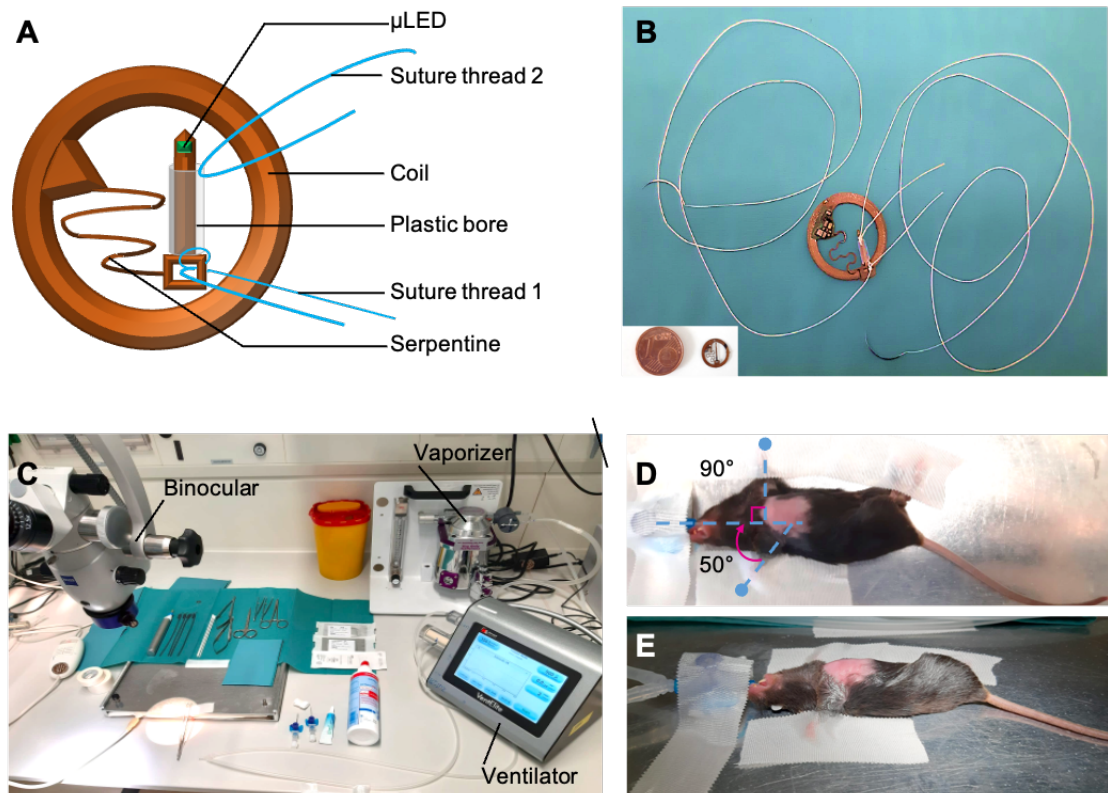


Figure 16| Preparation of the device and surgery field

(A and B) Schematic and real device after pulling the probe through the transparent plastic bore and tying of both suture threads. (C) prepared surgery tools, vaporizer and ventilator for anesthesia. (D and E) ventrodorsal and right-lateral view of an intubated mouse prepared for device implantation on the right ventricle: back oriented perpendicularly towards surgeon, fixation of left forelimb $\approx 90^\circ$ and right forelimb $\approx 50^\circ$ from rostral median, right hindlimb crossed above left one.

1.2. Intrathoracic device implantation

The ECS sends rhythmic electrical impulses originating in the SAN which works as an intrinsic pacemaker. The heart is under parasympathetic influence via cholinergic cardiac neurons. Both, SAN and cholinergic cells are mostly located in or in proximity of the RA, close to the *Sinus venosus* (details in sections II.2.2. and II.2.3.2.). Pacemaker cells and cholinergic neurons in the RA region were targeted to modulate the HR.

The left anterior descending coronary artery (LAD) is ligated in MI models resulting in an abrupt stop of the blood flow (reviewed in [106]). The tissue damaged by this ischemic injury undergoes remodeling processes which are orchestrated by the immune system; that is why we aimed to attract PA-CXCR4 lymphocytes into the LV wall.

Hence, depending on the approach, two specific cardiac regions needed to be illuminated to establish *in vivo* cardiac optogenetics models: the RA for HR modulation, and the LV to guide lymphocytes into the myocardium. The surgical procedure was adapted to each purpose. In this section, the device implantation on the RV is described and corresponded to the procedure performed in order to optically modulate the HR, thus target the cells close or within the RA. To investigate the migration of PA-CXCR4 cells, the attachment of the device to the LV was performed the same way but in a reversed mirror manner and can be visualized in the digital appendix (see Video 1, “Cardiac optogenetics – Device implantation on the left ventricle”).

As described in section III.3.2. and III.3.3., the surgical field was prepared and proper anesthesia depth checked. The skin incision was made from the right axilla to the xyphoid region and the pectoralis muscles were bluntly retracted to the side to access the fourth right intercostal space. There, the lateral thoracotomy was performed using an electric cautery kit to avoid bleeding of the intercostal muscles. The ribs were carefully spread with retractors to make the heart visible and accessible for device attachment (figure 17, A-D).

For easier handling, the implantation of the LED on the beating heart was performed using a needle holder with built-in suture cutter, which offered the advantage to perform both, stitching and cutting of the suture thread, without the need to change tools and therefore avoided unnecessary movements during this critical step. The device, which was prepared prior to surgical procedure (see section IV.1.1.; figure 16, A and B), was first tied to the apex of the RV with a simple interrupted suture (suture thread 1, figure 16, A and figure 17, E-G). To avoid rotation of the LED and therefore ensure focused illumination, the device was fixed below the RA on the heart base using the same technique (suture thread 2, figure 16, A and figure 17, H and I). Secured this way, the μ LED was pointing at the RA (figure 17, P). In the case of left ventricular implantation, the second suture was performed in order angle the μ LED towards the LAD. Both simple interrupted sutures were performed as superficially as possible to minimize myocardial damage, but still deep enough to avoid the threads to tear out. If the suture thread appeared under the superficial myocardial layers while pulling it through the tissue, adequate suture depth was reached.

Before closure of the thoracotomy wound, it was ensured that no bleeding had occurred (figure 17, J) and that the heartbeats remained strong and regular. If necessary, blood was removed with cotton swabs. The thoracotomy wound was closed from dorsal to ventral using four to five simple interrupted sutures (Silk, 6/0, 2 x DR-10, 45 cm Vömel, Kronberg, Germany) at a distance of one to two mm from one another. Each suture tightly approximated the facing edges of the first cranial and caudal intercostal space flanking the thoracotomy wound (figure 17, K). The ends of the first suture remained around seven cm long and were used later to secure the coil. The flexible and stretchable serpentine component of the device was placed between two simple interrupted sutures. Before tightening the last suture of the thoracotomy wound, gentle pressure was applied laterally on the chest with thumb and index finger to reduce the iatrogenic pneumothorax (figure 17, L). Afterwards, the retracted pectoralis muscles were replaced, and the circular coil could be gently bent to fit it to the thorax curvature. Thereafter, the coil was fixed subcutaneously using the remaining thread from the first thoracotomy suture and one to two additional simple interrupted sutures (Polypropylene 5/0, HR-16, monofil, 75 cm, Vömel, Kronberg, Germany; figure 17, M). The fixation of the coil in a subcutaneous pocket (figure 17, N) protected the coating and prevented displacement of the implanted device once the mouse would freely move.

The skin was closed using single interrupted sutures (Polypropylene 5/0, HR-16, monofil, 75 cm, Vömel, Kronberg, Germany; figure 17, O).

Isoflurane supply was interrupted and the animal continuously ventilated until showing spontaneous breathing. The wound was disinfected and the mouse allowed to recover as

described in section III.3.2.2.

With practice, the procedure was performed within 50 minutes. No postoperative mortality was observed. However, intraoperative mortality was 23% by implantation on the RV (n = 48, including animals for the establishment of the surgery) and 12% by procedures on the LV (n = 34).

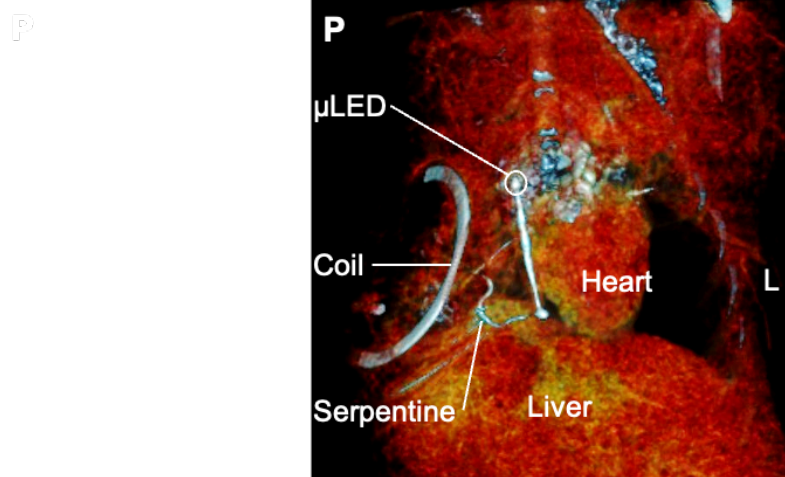
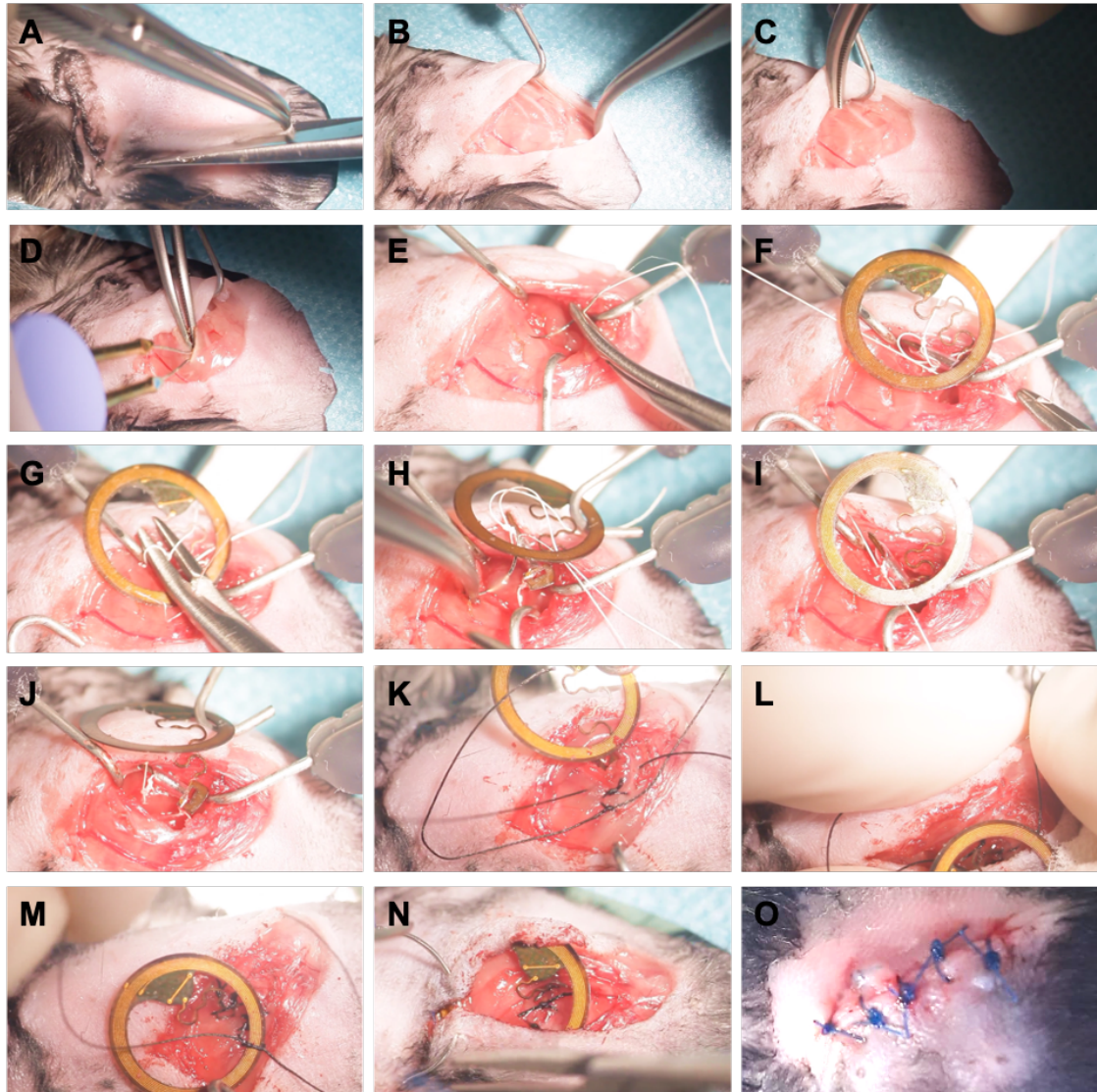


Figure 17| Step-by-step intrathoracic device implantation on the right ventricle *in vivo*

(A) Skin cut from the right axilla to xyphoid followed by (B) retraction of the pectoralis muscles. (C) Ventral perforation of the fourth intercostal space and subsequent (D) opening of the thorax with the cautery kit. (E) Stitch, (F) suture tightening and (G) shortening of the suture (≈ 1 mm) of the first fixation point performed apically with suture thread 1. (H) Stitch and (I) suture tightening for the second fixation point performed below the RA with suture thread 2. (J) Implanted device on two sites on the RV, μ LED pointing at the RA. (K) Closing of the thoracotomy wound, starting dorsally and leaving the first threads longer for later coil fixation. (L) Gentle pressure laterally on the thorax to reduce the iatrogenic pneumothorax before definitive closure of the thoracotomy wound. (M) Fixation of the coil with the thread from the first thoracotomy suture and two more subcutaneous single interrupted sutures (not shown here) before (N) forming the subcutaneous pocket. (O) Single interrupted sutures of the skin suture embedding the coil. (P) Computed tomography scan localizing the device *in situ* after implantation on the RV.

1.3. Surgery related effects

1.3.1. Weight evolution

Since pain leads to decreased appetite and therefore lowers food intake, also in early burden exposure stage [126], weight loss was assessed as an indicator for animal distress after surgical procedure.

The mice were weighed every day during the first week after the surgical procedure until they stabilized their weight close to their initial weight (d0). Thereafter, their bodyweight was monitored once a week until the end of the experiment to decrease handling-induced stress. According to the approved applications for animal experiments and the chosen experimental designs, to initiate lymphocyte migration the total experiment duration was five days post-surgery, whereas the experiments for HR modulation could last up to ten weeks. In latter experiments, depending on the findings, the animals were sacrificed before the end of the permitted time. This explains the changing number of animals throughout the time, which led also to the slight fluctuation of the curve.

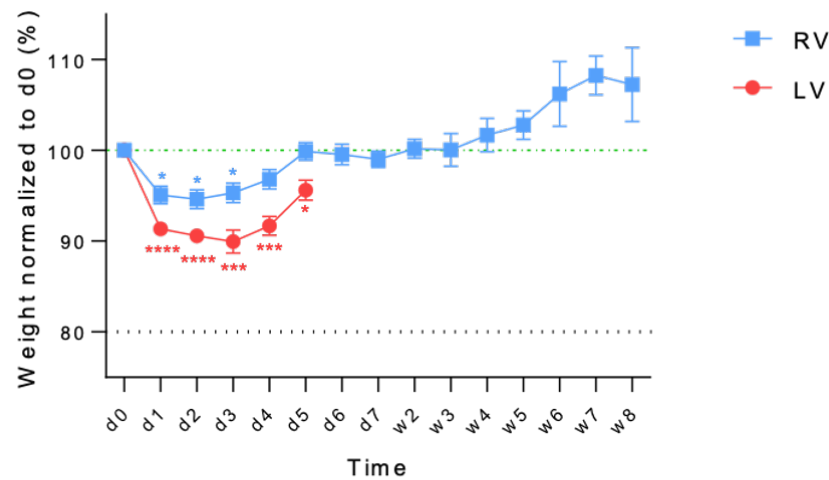
Note that different mouse strains and sexes were used according to the experiment objectives. Surgeries on the right ventricle were performed in males and females with Bl6-background (HCN4-Cre and CHAT-Cre), whereas only male Balb/c underwent the procedure on the left ventricle. The age of the mice was similar in the different groups.

The greatest weight loss occurred right after the surgery from d0 to d1 ($P = 0.014$ for RV, $P < 0.0001$ for LV, values compared to d0). Between d1 and d2, further weight loss was observed ($P = 0.012$ for RV, $P < 0.0001$ for LV, compared to d0) but was far less important as the weight reduction between d0 and d1. Although mice implanted on the RV started to recover their bodyweight from d3 onwards, mice implanted on the LV showed still a slight weight loss on that day ($P = 0.038$ for RV, $P = 0.0001$ for LV, compared to d0). On d4 and until the end of the experiment, the bodyweight loss after right ventricular surgery was not significant anymore, while mice operated on the LV started to gain weight ($P = \text{ns}$ for RV, $P = 0.0001$ for LV compared to d0). On d5, corresponding to the end of the experiment after left ventricular implantation, mice did not recover their initial bodyweight ($P = 0.025$ compared to d0) but showed an important weight gain compared to the day before (figure 18).

On average, mice operated on the RV lost 2.8% until bodyweight recovery (d7) and

mice operated on the LV lost 8.2% until the end of the experiment (d5). In both scenarios, the weight dropped first abruptly from d0 to d1, continued to decrease to a lesser extent until d2 after procedure on the RV and until d3 on the LV, to reach, on those days, the maximal weight loss of 5.4% and 10.1%, respectively. After left ventricular implantation, the weight loss was greater, lasted longer and represented at the end of the experiment 4.4% compared to the initial bodyweight, thus mice gained back 56.3% of the lost weight.

The transient weight loss observed after both type of surgical procedure, was then compensated by constant bodyweight increase until the end of the experiment, and for mice operated on the RV, even above the initial value, with 3.8% weight gain (week 8). None of the mice reached the humane endpoint of 20% bodyweight loss.



Time point	d0	d1	d2	d3	d4	d5	d6	d7	w2	w3	w4	w5	w6	w7	w8
n RV	12	12	12	12	8	8	11	11	11	10	10	9	3	3	3
n LV	11	11	11	11	11	11									

Figure 18| Weight evolution of the mice after left or right ventricular device implantation throughout the experiment

Ratio comparing the maximal weight loss after left and right ventricular surgery indicated a 1.86-fold weight loss after implantation on the LV. Ratio comparing the average weight loss until d5 after left and right ventricular surgery indicated a 2.23-fold weight loss after implantation on the LV. Weight and statistics compared to d0.

1.3.2. Histological assessment of myocardial damage

Device fixation was performed superficially with two punctures of the ventricular tissue, inevitably resulting in minor myocardial injury and subsequent scar formation. Due to the very limited capacity of regeneration in the adult heart (reviewed in [216]), it was crucial to assess tissue repair and the extent of the formed scar. The histological analysis was performed using Masson's trichrome staining five days after device implantation on the left or the right ventricle.

Overall, and independently from the implantation side, the heart shape and surrounding tissue organization remained unaffected by the device implantation (figure 19). An obvious but limited tissue damage on both, left and right ventricle after the surgical implantation was visible at the location where the suture threads passed through the

myocardium to anchor the device. The implantation sites close to the base and the apex showed intramural collagen deposition in the respective ventricular walls. The scar formation looked similar on both heart sides (figure 19 A, respectively B) and on both implantation sites. Subjectively, the fibrotic tissue visible in the section sequence represented less than 10% of the LV or RV. In comparison, it is known that cardiac injuries induced in MI models, do not lead to remodeling or heart failure when the infarct size remains below 30% [217, 218]. Hence, based on histological observations, an adverse effect of the surgery on the heart function was not expected.

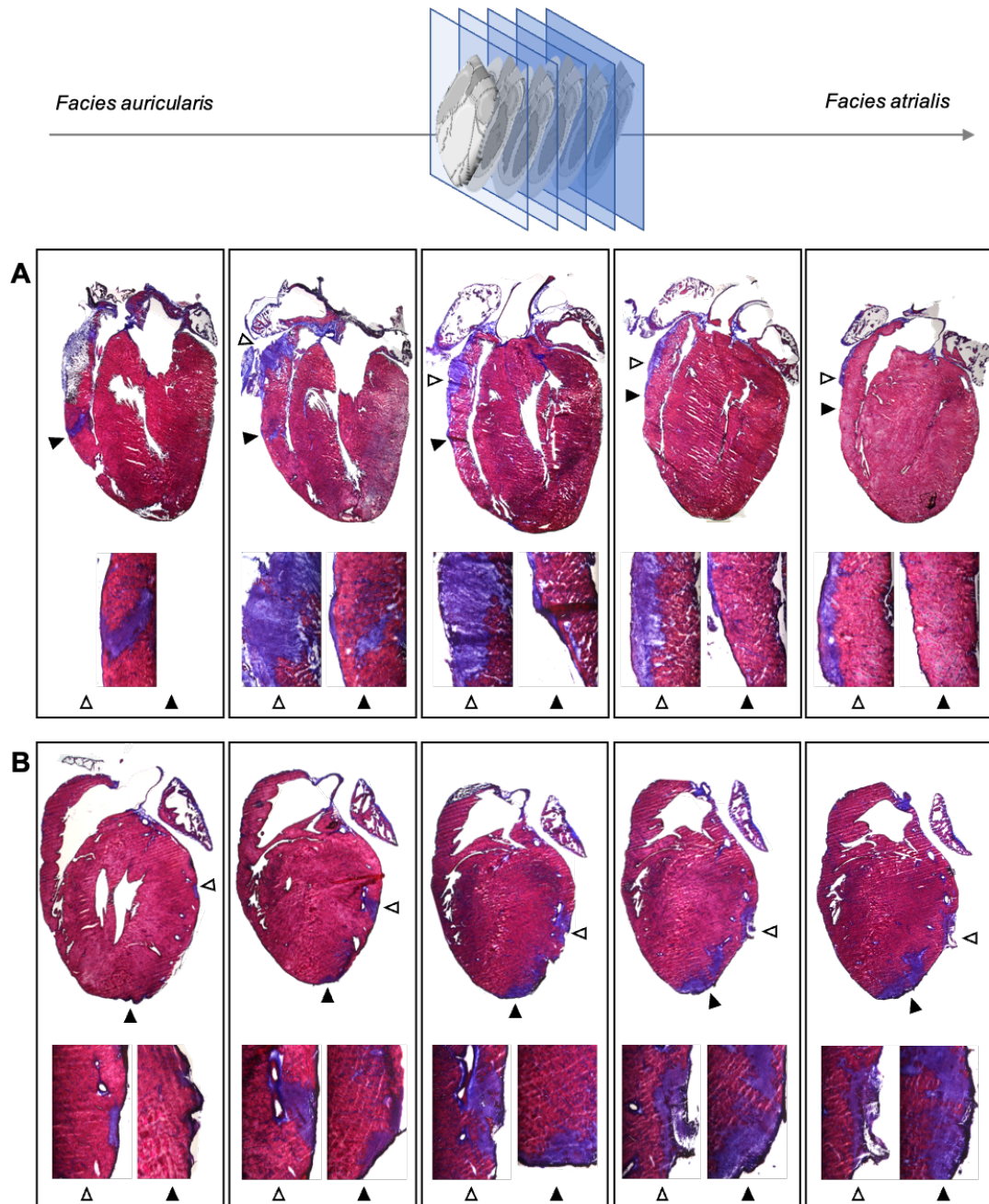


Figure 19| Histological assessment of myocardial damage after left and right ventricular device implantation

Masson's Trichrome staining performed five days after (A) implantation of the device on the RV (wildtype Bl6 mouse) and (B) on the LV (Balb/c mouse). Collagen fibers appear blue, nuclei black, muscle and cytoplasm are stained red.

15 μm longitudinal sections; $\approx 150 \mu\text{m}$ between slices.

Magnifications: overview x1.25 and zoom into scar areas x10.

1.3.3. Echocardiographic assessment of left and right ventricular function

Although histological assessment of scar formation allowed us to understand the morphological extent of the tissue damage, it did not provide information regarding heart function. Echocardiographic measurements were performed to evaluate both, left and right ventricular function after the surgical device implantation (figure 20). Reference values for right ventricular function are far less described in the literature as for left ventricular function. Hence, mice undergoing device implantation on the RV were examined twice: before surgery and seven days after the procedure (d7), in order to acquire comparable values for each animal. After implantation on the left ventricle, imaging was performed once on d5, corresponding to the maximal experiment duration for those mice.

Systolic left ventricular function was assessed by measurement of EF and FS describing the percentage of blood pumped out of the LV with each contraction and myocardial contractility, respectively [134]. Both parameters remained in the physiological range for all the animals implanted with the device either on the left or the right ventricle (figure 20, A and B). Values measured before right ventricular surgery were similar to the ones measured after the procedure.

The mitral valve flow profile represented by the E/A ratio, was used to assess the diastolic heart function. The recorded measures were in the physiological range for all the animals implanted with the device either on the left or the right ventricle (figure 20, C). Values recorded before and after surgery were in the same range.

The velocity peak of the pulmonary artery flow was recorded to assess right heart function [136, 137]. The recorded values were comparable before and after the surgery and within or above the physiological range ($n = 2/6$ for RV, $n = 6/11$ for LV; figure 20, D).

The TAPSE was taken as an indicator of both systolic and diastolic right heart function [135, 136] to describe right ventricular contraction. Due to artefacts caused by the device, measurement of the TAPSE was not feasible in mice implanted on the LV. Thus, the measurements were only performed after the right ventricular procedure and remained in the physiological range (figure 20, E).

The measurements listed above, gave an overview of left and right ventricular function as well as systolic and diastolic cardiac activity. Hence the function of the ventricles was checked individually and put into the context of the overall heart function. The results show preserved heart function after surgical device implantation either on the left or the right ventricle.

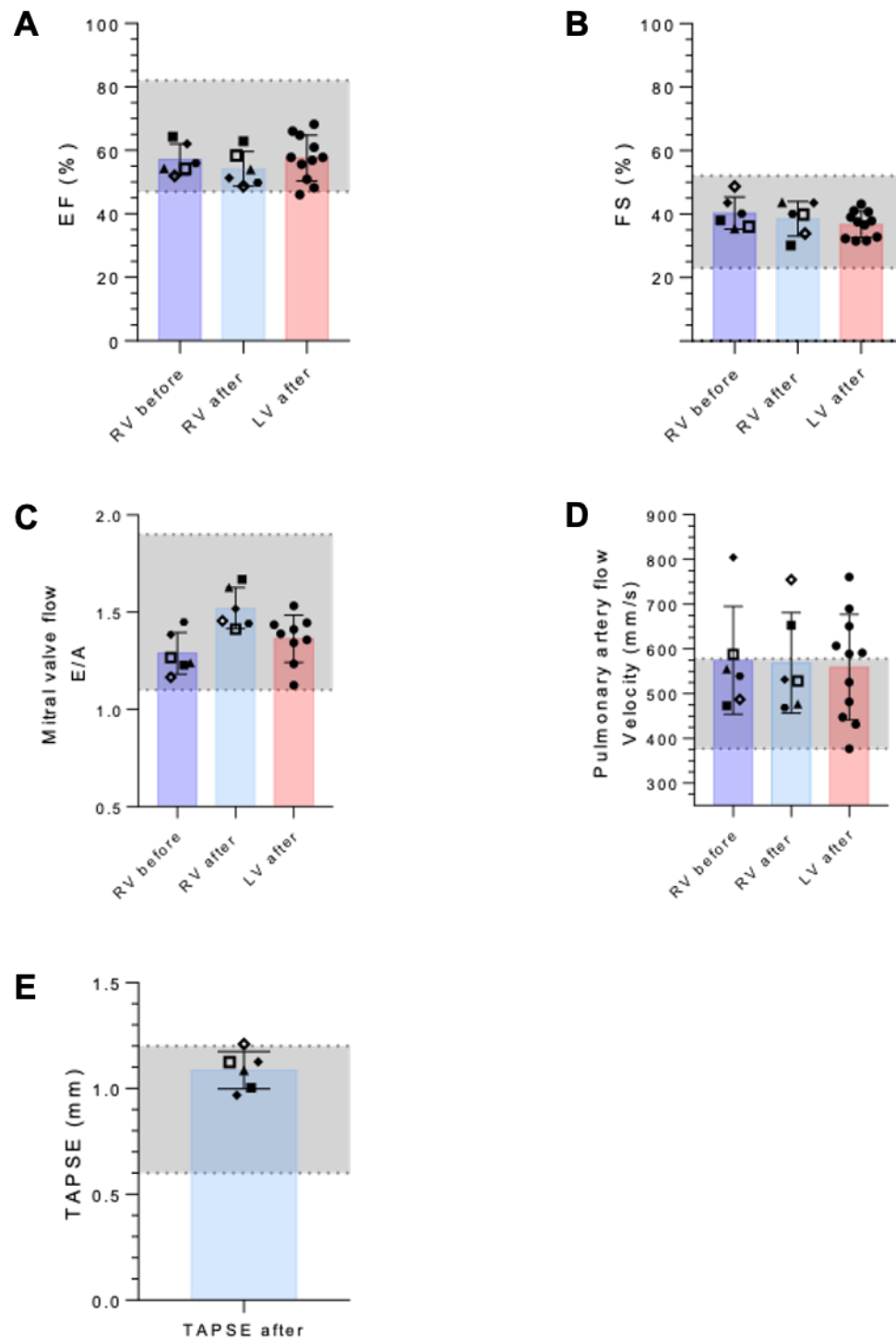


Figure 20| Transthoracic echocardiographic measurements of left and right ventricular heart function in anaesthetized mice

(A) Ejection fraction and (B) fractional shortening measured to assess systolic left ventricular function. (C) E/A ratio recorded to evaluate diastolic left ventricular function. (D) Pulmonary artery flow and (E) TAPSE measured to assess right ventricular function.

The grey overlay depicts reference values for each parameter. Since mice operated on the RV underwent the examination before and after the surgery, each animal is represented by one symbol. RV: n = 6; LV: n = 11.

2. Light-induced manipulation of the electrical conduction system of the heart and intrinsic cholinergic cardiac ganglia

2.1. Experimental design to modulate the heart rate

Manipulation of the HR depended on opsin expression in the ECS or cholinergic cardiac neurons. To achieve specific opsin expression in the cells of interest, floxed AAV vectors were injected i.v. in Cre-mouse strains. Echocardiographic measurements were performed prior to surgery. Three weeks elapsed between systemic vector administration and device attachment on the RV in order to provide enough time for viral transduction of the cells [147, 158] and ensure best integrity of the device throughout experiment duration. One week after intrathoracic implantation of the device, heart function was again estimated with echocardiography and compared to the results acquired before the procedure to assess a possible effect of the device implantation on the heart. Afterwards, the ECG electrodes were implanted subcutaneously. ECG measurements were performed up to eight weeks after electrode implantation with recording sessions taking place on several days. Finally, the mice were sacrificed and their heart collected to verify the opsin expression.

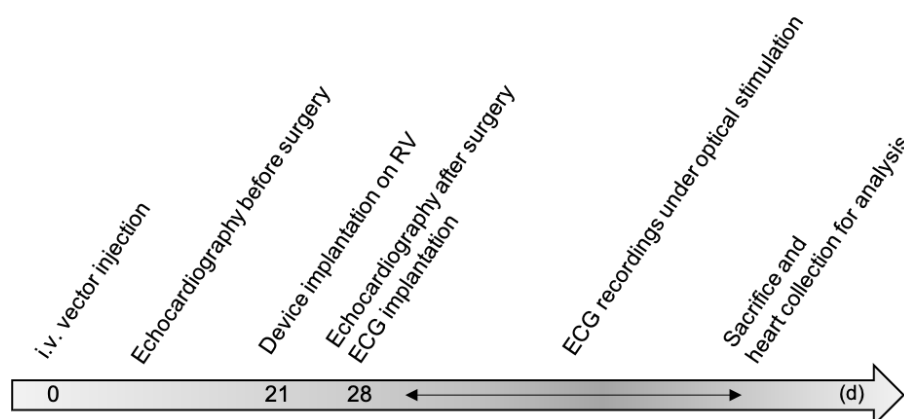


Figure 21| Experimental design for heart rate modulation

2.2. Heart rate modulation under optogenetic stimulation

The goal of optogenetic stimulation of intrinsic cardiac cells belonging to the ECS or cholinergic ganglia, was to modulate the HR. The physiological resting HR is 500 to 700 bpm in mice [100], with maximal HR under stressful conditions of up to 800 bpm [219]. With the chosen stimulation protocols (further details in section III.6.1.4.) we sought, on the one hand, to overwrite the pacemaker activity of the SAN in HCN4-cre mice in order to increase the HR, and on the other hand, to stimulate cholinergic intrinsic ganglia in ChAT-Cre mice to evoke a HR decrease.

With both approaches, i.e. stimulation of HCN4- or ChAT-cells, the measurements protocols were designed to address three questions in both mouse strains: first, whether HR changes correlated with optical stimulation itself (1); second, if the effect was stimulation type-dependent (2); and third, whether HR variations under stimulation were

position- or time-dependent (3).

(1) To determine if the illumination led to a HR change, thus is on/off-dependent, all data were pooled and compared to the respective baselines, independently from stimulation type and position.

(2) To test whether the effect was linked to a particular stimulation type, i.e. depended on pulse frequency and/or pulse duration (stimulation type-dependent), all the measurements for one stimulus type were pooled and compared to their respective baselines.

(3) Whether the effect of absolute time and the effect of one stimulation type influenced the following one, was evaluated by counterbalancing the order of the stimulation types in the different sessions; each stimulus type occurred at least once in first, second or third position. Therefore, a time/position-dependent effect could be assessed. Here the difference between stimulation and respective baseline was calculated:

$$\Delta = \text{mean HR during stimulation} - \text{mean HR during baseline}$$

The mean HR before stimulation (baseline) as well as during the stimulation, were both assessed over 30 s. The baseline, when no optical stimulation occurred, was taken as negative control, thus the effect of the light stimulus on the HR was evaluated “within” each mouse. Since it was unclear which wavelength fitted the best to activate the opsin ChRmine in the myocardium, orange (590 nm) and red (630 nm) devices were implanted in different mice.

2.2.1. Optogenetic stimulation of cardiac pacemaker cells

In HCN4-Cre mice, stimulations were meant to evoke a HR increase by pacing the heart in the upper physiological frequency range with pulses occurring every 67 ms and lasting 15 ms, therefore corresponding to around 895 bpm. To investigate further possibilities for HR modulation and its limitations, measurements were performed with a wider pulse (30 ms) as well as constant illumination to reach a possible ceiling corresponding to the maximal HR. All the animals were implanted with the orange μ LED, higher in energy but with lower tissue penetration.

The representative HR trace describing the HR change over time showed increased variability in the course of the session, independently from stimulation time points (figure 22, A).

(1) The pooled data, independently from the stimulation type, did not show significant HR change during illumination (figure 22, B). Moreover, no clear variation was observed in the peristimulus time histogram (PSTH) depicting the mean HR 30 s before and 30 s after stimulation onset.

(2) However, a particular stimulation type may have induced a HR increase without being important enough to influence the general results of the pooled data. Therefore, the HR variation during baseline vs. stimulation were plotted for each stimulation type. No significant stimulation-dependent HR variation was observed for a specific stimulation type. Similarly, the PSTH curves did not indicate any HR change upon stimulation (figure 22, C).

(3) As no stimulation-induced effect on the HR was observed, the analysis of the position effect would have been redundant and was not performed.

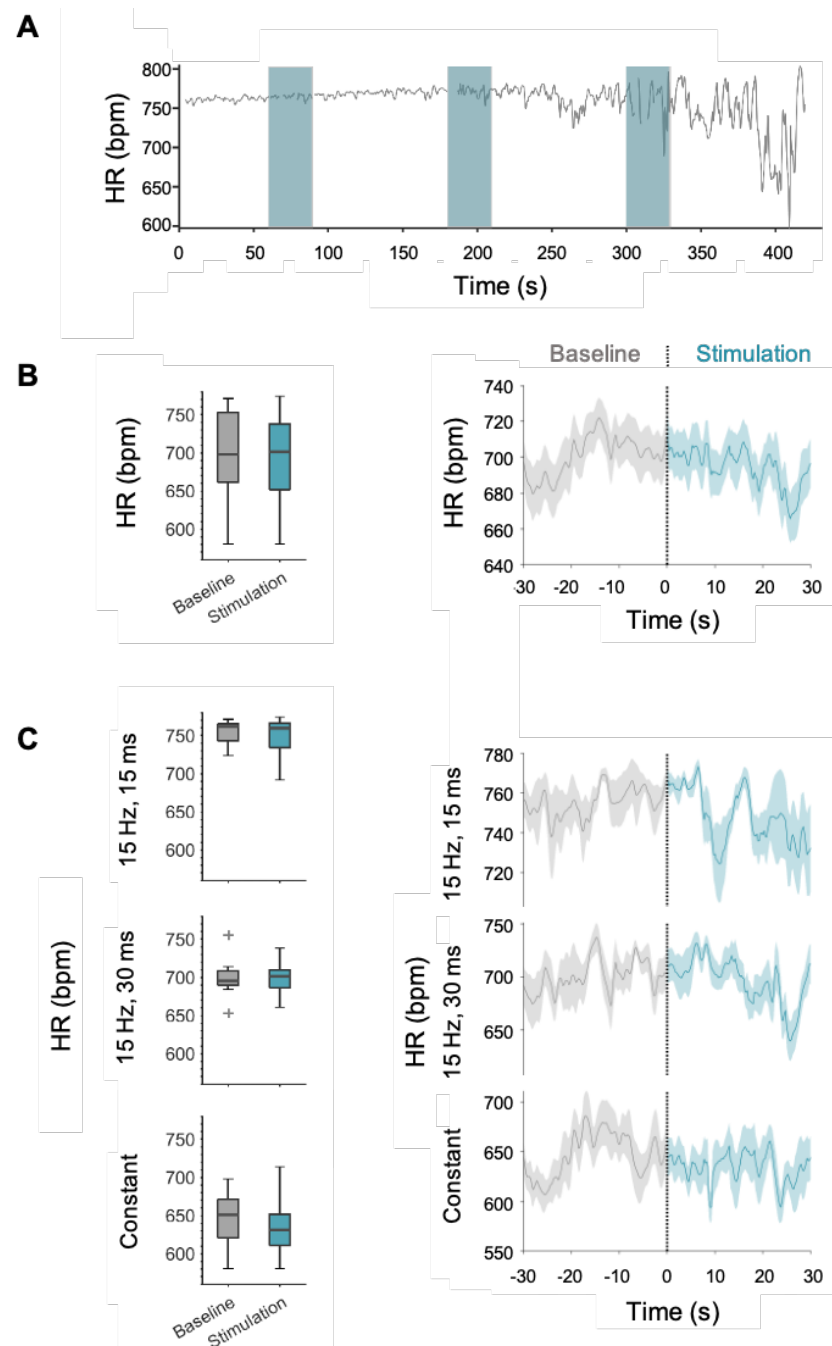


Figure 22| Heart rate change under optical stimulation in HCN4-Cre mice

(A) HR over time during a stimulation sequence. Blue bars correspond to stimulations. (B) HR change under optical stimulation, pooled data from all stimulations; 27 stimulations in 3 mice. (C) HR change depending on stimulation type; for each stimulation type, 9 stimulations performed in 3 mice.

All mice implanted with the orange device (590 nm).

Note: preliminary measurements for method establishment; *P* value calculated with repeated measures for illustrative purposes.

Individual HR variations may have been overseen in the pooled data; therefore, analysis for each mouse, depending on the stimulation type were performed (see section X, figure 32). However, individual assessments did not reveal any significant HR change under optical stimulation.

In a nutshell, no light-dependent, stimulation type-dependent, or time/position-dependent HR change were observed in HCN4-Cre mice; individual differences were not detected either.

2.2.2. Optogenetic stimulation of cardiac cholinergic cells

In ChAT-Cre mice, we sought to optically induce a HR decrease. First, illumination frequency corresponding to 600 bpm (i.e. 10 Hz, 10 ms), thus within the physiological range, was set to induce a mild HR decrease. This frequency was successfully used in combination with a blue-shifted opsin, in Langendorff-perfused hearts of ChAT-Cre mice [54]. Then, as in HCN4-Cre mice, the effect of further stimulation types was studied; measurements using high frequency stimulation (50 Hz, 15 ms), as well as constant illumination were performed. Light of orange and red wavelengths are potentially able to activate the opsin ChRmine [117]. Since this opsin was never used in the heart before, both types of devices were implanted to test which optical parameter, energy or tissue penetration, would be favorable to opsin actuation in the myocardium.

As in HCN4-Cre mice, the general HR evolution over time showed fluctuations increasing in the course of a recording sequence (figure 23, A).

(1) Altogether, independently from the wavelength and the stimulation type, a significant HR decrease ($P < 0.001$) was observed under illumination. The drop in HR upon stimulation was also visible in the PSTH (figure 23, B).

(2) Regardless from the wavelength, the analysis of each stimulus type for the whole mouse group demonstrated a significant HR decrease for 50 Hz, 15 ms as well as for constant stimulation (figure 23, C). HR reduction was more pronounced under constant stimulation ($P = 0.003$) compared to 50 Hz, 15 ms ($P = 0.11$).

(3) The position of the stimulus types relatively to each other, i.e. the sequence in which they were presented, did not have a significant influence on the HR change, thus a stimulus type did not have an effect on the following one. However, stimulations occurring in second or third positions showed greater variability and a general trend towards a HR decrease could be seen. Indeed, the median Δ HR was always lower in second and third position compared to the first one (figure 23, D).

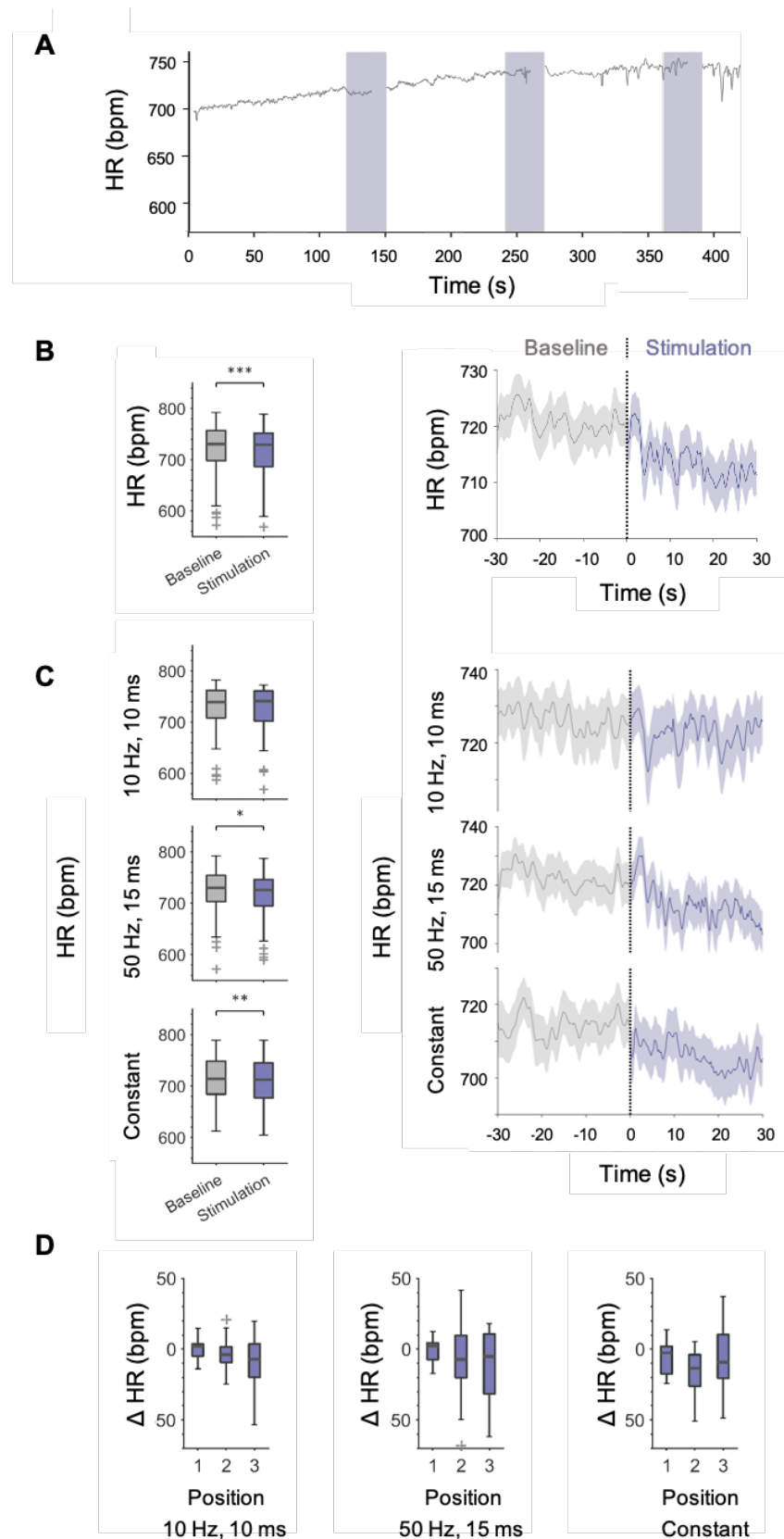


Figure 23| Heart rate change under optical stimulation in ChAT-Cre mice

(A) HR over time during a stimulation sequence. Purple bars correspond to stimulations. (B) HR change under optical stimulation, pooled data from all stimulations; 177 stimulations in 6 mice. (C) HR change depending on stimulation type; 10 Hz, 10 ms: 57 stimulations, 50 Hz, 15 ms: 58 stimulations, constant: 62 stimulations, all performed in 6 mice. (D) HR change depending on stimulation position. Note: preliminary measurements for method establishment; *P* value calculated with repeated measures for illustrative purposes.

In order to assess whether a significant effect was observed in all the animals and to see if it was wavelength-dependent, each stimulus type was plotted separately for the single mice (figure 24). Out of six mice, one animal (#4) showed a significant HR decrease for 10 Hz, 10 ms-stimulation ($P = 0.035$), and the most significant effect was observed in two mice (#4, #6) under constant stimulation ($P = 0.001$ and $P = 0.0025$, respectively). The maximal recorded HR decrease compared to the baseline in #4 was 4.2%, while #4 and #6 had a maximal HR decrease of 5.9% and 7.5%, respectively. All the significant effects were observed in three out of four mice implanted with a red (630 nm) device; no HR change was assessed under stimulation with orange light. Those results indicate that the effect is stimulus type-dependent as well as wavelength-dependent.

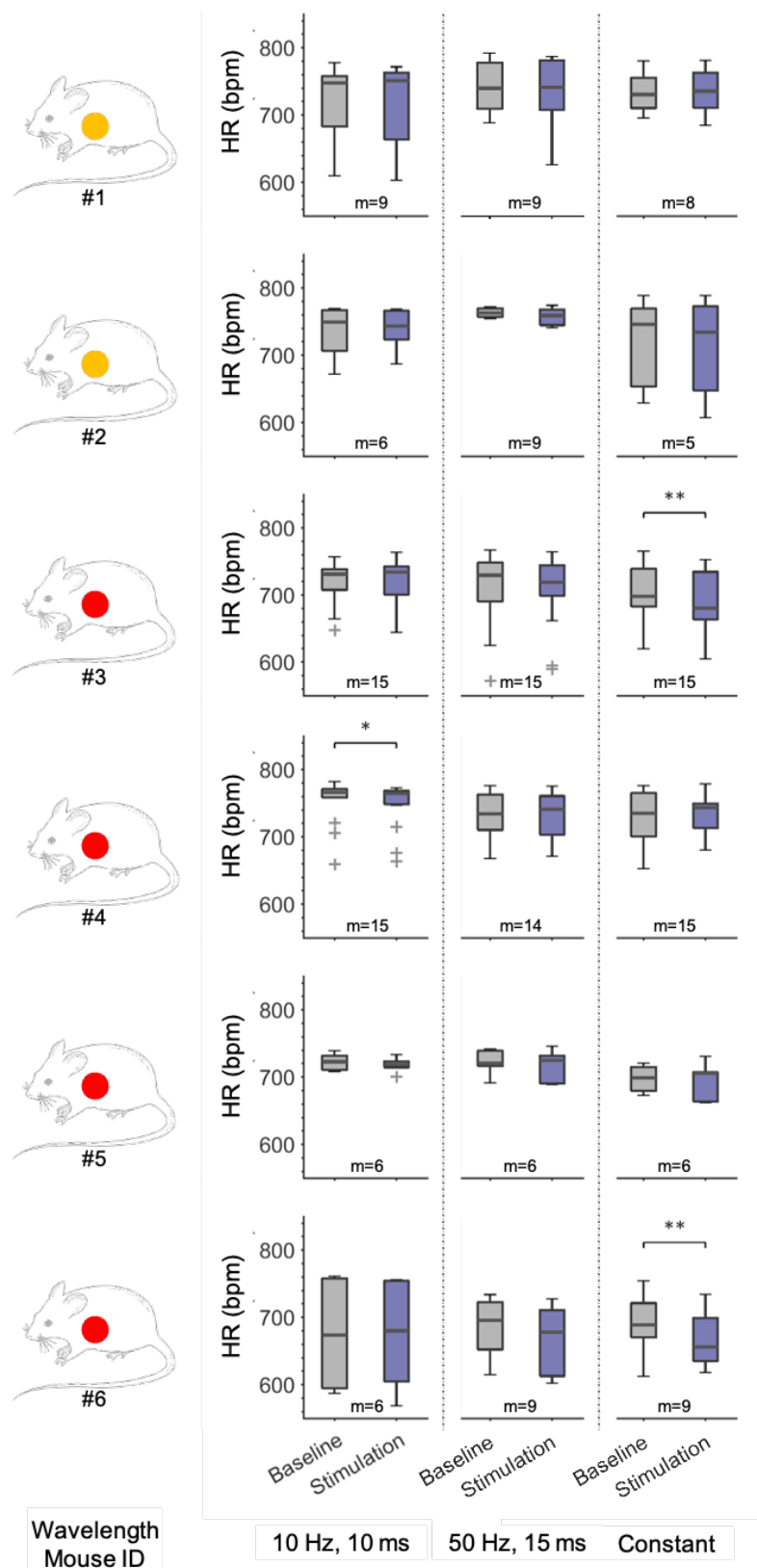


Figure 24| Individual effect of the different stimulation types in ChAT-Cre mice implanted with an orange or red device

Four mice implanted with the red device, two implanted with the orange one. HR change most significant for constant stimulation and red light.

m = number of measurements for each stimulation type; due to interferences of the optogenetics system with the ECG- recording system, not all the HR could be extracted and used, explaining the different number of stimulations (m) between mice.

Note: preliminary measurements for method establishment; *P* value calculated with repeated measures for illustrative purposes.

In summary, HR could not be modulated in HCN4-cre mice via stimulation of the pacemaker cells with the orange device, nonetheless, a HR decrease under stimulation was observed in three ChAT-Cre mice out of six. This effect was observed in mice implanted with the red device and was more significant under constant pulses (see figures 23, C and 24), thus was wavelength- and stimulus type-dependent. An increased HR variability over time was observed, but no significant position-dependent HR change was assessed, hence the position during the recording sessions did not influence the optical HR modulation.

2.3. Verification of opsin expression in intrinsic cardiac cells of interest with qPCR

Floxed AAV were used as vector to deliver the opsin (ChRmine) and the red fluorescent protein (mScarlet) into Cre-expressing cells. These genes were expected to be transcribed into mRNA in the target cell and subsequently translated into protein. qPCR was used to detect the mRNA sequences of both, opsin and RFP, and indirectly confirm their synthesis as effector proteins.

2.3.1. Verification of primer specificity

The mathematical derivation of the melt curve was crucial to determine whether the qPCR products were specific or not. The melt curves obtained for both self-designed primer pairs, ChRmine (opsin) as well as mScarlet (RFP), were comparable to the standard housekeeping gene GAPDH (figure 25). For each primer pair, the tested samples showed a single peak, which was consistent for all the tested samples.

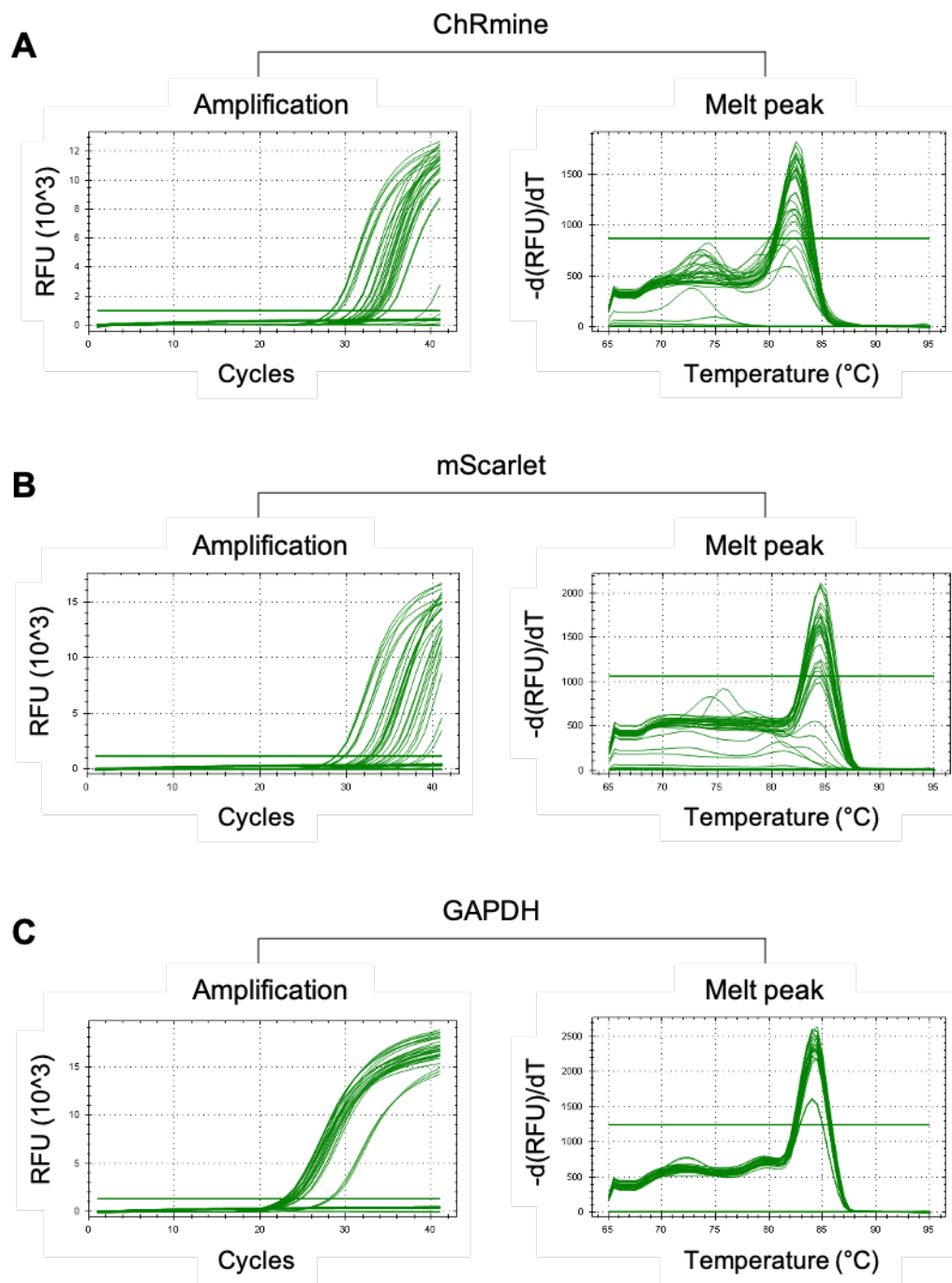


Figure 25| Representative qPCR reactions obtained with custom-designed primers

Amplifications curves and melt peaks for the designed primer pairs (A) ChRmine, (B) mScarlet and (C) the housekeeping gene GAPDH.

RFU: relative fluorescence units; $-d(\text{RFU})/dT$: negative first derivative of the change in fluorescence. Representative results of one experiment.

2.3.2. Opsin and RFP expression in the target cells

In HCN4-Cre mice, the ECS, more specifically the SAN, was targeted, whereas ChAT-Cre mice were used to stimulate intrinsic cholinergic ganglia. The SAN is located in the RA and the cholinergic neurons are mostly located in the caudal heart base within three intrinsic plexus ([57, 70], see sections II.2.2 and II.2.3.2.). In order to assess a possible preferential anatomical distribution of the expression, the collected hearts were dissected to obtain three samples: RA, LA, V (see section III.6.2.3.).

Evidence for construct expression were assessed in all the samples belonging to injected mice (figure 26). Both primer pairs provided results with a similar trend, showing stronger expression in the RA than in the LA, followed by the ventricle tissue. The anatomical distribution of the expression correlated with the most abundant location of the target cells within the heart and was confirmed with two primer pairs in two mouse strains. In comparison to the ubiquitous GAPDH, in both mouse strains the gene expression of ChRmine and mScalet was far lower. However, only Cre-expressing target cells are able to express the opsin and the RFP; as the number of Cre-cells is considerably less than the number of cells expressing the housekeeping gene, those results were consistent with the expected expression frequency of the construct. Relatively to the GAPDH expression, the ChRmine expression seemed to be slightly higher than the mScarlet expression. Relative expression was similar for both genes, i.e. the values for both genes showed similar trend within one mouse. Noteworthy, mice showing a HR modulation under optical stimulation did not show a higher expression level as non-responsive animals.

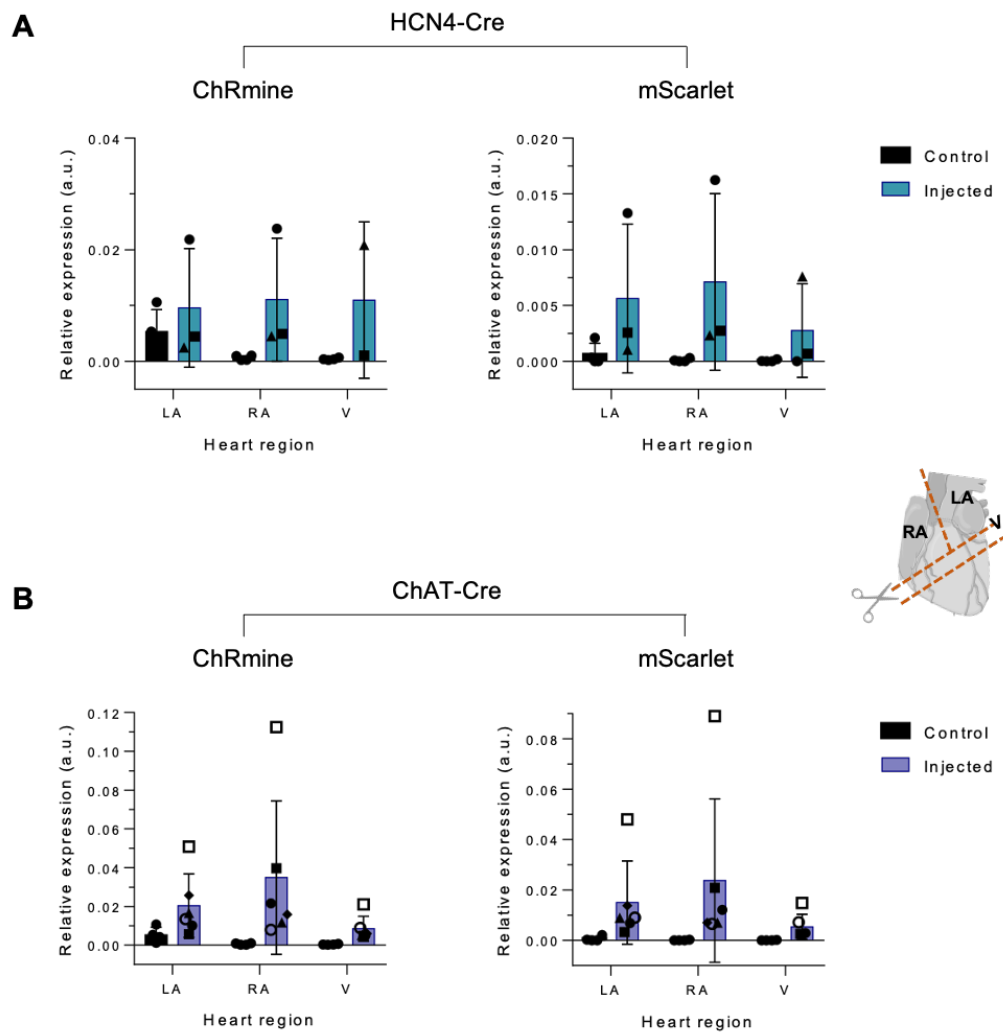


Figure 26 | Assessment of viral transduction and expression of opsin and RFP by qPCR

(A) qPCR results for HCN4-Cre mice for the opsin and the RFP, respectively, after systemic vector injection ($n = 3$). (B) qPCR results for ChAT-Cre mice for the opsin and the RFP, respectively, after systemic vector injection ($n = 6$).

Results normalized to GAPDH expression and expressed in arbitrary units (a.u.).

Hearts harvested maximum ten weeks after vector injection. As negative controls, hearts from naïve ChAT-Cre mice ($n = 4$) were harvested and processed the same way as the samples from mice receiving the AAV. Each heart was divided three samples: RA, LA, V. Samples from one animal are labelled with one symbol.

3. Light-induced PA-CXCR4 lymphocyte migration

3.1. Experimental design to attract PA-CXCR4 lymphocytes into the myocardium

Controlling lymphocyte trafficking relied on *in vitro* and *in vivo* steps performed in parallel to meet the need to produce phototactic cells as well as to bring light to the heart (figure 27). To begin with, lymphocytes were isolated from a donor mouse and cultured. The next day, the cells were transduced with a retroviral vector to render them photoactivable and incubated for three days to support their proliferation. Meanwhile, the device was surgically implanted on the LV. The modified cells were injected i.p. in

the operated mouse two days post-surgery and, after resorption, PA-CXCR4 cells entered the circulation. On the fifth day after device implantation, corresponding to the third day after cell injection, echocardiography was performed to assess heart function. Subsequently, illumination by maximal system power (10 W) was performed continuously during eight hours and finally, the organs were collected for analysis to assess light-induced migration in the illuminated tissues.

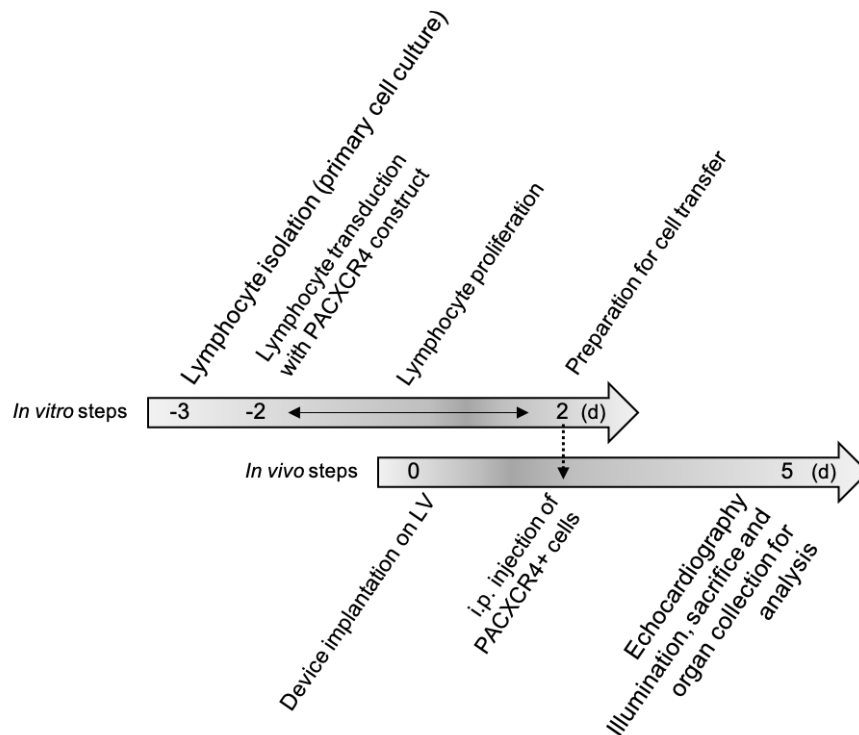


Figure 27| Experimental design to induce migration of phototactic lymphocytes into illuminated tissue

3.2. *In vitro* photoactivation of PA-CXCR4 lymphocytes

Chemotaxis is linked to an increased intracellular Ca^{2+} mobilization [97]. In PA-CXCR4 lymphocytes, chemotaxis was replaced by phototaxis. The latter was expected to trigger the same intracellular signaling cascade as chemotaxis, thus result in an increased intracellular calcium release. Before performing *in vivo* experiments, the ability of the photoactive cells to respond to light stimulus was tested *in vitro* by measurement of $[\text{Ca}^{2+}]_i$. Out of the two devices available (470 and 530 nm) with a close wavelength to the one described in the publication from Xu et al. (505 nm,[99]), we found out that the cells showed the greatest activation under illumination with the green μLED (530 nm). Maximal system power (10 W) to saturate the device, provided stronger activation – experiments performed with Dr. Murilo Delgobo (Immuno Cardiology Lab, CHFC). Assuming that scattered light could possibly reach several intrathoracic organs surrounding the heart, the responsiveness of the cells when exposed to a light gradient was assessed. Cells directly illuminated (PA-CXCR4 +++) showed the strongest activation by illumination with ≈ 0.5 -fold fluorescence compared to the positive control (figure 28). Cells in the direct neighbor well (PA-CXCR4 ++) had a slightly lower

activation, but still comparable to the directly illuminated lymphocytes. In contrast, the activation of the cells in the second neighbor well (PA-CXCR4 +) was \approx 6-fold lower compared to the wells receiving more light; nevertheless, compared to the negative control (dark +++), those cells showed activation after light-exposure. Negative controls contained the construct and therefore GFP as well. The measurements were normalized against the values obtained for negative controls, thus the normalized values corresponded to the fluorescence increase caused by calcium release upon cell activation and were not biased by GFP-fluorescence.

Thus, PA-CXCR4 lymphocytes responded to both, direct and indirect light *in vitro*.

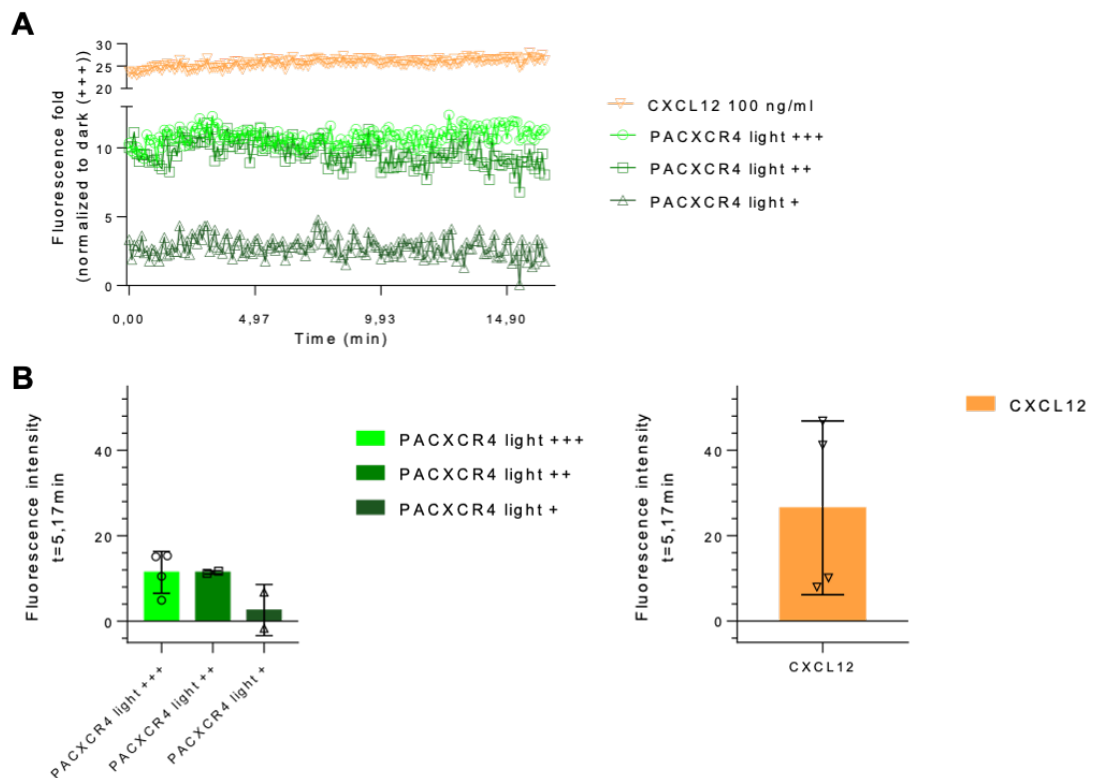


Figure 28| *In vitro* photoactivation of PA-CXCR4 lymphocytes

(A) Temporal evolution of fluorescence in cells after light exposure at different distances from the μ LED (pooled data from three experiments). (B) Representative fluorescence intensity to one time point ($t = 5,17$ minutes) after illumination.

Exposure parameters: μ LED: 530 nm, 10 minutes, 10 W; CXCL12: positive control ($n = 4$); PACXCR4 light +++: cells directly illuminated ($n = 4$); PACXCR4 light ++: cells ≈ 1 cm from the light source ($n = 2$); PACXCR4 light +: cells ≈ 2 cm from the light source ($n = 2$); dark +++: negative control, modified cells without illumination ($n = 3$).

3.3. Visualization of intrathoracic light scattering

Intrathoracic LED implantation has never been described before. To gain better insight into the illumination of the thoracic cavity, a whole mouse was subjected to a clearing protocol. The different tissues became gradually transparent and provided better understanding of the intrathoracic illumination pattern *in situ*. *In vitro* experiments (see section IV.3.2.) provided strong evidence for light activation of the cells even by indirect illumination, meaning that lymphocyte migration may also occur in tissues indirectly exposed to the light. Based on that information, we decided to figure out, which intrathoracic organs could possibly be reached by the scattered light in order to analyze

them too. The device pointing cranially illuminated preferentially the cranial and middle mediastinum with an illumination gradient appearing to be brighter on the left thorax side and decreasing towards the contralateral side (figure 29, A). Besides the directly illuminated heart, the observations made in the CUBIC-mouse led us to harvest the lungs and the thymus. To assess an accumulation of PA-CXCR4 in relation to the light exposure, illuminated and dark tissues were processed individually and compared to their respective opposite side during analysis. Since the device was implanted on the LV, the left part of the organs was always associated to the illuminated side while the right part referred to the dark region of the organ (figure 29, B). In the case of unpaired organs (heart and thymus), the samples were dissected and divided into equal portions close (left), respectively far (right), from the μ LED, while the paired lungs were merely cut at the hilum and differentiated in “left” and “right”.

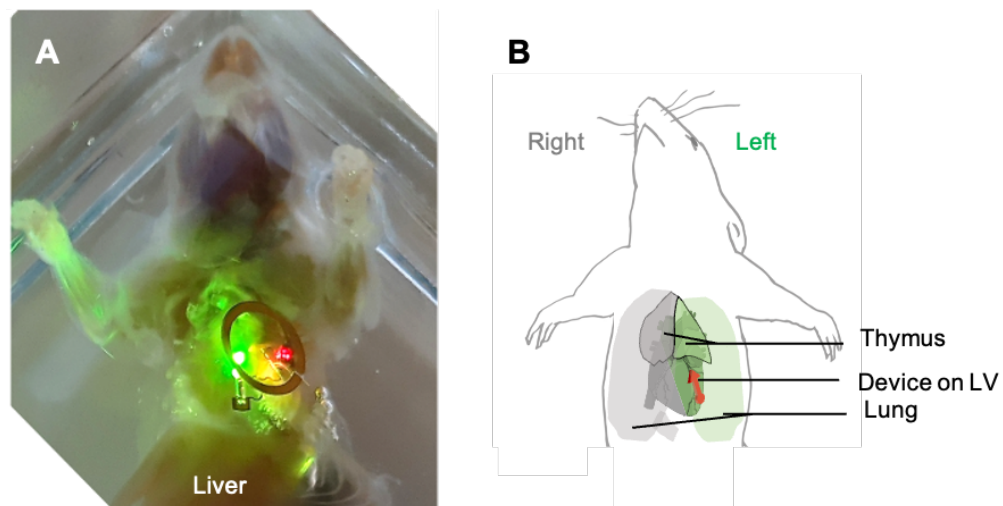


Figure 29| Intrathoracic light diffusion pattern after whole-body clearing

(A) Whole mouse in ScaleCUBIC-1-solution (d8) with turned on device for in situ visualization of light scattering. (B) Schematic organ division in illuminated (left) vs dark (right) side.

3.4. *In vivo* migration of PA-CXCR4 lymphocytes

FC analyses were performed to assess a preferential migration of the cells into illuminated parts of the collected organs. The experiments were repeated and the tissues showing positive accumulation of the modified cells in FC-analysis were processed for LSM in order to visualize the three-dimensional distribution of the PA-CXCR4 cells within the illuminated tissues. The distinction between left (close to the LED) and right (opposite side) side of each organ was made for all the analysis as described above (see section IV.3.3.).

3.4.1. Flow cytometry-based detection of PA-CXCR4

FC analysis was used to quantify the accumulation of photoactivable cells within the harvested tissues. The absolute number of modified cells per mg tissue was determined to provide indication about the density of the PA-CXCR4 normalized to the organ size. The number of photoactivable CD4⁺ lymphocytes in comparison to the total number of

CD4⁺ lymphocytes (PA-CXCR4⁺/CD4⁺-ratio) was used to confirm that the modified cells migrated into the illuminated tissue because they were attracted by the light but not by any inflammation reaction that would activate the CD4⁺ receptor still carried by the modified cells.

In each mouse, the spleen, as filter for the circulating blood [220], was taken as a baseline to assess whether the cells could be found on the illumination day in the mice. PA-CXCR4 lymphocytes were present in all the analyzed spleens, indicating that the transferred cells survived and still circulated three days after their i.p. administration into the recipient mice. Their number was proportional to the number of injected cells. Indeed, two of the negative controls received 3.5×10^6 instead of 5.0×10^6 PA-CXCR4, thus showed a lower number of circulating modified cells (figure 30, A).

In the heart, compared to the dark and the negative controls, no cell migration into the left side of the organ (LA and LV) was visible (figure 30, B). Moreover, no difference between atria and ventricles was reported. Moreover, the results were similar to the negative controls. Inflammation related to the procedure did not influence the cell distribution, regardless of the illumination status.

In comparison to the heart, a higher number of cells was found in the lungs (figure 30, C), however, no significant accumulation in the left, compared to the right lung was assessed. Illuminated mice and negative controls showed results in a comparable range for the lung.

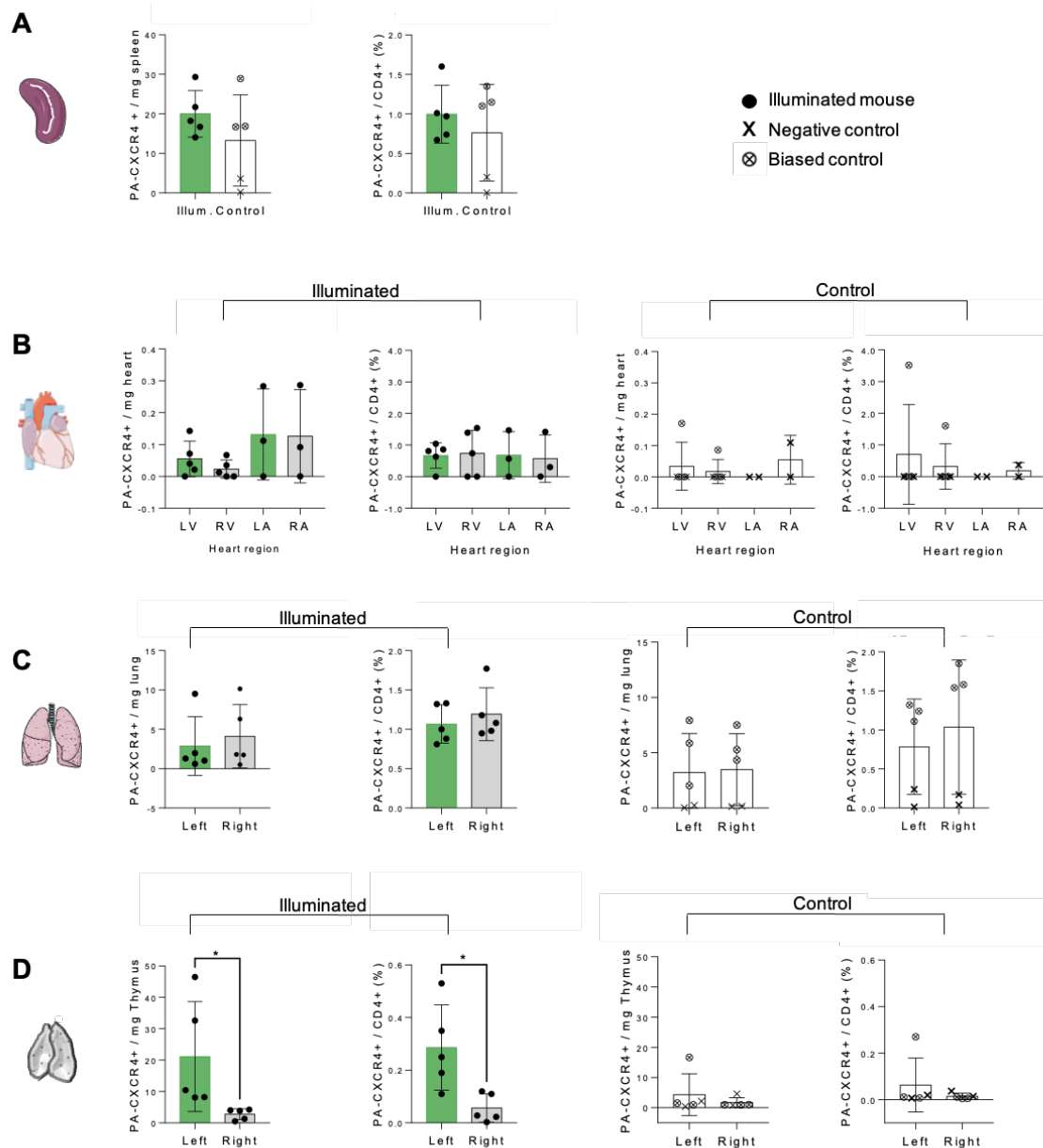
In the thymus a significant difference between the left and right thymus lobe was visible (figure 30, D). Both, the number of photoactivable cells per mg (mean \pm SEM: thymus light = 21.2 ± 7.83 ; thymus dark = 2.78 ± 0.78 ; $P = 0.048$) and the number of photoactivable cells per total CD4⁺ lymphocytes (mean \pm SEM: thymus light = 0.29 ± 0.07 ; thymus dark = 0.057 ± 0.024 ; $P = 0.017$) were significantly higher in the left thymus lobe, close to the μ LED. In contrast, the modified cells did not preferentially accumulate in the left lobe of control animals and both regions of the organ showed similarly low number of modified cells. The number of PA-CXCR4 cells in the right thymus lobe of illuminated mice was in the same range as in negative controls.

In some mice, the device broke after implantation and the μ LED was not able to shine. Those mice were added to the control group as “biased controls” but analyzed separately and depicted with another symbol among the control animals (figure 30, legend). In one mouse, the device stopped working after around five hours of illumination. The organs were collected at the end of the regular illumination duration, meaning that the organs remained unexposed to light during three hours before processing. This animal showed a higher number of PA-CXCR4 cells than the other control mice with an accumulation of modified cells, comparable to the illuminated mice for the thymus.

In summary, the transferred cells were found in the spleen, thus engrafted in all the recipient mice. Among the collected intrathoracic organs, the left thymus lobe, close to the μ LED, showed several evidence for light-induced PA-CXCR4 migration. The significant higher number of cells in the left illuminated lobe compared to the right one for both, absolute number and PA-CXCR4⁺/CD4⁺-ratio, indicated that the cell migration was induced by light and not due to activation of the CD4 receptor. Furthermore, the

number of modified cells found in the right (dark) thymus of illuminated mice, was comparable to the number found in both lobes of the negative controls. Taken together, those results demonstrated that the migration of the transferred cells was triggered by light. The observations made in the control mice indicate that cell engraftment required a minimal exposure time to light and may be proportional to the illumination duration.

Figure 30| Comparative FC analysis of left and right organ sides of illuminated and negative control



mice

(A) Photoactivable cells in the spleen taken as a baseline and reference for the systemic distribution of immune cells. PA-CXCR4⁺ per mg tissue and per CD4⁺ in illuminated and negative control mice (B) in the heart, (C) in the lung and (D) in the thymus.

Illum.: illuminated; control: negative control.

Illuminated mice (n = 5) underwent the surgery, cell transfer and eight hours constant illumination by 530 nm, 10 W; negative control mice (n = 5) underwent surgery and cell transfer, one of them partial illumination. “Left” corresponds to the organ region close to the μ LED; “right” corresponds to the contralateral organ region.

3.4.2. Spatial distribution of PA-CXCR4 in the illuminated thymus

FC analysis provided clear evidence for an accumulation of photoactivable cells into the left illuminated lobe of the thymus. LSFM enabled to evaluate the light-induced distribution of photoactivable cells labelled with a fluorescent antibody in three-dimensions within the thymus. First, we performed a staining control, in order to characterize possible unspecific binding of the antibody with background structures; next the illuminated tissues were processed the same way, each lobe separately.

For visualization, autofluorescence was displayed in cyan and was contrasted with the signal corresponding to the cells (anti-GFP Alexa 647) depicted in magenta. The overview images provided information about the shape and the general distribution of the cells, while the zoomed images enabled to magnify areas of interest. Both, staining control and illuminated thymus appeared with a diffuse, homogenic granularity and defined contour (figure 31).

Staining control to assess the antibody specificity

In order to differentiate the true signal from possible cross-reactivity of the antibody against GFP with the background, we performed a staining control with the thymus from a naïve mouse, which neither received cells nor underwent illumination.

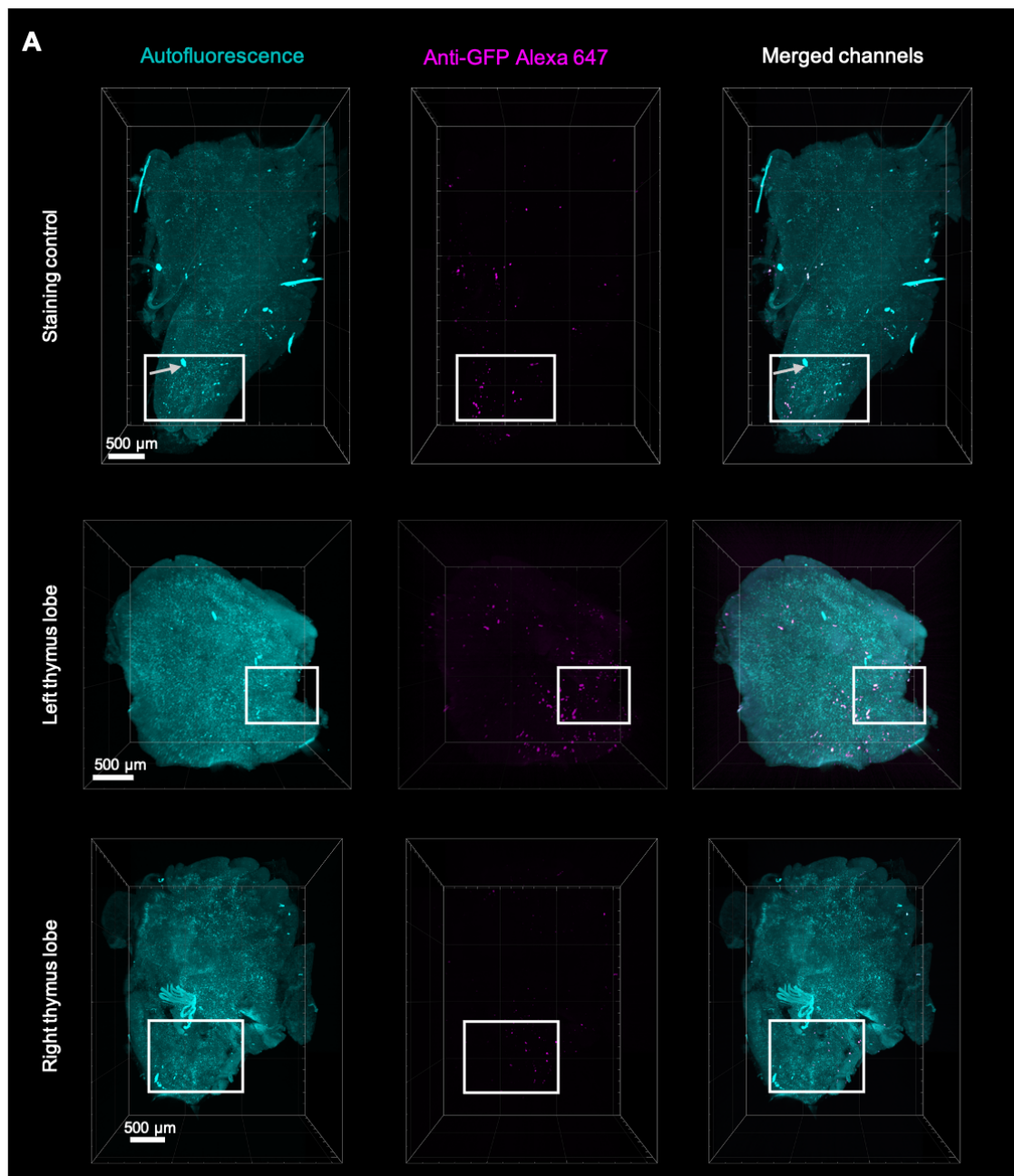
The autofluorescence channels displayed bright signals (grey arrows in figure 31, A, staining control), some of them had an elongated shape, which corresponded to impurity stuck in the tissue or on the surface during sample processing. The mouse did not receive cells, however, the channel corresponding to the GFP-staining presented positive signals. Moreover, the overlay of both channels displayed white events (red arrows in figure 31, B, staining control) at the localization of those false signals, highlighting that the latter corresponded to background staining and indicating that the fluorescent antibody bound to unintended antigens present in the tissue. Those non-specific signals appeared heterogenous, with irregular contour and diverse sizes. Nonetheless, the staining control provided useful information about the shape of non-specific background staining and this knowledge was helpful for image interpretation of the illuminated thymus.

Histological distribution of photoactivable cells within the thymus after illumination

Regarding fluorescence intensity, staining control and illuminated thymus lobes showed similar characteristics in both channels, autofluorescence and photoactivable cells. Unspecific signals with the same characteristics as observed in the staining controls were present in the illuminated organs as well (red arrows in figure 31, B, left and right thymus lobes). Besides those events, in both lobes, sparse positive labelling of small, round events was visible in the channel corresponding to the photoactivable cells, but was absent in the autofluorescence channel and did not appear white in the merged channels (green arrows in figure 31, B, left and right thymus lobes). Compared to the non-specific staining observed in both, the illuminated mouse and the staining control, the small events had a spherical shape with a smooth contour and rather homogeneous size (diameter $\sim 10 - 20 \mu\text{m}$). Only those small signals represented true positive staining, thus cells attracted with light into the illuminated thymus. Moreover, the number of such events was subjectively higher in left thymus lobe (figure 31, A), closer

to the light source than in the right one. This distribution is also visible in the three-dimensional organ videos (see digital appendix: video 2 and 3, left and right thymus lobe, respectively). Hence, the distribution of the cells correlated positively with the light exposure gradient assessed in the CUBIC-mouse (see section IV.3.3.). Due to processing steps, shrinking and rotation, it was possible to differentiate neither the cranial pole from the caudal one, nor the dorsal surface from the ventral one. However, in the right thymus lobe (figure 31, B), the positive signal remained localized in one region of the organ, likely corresponding to an area where the limit of light intensity required to initiate the migration of photoactivable cells was reached.

Overall, the histological observations confirmed preferential migration of the cells into the light-exposed thymus lobe, and therefore reinforced the FC findings.



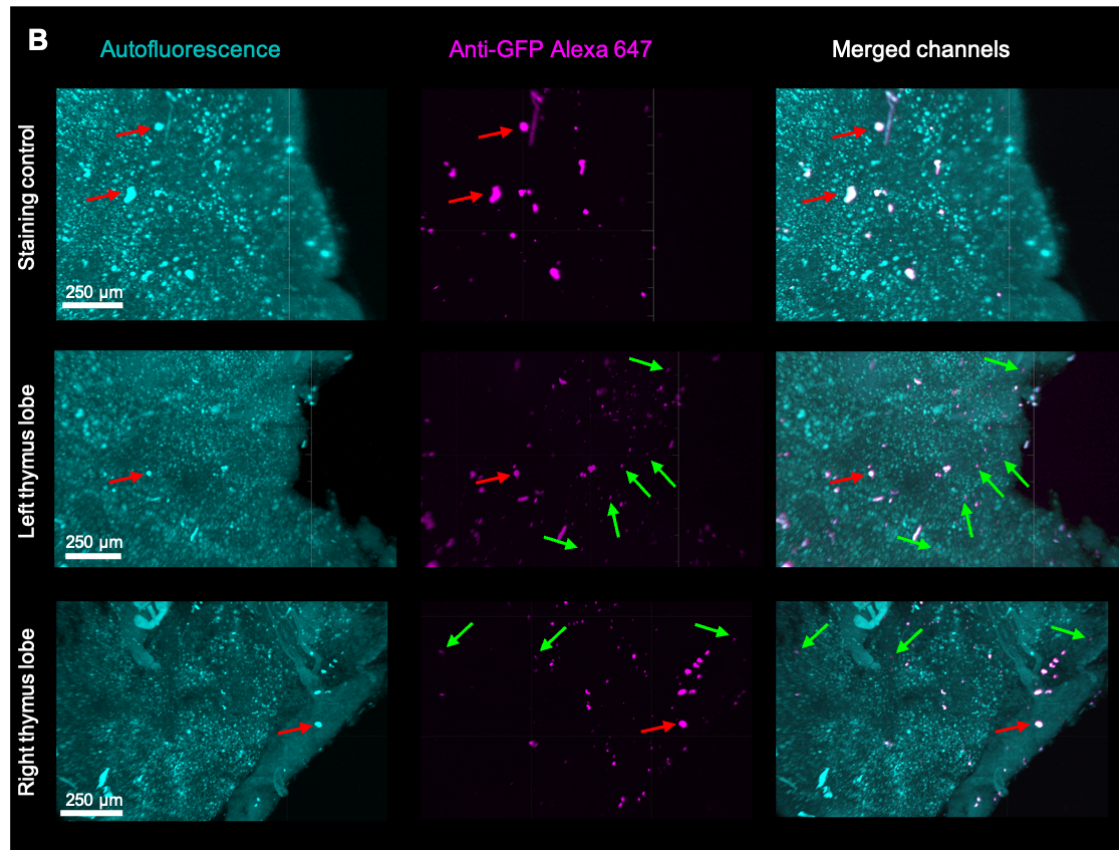


Figure 31 | Morphological distribution of PA-CXCR4 in staining control and illuminated thymus

(A) Overview and (B) magnification of the staining control as well as illuminated left and right thymus lobes after staining, clearing, imaging and three-dimensional reconstruction.

The region within the white square was magnified and represented below the corresponding image.

Grey arrow: impurity; green arrow: positive signal corresponding to photoactivable cells; red arrow: false positive signal appearing white in the merged channels.

V. DISCUSSION

Cardiac optogenetics is an emerging field in the life sciences, especially in cardiology. So far, cardiac optogenetics has never been applied in freely moving animals. The establishment of models for cardiac optogenetics in freely moving mice was composed of several milestones. Starting with the choice of appropriate opsin/wavelength combinations depending on the purpose, the device then had to be adapted for surgical implantation on the heart. A sophisticated implantation procedure was developed to bring light to the beating heart on both, left and right ventricles. Once the technical bottleneck was overcome, two distinct arms of the project developed. One goal was to manipulate intrinsic heart cells belonging either to the ECS or cholinergic ganglia in order to achieve HR modulation. The other aim of this work was to control trafficking of extrinsic lymphocytes by light in the heart. Both approaches seek to better understand the central role of heart and its influence in organism maintenance in healthy and pathological contexts.

1. Adaptation of wavelength and device to the purpose

1.1. Choice of the wavelength

Weighing the pros and the cons to choose an appropriate wavelength for optical stimulation was crucial and required to make a compromise in either penetration depth or energy. Numerous structures containing endogenous chromophores (hemoglobin, flavin, melanin) prevent light progression deep into the tissue. Moreover, light with longer wavelengths penetrates deeper in the tissue but is lower in energy; conversely, the shorter the wavelength, the less the tissue penetration but the higher the energy [111]. Besides wavelength, tissue penetration is also influenced by the size of the light source, its proximity to the target as well as its power [113, 114]. The latter decreases with increasing tissue thickness [115] (see section III.2.1.; figure 6). The heart is perpetually beating and perfused by blood; besides, it presents dark and dense tissue properties. Therefore, proper illumination of the myocardium to achieve opsin activation was challenging.

SAN and cholinergic cardiac neurons are both present in or around the RA. The structures of interest are located within the myocardium, thus providing a strong argument for the use of long wavelength, and motivating us to use focused illumination of the RA with orange (590 nm) or red (630 nm) light. The chosen wavelength was able to activate the red-shifted opsin ChRmine which regenerates rapidly after activation and is highly sensitive [117]. Indeed, transcranial activation of ChRmine up to a depth of seven mm in brain tissues has been described previously [160]. We therefore deduced that sufficient activation of target cells in the heart by illumination with the orange and red μ LED was feasible.

The experiment for light-induced migration of photoactivable cells was primarily designed to attract the modified cells into the left ventricle and evoke their intramural distribution. The photoactivable construct integrated into CD4⁺ lymphocytes derived

from the bovine rhodopsin [99] and showed best responsiveness after exposure to a 530 nm- μ LED *in vitro* (see section IV.3.2.). Therefore, the same wavelength was used for *in vivo* applications.

Working with light allows a broad panel of stimulation parameters, yet can represent a double-edged sword; indeed, determination of optimal illumination properties is challenging and requires compromises to select the best fitting light. Different tools were put together and tuned to make their combination become a working system to serve different purposes. To manipulate the HR, the choice of the opsin could be adapted to the wavelength while for manipulation of cell trafficking, the wavelength was adapted to the available opsin. Nonetheless the major question regarding the capacity of tissue penetration of the used wavelengths still needs to be solved and would confirm that the target structures can be reached by light. For instance, the use of the proto-oncogene c-FOS, a marker of neuronal activation which also increases by noradrenergic activation of cardiomyocytes [221, 222], could be used to map the light scattering in the heart. Thus, the activation of neurons distributed in the heart, and therefore the light penetration, could be assessed via immunohistology. Determining the penetration capacity of the used light would enable to set the framework of future studies.

1.2. Choice of the device and adaptation for intrathoracic implantation

By establishing a model for cardiac optogenetics *in vivo*, we strove to find a system that would minimally restrict the mice behavior, hence prevent the influence of external factors on the studied parameters. The NeuroLux system [116] (see section III.2.2.) enabled a wireless activation of the μ LED while illumination intensity and frequency could be set remotely via the provided software. Thus, minimal interference with the mouse undergoing experiments was ensured and perturbation of parameters, such as the measured HR, was avoided. The chosen μ LED was able to deliver light power at least as high as previously published for optogenetics applications ([11, 118, 119] and reviewed in [7]). The light output depended on the angular orientation between the coil and the antenna [116] being the highest when the coil remained parallel to the antenna and therefore the cage bottom. After fixation of the coil in the subcutaneous pocket on the thorax, the coil was positioned parallel to the antenna when the mouse was standing on its four limbs, walking or resting in prone position. Since the mice could freely move, they remained more or less in such postures; however, some of them tended to spend more time in a rearing position which did not impede device shining. Indeed, a control light on the coil indicated that the μ LED was operating in raised position as well. According to the device description, a 60° angle between antenna and coil would reduce in half the light output. This information should be kept in mind for data interpretation.

The device was modified with two suture threads to ensure a durable and precise orientation of the μ LED after its implantation on the beating heart (see section IV.1.1.). Using its flexibility and stretchability, the device was implanted in a way that the light emitting part could remain close to the target region, whereas the larger coil, which could not stay inside the thorax due to the limited space, was secured subcutaneously (see section IV.1.2. and digital appendix, video 1). The device was developed for brain surgeries where the coil is meant to be fixed on the skull. Some devices broke after

implantation. This could be related to the high mobility of the thorax compared to the skull, applying excessive strain to the device. Broken devices could be explained by a manufacturing defect too.

Overall, device modifications were achieved to adapt it to the needs of an intrathoracic implantation. The changes did not impair the light emission by the μ LED and the wireless activation of the device ensured minimal interferences with the movement of the mice during optogenetic stimulations.

2. Surgery

A fundamental prerequisite for both, optical HR modulation and control of lymphocyte trafficking, was to bring light to the heart. The surgical method was developed on both heart sides for a flexible adaptation to the illumination purpose. Implantation of the device was tolerated and did not impair the heart function.

2.1. Development of a novel surgical technique to illuminate the heart in freely moving mice

Accurate illumination with minimal loss of light intensity was required. To place the μ LED as close as possible to the target cells, the device was directly attached on the myocardium in two points (see section IV.1.2.). Direct anchorage on the heart requires thoracotomy, thus represents an invasive procedure, but was necessary to enable illumination of the cells of interest with the maximal light power and intensity and avoid energy loss. The technique to secure the adapted device on the beating heart, allowed to place the LED in the desired orientation and preferentially illuminate regions of interest. Implantation of the device was successfully performed on both, left and right ventricle, following the same protocol but in a reversed mirror manner. No mouse needed to be euthanized for burden caused by the implanted device. Furthermore, no postoperative mortality was observed. Since heart beats were regular and strong and the mucous membrane color showed proper perfusion and oxygenation, the fact that mice did not wake up was likely due to anesthetic complication and dyspnea. Massive bleedings after ventricle perforation or vessel damage happened, but were rare and expected in view of the challenging aspect of the procedure. Bleeding and mortality were more frequent on the RV, because of the thinness of the RV wall. Moreover, the surgery was first established on the RV and the mortality decreased with experience. Thus, the higher mortality after procedure on the RV is likely due to anatomical properties but also slightly biased by the development of manual skills. In comparison, after MI induction by ligation of the LAD, 50-60% of the LV wall can be infarcted [223] and a mortality rate between 37-50% was reported [224]. Morphological differences between mice cannot be foreseen and accessing dorsal regions of the heart remains difficult due to blood vessels, lung and mediastinal structures. Although the method presents some anatomical limitations, it can be used on both ventricles and, through orientation and rotation of the device, bring the μ LED in immediate proximity of the region of interest.

Slight displacements of the device during mice movements cannot be excluded and represent a limitation for the reproducibility of illumination.

2.2. Surgery effects on general condition, heart structure and heart function

Behavioral changes in operated mice were sometimes observed in the first 24 hours following the surgery and were related to side effects of the surgical intervention. More striking was the weight loss after left or right ventricular implantation (see section IV.1.3.1). Bodyweight loss after procedure on the LV was more pronounced than after implantation on the RV. Indeed, mice operated on the RV lost in average 2.9-fold less weight compared to mice operated on the LV. Weight gain two or three days after device implantation on the RV, respectively LV, was observed after both surgery types. Due to a longer experiment duration, mice implanted on the RV were kept up to eight weeks after surgery and showed continuous weight gain until the trial came to its end. According to the protocol, experiments with mice operated on the LV ended before the animals had enough time to recover their initial bodyweight, but the bodyweight curve showed a similar trend to the one describing the weight evolution of mice operated on the RV. Hence, it is likely that the mice operated on the LV would completely recover after a few more days. Differences in weight recovery may be related to the surgery type (RV vs. LV), indicating that the left ventricular implantation is less tolerated in the acute phase after the surgery compared to the procedure on the RV. Nonetheless, the differences in weight loss can also be explained by the use of genetically different inbred mouse strains and sexes. Indeed, males and females with B16-background underwent right ventricular implantation, whereas wildtype Balb/c males were implanted on the LV. Balb/c mice are known to be more emotive and sensitive to stress than B16 mice [225, 226]. Moreover, male and female display differences in pain perception and drug metabolism, but sex has less influence on the sensitivity to pain than the strain (reviewed in [227]). The weight loss observed in all the mice subjected to surgery is certainly related to postoperative pain, but also to the side effects of analgesic medication with opioids as nausea and reduction of food intake [122]. Buprenorphine was injected for perioperative pain treatment twice a day during three days, starting at the surgery day. Repeated restraining for drug administration is known to induce handling stress resulting in a decreased food intake. This burden can be diminished by sustained release of the drug [228, 229] and should be considered in future experiments.

Scar formation was assessed with Masson's trichrome staining procedure on d5, corresponding to the maximal experiment duration for mice operated on the LV. Hence, for a fair comparison, tissue damage was assessed on d5 after both implantation types, right or left ventricular. Histologically, reparative fibrosis was assessed at the device attachment points and was similar on both heart sides (see section IV.1.3.2). The trauma inflicted by the suture perforation resulted in scar formation driven by myofibroblasts, whose proliferation peaks four days after injury [230]; thus, fibrosis already occurred five days after surgery when the tissues were stained. Although the staining was performed for several layers through the heart, scar formation was not precisely quantified. Yet, tissue damage did not spread in the surrounding areas and remained

localized around both implantation sites corresponding to the anchorage of the device. Tissue damage represented far less than 30% of the left or right ventricular wall, thus adverse remodeling was unlikely [217, 218]; nonetheless, dynamic assessment of the heart function was performed with echography.

Echocardiography is a standardized method to assess heart function in rodents (reviewed in [133, 134]). For better reproducibility and comparison, imaging and analysis were performed by one person and also compared to results in naïve mice. Measurements enabled to determine left as well as right ventricular function and provided an overview of heart activity. Due to so-called ventricular interdependence, the left ventricular heart function has an impact on right ventricular function and *vice versa* [231], meaning that assessment of the functional state of one ventricle indirectly provided information about the function of the other one. Results confirmed that heart contractility (FS, EF, TAPSE, pulmonary artery flow) and relaxation (E/A ratio) were preserved after device implantation on the LV and RV (see section IV.1.3.3.). In addition, the myocardium looked homogenous and showed strong and regular contraction similar to the measurements acquired before surgery. Since HR influences the cardiac function, during imaging, mice were under anesthesia and their HR was kept in the lower physiological range between 450 ± 50 bpm [133]. Whether heart function was impaired under physical activity and increased HR, was not investigated but could be addressed in complementary experiments. Adrenergic drugs with positive chronotropic and inotropic effect could increase HR during echocardiographic measurements and help to further investigate the effect of the surgery. Nonetheless, the recovery and survival of the mice for at least eight weeks, speaks for cardiac tolerance in stress situations and therefore preserved heart function by increased HR.

Overall, the present work describes a breakthrough surgical technique to illuminate the heart and the thoracic cavity in freely moving mice. Implantations on the left as well as on the right ventricle were tolerated and offer the possibility to adjust the procedure in order to illuminate target cells present in different heart region.

Mice implanted with the light-emitting device, either on the left or the right ventricle showed a transient weight loss followed by bodyweight increase. If the experiment duration was long enough, mice operated on the RV gained back the lost weight, or even had an increased body mass compared to the initial day. We assume that mice operated on the LV would show a similar weight evolution if the experiment would have lasted longer. The developed surgical technique led to tissue damage with associated repair at the respective implantation points, but did deteriorate neither the systolic nor the diastolic heart function. However, assessment of the scar extent and heart function under tachycardia were not performed.

3. Optical heart rate modulation via intrinsic heart cells

Over the past ten years, cardiac optogenetics gained attention but has not been developed in freely moving mice at the level of the heart so far. Our strategy to optically pace the

heart relied on several milestones. First, the opsin expression in the cells of interest was achieved with an AAV. Second, the shining device was implanted using the method developed on the RV to precisely illuminate the regions of interest. Third, ECG were measured to assess the effect of the illumination protocol on optically stimulated target cells. Last but not least, qPCR was used to verify opsin expression and confirm that the observed effects were related to the activation of the light-sensitive protein.

3.1. Rationale and experimental design for heart rate modulation

Anxiety disorders show comorbidity with heart diseases [232, 233]. Optogenetics provides a powerful tool for modulation of cell activity with high spatiotemporal resolution and could be used to dissect the interactions between organ systems by influencing precisely selected circuit components. The characterization of information flow between heart and brain in physiological and pathological states would enable to understand neuropsychiatric mechanisms associated with cardiac function.

Specific spatial expression of the opsin was achieved with a *Cre/lox* system. Two mouse strains with the Cre recombinase expression linked to the cells of interest, either belonging to the ECS (HCN4-Cre) or cholinergic ganglia (Chat-Cre), were used. Respectively, two AAV capsids were used to preferentially deliver the floxed construct to the target cells. A ubiquitous promoter drove the expression of red-shifted and highly sensitive opsin (ChRmine) under Cre-conditionality (see section III.5.2.). Thus, opsin expression was spatially bound to the target cells with different biological functions. The use of mouse strains which express the opsin constitutively would represent a safer method than employing a vector dependent *Cre/lox* system. This alternative would enable to overcome hurdles and variabilities related to the use of a viral vector which are related to production steps, way of delivery, administrated amount and choice of the different construct components (capsid, promoter, opsin) (reviewed in [35]). However, mouse strains expressing ChRmine in HCN4- or ChAT-cells are not available yet.

The choice of a red-shifted opsin, ChRmine, was supported by the deep location of the target cells within the heart which could better be reached by longwave light. Optogenetics studies mainly used the blue-shifted ChR2 to achieve actuation of heart cells in heart preparations [52-54]. Thus, making the compromise to use shorter wavelength with lower tissue penetration but higher energy represents another promising constellation.

Previous works principally describe the stimulation of cardiomyocytes to evoke ectopic myocardial contraction which relies on the electrical coupling between the cells [53, 234-237]. Instead of initiating ectopic heart beats, we sought to optically manipulate the SAN, the autonomous pacemaker [57]. The experimental design aimed to modulate the HR by direct stimulation of components of the ECS (HCN4 cells for HR increase), or in an indirect way via activation of cholinergic cells which stand in close interaction with the SAN (ChAT cells for HR decrease) [238]. Thereby, heart contraction could directly be modulated at its origin and therefore result in a physiological propagation of the depolarization wave through the myocardium.

3.2. Focused illumination of the region of interest in freely moving mice

Optogenetics offers the advantage of precise temporal modulation through the exact control of the on- and offset of the light pulse within milliseconds. In comparison, the use of drugs, does not provide such an accurate regulation of the HR. Indeed pharmacokinetics are only partially predictable due to different individual metabolization [239] and no possibility for immediate antagonization. Moreover, current electrical strategies for stimulation present drawbacks such as hyperactivity, production of free radicals at the electrode, tissue damage and inhomogeneous depolarization of the functional syncytium [240, 241].

Both, SAN and intrinsic cholinergic neurons, are located in the RA or in its surrounding area. The opsin was expressed in those specific cells; thus, the device was implanted on the RV and the μ LED angled towards the RA. Focused illumination added spatial specificity to the method. However, experiments were performed in freely moving mice and on a continually beating organ, what likely induced slight displacement of the device. As a consequence, it may have led to inappropriate illumination of the very specific region of interest. Furthermore, the coil inclination influences the light output (see section V.1.2.) and adds variability to the light exposure during experiments. To compensate device shifts and inconsistent light output, μ LED covering a larger area and with greater light output could be developed.

A previous study demonstrated that higher light intensities were required to stimulate ChR2 in myocytes within the atria [52], but expression of ChRmine in the heart was never reported before. ChRmine activation was described for illumination with 585 – 650 nm. It was not clear whether it would be preferable to use higher energy at the expense of tissue penetration (orange), or rather favor better tissue penetration at the expense of light energy (red). That is why orange (590 nm) and red (630 nm) devices, which both could potentially lead to HR modulation, were implanted in the mice.

Due to the light-attenuating properties of the myocardium, light power was set at its maximum during all the experiments (10 W). Parameters as light power, pulse width and frequency, influence the experiment outcome [54] and offer infinite ways to set the stimulation. Finding out the optimal stimulation settings definitely represent a major aspect of cardiac optogenetics and requires additional experimentation.

3.2.1. Modulation of the pacemaker activity of intrinsic cardiac HCN4 cells

HCN4-Cre mice were all implanted with an orange μ LED. Pooled and individual data did not show HR increase under stimulation (see section IV.2.2.1.). Opsin expression was demonstrated in all the mice, but no on/off-dependence or stimulation type-dependence was observed. According to the observations made in ChAT-Cre mice, the orange device might not be appropriate to evoke opsin activation.

The SAN triggers heart contraction which is transmitted to the AVN and finally spreads across the entire myocardium [57]. Besides its function for conduction of electrical pulses or even as secondary pacemaker, the AVN represents a protection mechanism by acting as filter for high frequency, thus is a barrier against arrhythmia originating in the SAN [242]. Therefore, the AVN could act as limiting factor for optical pacing of the whole heart by illumination of the SAN. However, the ECG traces did not present signs

of atrial fibrillation under optical stimulation, indicating that even if the stimulus could not pass the AVN-barrier, illumination did not initiate local atrial pacing. The chosen stimulation frequencies were beyond the physiological HR of mice in order to reach a possible ceiling effect. The stimulations could have induced refractoriness of the illuminated cells which may have been stimulated in too short intervals. Trials with lower frequencies could easily clarify this matter. Targeting directly the AVN could represent another approach to pace the heart; however, due to its localization in the septum, reaching it with light would be even more challenging and the stimulation would not propagate like a physiological heartbeat originating in the SAN.

3.2.2. Modulation of intrinsic cardiac cholinergic cells

Indirect modulation of the SAN function was performed by stimulating neurons forming a dense meshwork around the SAN and are predominantly cholinergic [243]. ChAT-expressing cells belong to the parasympathetic part of the ANS; therefore, through increase of the parasympathetic tone, reduction of the HR was rather expected than true pacing [244]. Stimulation parameters reproducing a HR in the lower physiological range were used as well as longer pulse durations and constant stimulation. In ChAT-Cre, both device types were implanted: two mice received an orange device and four received a red device. Only red μ LED devices induced a HR decrease in three different mice, which was on/off-dependent and stimulation type-dependent (see section IV.2.2.2.). Indeed, the constant stimulation, which was supposed to have the strongest effect, induced the most significant HR decrease. The switch of the relative position of the stimulations to each other during different recording sessions, was meant to highlight the possible effect of one stimulation type on another one, and the effect of recording time on the HR variability. No significant time/position-effect was assessed, but an increased HR variability over time was observed. During ECG recording sessions, the mice were placed in a new environment, leading to stress but progressively, they relaxed and their HR varied more. Once the animals relaxed, the heart appeared to react more sensitively to stimulation, thus responsiveness to light stimulus seemed to correlate with the adaptation to the environment. Nonetheless, the HR decrease observed under optical stimulation might be slightly biased by the general increasing HR variability in the course of the recording session and the high number of repetitions of the measurements. Moreover, the basal HR of the mouse also influences the results. Indeed, HR decrease is more pronounced when the basal HR is high, leaving a larger scope for the HR to drop. Conversely, if the basal HR is high, tachycardia would be harder to induce.

Although only mice implanted with the red μ LED showed a HR decrease, it cannot be excluded that those effects could also be achieved with shorter wavelengths. Moreover, not every mouse implanted with the red device responded with HR decrease under optical stimulation. As the opsin expression was verified in all the mice, the lack of consistency between the animals might be explained by the device shift during mouse movements. Slight displacements of the μ LED from the target area could impair the illumination of the opsins expressed in the region of interest, thus be an obstacle to focused illumination. The hypothesis of device displacement is further supported by the fact, that according to the qPCR results, mice showing a HR modulation do not

correspond to the animals with the highest ChRmine expression.

In summary, experiments should be repeated to draw further conclusion regarding the reproducibility, the influence of the wavelength and the stimulation type in both mouse strains.

Even if lower in energy, red light appeared to better reach the opsin and evoke an effect on the HR. Due to small animal numbers, an effect of orange light cannot be excluded. The implantation of red devices should be performed in HCN4-Cre mice to provide more information regarding the best fitting wavelength. Furthermore, experimental designs using shorter wavelengths represent complementary approach to address this question. Apart from the wavelength, additional stimulation parameters should be tested. Moreover, negative controls need to be subjected to the same illumination conditions in order to exclude that the HR changes rely on any side effect of the illumination such as potential tissue heating. As negative controls, mice would undergo exactly the same procedure and stimulation protocols, except that the viral vector would not contain the gene for ChRmine. Those negative controls would confirm that the observed HR modulations are exclusively based on optical stimulation of the opsin.

3.3. Verification of opsin expression in the target cells after systemic delivery

Intravenous injection of AAV particles provide consistent results *in vivo* [147, 156, 158] and appeared to be the appropriate delivery way to achieve homogenous distribution of the virus and reach, via the circulation, the areas of interest. Expression was verified by qPCR in both used mouse strains with two self-designed primers specific for the opsin and the RFP composing the construct (see section IV.2.3.2.). Both genes showed lower expression than the housekeeping gene but, as expression was expected to occur only in small cell populations, this finding was plausible. Moreover, the observed tendency for increased expression in the RA region followed by the LA and the ventricle base, correlates with the anatomical distribution of the cells of interest and reinforces the evidences for true opsin expression. Local virus administration into the ventricles is feasible, but leads to variable expression, and the vector remains localized around the injection site without spreading across the myocardium uniformly [144, 245]. Unless the vector can be precisely injected into the region of interest, gene transfer may not take place. Furthermore, direct injection in the atria remains even harder, due to the high beating frequency and wall thinness. Rather than risking to injure the heart by injection, gene painting, a technique for local gene transfer, puts the viral particles in contact with the epicardium for transmural gene delivery, and could represent another possibility for myocardial transduction [246]. Nonetheless, local injection as well as gene painting, require the access to the heart via thoracotomy and represent an additional procedure to the device implantation, hence longer or repeated surgeries. Again, using a mouse strain expressing the opsin in the target cells constitutively would be a safe and consistent way to circumvent viral delivery, but appropriate mouse strains are not available yet. Altogether, intravenous administration still represents a promising way for homogenous vector distribution to the regions of interest and is associated with less burden than local epicardial or intramural administration. Hence, the chosen approach put several tools

together which have been proved valuable in other organ systems like the CNS ([11, 247]; reviewed in [28]).

3.4. Conclusion: *in vivo* model for heart rate modulation

The coupling of optics and genetics defines optogenetics and was used to achieve HR manipulation with high spatiotemporal resolution. In a nutshell, Cre-dependent expression combined with focused illumination of the region of interest, provided spatial specificity. Opsin expression was confirmed by qPCR in both used mouse strains, thus providing proof of successful recombination in the target cells. The use of transgenic mouse strains expressing the opsin in the target cells would circumvent the variability linked to virus delivery and ensure spatial specificity as well.

Manipulation of the HCN4-pacemaker cells was not successful. Due to complex feedback controls and protection mechanisms, it remains unclear if activity of HCN4-cells can be overwritten by light in freely moving mice, in contrast to what has been described in *in vitro* experiments [50].

We managed to evoke light-induced HR decrease in ChAT-Cre, showing results which were stimulation-type dependent and were more pronounced under stimulation occurring later in the course of recording. The modulation of HR via manipulation of intrinsic cholinergic cardiac ganglia appears easier than to control the pacemaker cells, likely due to a more diffuse distribution of the former compared to the latter and different kinetics. In both cases, additional experiments with optimized illumination protocols regarding frequency, pulse width and light power, are needed to complete those preliminary observations and draw further conclusions.

Device displacement combined to the limited capacity of the light to penetrate the tissue represents a major hurdle to achieve opsin activation in the myocardium. Device shift after implantation represents a technical limitation occurring in both scenarios, HCN4 and ChAT stimulations. Illumination reproducibility could be improved by the use of a larger μ LED and higher power. Our results suggest that red light may be more prone to reach target cells in the dark myocardium and evoke HR manipulation. However, red light did not induce consistent HR modulation in all the mice. Experiments should be repeated in both mouse strains with the different wavelengths to draw further conclusion.

Those preliminary results need to be completed with additional experiments, but already provide strong evidences of the feasibility to modulate specific intrinsic cardiac cells. The data support that cardiac optogenetics can be a powerful tool to investigate and deepen the understanding of underlying heart function at the core of complex interconnected systems.

4. Optical T cell migration

The role of lymphocytes in myocardial healing processes has been studied and described as a dynamic process governed by successive leucocyte infiltrations into the myocardium [4]. Controlling lymphocyte trafficking was a multistep approach. Starting

with the engineering of photoactivable CD4⁺ cells, we next investigated the best light parameters to activate, and therefore polarize them for directional migration, *in vitro*. In order to visualize the light coverage during *in vivo* experiments, the intrathoracic illumination pattern was assessed in a transparent mouse model. Then, adoptive transfer of photoactivable lymphocytes in recipient mice was performed in order to conduct experiments in freely moving mice.

4.1. Rationale and experimental design for the migration of photoactivable lymphocytes

Cardiovascular diseases are the leading cause of death in humans worldwide and show increasing incidence in aging population [248]. It is known that CD4⁺ T cells play a cardioprotective role after myocardial infarction [4, 10, 249]. Having in mind to investigate the effect of lymphocytes in myocardial infarction models in later studies, we decided to provide CD4⁺ T cells with phototaxis. Based on the work of Xu et al. [99], we isolated and transduced CD4⁺ lymphocytes with a tailored PA-CXCR4-receptor (see sections III.7.1.2. and III.7.2.) in order to make them responsive to light, which was essential to guide the extrinsic cells into illuminated tissue. T cells are recruited to the inflammation site by travelling along a chemokine gradient [96]. Activation of the CXCR4 receptor by its natural ligand CXCL12, leads to accumulation of the cells into the “immunological synapse” [250]. In PA-CXCR4 cells, responsiveness to chemokines was replaced by light-induced activation; thus, instead of a chemokine gradient, we strove to attract cells along a light gradient using constant illumination.

Models for ischemic heart disease have been established in rodents with methods focusing on the LV by ligation of the left anterior descending coronary artery (LAD) or cryoinjury [106]. In the present work, photoactivable CD4⁺ cells as well as adapted device implantation of the μ LED on the LV were achieved and combined, hence providing a new a tool to study the effect of CD4⁺ cells after MI induction in further experiments.

4.2. Properties of *in vitro* photoactivation and intrathoracic illumination pattern

Prior to *in vivo* experiments, the responsiveness of the modified cells to constant illumination was verified *in vitro*. Intracellular calcium concentration was taken as indicator for photoactivation [97]. *In vitro* experiments demonstrated that the responsiveness of the cells was wavelength-dependent and correlated positively with increasing light intensity. The strongest effect was recorded after exposure to green light (530 nm) by maximal power (10 W); those settings were then used *in vivo*. Moreover, direct and indirect illuminated cells answered to light stimulation, indicating that scattered light may also be sufficient to induce cell migration *in vivo*. Subsequently, clearing a whole mouse provided insights into the intrathoracic illumination pattern after left ventricular surgery. The device was implanted *post mortem* and the mouse was immersed in clearing solution. Despite the fact that the conditions were not completely matching to *in vivo* experimental circumstances, observations made in this model enabled to visualize which organs could be reached by scattered light and precisely plan

the organ collection. Knowing from *in vitro* experiments that indirect light is able to activate cells, additionally to the heart, lungs and thymus, corresponding to indirectly illuminated organs, were collected too. Each organ was dissected in a left and right side, respectively close and further away from the light source and analyzed for the detection of PA-CXCR4.

4.3. *In vivo* migration of extrinsic photoactivable lymphocytes

Engraftment of the modified cells in the recipient mice was assessed with FC analysis, a high-sensitive method [251]. The spleen filters the circulating blood (reviewed in [220]) and was taken as baseline for the detection of photoactivable cells in the organism. The number of modified cells found in the spleen correlated with the number of injected PA-CXCR4 lymphocytes. Light induced migration was evaluated in the heart, the lungs and the thymus.

Besides from dividing the heart in illuminated vs. dark side, we analyzed whether tissue thickness would influence PA-CXCR4 migration by differentiating atria from ventricles. Independently from wall thickness, no PA-CXCR4 cells could be found in the directly illuminated heart, neither in regions close to the μ LED, nor in dark ones. Green light is high in energy but more absorbed by the tissue than long wavelengths. The light fitting for receptor activation may not fulfill the conditions to penetrate deeply into dark tissues like the myocardium. Adapting the PA-CXCR4 construct to longer wavelengths could overcome this hurdle and induce cell migration in deep and dark tissues.

The modified cells were found in the lungs, in both sides, without showing side-specific accumulation. In spite of detecting the cells in the lung, no preferential accumulation of the transferred cells into the light-exposed tissue was assessed, indicating that the presence of the cells in the lung was not attributable to illumination. To circumvent the “pulmonary first pass effect” after systemic injection [252], the cells were injected intraperitoneally. Nonetheless, once resorbed, the cells reached the circulation and passed through the lungs. Due to their increased size during blasting in cell culture (reviewed in [191]), part of the injected lymphocytes may have been trapped in the lung capillaries and could explain the findings.

Preferential accumulation of cells in the illuminated thymus lobe receiving indirect light was demonstrated in FC as well as LSFM analysis. The anatomical distribution of the photoactivable cells showing an increased accumulation in the left illuminated lobe compared to the contralateral side, demonstrated the phototactic migration of the cells in both, FC and LSFM. Moreover, the significant higher PA-CXCR4⁺/CD4⁺-ratio in the illuminated part of the organ is an additional proof of their light-induced migration. Undeniably, the ratio indicated that the cells were guided to the thymus by light and not through activation of the CD4 receptor due to inflammation related to the surgery. “Biased controls” in which the device broke, may indicate that the PA-CXCR4 cells need constant light to stay in the tissue. However, in one “biased control”, where the LED likely shined for a longer time period but broke before organ collection, cells could be found in a similar distribution as in properly illuminated mice. This “biased control” was considered, since it provided relevant information regarding the influence of

illumination duration on PA-CXCR4 cell migration. Indeed, it suggests that a certain amount of light may be required for a certain duration to evoke long-lasting accumulation of the cells in the illuminated area. Imaging the whole thymus with LSFM provided information regarding the spatial distribution of photoactivable cells within the illuminated organ. As demonstrated in FC, whole-mount preparations of the thymus showed an increased density of modified cells in the illuminated lobe compared to the dark one. The fact that the signal was not homogenous throughout the organ supported the evidences for light-induced migration into illuminated thymus areas. The accumulation of cells seemed to follow a gradient, being more important in the left lobe and decreasing towards the right thymus lobe. Thus, the distribution of the cells in the organ could match with the emitted light gradient. To distinguish autofluorescence from true signal was difficult, as the GFP present in the PA-CXCR4 construct, even after clearing, may show residual fluorescence in the same range as the organ autofluorescence [211]. Similar clusters which could have corresponded to light-induced cell aggregation, were identified in both, staining control and illuminated thymus, showing that the staining partially displayed unspecific structures. However, in the illuminated thymus, especially in the left lobe, an increased number of smaller events in the range of blasting T cell size (reviewed in [188, 189]) was detected. Thus, the histological findings were in accordance with the FC results, but image analysis is needed to make a comparative quantification of the cells in the different part of the organ. An objective differentiation of the true signal from the artifacts is crucial in order to subtract unspecific staining events from the real labelling. This could be achieved with machine learning and subsequent image analysis in order to quantify the number and the volume of the detected signal in illuminated vs. dark tissues. The use of another antibody, without cross-reactivity, could also solve the issue of unspecific signals.

4.4. Conclusion: *in vivo* model for optical control of lymphocyte migration

In summary, photoactivable cells were engineered, showed proof of light-induced activation and migration *in vitro* and *in vivo*, respectively. *In vitro* experiments showed that indirect illumination can be sufficient to activate the cells, and combined with the observations made in a transparent mouse model, we harvested the directly illuminated heart as well as adjacent organs receiving scattered light. PA-CXCR4 lymphocytes could neither be guided into the myocardium nor in the lungs with light, but the modified extrinsic cells were found in the thymus, displaying a preferential accumulation close to the light source. Repetition and complementary experiments need to be performed to precisely understand the relation between cell trafficking, accumulation and light exposure. It is also crucial to figure out the influence of light power and light penetration to achieve fine tuning. The responsiveness to green light could also be further investigated on “clear” organs such as submandibular salivary glands or lymph nodes which may have similar properties regarding light penetration as the relatively transparent thymus. On top of that, modifying the photoactivable construct and making it responsive to longer wavelengths could facilitate the cell migration into deeper and darker tissue layers of the heart and other organs. Indeed, modulating immune cell trafficking also represents a tool for immunotherapy by supporting the elimination of cancer cells for instance (reviewed in [253]).

Our results illustrate the feasibility of attracting extrinsic cells into tissues but highlight also the impact of tissue properties on light absorption. The principle of this method could be extended to further cell types and organs to better understand interactions and the role of the proliferation and recruitment of specific cell populations in homeostasis or in the context of diseases. On the other hand, instead of bringing light to the heart with an external light source, one could illuminate the heart from “within”, i.e., make the heart itself become an intrinsic bioluminescent light source. For this purpose, an enzyme, for instance the luciferase Rluc8 [254], would be expressed specifically in the heart using a promoter specific for cardiomyocytes and a cardiotropic AAV. Following transduction of the heart muscle and substrate application (colenterazine H), the reaction catalyzed by the enzyme produces a bioluminescent product [255]. The latter emits maximal bioluminescence at 540 nm [254] which is close to the wavelength used to activate our engineered cells, thus could attract them in the heart upon substrate application and concomitant bioluminescence emission. Experiments for this alternative approach are planned to further investigate cell migration towards the heart.

5. Translational outlooks and limitations of cardiac optogenetics

The intrinsic and extrinsic approaches described in the present work, emphasize the far-reaching potential of cardiac optogenetics in interdisciplinary projects. Cardiac optogenetics represents an emerging research area with noteworthy tools for high-resolution spatiotemporal cell control with light [256]. In addition, the availability of different opsins, which elicit either activation or inhibition of the target cells, as well as the use of optogenetic sensors to study cellular mechanisms *in vivo* (reviewed in [257, 258]), widens the scope of possibilities for tailored studies.

The heart links the function of different organ systems. Blood supply of the whole organism occurs through the vascular system coupled to the heart, thereby underlining the connecting role of this organ at the center of the intra-organism networks. Strong evidences for comorbidity between heart diseases, cognitive deficits [233] and mental disorders exist (reviewed in [2]). Furthermore, the relation between ischemic heart failure and depression-like behavior has been demonstrated in mice [232]; correspondingly, the prevalence of depression in heart failure patients is up to 51% (reviewed in [2]). Depression and heart failure were also associated with inflammation, but their interrelationship remains unclear [259]. Inflammatory markers are increased in patients with heart fibrosis [260] and atrial fibrillation [261]; the severity of the latter correlates with the anxiety level [262]. Other studies demonstrated that different lymphocytes can have beneficial and detrimental influence on myocardial healing (reviewed in [249]). Macrophages improve electrical conduction in the AVN [263], whereas neutrophils negatively influence the outcome during reperfusion after ischemic injury [264]. Taken together, heart, immune and nervous systems form a connected triad, influence each other and shape the general condition on a larger scale, highlighting the need to explore them in detail. Peripheral, and specifically cardiac optogenetics bears promise as tools to support this research effort in the future. However, the model for cardiac optogenetics as described in this work, presents technical, ethical and safety

limitations. The light power required to reach deep tissues may lead to adverse effects such as heating. Optical pacing of the SAN to initiate heart contraction through physiological electrical propagation of the depolarization wave, represents a tempting alternative to conventional pacemakers. The latter induce heart pacing by generating an ectopic heartbeat starting mostly in the ventricles and can sometimes lead to “pacemaker syndrome” with impairing side effects due to asynchronous atrial and ventricular contraction such as hypotension, dizziness and syncope [265]. However, an optical pacemaker goes along with opsin expression, thus gene transfer, which is an integral part of optogenetics. Gene and cellular therapy are promising treatments with translational and cross-species reach. Indeed, xenografted human cells were used as delivery vehicles to increase responsiveness to catecholamines in dogs [266] and local AAV injection containing an opsin enabled to partially restore vision [267]. However, the required opsin expression represents an ethical limitation for clinical applications. Moreover, we do not yet have enough hindsight about the bio-distribution and the long-lasting expression of opsins, as well as possible toxicity and oncogenicity [35, 268]. Hence there is still a long way to go until opsin delivery or administration of modified cells becomes democratized in patients.

Heart diseases are prevalent in mammals and share similar interspecies pathomechanisms. Indeed, heart failure, myocardial diseases and arrhythmia are described in horses (reviewed in [269]). Moreover, hypertrophic cardiomyopathy associated with extensive cardiac remodeling, congestive heart failure and arterial thromboembolism, is the main heart disease in cats [270, 271]. In dogs, myocardial infarction is rare due to well-developed collateral circulation and low prevalence of atherosclerosis (reviewed in [272]), but myocarditis accompanied with leucocyte infiltration and interstitial fibrosis can result in disturbance of the heart rhythm [273, 274]. Besides, as in people, atrial fibrillation is a predictive factor for survival time in large dogs with congestive heart failure and dilated cardiomyopathy [275]. Autoimmune dilated cardiomyopathy presents similar pathomechanisms in Doberman Pinscher and people too [276]. Obviously, there is a substantial need to causally understand pathomechanisms in the heart and cardiac function, and to shed light onto underlying interactions of the heart with other organ systems. Although relevant limitations exist, cardiac optogenetics represents an interdisciplinary and translational application which can contribute to the development of therapeutic tools for mammals in general.

VI. SUMMARY

Heart optogenetics for *in vivo* intrinsic and extrinsic cardiac applications in mice

Comorbidities between heart diseases and anxiety disorders as well as cardiac immune response are known but their influence on each other and pathomechanisms remain poorly understood [10, 89, 232, 233, 249]. In the present work, optogenetics was used to specifically modulate intrinsic and extrinsic cells in the heart. This novel technique provides the necessary precision to achieve the control of cells within milliseconds through the combination of optics and genetics (reviewed in [8]). Optogenetics is already well established in neurosciences, but cardiac optogenetics represents an emerging field of the method and was never achieved in conscious animals [257]. Here we sought to establish models for cardiac optogenetics in freely moving mice aiming to, on the one hand, selectively activate intrinsic cardiac cells to modulate the HR, and on the other hand, to guide extrinsic lymphocytes into the myocardium. In the future, those models should enable to understand the circuits involved in heart-brain interactions and investigate the effect of lymphocytes in the injured myocardium after MI.

A fundamental milestone in the establishment of cardiac optogenetics was to develop the surgical implantation of a light source (μ LED) to illuminate the heart. So far, no procedure for the illumination of the thoracic cavity in conscious mice has been described. The technique was adapted to the left and the right heart to enable the illumination of different heart regions. The surgery was tolerated and did not impair the heart function; however, the movements of the animal may lead to slight shift of the device, increasing the distance of the μ LED to the target cells, thus decreasing the illumination power. After the establishment of the surgery, which represented a common bottleneck for the manipulation of cardiac cells on intrinsic and extrinsic levels, two independent arms were developed.

In order to modulate the HR and initiate a physiological heart contraction the *Cre/lox*-system was used to selectively express a red-shifted opsin in target cells either belonging to the ECS or to cholinergic plexus. The choice of long-wave light was justified by a deeper penetration into the tissue as short-wave light, but is lower in energy, what can present a limitation for cell activation. Stimulation of the SAN with orange light did not lead to HR change. Although the opsin expression was verified in all the mice with qPCR, the activation of cholinergic cardiac cells induced a significant HR decrease in three out of six animals. The HR drop was observed in mice implanted with the red μ LED, correlated with stimulation periods and was more pronounced under constant illumination compared to pulsed light. These results demonstrate that the effect depends on the wavelength and on the stimulation type. Fine-tuning of the illumination parameters needs to be performed in additional trials. Furthermore, the number of animals should be increased to draw conclusions about the effect and the reproducibility of the experiments.

To achieve light-induced migration of lymphocytes into the tissue, we first engineered photoactivable CD4⁺ cells, second assessed the best illumination settings *in vitro*, third determined the intrathoracic illumination pattern and last but not least, performed *in vivo*

illumination. *In vitro*, scattered light appeared to be sufficient to activate the PA-CXCR4 cells; therefore, apart from the directly illuminated heart, lungs and thymus were harvested too. FC analysis revealed that the cells did not accumulate in the heart or the lung following illumination; however, a preferential accumulation of photoactivable lymphocytes was detected in the illuminated thymus lobe. LSMF imaging confirmed the migration of the modified cells to the light-exposed pole of the organ too. The relation between illumination duration, power and cell trafficking still needs to be elucidated. To attract cells by phototaxis into the heart, cell responsiveness to a longer wavelength should be considered.

Some hurdles still need to be overcome until cardiac optogenetics may become a standard research model in rodents, but those preliminary data demonstrate the feasibility to manipulate intrinsic cardiac cells and the migration of extrinsic cells into deep tissue in freely moving mice. There is an interdisciplinary need to shed light onto underlying interactions of the heart with other organ systems. The two overarching goals of this project consisted of establishing models enabling to causally understand mechanisms within the heart and the role of the heart in relation to other organ systems. By supplying the whole organism with blood, the cardiovascular system stands at the core of a complex network connecting central and peripheral mechanisms as well as autonomous and somatic responses. The approaches described in this work contribute to pave the way for cardiac optogenetics applications and highlight the flexibility of the method to address diverse biological questions. Optogenetics has a broad interspecies translational potential to increase the knowledge of networks underlying physiological responses and pathomechanisms in complex organisms.

VII. ZUSAMMENFASSUNG

Herzoptogenetik

für intrinsisch und extrinsisch kardiale Anwendungen in Mäusen *in vivo*

Während Komorbiditäten zwischen Herzkrankheiten und Angststörungen sowie kardialen Immunreaktionen schon länger bekannt sind, sind ihre gegenseitigen Wechselwirkungen und die zugrunde liegenden Pathomechanismen weitgehend unverstanden [10, 89, 232, 233, 249]. Durch die Kombination von Optik und Genetik ermöglicht diese neuartige Technik es, Zellen innerhalb von Millisekunden präzise zu steuern [8]. Die Optogenetik ist in den Neurowissenschaften bereits etabliert, am Herzen ist sie allerdings wenig erforscht und wurde bisher noch nie an Tieren bei Bewusstsein durchgeführt [257]. Im Rahmen dieser Arbeit wurde die Etablierung von Modellen in Mäusen bei Bewusstsein erzielt, um einerseits intrinsische Herzzellen selektiv zu aktivieren und die Herzfrequenz zu modulieren, und um andererseits extrinsische Lymphozyten in das Myokard anzulocken. Diese Modelle sollen es in Zukunft ermöglichen, die Netzwerke zu verstehen, die an Herz-Hirn-Interaktionen beteiligt sind, und die Wirkung von Lymphozyten im geschädigten Myokard nach einem Herzinfarkt zu untersuchen.

Ein grundlegender Meilenstein bei der Etablierung kardialer Optogenetik war die Entwicklung der chirurgischen Implantation einer Lichtquelle (μ LED), um das Herz zu beleuchten. Bislang wurde noch kein Verfahren zur Beleuchtung der Brusthöhle in Mäusen bei Bewusstsein beschrieben. Die Technik wurde sowohl an das linke als auch an das rechte Herz angepasst, um die Beleuchtung verschiedener Regionen des Organs zu ermöglichen. Der Eingriff wurde von den Versuchstieren toleriert und führte zu keiner Beeinträchtigung der Herzfunktion. Allerdings war es nicht auszuschließen, dass es bei freier Bewegung des Tieres zu einer leichten Verschiebung der Leuchtquelle kommen konnte. Dadurch würde sich der Abstand der μ LED zu den Zielzellen vergrößern und die Beleuchtungsintensität der Zielregion abnehmen. Nachdem der chirurgische Eingriff etabliert wurde, der eine Voraussetzung für die Manipulation von Herzzellen auf sowohl in- als auch extrinsischer Ebene darstellte, teilte sich das Projekt in zwei unabhängige Anwendungsbereiche.

Um die Herzfrequenz zu modulieren und eine physiologische Herzkontraktion auszulösen, wurde das *Cre/lox*-System in transgenen Mäusen angewendet. Dadurch konnte ein Opsin, das auf rotes Licht reagierte, in Zielzellen selektiv exprimiert werden, die entweder zum Reizleitungssystem des Herzens oder zu cholinergen Plexus gehörten. Dabei wurde langwelliges Licht gewählt, weil es eine höhere Eindringtiefe als kurzwelliges Licht hat. Da Licht mit einer größeren Wellenlänge auch weniger Energie besitzt, konnte nicht ausgeschlossen werden, dass die Zellstimulation weniger stark ausfällt. Die Stimulation des Sinusknotens mit orangefarbenem Licht hatte keinen Einfluss auf die Herzfrequenz. Obwohl die Opsin-Expression bei allen Mäusen mittels qPCR nachgewiesen wurde, führte die Aktivierung der cholinergen Herzzellen bei drei von sechs Mäusen zu einem signifikanten Abfall der Herzfrequenz. Die Senkung der Herzfrequenz wurde ausschließlich bei Mäusen beobachtet, denen die rote μ LED implantiert wurde. Sie korrelierte mit optischen Stimulationsperioden und war bei

konstanter Beleuchtung stärker ausgeprägt als bei gepulstem Licht. Diese Ergebnisse zeigen, dass der Effekt nicht nur von der Wellenlänge, sondern auch von der Stimulationsart abhängig ist. Zur Feinabstimmung der Beleuchtungsparameter müssten weitere Versuche durchgeführt werden. Außerdem sollte die Tierzahl erhöht werden, um Rückschlüsse auf die Wirkung und die Reproduzierbarkeit der Versuche ziehen zu können.

Um die lichtinduzierte Migration von Lymphozyten in das Gewebe zu erreichen, wurden zunächst photoaktivierbare CD4⁺-Zellen hergestellt und anschließend die besten Beleuchtungseinstellungen *in vitro* ermittelt. Danach wurde das intrathorakale Beleuchtungsmuster bestimmt und es erfolgten *in-vivo*-Beleuchtungen. *In vitro* schien gestreutes Licht ausreichend zu sein, um PA-CXCR4-Zellen zu aktivieren. Daher wurde das Vorkommen modifizierter Zellen neben dem direkt beleuchteten Herzen auch in der Lunge und dem Thymus geprüft. Die FC-Analyse ergab, dass sich die Zellen nach der Beleuchtung weder im Herzen noch in der Lunge anhäuferten. Eine bevorzugte Anreicherung von photoaktivierbaren Lymphozyten wurde jedoch im beleuchteten Thymuslappen festgestellt. Auch die LSFM-Verfahren bestätigten die Migration der modifizierten Zellen zum beleuchteten Pol des Organs. Der Zusammenhang zwischen Beleuchtungsdauer, -leistung und einer daraus resultierenden Zellmigration erfordert allerdings noch weitere Beweise. Zudem sollte eine Anpassung der Aktivierbarkeit der Zellen an eine längere Wellenlänge in Erwägung gezogen werden, um Zellen durch Phototaxis in das dunkle, blutgefüllte Herz anzulocken.

Bis kardiale Optogenetik als standardisiertes Forschungsmodell bei Nagetieren eingesetzt werden kann, müssen noch einige Fragen geklärt werden. Die in dieser Arbeit erhobenen Daten zeigen jedoch, dass es möglich ist, intrinsische Herzzellen und die Migration von extrinsischen Zellen in tiefes Gewebe in Mäusen bei Bewusstsein zu modulieren. Es besteht ein interdisziplinärer Bedarf an weiterer Forschung im Hinblick auf die zugrunde liegenden Interaktionen des Herzens mit anderen Organsystemen. Das wesentliche Ziel der vorliegenden Arbeit bestand darin, Modelle zu etablieren, um Mechanismen innerhalb des Herzens und die Rolle des Herzens im Zusammenspiel mit anderen Organsystemen kausal zu untersuchen. Da das Herz-Kreislauf-System den gesamten Organismus mit Blut versorgt, steht es im Zentrum eines komplexen Netzwerks, das zentrale und periphere Mechanismen sowie autonome und somatische Reaktionen miteinander verbindet. Die hier beschriebenen Ansätze sind Wegbereiter für die kardiale Optogenetik und betonen die Flexibilität der eingesetzten Methode zur Beantwortung verschiedener biologischer Fragen. Schließlich eröffnet die Optogenetik artenübergreifend neue Wege, jene Netzwerke besser zu verstehen, auf denen physiologischen Reaktionen und Pathomechanismen in komplexen Organismen basieren.

VIII. ABBREVIATIONS

A	Absorbance
AAV	Adeno-associated virus
ANS	Autonomous nervous system
APC	Antigen presenting cell
a.u.	Arbitrary units
AVN	Atrioventricular node
BABB	Benzoic acid benzyl benzoate
BHK	Baby hamster kidney
B-mode	Brightness mode
bp	Base pair
bpm	Beats per minute
BSA	Bovine serum albumin fraction V
Ca ²⁺	Calcium ion
[Ca ²⁺] _i	Intracellular calcium concentration
cAMP	Cyclic adenosine monophosphate
CCL, CXCL, XCL, CX ₃ CL	Chemokine ligands
CCR, CXCR, XCR, CX ₃ CR	Chemokine receptors
CD	Cluster of differentiation
cDNA	Complementary deoxyribonucleic acid
cGMP	Cyclic guanosine monophosphate
ChAT	Choline acetyltransferase
CHFC	Comprehensive Heart Failure Center
ChR	Channelrhodopsin
CNS	Central nervous system
Ct	Cycle threshold
CT	Computed tomography
CUBIC	Clear, Unobstructed Brain/Body Imaging Cocktails and Computational analysis
CXCL12	Chemokine ligand 12
CXCR4	Chemokine receptor 4
d	day
Da	Dalton
DIO	Double-floxed inverse open reading frame
DNA	Deoxyribonucleic acid
E1	Early region 1
E/A	Early wave/Atrial filling
ECG	Electrocardiogram

ECS	Electrical conduction system
EF	Ejection fraction
EF-1 α	Elongation factor 1 alpha
FACS	Fluorescence-activated cell sorting
FAK	Focal adhesion kinase
FBS	Fetal bovine serum
FC	Flow cytometry
FELASA	Federation of European Laboratory Animal Science Association
FP	Fluorescent protein
FS	Fractional shortening
g	Gravity
G	Gauge
GAPDH	Glyceraldehyde 3-phosphate dehydrogenase
gDNA	Genomic deoxyribonucleic acid
GFP	Green fluorescent protein
GPCR	G protein-coupled receptor
HBSS	Hanks' balanced salt solution
HCN1, 2, 3, 4	Hyperpolarization-activated cyclic nucleotide-gated channel 1, 2, 3, 4
HEK	Human embryonic kidney
ICN	Institute of Clinical Neurobiology
I_f	Funny current
IL	Interleukin
i.p.	Intraperitoneal
IRES	Internal ribosome entry site
ITR	Inverted terminal repeat
i.v.	Intravenous
K ⁺	Potassium ion
kbp	Kilobase pair
LA	Left atrium
LAD	Left anterior descending coronary artery
LamR	Laminin receptor
LED	Light-emitting diode
LV	Left ventricle
LVEDL	Left ventricular end-diastolic length
LVEDV	Left ventricular end-diastolic volume
LVESL	Left ventricular end-systolic length
LVESV	Left ventricular end-systolic volume

LVIDd	left ventricular end-diastolic diameter
LVIDs	left ventricular end-systolic diameter
M2	Muscarinic receptor type 2
MAC	Minimum alveolar concentration
MAPK	Mitogen activated protein kinase
MGS	Mouse grimace scale
MHC	Major histocompatibility complex
MI	Myocardial infarction
M-mode	Motion mode
MMP	Metalloproteinase
mRNA	Messenger ribonucleic acid
MSCV	Murine stem cell virus
MYHCA	Alpha-myosin heavy chain
Na ⁺	Sodium ion
NaCl	Sodium chloride
ORF	Open reading frames
ORL1	Opioid receptor like-1 receptor
PA flow	Pulmonary artery flow
PA-CXCR4	Photoactivable chemokine receptor 4
PBS	Phosphate-buffered saline
PCR	Polymerase chain reaction
PDMS	Polydimethylsiloxane
PEEP	Positive end-expiratory pressure
PI3K	Phosphoinositol-3-kinase
Plat-E cells	Platinum retroviral packaging cell lines
PLAX	Parasternal long axis
PSAX	Parasternal short axis
PSTH	Peristimulus time histogram
Pulm. Artery	Pulmonary artery
PW	Pulsed-wave
qPCR	Quantitative polymerase chain reaction
RA	Right atrium
rAAV	Recombinant adeno-associated virus
RFP	Red fluorescent protein
RNA	Ribonucleic acid
rpm	Rounds per minute
RV	Right ventricle
s	Second

SAN	Sinoatrial node
s.c.	subcutaneous
SDF-1	Stromal cell-derived factor 1
SEM	Standard error of the mean
SPECT	Single-photon emission computed tomography
SPIM	Selective plane illumination microscopy
TAPSE	Tricuspid annular plane systolic excursion
TCR	T cell receptor
T _m	Melting temperature
Treg	Regulatory T cell
μLED	Micro light-emitting diode
vg	Viral genome
V	Ventricle
W	Watt
WPRE	Woodchuck hepatitis virus post-transcriptional regulatory element

IX. REFERENCES

1. McDonagh, T.A., et al., *2021 ESC Guidelines for the diagnosis and treatment of acute and chronic heart failure: Developed by the Task Force for the diagnosis and treatment of acute and chronic heart failure of the European Society of Cardiology (ESC) With the special contribution of the Heart Failure Association (HFA) of the ESC*. European Heart Journal, 2021. **42**(36): p. 3599-3726.
2. Wu, Y., et al., *New Insights Into the Comorbidity of Coronary Heart Disease and Depression*. Current Problems in Cardiology, 2021. **46**(3): p. 100413.
3. Polyakova, V., et al., *Atrial extracellular matrix remodelling in patients with atrial fibrillation*. J Cell Mol Med, 2008. **12**(1): p. 189-208.
4. Nunes-Silva, V., S. Frantz, and G.C. Ramos, *Lymphocytes at the Heart of Wound Healing*. Adv Exp Med Biol, 2017. **1003**: p. 225-250.
5. Deisseroth, K., et al., *Next-Generation Optical Technologies for Illuminating Genetically Targeted Brain Circuits*. The Journal of Neuroscience, 2006. **26**(41): p. 10380-10386.
6. Deisseroth, K., *Optogenetics: 10 years of microbial opsins in neuroscience*. Nature Neuroscience, 2015. **18**(9): p. 1213-1225.
7. Deisseroth, K., *Optogenetics*. Nature Methods, 2011. **8**(1): p. 26-29.
8. Xu, X., T. Mee, and X. Jia, *New era of optogenetics: from the central to peripheral nervous system*. Crit Rev Biochem Mol Biol, 2020. **55**(1): p. 1-16.
9. Hofmann, U., et al., *Activation of CD4⁺ T Lymphocytes Improves Wound Healing and Survival After Experimental Myocardial Infarction in Mice*. Circulation, 2012. **125**(13): p. 1652-1663.
10. Rieckmann, M., et al., *Myocardial infarction triggers cardioprotective antigen-specific T helper cell responses*. The Journal of Clinical Investigation, 2019. **129**(11): p. 4922-4936.
11. Boyden, E.S., et al., *Millisecond-timescale, genetically targeted optical control of neural activity*. Nature Neuroscience, 2005. **8**(9): p. 1263-1268.
12. Oesterhelt, D. and W. Stoeckenius, *Rhodopsin-like protein from the purple membrane of Halobacterium halobium*. Nature new biology, 1971. **233**(39): p. 149-152.
13. Nagel, G., et al., *Channelrhodopsin-2, a directly light-gated cation-selective membrane channel*. Proceedings of the National Academy of Sciences, 2003. **100**(24): p. 13940-13945.

14. Ernst, O.P., et al., *Microbial and Animal Rhodopsins: Structures, Functions, and Molecular Mechanisms*. Chemical Reviews, 2014. **114**(1): p. 126-163.
15. Nagel, G., et al., *Channelrhodopsin-1: a light-gated proton channel in green algae*. Science, 2002. **296**(5577): p. 2395-8.
16. Carter, M. and J.C. Shieh, *Guide to research techniques in neuroscience*. 2015: Academic Press.
17. Bogomolni, R.A. and J.L. Spudich, *Identification of a third rhodopsin-like pigment in phototactic Halobacterium halobium*. Proceedings of the National Academy of Sciences, 1982. **79**(20): p. 6250-6254.
18. Miesenböck, G., *Optogenetic Control of Cells and Circuits*. Annual Review of Cell and Developmental Biology, 2011. **27**(1): p. 731-758.
19. Polli, D., et al., *Tracking the primary photoconversion events in rhodopsins by ultrafast optical spectroscopy*. Photochemical & Photobiological Sciences, 2015. **14**(2): p. 213-228.
20. Gutruf, P. and J.A. Rogers, *Implantable, wireless device platforms for neuroscience research*. Current Opinion in Neurobiology, 2018. **50**: p. 42-49.
21. Gupta, N., H. Bansal, and S. Roy, *Theoretical optimization of high-frequency optogenetic spiking of red-shifted very fast-Chrimson-expressing neurons*. Neurophotonics, 2019. **6**(2): p. 025002-025002.
22. Kuhne, J., et al., *Unifying photocycle model for light adaptation and temporal evolution of cation conductance in channelrhodopsin-2*. Proceedings of the National Academy of Sciences of the United States of America, 2019. **116**(19): p. 9380-9389.
23. Igarashi, H., et al., *Targeted expression of step-function opsins in transgenic rats for optogenetic studies*. Scientific Reports, 2018. **8**(1): p. 5435.
24. Kim, C.K., A. Adhikari, and K. Deisseroth, *Integration of optogenetics with complementary methodologies in systems neuroscience*. Nature Reviews Neuroscience, 2017. **18**(4): p. 222-235.
25. Govorunova, E.G., et al., *Microbial Rhodopsins: Diversity, Mechanisms, and Optogenetic Applications*. Annual review of biochemistry, 2017. **86**: p. 845-872.
26. Barnett, S., et al., *Optogenetic stimulation: Understanding memory and treating deficits*. Hippocampus, 2018. **28**(7): p. 457-470.
27. Kim, K., et al., *Seeing the electroporative uptake of cell-membrane impermeable fluorescent molecules and nanoparticles*. Nanoscale, 2012. **4**(16): p. 5051-5058.
28. Fenno, L., O. Yizhar, and K. Deisseroth, *The development and application of optogenetics*. Annu Rev Neurosci, 2011. **34**: p. 389-412.

29. Madisen, L., et al., *A toolbox of Cre-dependent optogenetic transgenic mice for light-induced activation and silencing*. *Nature neuroscience*, 2012. **15**(5): p. 793-802.
30. Fenno, L.E., et al., *Targeting cells with single vectors using multiple-feature Boolean logic*. *Nature Methods*, 2014. **11**(7): p. 763-772.
31. Gradinaru, V., et al., *Molecular and Cellular Approaches for Diversifying and Extending Optogenetics*. *Cell*, 2010. **141**(1): p. 154-165.
32. Sizemore, R.J., et al., *Viral vector-based tools advance knowledge of basal ganglia anatomy and physiology*. *Journal of neurophysiology*, 2016. **115**(4): p. 2124-2146.
33. Hocquemiller, M., et al., *Adeno-Associated Virus-Based Gene Therapy for CNS Diseases*. *Human gene therapy*, 2016. **27**(7): p. 478-496.
34. Nathanson, J.L., et al., *Short Promoters in Viral Vectors Drive Selective Expression in Mammalian Inhibitory Neurons, but do not Restrict Activity to Specific Inhibitory Cell-Types*. *Frontiers in neural circuits*, 2009. **3**: p. 19-19.
35. Chowdhury, E.A., et al., *Current progress and limitations of AAV mediated delivery of protein therapeutic genes and the importance of developing quantitative pharmacokinetic/pharmacodynamic (PK/PD) models*. *Advanced Drug Delivery Reviews*, 2021. **170**: p. 214-237.
36. Forcelli, P.A., *Applications of optogenetic and chemogenetic methods to seizure circuits: Where to go next?* *J Neurosci Res*, 2017. **95**(12): p. 2345-2356.
37. Juarez, B., et al., *Optogenetic investigation of neural mechanisms for alcohol-use disorder*. *Alcohol (Fayetteville, N.Y.)*, 2019. **74**: p. 29-38.
38. Goldstein, N., et al., *Hypothalamic Neurons that Regulate Feeding Can Influence Sleep/Wake States Based on Homeostatic Need*. *Current biology : CB*, 2018. **28**(23): p. 3736-3747.e3.
39. Stuber, G.D., et al., *Excitatory transmission from the amygdala to nucleus accumbens facilitates reward seeking*. *Nature*, 2011. **475**(7356): p. 377-380.
40. Adhikari, A., et al., *Basomedial amygdala mediates top-down control of anxiety and fear*. *Nature*, 2015. **527**(7577): p. 179-185.
41. Tovote, P., et al., *Midbrain circuits for defensive behaviour*. *Nature*, 2016. **534**(7606): p. 206-212.
42. Yi, M.-H., et al., *Optogenetic activation of spinal microglia triggers chronic pain in mice*. *PLoS biology*, 2021. **19**(3): p. e3001154.
43. Lanshakov, D.A., U.S. Drozd, and N.N. Dygalo, *Optogenetic Stimulation Increases Level of Antiapoptotic Protein Bcl-xL in Neurons*. *Biochemistry (Mosc)*,

2017. **82**(3): p. 340-344.

44. Ortiz, F.C., et al., *Neuronal activity in vivo enhances functional myelin repair*. JCI Insight, 2019. **4**(9).

45. Towne, C., et al., *Optogenetic control of targeted peripheral axons in freely moving animals*. PloS one, 2013. **8**(8): p. e72691.

46. Sun, L., et al., *Neuronal regeneration in C. elegans requires subcellular calcium release by ryanodine receptor channels and can be enhanced by optogenetic stimulation*. J Neurosci, 2014. **34**(48): p. 15947-56.

47. Park, S., et al., *Optogenetic control of nerve growth*. Scientific reports, 2015. **5**: p. 9669-9669.

48. Lee, S.-Y., et al., *Optogenetic control of iPS cell-derived neurons in 2D and 3D culture systems using channelrhodopsin-2 expression driven by the synapsin-1 and calcium-calmodulin kinase II promoters*. Journal of Tissue Engineering and Regenerative Medicine, 2019. **13**(3): p. 369-384.

49. Jung, K., et al., *Optogenetic stimulation promotes Schwann cell proliferation, differentiation, and myelination in vitro*. Scientific reports, 2019. **9**(1): p. 3487-3487.

50. Arrenberg, A.B., et al., *Optogenetic control of cardiac function*. Science, 2010. **330**(6006): p. 971-4.

51. Kamino, K., A. Hirota, and S. Fujii, *Localization of pacemaking activity in early embryonic heart monitored using voltage-sensitive dye*. Nature, 1981. **290**(5807): p. 595-597.

52. Bruegmann, T., et al., *Optogenetic control of heart muscle in vitro and in vivo*. Nat Methods, 2010. **7**(11): p. 897-900.

53. Nussinovitch, U. and L. Gepstein, *Optogenetics for in vivo cardiac pacing and resynchronization therapies*. Nature Biotechnology, 2015. **33**(7): p. 750-754.

54. Rajendran, P.S., et al., *Identification of peripheral neural circuits that regulate heart rate using optogenetic and viral vector strategies*. Nat Commun, 2019. **10**(1): p. 1944.

55. Meijler, F.L. and T.D. Meijler, *Archetype, adaptation and the mammalian heart*. Netherlands heart journal : monthly journal of the Netherlands Society of Cardiology and the Netherlands Heart Foundation, 2011. **19**(3): p. 142-148.

56. Loeffler, K. and G. Gäbel, *Anatomie und Physiologie der Haustiere*. Vol. 13. 2015: UTB.

57. Habermehl, K.H., et al., *Lehrbuch der Anatomie der Haustiere: Kreislaufsystem, Haut und Hautorgane*. 2005: Parey.

58. Nickel, R., *Lehrbuch der Anatomie der Haustiere: Eingeweide*. Vol. 2. 2004: Georg Thieme Verlag.
59. Woodcock, E.A. and S.J. Matkovich, *Cardiomyocytes structure, function and associated pathologies*. The International Journal of Biochemistry & Cell Biology, 2005. **37**(9): p. 1746-1751.
60. Severs, N.J., et al., *Remodelling of gap junctions and connexin expression in heart disease*. Biochimica et Biophysica Acta (BBA) - Biomembranes, 2004. **1662**(1): p. 138-148.
61. von Engelhardt, W. and G. Breves, *Physiologie der Haustiere*. Schweizer Archiv für Tierheilkunde, 2005. **147**(11): p. 507-507.
62. DiFrancesco, D., *The Role of the Funny Current in Pacemaker Activity*. Circulation Research, 2010. **106**(3): p. 434-446.
63. Stieber, J., et al., *The hyperpolarization-activated channel HCN4 is required for the generation of pacemaker action potentials in the embryonic heart*. Proceedings of the National Academy of Sciences of the United States of America, 2003. **100**(25): p. 15235-15240.
64. Herrmann, S., B. Layh, and A. Ludwig, *Novel insights into the distribution of cardiac HCN channels: an expression study in the mouse heart*. Journal of molecular and cellular cardiology, 2011. **51**(6): p. 997-1006.
65. Fenske, S., et al., *cAMP-dependent regulation of HCN4 controls the tonic entrainment process in sinoatrial node pacemaker cells*. Nature Communications, 2020. **11**(1): p. 5555.
66. Biel, M., et al., *Hyperpolarization-Activated Cation Channels: From Genes to Function*. Physiological Reviews, 2009. **89**(3): p. 847-885.
67. Böhme, G., *Lehrbuch der Anatomie der Haustiere Band 4: Nervensystem, Sinnesorgane, Endokrine Drüsen*. Vol. 4. 2004: Georg Thieme Verlag.
68. Hildreth, V., R.H. Anderson, and D.J. Henderson, *Autonomic innervation of the developing heart: origins and function*. Clin Anat, 2009. **22**(1): p. 36-46.
69. Opie, L.H., *Heart physiology: from cell to circulation*. 2004: Lippincott Williams & Wilkins.
70. Achanta, S., et al., *A Comprehensive Integrated Anatomical and Molecular Atlas of Rat Intrinsic Cardiac Nervous System*. iScience, 2020. **23**(6): p. 101140.
71. Ai, J., et al., *Morphology and topography of nucleus ambiguus projections to cardiac ganglia in rats and mice*. Neuroscience, 2007. **149**(4): p. 845-60.
72. Oda, Y., *Choline acetyltransferase: the structure, distribution and pathologic*

- changes in the central nervous system*. *Pathol Int*, 1999. **49**(11): p. 921-37.
73. Dong, R., et al., *A Protocol for Dual Calcium-Voltage Optical Mapping in Murine Sinoatrial Preparation With Optogenetic Pacing*. *Frontiers in Physiology*, 2019. **10**.
74. Parnham, M.J. and F.P. Nijkamp, *Principles of immunopharmacology*. 2005: Springer.
75. Davis, M.M., *T CELL RECEPTOR GENE DIVERSITY AND SELECTION*. *Annual Review of Biochemistry*, 1990. **59**(1): p. 475-496.
76. Haftmann, C., et al., *Protection against autoimmunity is driven by thymic epithelial cell-mediated regulation of T(reg) development*. *Sci Immunol*, 2021. **6**(65): p. eabf3111.
77. Burkly, L.C., et al., *Clonal deletion of V beta 5+ T cells by transgenic I-E restricted to thymic medullary epithelium*. *The Journal of Immunology*, 1993. **151**(8): p. 3954-3960.
78. Frangogiannis, N.G., *Inflammation in cardiac injury, repair and regeneration*. *Current opinion in cardiology*, 2015. **30**(3): p. 240-245.
79. Kaya, Z., et al., *Autoantibodies in Heart Failure and Cardiac Dysfunction*. *Circulation Research*, 2012. **110**(1): p. 145-158.
80. Lv, H., et al., *Impaired thymic tolerance to α -myosin directs autoimmunity to the heart in mice and humans*. *The Journal of Clinical Investigation*, 2011. **121**(4): p. 1561-1573.
81. Blanton, R.M., F.J. Carrillo-Salinas, and P. Alcaide, *T-cell recruitment to the heart: friendly guests or unwelcome visitors?* *American Journal of Physiology-Heart and Circulatory Physiology*, 2019. **317**(1): p. H124-H140.
82. Weil, B.R. and S. Neelamegham, *Selectins and Immune Cells in Acute Myocardial Infarction and Post-infarction Ventricular Remodeling: Pathophysiology and Novel Treatments*. *Frontiers in immunology*, 2019. **10**: p. 300-300.
83. Weirather, J., et al., *Foxp3⁺ CD4⁺ T Cells Improve Healing After Myocardial Infarction by Modulating Monocyte/Macrophage Differentiation*. *Circulation Research*, 2014. **115**(1): p. 55-67.
84. Li, N., et al., *The Th17/Treg imbalance exists in patients with heart failure with normal ejection fraction and heart failure with reduced ejection fraction*. *Clin Chim Acta*, 2010. **411**(23-24): p. 1963-8.
85. Tang, H., et al., *Low responder T cell susceptibility to the suppressive function of regulatory T cells in patients with dilated cardiomyopathy*. *Heart*, 2010. **96**(10): p.

765-71.

86. Prabhu, S.D. and N.G. Frangogiannis, *The Biological Basis for Cardiac Repair After Myocardial Infarction: From Inflammation to Fibrosis*. *Circulation research*, 2016. **119**(1): p. 91-112.
87. Fan, D., et al., *Cardiac fibroblasts, fibrosis and extracellular matrix remodeling in heart disease*. *Fibrogenesis & tissue repair*, 2012. **5**(1): p. 15-15.
88. Xia, N., et al., *A Unique Population of Regulatory T Cells in Heart Potentiates Cardiac Protection From Myocardial Infarction*. *Circulation*, 2020. **142**(20): p. 1956-1973.
89. Mathes, D., et al., *CD4⁺ Foxp3⁺ T-cells contribute to myocardial ischemia-reperfusion injury*. *Journal of Molecular and Cellular Cardiology*, 2016. **101**: p. 99-105.
90. Thiele, S. and M.M. Rosenkilde, *Interaction of chemokines with their receptors- from initial chemokine binding to receptor activating steps*. *Curr Med Chem*, 2014. **21**(31): p. 3594-614.
91. Bianchi, M.E. and R. Mezzapelle, *The Chemokine Receptor CXCR4 in Cell Proliferation and Tissue Regeneration*. *Frontiers in Immunology*, 2020. **11**.
92. Décaillot, F.M., et al., *CXCR7/CXCR4 heterodimer constitutively recruits β -arrestin to enhance cell migration*. *Journal of Biological Chemistry*, 2011. **286**(37): p. 32188-32197.
93. Marchese, A., et al., *The ins and outs of G protein-coupled receptor trafficking*. *Trends in Biochemical Sciences*, 2003. **28**(7): p. 369-376.
94. Thelen, M. and J.V. Stein, *How chemokines invite leukocytes to dance*. *Nature Immunology*, 2008. **9**(9): p. 953-959.
95. Freeley, M., et al., *L-Plastin Regulates Polarization and Migration in Chemokine-Stimulated Human T Lymphocytes*. *The Journal of Immunology*, 2012. **188**(12): p. 6357-6370.
96. Hannigan, M., et al., *Neutrophils lacking phosphoinositide 3-kinase γ show loss of directionality during N-formyl-Met-Leu-Phe-induced chemotaxis*. *Proceedings of the National Academy of Sciences*, 2002. **99**(6): p. 3603-3608.
97. Bach, T.L., et al., *Phospholipase c β is critical for T cell chemotaxis*. *Journal of immunology (Baltimore, Md. : 1950)*, 2007. **179**(4): p. 2223-2227.
98. Otsuka, S. and G. Bebb, *The CXCR4/SDF-1 Chemokine Receptor Axis: A New Target Therapeutic for Non-small Cell Lung Cancer*. *Journal of Thoracic Oncology*, 2008. **3**(12): p. 1379-1383.

99. Xu, Y., et al., *Optogenetic control of chemokine receptor signal and T-cell migration*. Proc Natl Acad Sci U S A, 2014. **111**(17): p. 6371-6.
100. Fox, J.G., et al., *The mouse in biomedical research: normative biology, husbandry, and models*. Vol. 3. 2006: Elsevier.
101. Bryda, E.C., *The Mighty Mouse: the impact of rodents on advances in biomedical research*. Mo Med, 2013. **110**(3): p. 207-11.
102. Casellas, J., *Inbred mouse strains and genetic stability: a review*. Animal, 2011. **5**(1): p. 1-7.
103. Rossi, J., et al., *Melanocortin-4 receptors expressed by cholinergic neurons regulate energy balance and glucose homeostasis*. Cell Metab, 2011. **13**(2): p. 195-204.
104. Rivolta, I., et al., *Cardiac and neuronal HCN channelopathies*. Pflugers Arch, 2020. **472**(7): p. 931-951.
105. D'Souza, A., et al., *A circadian clock in the sinus node mediates day-night rhythms in Hcn4 and heart rate*. Heart Rhythm, 2021. **18**(5): p. 801-810.
106. Martin, T.P., et al., *Preclinical models of myocardial infarction: from mechanism to translation*. Br J Pharmacol, 2021.
107. Mota-Rojas, D., et al., *The Utility of Grimace Scales for Practical Pain Assessment in Laboratory Animals*. Animals (Basel), 2020. **10**(10).
108. Mittal, A., et al., *Quantification of pain in sickle mice using facial expressions and body measurements*. Blood Cells Mol Dis, 2016. **57**: p. 58-66.
109. Langford, D.J., et al., *Coding of facial expressions of pain in the laboratory mouse*. Nat Methods, 2010. **7**(6): p. 447-9.
110. Steinke, H. and W. Wolff, *A modified Spalteholz technique with preservation of the histology*. Annals of Anatomy - Anatomischer Anzeiger, 2001. **183**(1): p. 91-95.
111. Costantino, A.J., et al., *Determining the light scattering and absorption parameters from forward-directed flux measurements in cardiac tissue*. J Biomed Opt, 2017. **22**(7): p. 76009.
112. Kwon, K., et al., *Enhancement of light propagation depth in skin: cross-validation of mathematical modeling methods*. Lasers Med Sci, 2009. **24**(4): p. 605-15.
113. Ash, C., et al., *Effect of wavelength and beam width on penetration in light-tissue interaction using computational methods*. Lasers Med Sci, 2017. **32**(8): p. 1909-1918.
114. Hochman-Elam, L.N., R.E. Heidel, and J.W. Shmalberg, *Effects of laser power, wavelength, coat length, and coat color on tissue penetration using photobiomodulation in healthy dogs*. Can J Vet Res, 2020. **84**(2): p. 131-137.

115. Johannsmeier, S., et al., *Light-cell interactions in depth-resolved optogenetics*. Biomed Opt Express, 2020. **11**(11): p. 6536-6550.
116. Shin, G., et al., *Flexible Near-Field Wireless Optoelectronics as Subdermal Implants for Broad Applications in Optogenetics*. Neuron, 2017. **93**(3): p. 509-521 e3.
117. Marshel, J.H., et al., *Cortical layer-specific critical dynamics triggering perception*. Science, 2019. **365**(6453).
118. Al-Hasani, R., et al., *Distinct Subpopulations of Nucleus Accumbens Dynorphin Neurons Drive Aversion and Reward*. Neuron, 2015. **87**(5): p. 1063-1077.
119. Aravanis, A.M., et al., *An optical neural interface: in vivo control of rodent motor cortex with integrated fiberoptic and optogenetic technology*. Journal of Neural Engineering, 2007. **4**(3): p. S143-S156.
120. Elkader, A. and B. Sproule, *Buprenorphine*. Clinical Pharmacokinetics, 2005. **44**(7): p. 661-680.
121. Erhardt, W., et al., *Anästhesie und Analgesie beim Klein-und Heimtier: mit Exoten, Labortieren, Vögeln, Reptilien, Amphibien und Fischen*. 2012: Schattauer Verlag.
122. Jirkof, P., *Side effects of pain and analgesia in animal experimentation*. Lab animal, 2017. **46**(4): p. 123-128.
123. Althaus, F.R., *Lehrbuch der Pharmakologie und Toxikologie für die Veterinärmedizin*. 2007, Althaus, F. R. (2007). Lehrbuch der Pharmakologie und Toxikologie für die Veterinärmedizin: 131 Tabellen. Deutschland: Enke.
124. Navarro, K.L., et al., *Mouse Anesthesia: The Art and Science*. ILAR J, 2021.
125. Bignami, E., F. Saglietti, and A. Di Lullo, *Mechanical ventilation management during cardiothoracic surgery: an open challenge*. Annals of translational medicine, 2018. **6**(19): p. 380-380.
126. Talbot, S.R., et al., *Defining body-weight reduction as a humane endpoint: a critical appraisal*. Laboratory Animals, 2020. **54**(1): p. 99-110.
127. Bacha, W.J. and L.M. Bacha, *Color Atlas of Veterinary Histology*. 2012: Wiley.
128. Cowling, R.T., et al., *Mechanisms of cardiac collagen deposition in experimental models and human disease*. Transl Res, 2019. **209**: p. 138-155.
129. Andreas Hagendorff, S.S., *Basiswissen Echokardiografie "Ars echocardiographica" - Schritt für Schritt zur korrekten Diagnose 2. Auflage*. Vol. 2.
130. Greim, C.-A.R., Norbert:, *Transösophageale Echokardiographie für Intensivmediziner und Anästhesisten*. Vol. 2. 2007.

131. Kaps, M.e.a., *Sonographie in der Neurologie*. Vol. 3. 2017, Thieme.
132. Gao, S., et al., *Echocardiography in Mice*. *Curr Protoc Mouse Biol*, 2011. **1**: p. 71-83.
133. Lindsey, M.L., et al., *Guidelines for measuring cardiac physiology in mice*. *Am J Physiol Heart Circ Physiol*, 2018. **314**(4): p. H733-H752.
134. Zacchigna, S., et al., *Towards standardization of echocardiography for the evaluation of left ventricular function in adult rodents: a position paper of the ESC Working Group on Myocardial Function*. *Cardiovasc Res*, 2021. **117**(1): p. 43-59.
135. Dayeh, N.R., et al., *Echocardiographic validation of pulmonary hypertension due to heart failure with reduced ejection fraction in mice*. *Sci Rep*, 2018. **8**(1): p. 1363.
136. Kohut, A., N. Patel, and H. Singh, *Comprehensive Echocardiographic Assessment of the Right Ventricle in Murine Models*. *J Cardiovasc Ultrasound*, 2016. **24**(3): p. 229-238.
137. Shah, M., et al., *Echocardiography allows for analysis of pulmonary arterial flow in mice with congenital diaphragmatic hernia*. *J Surg Res*, 2018. **221**: p. 35-42.
138. Seeram, E., *Computed Tomography, 4th Edition Physical Principles, Clinical Applications, and*. 4 ed. 2016. 576.
139. O'Connor, M.K. and B.J. Kemp, *Single-Photon Emission Computed Tomography/Computed Tomography: Basic Instrumentation and Innovations*. *Seminars in Nuclear Medicine*, 2006. **36**(4): p. 258-266.
140. Klein, R., et al., *PET and SPECT Tracers for Myocardial Perfusion Imaging*. *Seminars in Nuclear Medicine*, 2020. **50**(3): p. 208-218.
141. Achenbach, S., et al., *Comparative assessment of image quality for coronary CT angiography with iobitridol and two contrast agents with higher iodine concentrations: iopromide and iomeprol. A multicentre randomized double-blind trial*. *European radiology*, 2017. **27**(2): p. 821-830.
142. Loening, A.M. and S.S. Gambhir, *AMIDE: a free software tool for multimodality medical image analysis*. *Mol Imaging*, 2003. **2**(3): p. 131-7.
143. Drouin, L.M. and M. Agbandje-McKenna, *Adeno-associated virus structural biology as a tool in vector development*. *Future Virol*, 2013. **8**(12): p. 1183-1199.
144. Lopez-Gordo, E., et al., *AAV Vectors for Efficient Gene Delivery to Rodent Hearts*. *Methods in molecular biology (Clifton, N.J.)*, 2019. **1950**: p. 311-332.
145. Martino, A.T. and D.M. Markusic, *Immune Response Mechanisms against AAV Vectors in Animal Models*. *Mol Ther Methods Clin Dev*, 2020. **17**: p. 198-208.

146. Zaiss, A.-K., et al., *Differential Activation of Innate Immune Responses by Adenovirus and Adeno-Associated Virus Vectors*. Journal of Virology, 2002. **76**(9): p. 4580-4590.
147. Zincarelli, C., et al., *Analysis of AAV serotypes 1-9 mediated gene expression and tropism in mice after systemic injection*. Mol Ther, 2008. **16**(6): p. 1073-80.
148. Nagy, A., *Cre recombinase: the universal reagent for genome tailoring*. Genesis, 2000. **26**(2): p. 99-109.
149. Xu, J. and Y. Zhu, *A rapid in vitro method to flip back the double-floxed inverted open reading frame in a plasmid*. BMC Biotechnology, 2018. **18**(1): p. 52.
150. Qin, J.Y., et al., *Systematic Comparison of Constitutive Promoters and the Doxycycline-Inducible Promoter*. PLOS ONE, 2010. **5**(5): p. e10611.
151. Araki, K., et al., *Efficiency of recombination by Cre transient expression in embryonic stem cells: comparison of various promoters*. J Biochem, 1997. **122**(5): p. 977-82.
152. Colon-Thillet, R., K.R. Jerome, and D. Stone, *Optimization of AAV vectors to target persistent viral reservoirs*. Virol J, 2021. **18**(1): p. 85.
153. Liang, X., et al., *Transcription factor ISL1 is essential for pacemaker development and function*. J Clin Invest, 2015. **125**(8): p. 3256-68.
154. Liang, X., et al., *HCN4 dynamically marks the first heart field and conduction system precursors*. Circ Res, 2013. **113**(4): p. 399-407.
155. Prasad, K.M., et al., *Robust cardiomyocyte-specific gene expression following systemic injection of AAV: in vivo gene delivery follows a Poisson distribution*. Gene Ther, 2011. **18**(1): p. 43-52.
156. Ambrosi, C.M., et al., *Adeno-Associated Virus Mediated Gene Delivery: Implications for Scalable in vitro and in vivo Cardiac Optogenetic Models*. Front Physiol, 2019. **10**: p. 168.
157. Rysevaite, K., et al., *Immunohistochemical characterization of the intrinsic cardiac neural plexus in whole-mount mouse heart preparations*. Heart Rhythm, 2011. **8**(5): p. 731-8.
158. Challis, R.C., et al., *Systemic AAV vectors for widespread and targeted gene delivery in rodents*. Nat Protoc, 2019. **14**(2): p. 379-414.
159. Kishi, K.E., et al., *Structural basis for channel conduction in the pump-like channelrhodopsin ChRmine*. Cell, 2022.
160. Chen, R., et al., *Deep brain optogenetics without intracranial surgery*. Nat Biotechnol, 2021. **39**(2): p. 161-164.

161. Chalfie, M. and S.R. Kain, *Green Fluorescent Protein: Properties, Applications and Protocols*. 2005: Wiley.
162. Day, R.N. and M.W. Davidson, *The fluorescent protein palette: tools for cellular imaging*. Chemical Society reviews, 2009. **38**(10): p. 2887-2921.
163. Kremers, G.-J., et al., *Fluorescent proteins at a glance*. Journal of cell science, 2011. **124**(Pt 2): p. 157-160.
164. Day, R.N. and M.W. Davidson, *The Fluorescent Protein Revolution*. 2014: CRC Press.
165. Bindels, D.S., et al., *mScarlet: a bright monomeric red fluorescent protein for cellular imaging*. Nature Methods, 2017. **14**(1): p. 53-56.
166. Patrício, M.I., et al., *Inclusion of the Woodchuck Hepatitis Virus Posttranscriptional Regulatory Element Enhances AAV2-Driven Transduction of Mouse and Human Retina*. Molecular Therapy - Nucleic Acids, 2017. **6**: p. 198-208.
167. Chan, K.Y., et al., *Engineered AAVs for efficient noninvasive gene delivery to the central and peripheral nervous systems*. Nature neuroscience, 2017. **20**(8): p. 1172-1179.
168. Fang, H., et al., *Comparison of adeno-associated virus serotypes and delivery methods for cardiac gene transfer*. Hum Gene Ther Methods, 2012. **23**(4): p. 234-41.
169. Lichtlen, P., *Klinische Vektor-Elektrokardiographie*. Springer-Verlag. 236 Seiten.
170. Engelhardt, W.v., *Physiologie der Haustiere*. Vol. 3. Georg Thieme Verlag.
171. Tandon, S. and T. Alzahrani, *Physiology, AV Junction*, in *StatPearls*. 2021: Treasure Island (FL).
172. Boukens, B.J., et al., *Misinterpretation of the mouse ECG: 'musing the waves of Mus musculus'*. J Physiol, 2014. **592**(21): p. 4613-26.
173. Ramalingam, V.B.a.S., *Reverse Transcription Polymerase Chain Reaction (RT-PCR)*, in *Essential Techniques for Medical and Life Scientists: A Guide to Contemporary Methods and Current Applications with the Protocols: Part I*. Doi: 10.2174/9781681087092118010007. p. 109-118 (10).
174. Arya, M., et al., *Basic principles of real-time quantitative PCR*. Expert review of molecular diagnostics, 2005. **5**(2): p. 209-219.
175. *Molecular Diagnostics: Part 1: Technical Backgrounds and Quality Aspects.*, ed. D.S. Singapore. 2019.
176. Bustin, S. and J. Huggett, *qPCR primer design revisited*. Biomol Detect Quantif,

2017. **14**: p. 19-28.

177. Untergasser, A., et al., *Primer3--new capabilities and interfaces*. Nucleic Acids Res, 2012. **40**(15): p. e115.

178. Kent, W.J., *BLAT--the BLAST-like alignment tool*. Genome Res, 2002. **12**(4): p. 656-64.

179. Hays, J.P., Pelt-Verkuil, E. v., Belkum, A. v. , *Principles and Technical Aspects of PCR Amplification*. 2008, Niederlande: Springer Netherlands.

180. Rodriguez, A., et al., *Comparison of procedures for RNA-extraction from peripheral blood mononuclear cells*. PLoS One, 2020. **15**(2): p. e0229423.

181. Hu, P., M. Hegde, and P.A. Lennon, *Modern Clinical Molecular Techniques*. 2012: Springer New York.

182. Simmons, A. and J. Alberola-Ila, *Retroviral Transduction of T Cells and T Cell Precursors*. Methods Mol Biol, 2016. **1323**: p. 99-108.

183. Thorn, K., *Genetically encoded fluorescent tags*. Mol Biol Cell, 2017. **28**(7): p. 848-857.

184. Martinez-Salas, E., et al., *Insights into Structural and Mechanistic Features of Viral IRES Elements*. Frontiers in Microbiology, 2018. **8**.

185. Morita, S., T. Kojima, and T. Kitamura, *Plat-E: an efficient and stable system for transient packaging of retroviruses*. Gene Ther, 2000. **7**(12): p. 1063-6.

186. Vaeth, M., et al., *Store-Operated Ca(2+) Entry Controls Clonal Expansion of T Cells through Metabolic Reprogramming*. Immunity, 2017. **47**(4): p. 664-679.e6.

187. Coppola, C., et al., *Investigation of the Impact from IL-2, IL-7, and IL-15 on the Growth and Signaling of Activated CD4(+) T Cells*. Int J Mol Sci, 2020. **21**(21).

188. Iritani, B.M., et al., *Modulation of T-lymphocyte development, growth and cell size by the Myc antagonist and transcriptional repressor Mad1*. The EMBO journal, 2002. **21**(18): p. 4820-4830.

189. O'Connell, K.E., et al., *Practical murine hematopathology: a comparative review and implications for research*. Comparative medicine, 2015. **65**(2): p. 96-113.

190. Tan, T.C.J., et al., *Suboptimal T-cell receptor signaling compromises protein translation, ribosome biogenesis, and proliferation of mouse CD8 T cells*. Proc Natl Acad Sci U S A, 2017. **114**(30): p. E6117-E6126.

191. Obst, R., *The Timing of T Cell Priming and Cycling*. Frontiers in immunology, 2015. **6**: p. 563-563.

192. Franz-Viktor Salomon, H.G., Uwe Gille, *Anatomie für die Tiermedizin*, ed. Thieme. 2015.
193. Susaki, Etsuo A. and Hiroki R. Ueda, *Whole-body and Whole-Organ Clearing and Imaging Techniques with Single-Cell Resolution: Toward Organism-Level Systems Biology in Mammals*. Cell Chemical Biology, 2016. **23**(1): p. 137-157.
194. Cicchi, R., et al., *Contrast and depth enhancement in two-photon microscopy of human skin ex vivo by use of optical clearing agents*. Optics Express, 2005. **13**(7): p. 2337-2344.
195. Tuchin, V., *Tissue optics and photonics: Light-tissue interaction II*. J. Biomed. Photonics Eng, 2016. **2**(3): p. 030201.
196. Ding, Y., et al., *Light-sheet Fluorescence Microscopy for the Study of the Murine Heart*. J Vis Exp, 2018(139).
197. Richardson, D.S. and J.W. Lichtman, *Clarifying Tissue Clearing*. Cell, 2015. **162**(2): p. 246-257.
198. Susaki, E.A., et al., *Advanced CUBIC protocols for whole-brain and whole-body clearing and imaging*. Nat Protoc, 2015. **10**(11): p. 1709-27.
199. Valeur, B. and M.N. Berberan-Santos, *Molecular Fluorescence: Principles and Applications*. 2013: Wiley.
200. Ramos-Vara, J.A. and M.A. Miller, *When Tissue Antigens and Antibodies Get Along: Revisiting the Technical Aspects of Immunohistochemistry—The Red, Brown, and Blue Technique*. Veterinary Pathology, 2013. **51**(1): p. 42-87.
201. Yarilin, D., et al., *Machine-based method for multiplex in situ molecular characterization of tissues by immunofluorescence detection*. Scientific Reports, 2015. **5**(1): p. 9534.
202. Macey, M.G., *Flow Cytometry: Principles and Applications*. 2007: Humana Press.
203. Michl, M., *Basics Hämatologie*, ed. E.H. Sciences. 2019.
204. Cossarizza, A., et al., *Guidelines for the use of flow cytometry and cell sorting in immunological studies*. Eur J Immunol, 2017. **47**(10): p. 1584-1797.
205. McKinnon, K.M., *Flow Cytometry: An Overview*. Curr Protoc Immunol, 2018. **120**: p. 5 1 1-5 1 11.
206. Pockley, A.G., et al., *Immune Cell Phenotyping Using Flow Cytometry*. Curr Protoc Toxicol, 2015. **66**: p. 18 8 1-18 8 34.
207. Odell, I.D. and D. Cook, *Immunofluorescence techniques*. The Journal of

investigative dermatology, 2013. **133**(1): p. e4.

208. Im, K., et al., *An Introduction to Performing Immunofluorescence Staining*. Methods in molecular biology (Clifton, N.J.), 2019. **1897**: p. 299-311.
209. Adams, M.W., et al., *Light Sheet Fluorescence Microscopy (LSFM)*. Curr Protoc Cytom, 2015. **71**: p. 12 37 1-12 37 15.
210. Huisken, J. and D.Y.R. Stainier, *Selective plane illumination microscopy techniques in developmental biology*. Development (Cambridge, England), 2009. **136**(12): p. 1963-1975.
211. Ertürk, A. and F. Bradke, *High-resolution imaging of entire organs by 3-dimensional imaging of solvent cleared organs (3DISCO)*. Experimental Neurology, 2013. **242**: p. 57-64.
212. Tainaka, K., et al., *Whole-body imaging with single-cell resolution by tissue decolorization*. Cell, 2014. **159**(4): p. 911-24.
213. Alnuami, A.A., et al., *Oxyradical-induced GFP damage and loss of fluorescence*. Int J Biol Macromol, 2008. **43**(2): p. 182-6.
214. Amich, J., et al., *Three-Dimensional Light Sheet Fluorescence Microscopy of Lungs To Dissect Local Host Immune-Aspergillus fumigatus Interactions*. mBio, 2020. **11**(1).
215. Emmenlauer, M., et al., *XuvTools: free, fast and reliable stitching of large 3D datasets*. J Microsc, 2009. **233**(1): p. 42-60.
216. Vujic, A., N. Natarajan, and R.T. Lee, *Molecular mechanisms of heart regeneration*. Seminars in Cell & Developmental Biology, 2020. **100**: p. 20-28.
217. Lindsey, M.L., et al., *Guidelines for in vivo mouse models of myocardial infarction*. American Journal of Physiology-Heart and Circulatory Physiology, 2021. **321**(6): p. H1056-H1073.
218. Lindsey, M.L., et al., *Guidelines for experimental models of myocardial ischemia and infarction*. American Journal of Physiology-Heart and Circulatory Physiology, 2018. **314**(4): p. H812-H838.
219. Kass, D.A., J.M. Hare, and D. Georgakopoulos, *Murine Cardiac Function*. Circulation Research, 1998. **82**(4): p. 519-522.
220. Moghimi, S.M., *Mechanisms of splenic clearance of blood cells and particles: towards development of new splenotropic agents*. Advanced Drug Delivery Reviews, 1995. **17**(1): p. 103-115.
221. Perrin-Terrin, A.-S., et al., *The c-FOS Protein Immunohistological Detection: A Useful Tool As a Marker of Central Pathways Involved in Specific Physiological*

- Responses In Vivo and Ex Vivo*. Journal of visualized experiments : JoVE, 2016(110): p. 53613.
222. Singal, T., N.S. Dhalla, and P.S. Tappia, *Regulation of c-Fos and c-Jun gene expression by phospholipase C activity in adult cardiomyocytes*. Mol Cell Biochem, 2009. **327**(1-2): p. 229-39.
223. Takagawa, J., et al., *Myocardial infarct size measurement in the mouse chronic infarction model: comparison of area- and length-based approaches*. J Appl Physiol (1985), 2007. **102**(6): p. 2104-11.
224. Klocke, R., et al., *Surgical animal models of heart failure related to coronary heart disease*. Cardiovascular Research, 2007. **74**(1): p. 29-38.
225. Palumbo, M.L., et al., *Different effect of chronic stress on learning and memory in BALB/c and C57BL/6 inbred mice: Involvement of hippocampal NO production and PKC activity*. Stress, 2009. **12**(4): p. 350-361.
226. Tagawa, N., et al., *Strain differences of neurosteroid levels in mouse brain*. Steroids, 2006. **71**(9): p. 776-84.
227. Smith, J.C., *A Review of Strain and Sex Differences in Response to Pain and Analgesia in Mice*. Comparative medicine, 2019. **69**(6): p. 490-500.
228. Jirkof, P., et al., *Buprenorphine for pain relief in mice: repeated injections vs sustained-release depot formulation*. Lab Anim, 2015. **49**(3): p. 177-87.
229. Clark, T.S., D.D. Clark, and R.F. Hoyt, *Pharmacokinetic comparison of sustained-release and standard buprenorphine in mice*. Journal of the American Association for Laboratory Animal Science, 2014. **53**(4): p. 387-391.
230. Virag, J.I. and C.E. Murry, *Myofibroblast and endothelial cell proliferation during murine myocardial infarct repair*. Am J Pathol, 2003. **163**(6): p. 2433-40.
231. Naeije, R. and R. Badagliacca, *The overloaded right heart and ventricular interdependence*. Cardiovasc Res, 2017. **113**(12): p. 1474-1485.
232. Frey, A., et al., *Experimental heart failure causes depression-like behavior together with differential regulation of inflammatory and structural genes in the brain*. Frontiers in behavioral neuroscience, 2014. **8**: p. 376-376.
233. Frey, A., et al., *Cognitive Deficits and Related Brain Lesions in Patients With Chronic Heart Failure*. JACC: Heart Failure, 2018. **6**(7): p. 583-592.
234. Ambrosi, C.M. and E. Entcheva, *Optogenetic control of cardiomyocytes via viral delivery*. Methods in molecular biology (Clifton, N.J.), 2014. **1181**: p. 215-228.
235. Zaglia, T., et al., *Optogenetic determination of the myocardial requirements for extrasystoles by cell type-specific targeting of ChannelRhodopsin-2*. Proceedings of the

- National Academy of Sciences of the United States of America, 2015. **112**(32): p. E4495-E4504.
236. Vogt, C.C., et al., *Systemic gene transfer enables optogenetic pacing of mouse hearts*. Cardiovascular Research, 2015. **106**(2): p. 338-343.
237. Ambrosi, C.M., et al., *Optogenetics-enabled assessment of viral gene and cell therapy for restoration of cardiac excitability*. Scientific reports, 2015. **5**: p. 17350-17350.
238. Lyashkov, A.E., et al., *Cholinergic receptor signaling modulates spontaneous firing of sinoatrial nodal cells via integrated effects on PKA-dependent Ca(2+) cycling and I(KACh)*. American journal of physiology. Heart and circulatory physiology, 2009. **297**(3): p. H949-H959.
239. Dorne, J., *Impact of inter-individual differences in drug metabolism and pharmacokinetics on safety evaluation*. Fundamental & clinical pharmacology, 2004. **18**(6): p. 609-620.
240. Merrill, D.R., M. Bikson, and J.G.R. Jefferys, *Electrical stimulation of excitable tissue: design of efficacious and safe protocols*. Journal of Neuroscience Methods, 2005. **141**(2): p. 171-198.
241. Knisley, S.B., N. Trayanova, and F. Aguel, *Roles of Electric Field and Fiber Structure in Cardiac Electric Stimulation*. Biophysical Journal, 1999. **77**(3): p. 1404-1417.
242. Britin, S.N., M.A. Britina, and R.Y. Vlasenko, *Cardiac Conduction System: A Generalized Electrical Model*. Biomedical Engineering, 2021. **55**(1): p. 41-45.
243. Hanna, P., et al., *Innervation and Neuronal Control of the Mammalian Sinoatrial Node a Comprehensive Atlas*. Circ Res, 2021. **128**(9): p. 1279-1296.
244. Gordan, R., J.K. Gwathmey, and L.-H. Xie, *Autonomic and endocrine control of cardiovascular function*. World journal of cardiology, 2015. **7**(4): p. 204-214.
245. Hou, D., et al., *Radiolabeled Cell Distribution After Intramyocardial, Intracoronary, and Interstitial Retrograde Coronary Venous Delivery*. Circulation, 2005. **112**(9_supplement): p. I-150-I-156.
246. Liu, Z. and J.K. Donahue, *The Use of Gene Therapy for Ablation of Atrial Fibrillation*. Arrhythm Electrophysiol Rev, 2014. **3**(3): p. 139-44.
247. Li, X., et al., *Fast noninvasive activation and inhibition of neural and network activity by vertebrate rhodopsin and green algae channelrhodopsin*. Proceedings of the National Academy of Sciences of the United States of America, 2005. **102**(49): p. 17816-17821.

248. Khan, M.A., et al., *Global Epidemiology of Ischemic Heart Disease: Results from the Global Burden of Disease Study*. *Cureus*, 2020. **12**(7): p. e9349-e9349.
249. Hofmann, U. and S. Frantz, *Role of Lymphocytes in Myocardial Injury, Healing, and Remodeling After Myocardial Infarction*. *Circulation Research*, 2015. **116**(2): p. 354-367.
250. Contento, R.L., et al., *CXCR4-CCR5: a couple modulating T cell functions*. *Proceedings of the National Academy of Sciences of the United States of America*, 2008. **105**(29): p. 10101-10106.
251. Sommer, U., et al., *High-sensitivity flow cytometric assays: Considerations for design control and analytical validation for identification of Rare events*. *Cytometry B Clin Cytom*, 2021. **100**(1): p. 42-51.
252. Fischer, U.M., et al., *Pulmonary passage is a major obstacle for intravenous stem cell delivery: the pulmonary first-pass effect*. *Stem cells and development*, 2009. **18**(5): p. 683-692.
253. Tan, P., et al., *Optogenetic Immunomodulation: Shedding Light on Antitumor Immunity*. *Trends in biotechnology*, 2017. **35**(3): p. 215-226.
254. Rahnama, S., et al., *Super RLuc8: A novel engineered Renilla luciferase with a red-shifted spectrum and stable light emission*. *Enzyme and Microbial Technology*, 2017. **96**: p. 60-66.
255. Aswendt, M., et al., *Boosting bioluminescence neuroimaging: an optimized protocol for brain studies*. *PLoS One*, 2013. **8**(2): p. e55662.
256. Boyle Patrick, M., V. Karathanos Thomas, and A. Trayanova Natalia, *Cardiac Optogenetics: 2018*. *JACC: Clinical Electrophysiology*, 2018. **4**(2): p. 155-167.
257. Entcheva, E. and M.W. Kay, *Cardiac optogenetics: a decade of enlightenment*. *Nat Rev Cardiol*, 2021. **18**(5): p. 349-367.
258. Koopman, C.D., et al., *Cardiac optogenetics: using light to monitor cardiac physiology*. *Basic research in cardiology*, 2017. **112**(5): p. 56-56.
259. Vaccarino, V., et al., *Depression, Inflammation, and Incident Cardiovascular Disease in Women With Suspected Coronary Ischemia: The National Heart, Lung, and Blood Institute–Sponsored WISE Study*. *Journal of the American College of Cardiology*, 2007. **50**(21): p. 2044-2050.
260. Frantz, S., J. Bauersachs, and G. Ertl, *Post-infarct remodelling: contribution of wound healing and inflammation*. *Cardiovascular Research*, 2008. **81**(3): p. 474-481.
261. Marcus, G.M., et al., *Interleukin-6 and atrial fibrillation in patients with coronary artery disease: Data from the Heart and Soul Study*. *American Heart Journal*,

2008. **155**(2): p. 303-309.

262. Thompson, T.S., et al., *The effect of anxiety and depression on symptoms attributed to atrial fibrillation*. Pacing Clin Electrophysiol, 2014. **37**(4): p. 439-46.

263. Hulsmans, M., et al., *Macrophages Facilitate Electrical Conduction in the Heart*. Cell, 2017. **169**(3): p. 510-522 e20.

264. Carbone, F., et al., *Treatment with anti-RANKL antibody reduces infarct size and attenuates dysfunction impacting on neutrophil-mediated injury*. Journal of Molecular and Cellular Cardiology, 2016. **94**: p. 82-94.

265. Ellenbogen, K.A. and K. Kaszala, *Cardiac pacing and ICDs*. 2014: John Wiley & Sons.

266. Plotnikov, A.N., et al., *Xenografted Adult Human Mesenchymal Stem Cells Provide a Platform for Sustained Biological Pacemaker Function in Canine Heart*. Circulation, 2007. **116**(7): p. 706-713.

267. Sahel, J.-A., et al., *Partial recovery of visual function in a blind patient after optogenetic therapy*. Nature Medicine, 2021. **27**(7): p. 1223-1229.

268. Wang, D., P.W.L. Tai, and G. Gao, *Adeno-associated virus vector as a platform for gene therapy delivery*. Nature Reviews Drug Discovery, 2019. **18**(5): p. 358-378.

269. Bonagura, J.D., *Overview of Equine Cardiac Disease*. Vet Clin North Am Equine Pract, 2019. **35**(1): p. 1-22.

270. Fox, P.R., et al., *International collaborative study to assess cardiovascular risk and evaluate long-term health in cats with preclinical hypertrophic cardiomyopathy and apparently healthy cats: The REVEAL Study*. J Vet Intern Med, 2018. **32**(3): p. 930-943.

271. Häggström, J., V. Luis Fuentes, and G. Wess, *Screening for hypertrophic cardiomyopathy in cats*. Journal of Veterinary Cardiology, 2015. **17**: p. S134-S149.

272. Langhorn, R. and J.L. Willesen, *Cardiac Troponins in Dogs and Cats*. Journal of veterinary internal medicine, 2016. **30**(1): p. 36-50.

273. Molesan, A., et al., *The Causes of Canine Myocarditis and Myocardial Fibrosis Are Elusive by Targeted Molecular Testing: Retrospective Analysis and Literature Review*. Vet Pathol, 2019. **56**(5): p. 761-777.

274. Janus, I., et al., *Myocarditis in dogs: etiology, clinical and histopathological features (11 cases: 2007-2013)*. Ir Vet J, 2014. **67**(1): p. 28.

275. Friederich, J., A.C. Seuß, and G. Wess, *The role of atrial fibrillation as a prognostic factor in doberman pinschers with dilated cardiomyopathy and congestive heart failure*. The Veterinary Journal, 2020. **264**: p. 105535.

-
276. Wess, G., et al., *Doberman pinschers present autoimmunity associated with functional autoantibodies: A model to study the autoimmune background of human dilated cardiomyopathy*. Plos one, 2019. **14**(7): p. e0214263.

X. APPENDIX

1. Individual heart rate modulation in HCN4-Cre mice

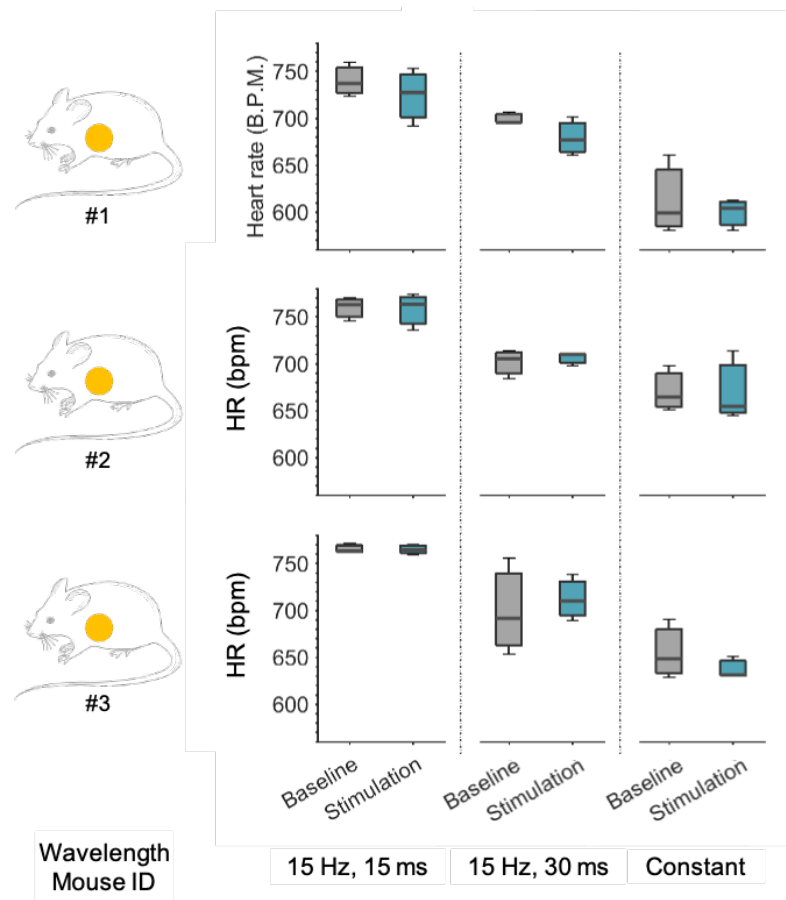


Figure 32| Individual effect of the different stimulation types in HCN4-cre mice implanted with an orange device

2. Digital appendix

Digital appendix containing the demonstration of the surgical procedure as well as videos of the illuminated thymus processed for LSFM and showing the three-dimensional distribution of the PA-CXCR4:

- Video 1: Cardiac Optogenetics - Device implantation on the left ventricle
- Video 2: Left thymus lobe
- Video 3: Right thymus lobe

XI. INDEX OF TABLES

Table 1 Scoring protocol from d0 to d3 post-surgery _____	23
Table 2 Scoring protocol from d4 post-surgery onwards _____	23
Table 3 Taken measures according to the scoring result _____	24
Table 4 Selected stimulation parameters for optogenetic stimulation of the ECS and cholinergic cardiac cells _____	48
Table 5 Properties of the primers used for qPCR _____	51
Table 6 qPCR-mastermix composition _____	53
Table 7 Thermal profile of the qPCR protocol set in the thermal cycle _____	53
Table 8 Antibodies and cell tracer for the detection of transferred PA-CXCR4-positive cells _____	67

XII. INDEX OF FIGURES

Figure 1 Milestones of the establishment of <i>in vivo</i> cardiac optogenetics based on two approaches with a common bottleneck	2
Figure 2 Structure and activation mechanism of microbial opsins	5
Figure 3 Electrical conduction system of the heart and action potential in the sinoatrial node	11
Figure 4 Myocardial healing phases after ischemic damage	15
Figure 5 Signaling pathway induced by CXCR4 activation	17
Figure 6 Thickness- and wavelength-dependent light absorption in the myocardium	26
Figure 7 NeuroLux Optogenetics System for wireless optical stimulation of implanted devices	27
Figure 8 Representative examples of transthoracic echocardiography in anesthetized mice	35
Figure 9 Cre-mediated opsin expression in cells of interest for spatial control of opsin expression	42
Figure 10 Structure and implantation of the ECG electrodes	47
Figure 11 Stimulation protocol for heart rate modulation	49
Figure 12 Engineering of photoactivatable CXCR4 (PA-CXCR4)	54
Figure 13 Summary of the steps to produce photoactivatable CD4 ⁺ lymphocytes	59
Figure 14 Gating strategy for PACXCR4 detection in different tissues by flow cytometry	69
Figure 15 LSM setup for whole organ imaging	72
Figure 16 Preparation of the device and surgery field	76
Figure 17 Step-by-step intrathoracic device implantation on the right ventricle <i>in vivo</i>	79
Figure 18 Weight evolution of the mice after left or right ventricular device implantation throughout the experiment	80
Figure 19 Histological assessment of myocardial damage after left and right ventricular device implantation	81
Figure 20 Transthoracic echocardiographic measurements of left and right ventricular heart function in anaesthetized mice	83
Figure 21 Experimental design for heart rate modulation	84
Figure 22 Heart rate change under optical stimulation in HCN4-Cre mice	86
Figure 23 Heart rate change under optical stimulation in ChAT-Cre mice	88
Figure 24 Individual effect of the different stimulation types in ChAT-Cre mice implanted with an orange or red device	90

Figure 25 Representative qPCR reactions obtained with custom-designed primers _	92
Figure 26 Assessment of viral transduction and expression of opsin and RFP by qPCR _____	94
Figure 27 Experimental design to induce migration of phototactic lymphocytes into illuminated tissue _____	95
Figure 28 <i>In vitro</i> photoactivation of PA-CXCR4 lymphocytes _____	96
Figure 29 Intrathoracic light diffusion pattern after whole-body clearing_____	97
Figure 30 Comparative FC analysis of left and right organ sides of illuminated and negative control mice _____	99
Figure 31 Morphological distribution of PA-CXCR4 in staining control and illuminated thymus _____	102
Figure 32 Individual effect of the different stimulation types in HCN4-cre mice implanted with an orange device_____	147

XIII. ACKNOWLEDGMENT

The establishment of cardiac optogenetics was an interdisciplinary project, involving numerous people who all were indispensable to the development of this challenging experimental study.

Foremost, I would like to express my deep gratitude to PD Dr. Anna Frey for her guidance and supervision during my whole thesis work, for her prompt answers, supporting words and fair decisions. I wish to thank Dr. Gustavo Ramos for giving me the opportunity to explore a lot of different scientific techniques, his creativity and true passion for science, which was encouraging throughout my thesis. I would like to thank Prof. Philip Tovote for his innovative contribution, always providing challenging ideas and pushing the limits. I also would like to thank Prof. Katrin Heinze for providing me direct and highly knowledgeable advices as well as giving me access to breakthrough imaging techniques. My grateful thanks are also extended to Prof. Thomas Göbel from the Faculty of Veterinary Medicine in Munich for his essential inputs during my thesis. Overall, thanks to all my research supervisors, for giving me insight into high-flying science, their patient guidance, encouragement and useful critiques of this research work. Thank you for trusting me, enabling me to learn numerous methods, and giving me the opportunity, besides practical work, to actively participate to scientific seminars as well as to the writing of experimental applications. Those three years had an intellectual value, but were and also a school for life.

Special thanks should be given to the team members from AG Ramos (Immuno Cardiology Lab), AG Tovote (Defense Circuits Lab), AG Heinze, AG Higuchi and AG Briese. I wish to especially thank Dr. Murilo Delgobo and Emil Weiss for their support for the production of photoactivable cells and FC analysis. I wish to thank Dr. Jérémy Signoret-Genest for his patience and numerous script adaptation, programming and data extraction. Thanks to Dr. Katherina Hemmen for her troubleshooting during LSFM-analysis and great general advices. Thanks to Dr. Paula Arias-Loza for her constant support, patient teaching of echocardiography in mice and introduction to microsurgery, always in a good mood. I also would like to thank Prof. Takahiro Higuchi, Dr. Paula Arias-Loza and Lars Mayer for their expertise to perform high-quality CT-imaging. Thanks also to Dr. Michael Briese and Saeede Salehi for their precious advices and help to design the qPCR primers. I would also like to extend my thanks to the technicians of the laboratories, including the staff of the animal facilities, of the Comprehensive Heart Failure Center (CHFC) and Institute of Clinical Neurobiology (ICN), for sharing their experience and troubleshoot with me. Thanks to the CHFC and ICN for their contribution in offering me the resources to run the project.

Finally, I wish to sincerely thank Vincent and my parents for their unconditional support, understanding and encouragement over the years.

Thanks to all the people helping me to establish cardiac optogenetics by thought and/or action.